IMPROVED TECHNIQUES FOR AERODYNAMIC FLOW CONTROL SIMULATION WITH FLUIDIC OSCILLATORS

A Dissertation
Presented to
The Academic Faculty

By

Nicholson Konrad Koukpaizan

In Partial Fulfillment
of the Requirements for the Degree
Doctor of Philosophy in the
School of School of Aerospace Engineering

Georgia Institute of Technology

August 2020

IMPROVED TECHNIQUES FOR AERODYNAMIC FLOW CONTROL SIMULATION WITH FLUIDIC OSCILLATORS

Approved by:

Prof. Marilyn J. Smith, Advisor
School of Aerospace Engineering
Georgia Institute of Technology

Prof. Ari Glezer
School of Mechanical Engineering
Georgia Institute of Technology

Prof. Stephen M. Ruffin
School of Aerospace Engineering
Georgia Institute of Technology

Dr. David M. Schatzman
Technology Development Directorate
U.S. Army CCDC AvMC

Ethan A. Romander
Code AV
NASA Ames Research Center

Date Approved: May 14, 2020

To my parents,

Colette and Vincent de Paul Koukpaizan

ACKNOWLEDGEMENTS

First, I would like to express my gratitude to my advisor, Prof. Marilyn Smith, for taking me under her guidance and for her support during my graduate career. To my thesis committee members, Prof. Ari Glezer, Prof. Stephen Ruffin, Dr. David Schatzman and Mr. Ethan Romander, I wish to express my sincere appreciation for their comments and suggestions.

I would like to thank all of the members of the Nonlinear Computational Aeroelasticity Laboratory with whom I have had the privilege of working with. A special thanks to Joachim Hodara for the tremendous effort he put in writing and validating GTsim during his PhD. Without GTsim, I would have had to seek alternative open computational tools or write my own code, which would have added several months, if not years to my journey. Thanks to those who helped develop and improve GTsim later on, including but not limited to Jimmy, Adam, Lucas and Dan. I am also grateful for the help I received in submitting large simulations the clusters I did not have direct access to. Thanks to Kevin Jacobson for introducing me to some of the most valuable tools I used in my day to day work and simply being the kind of researcher I have aspired to be.

Thanks to the members of the Fluid Mechanics Research Laboratory who conducted the flow control experiments I used to validate my computations, in particular Curtis Peterson who was the other graduate student on the project that funded this work. I was also fortunate to share a laboratory space with members of Structures and Multidisciplinary Design Optimization Laboratory. I have enjoyed having riveting discussions with Jan, Ting Wei, Mark and Komahan. More generally, thanks to everyone who made my stay at Georgia Tech more enjoyable. Last, but not least, I would like to thank my family and friends, in particular my parent, for their unwavering support.

This work was partially funded through the U.S. Army/Navy/NASA Vertical Lift Research Center of Excellence at Georgia Tech via Task 5 under the direction of Mahendra Bhagwat of ADD-A, Agreement No. W911W6-17-2-0002. Computational time was, in part, provided through the Department of Defense (DoD) high Performance Computing Modernization Program (HPCMP) from the DoD HPC Center AFRL DSRC. Roger Strawn was the S/AAA for this HPC time, and his support is gratefully acknowledged. The Partnership for an Advanced Computing Environment (PACE) at the Georgia Institute of Technology also provided computational resources for initial developments and testing of the code.

TABLE OF CONTENTS

LIST OF TABLES

LIST OF FIGURES

NOMENCLATURE

Abbreviations

2D	Two-dimensional
3D	Three-dimensional
AFC	Active Flow Control
ALE	Arbitrary Lagrangian-Eulerian
BFS	Backward-Facing Step
CFD	Computational Fluid Dynamics
DDES	Delayed detached-eddy simulation
DES	Detached-Eddy Simulation
DNS	Direct Numerical Simulation
FAFC	Fluidic Active Flow Control
FDS	Flux Difference Splitting
FVL	Future Vertical Lift
HRLES	Hybrid RANS-LES
JICF	Jet In Cross Flow
LDKM	Localized Dynamic Kinetic-Energy Model
LES	Large Eddy Simulation
LU-SSOR	Lower-Upper Symmetric Successive Overrelaxation
MUSCL	Monotone Upstream-Centered Schemes for Conservation Laws
NS	Navier-Stokes
OML	Outer Mold Line
PIV	Particle Image Velocimetry

RANS	Reynolds-Averaged Navier-Stokes
RTLT	RANS to LES transition
SA	Spallart-Allmaras
tHRLES	transitional Hybrid RANS-LES
TMR	Turbulence Modeling Resource
WENO	Weighted Essentially Non-Oscillatory
WMH	Wall-Mounted Hump

Dimensionless Groups

C_D	Drag coefficient, $D/(q_\infty A)$
C_f	Skin friction coefficient, τ_w/q_∞
C_L	Lift coefficient, $L/(q_\infty A)$
C_M	Pitching moment coefficient, $M/(cq_\infty A)$
C_p	Pressure coefficient, $(p - p_\infty)/q_\infty$
C_μ	Jet momentum coefficient
M	Mach number, $\sqrt{u^2 + v^2 + w^2}/a$
Pr	Prandtl number, $c_p\mu/\kappa$
Re	Reynolds number, UL/ν
St	Strouhal number, fD/U
y^+	Wall unit normalized wall distance, yu_τ/ν

Greek

α	Angle of attack
β	Angle of yaw
$\Delta\tau$	Pseudo time step
Δt	Physical time step
γ	Ratio of specific heats, c_p/c_v
$\mathbf{\Gamma_C}$	Preconditioning matrix based on conservative variables
$\mathbf{\Gamma}$	Preconditioning matrix based on primitive variables

$\mathbf{\Lambda}$	Diagonal eigenvalue matrix
$\mathcal{V}_r$	Contravariant velocity
μ	Molecular viscosity
μ_T	Eddy viscosity
ν	Kinematic viscosity, μ/ρ
ν_T	Turbulent kinematic viscosity, μ_t/ρ
Ω	Control volume
$\overline{\beta}$	Artificial compressibility factor
$\partial\Omega$	Surface enclosing the control volume Ω
ρ	Non-dimensional density
τ	Pseudo time
τ_w	Wall shear stress
τ_{ij}	Viscous stress tensor
Δ	Local grid spacing

Roman

$\mathbf{F}_c$	Conservative flux vector
$\mathbf{F}_v$	Viscous flux vector
$\mathbf{R}$	Residuals vector
$\mathbf{U}$	State vector of conservative variables
$\mathbf{W}$	State vector of primitive variables
$\mathcal{F}$	RANS/LES blending function
$\mathcal{L}$, $\mathcal{L}^{-1}$	Left and right eigenvector matrices
A	Reference area
a	Speed of sound
c	Chord length
c_p	Specific heat at constant pressure
c_v	Specific heat at constant volume

D	Diameter
f	Frequency
F^+	Non dimensional actuation frequency, $\frac{fL_{ref}}{V_{ref}}$
H	Stagnation enthalpy
k	Thermal conductivity
k	Turbulent Kinetic Energy (TKE)
L	Length
n_x, n_y, n_z	Unit normal vector components
p	Static pressure
Q	Q criterion, $\frac{1}{2}\left(R_{ij}Rij - S_{ij}S_{ij}\right)$
q	Dynamic pressure, $0.5\rho U^2$
R	Specific gas constant
R_{ij}	Symmetric velocity gradient tensor, $\frac{1}{2}\left(\frac{\partial u_i}{\partial x_j} + \frac{\partial u_j}{\partial x_i}\right)$
S_{ij}	Antisymmetric velocity gradient tensor, $\frac{1}{2}\left(\frac{\partial u_i}{\partial x_j} - \frac{\partial u_j}{\partial x_i}\right)$
T	Temperature
t	Physical time
Tu	Turbulence intensity $100\sqrt{\frac{2k/3}{u^2+v^2+w^2}}[\%]$
U	Velocity magnitude
u, v, w	Velocity components in the x, y and z directions respectively
u_τ	Friction velocity, $\sqrt{\tau_w/\rho}$

Subscripts and Superscripts

$(\ )_\infty$	Freestream
$(\ )_{ref}$	Reference

SUMMARY

Fluidic Active Flow Control (FAFC) has emerged as a promising technology to improve the performance of flight vehicles. Several key questions remain unanswered and hinder the implementation of FAFC at full-scale. This dissertation presents a detailed study of a specific type of FAFC: jet-interaction fluidic oscillators. These actuators generate oscillatory jets at their exit, when they are provided with a steady supply of pressurized fluid, without moving parts. Important questions regarding the internal flow physics, sweeping jet characteristics and mechanisms of flow separation control are addressed.

A state-of-the-art finite volume Computational Fluid Dynamics (CFD) solver was extended to enable the simulation of fluidic oscillators and their interactions with a separating shear layer. The extensions include a multiblock methodology, that was implemented to support block-structured grid topologies and permit the discretization of complex geometries such as fluidic oscillators. The ability to accurately compute high-speed flows and capture shock waves, warranted by the supersonic speeds encountered at the nozzle of the fluidic oscillators, was demonstrated.

The flow solver was utilized to resolve with high fidelity the behavior of an isolated jet-interaction fluidic oscillator generating a jet in a quiescent ambient. Time-accurate three-dimensional simulation were necessary to obtain oscillating jets free from spurious asymmetries. The mechanisms leading to the self-sustaining jet oscillations are discussed, and the correlation of the oscillation frequency and time-averaged velocity characteristics with experiments confirm the correct prediction of the relevant physics. The fully-resolved spatio-temporal characterization of the fluidic oscillator served as a basis for the development and validation of an improved boundary condition model. Such a model obviates the need to resolve the interior of the fluidic oscillator, when flow control applications are evaluated.

A wall-mounted model based on the VR-12 airfoil was designed computationally as part of this research, and it was subsequently evaluated experimentally by the Fluid Mechanics Research Laboratory at the Georgia Institute of Technology. The model integrates an array of fluidic oscillators to assess their effectiveness in controlling the otherwise separated flow. Computations of the unactuated and actuated flows were correlated with the experimental data for the first-order and second-order statistics, and the rich flow field provided by CFD permitted the assessment of the mechanisms governing the flow control. Finally, the new validated boundary condition model was leveraged to further explore the flow control design space and assess the effect of installation parameters such as the jet orientation and spacing.

CHAPTER 1
INTRODUCTION AND BACKGROUND

1.1 Motivation

The need for improved performance, reduced drag, and more energy efficient rotary-wing and fixed-wing vehicles has motivated the aerospace community to design and implement various flow control techniques. Active Flow Control (AFC), specifically fluidic Active Flow control (FAFC) has been identified as one of key transformative technologies for the future generation of vertical lift vehicles [1]. The global effectiveness of these techniques has been demonstrated in multiple scaled experiments, but the fundamental physics leading to the overall control is not yet fully understood [2]. Simulations can aid to fill many of the gaps in experiments by resolving features that are difficult to measure and evaluate new designs, but they also have their challenges [3]. This dissertation focuses on the development of computational techniques for a specific type of flow control technique: fluidic oscillators.

1.2 Literature review

1.2.1 Aerodynamic flow control

A multitude of flow control techniques have been designed to manipulate flow fields to achieve specific gains in performance, such as transition delay or trip, separation mitigation, lift enhancement, drag reduction, turbulence augmentation, or noise suppression [4]. Flow control techniques have been reviewed in detail in the literature. Gad-el-Hak published a series of papers describing flow control techniques and their evolution throughout the years [4–6]. Greenblatt and Wygnanski [7] reviewed the fundamentals and application of periodic excitation to control flow separation,

with a special emphasis on experimentation. Cattafesta and Sheplak [8] presented an overview of actuators for active flow control.

Flow control techniques can be categorized as illustrated in Fig. 1.1. Passive flow control techniques modify the surface geometries exposed to the flow, while AFC techniques add or subtract energy to the flow through a controlled actuator. Active techniques have two primary advantages over passive techniques: (1) AFC leverages and controls a natural stability of the flow to attain a large effect using small, localized energy input; (2) AFC can be used to control complex, dynamical processes such as turbulence production in turbulent boundary layers [9]. FAFC techniques have emerged as the preferred AFC technique due to their low power and high output behavior.

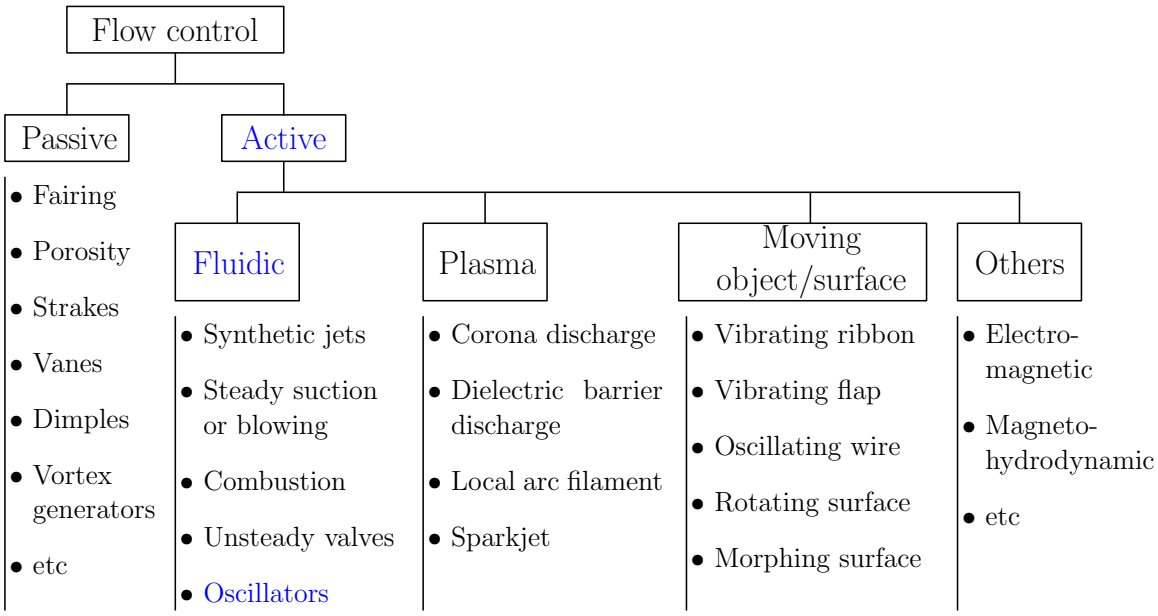

Figure 1.1: A type classification of flow control techniques, adapted from [8]

Greenblatt and Wygnanski [7] reviewed early investigations of periodic excitation for flow control, including both moving surfaces and fluidic actuation, with an emphasis on parameters governing the effectiveness of the techniques and experimental results available. At the time, fluidic periodic excitation consisted essentially in syn-

thetic jets, with or without steady blowing superimposed. The following parameters have been identified to be important in characterizing FAFC actuators:

- The mass flow coefficient is given by

$$C_Q = \frac{\dot{m}}{\rho_\infty V_\infty A} \,, \tag{1.1}$$

  where the time-averaged mass flow rate is

$$\dot{m} = \frac{1}{\tau} \int_0^\tau \oint_{\partial\Omega} \rho V dS dt \,, \tag{1.2}$$

  ρ and V are the local density and velocity in the plane of the jet orifice; ρ_∞ and V_∞ denote the freestream density and velocity; and A is a reference area.

- The definition of the jet momentum coefficient can be generalized as:

$$C_\mu = \frac{\overline{I}_j}{\frac{1}{2}\rho_\infty V_\infty^2 A} \,, \tag{1.3}$$

  where $\overline{I}_j$ is the time-averaged injection momentum flux given by

$$\overline{I}_j = \frac{1}{\tau} \int_0^\tau \oint_{\partial\Omega} \rho V^2 dS dt \,, \tag{1.4}$$

  The jet momentum is often only approximated in experiments if compressibility effects are present.

- The non-dimensional actuation frequency F^+, or reduced forcing frequency is defined as:

$$F^+ = \frac{f L_{ref}}{V_{ref}} \,, \tag{1.5}$$

  where f is the actuation frequency, L_{ref} is a characteristic length, and V_{ref} is a reference velocity, typically freestream velocity or speed of sound.

With vibrating flaps and synthetic jets, the generation and advection of large scale structures was identified as the mechanism affecting flow reattachment, as these structures transfer momentum to the otherwise separated layer. Reduced excitation frequency $F^+ \sim \mathcal{O}(1)$ was found to be effective for reattachment of separation prevention [7]. Higher F^+ values (2 to 4) are typically useful to fully suppress the

separation, while reattachment can be initiated at lower values. The corresponding momentum addition was on the order of a few percent ($0.01\% < C_\mu < 3\%$). More importantly, steady blowing was reported to require an order of magnitude higher momentum addition to be achieve performance gains comparable to periodic excitation on an airfoil [7]. When curvature effects are present, the actuator placement becomes an additional variable. Otherwise, actuators are traditionally placed as close to the separation point as possible.

Amitay and Glezer [10] notably reported effective flow control at high reduced forcing frequency ($F^+ \sim \mathcal{O}(10)$) using synthetic jets. They conducted experiments on a model consisting of a circular cylinder for its forward portion and a symmetric airfoil for its aft portion, that exhibits flow separation without actuation. Their results showed an unsteady attachment of the flow with actuation at $F^+ \sim \mathcal{O}(1)$, accompanied with the formation of large vortical structures. Actuation at $F^+ \sim \mathcal{O}(10)$ decouples the actuation from the natural instabilities of the flow, bypasses this unsteady attachment and maintains the flow attached without generating large scale structures.

1.2.2 Fluidic oscillators

One particularly promising FAFC technique is a fluidic oscillator to improve aerodynamic performance, including rotorcraft applications [11–16]. Martin et al. [14] observed a drag reduction on the order of 20% in their wind-tunnel experiments on the NASA ROBIN-mod7 fuselage with fluidic oscillators embedded in the fuselage ramp. Yadlin et al. [16] reported a 30% reduction in download by employing fluidic oscillators on a V-22 tilt-rotor during hover. In fixed-wing applications, this type of FAFC has been employed to enhance the effectiveness of the vertical tail [12]. Reduced actuation frequencies as high as $F^+ \simeq 80$ have been employed by DeSalvo et al. [17] to enhance the lift over a flapped airfoil by attaching the otherwise separated

flow over the flap. Fluidic oscillators also have applications in suppressing cavity oscillations [18]. Raghu [2], and Gregory and Tomac [19] provide reviews of fluidic oscillators, that include many more examples of their application.

A fluidic oscillator can be defined as a device without any moving parts that generates a sweeping or pulsing jet when supplied by a continuous pressurized fluid [8]. Fluidic oscillators are naturally unstable and capable of producing large disturbances to influence other flows. The sweeping or pulsing jets that are generated can reach sonic velocities, extending the control authority achievable to high subsonic flow, as encountered in full-scale applications [2]. They exist in various forms and shapes, and the most common actuators can be classified in two categories: bi-stable or wall-attachment (single or double feedback loop) and feedback-free (or jet interaction). These prominent configurations are illustrated in Fig. 1.2.

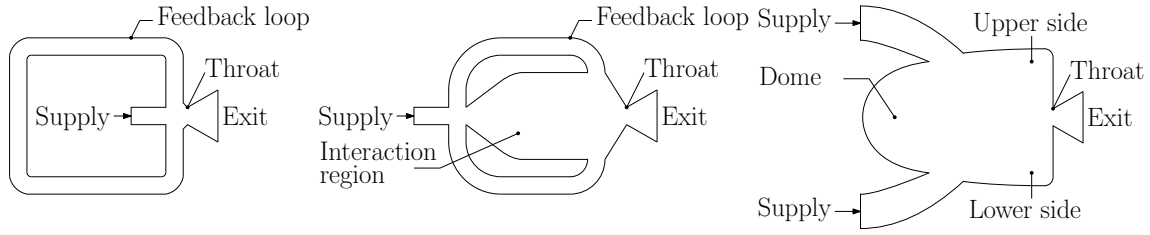

(a) Single feedback (b) Double feedback (c) Jet interaction

Figure 1.2: Common types of fluidic oscillators

In the bi-stable configurations, the jet oscillations are driven by the propagation of compression and expansion waves in the feedback tubes. These waves are created when the jet attaches to one of the two walls in the nozzle by Coendă effect. Pressure is lower between the wall and the jet attaching to it, and it is higher between the jet and the opposite wall. The jet is deflected towards the opposite wall when the disturbances created at one end of the feedback tube propagate to the other end.

Jet interaction fluidic oscillators rely on the natural instability that occurs when two supply jets meet in the interaction chamber. Part of each jet is periodically deflected towards the exit or towards the dome (left of the cavity), and recirculation

regions are formed in the upper and lower right corners of the cavity. As the recirculation region in the upper right corner grows, the upper supply jet is deflected towards the dome and away from the exit. Simultaneously, the recirculation region in the lower right corner shrinks, and the lower supply jet is pulled towards the exit. This process alternates naturally, provided the supply flow rates and pressures are adequate, giving rise to a sweeping jet at the exit of the device.

Fluidic oscillator designs can be enhanced with a splitter plate at the exit to reinforce the two dominant directions of the sweeping jet [20–22]. Other types of fluidic oscillators that do not fall into the two categories presented here have been reviewed by Campagnuolo and Lee [23].

Several physical phenomena are important in understanding the behavior of fluidic oscillators and how the technology can transfer efficiently on full-scale applications. The first subject of research is the cascade of internal mechanisms that lead to the generation of the pulsing or sweeping jets. In practical applications of fluidic oscillators to mitigate separation, the actuators are arranged into arrays, and integrated into the surface where separation occurs [2]. The self interaction between the sweeping jets, their interaction with the separated boundary layer, and the mechanisms leading to flow control constitute the second important and perhaps the least understood topic of research on fluidic oscillators. Separation and reattachment by themselves are complex phenomena to study, in particular in turbulent flows. A significant portion of the research on fluidic oscillators has been dedicated to defining scaling relations between different characteristics, such as flow rate, pressure ratio, oscillation frequency, and deflection angle. Both experiments and simulations have been employed to strengthen the community understanding of fluidic oscillators. Finally, the influence of jet momentum, spacing, frequency and orientation on the control effectiveness and efficiency are of interest, as with any flow control technique.

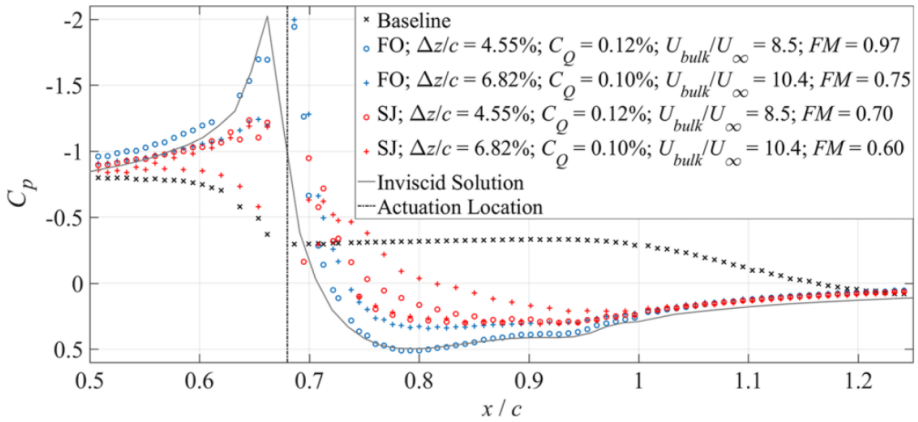

(a) Pressure coefficient distribution for $C_\mu = 2\%$

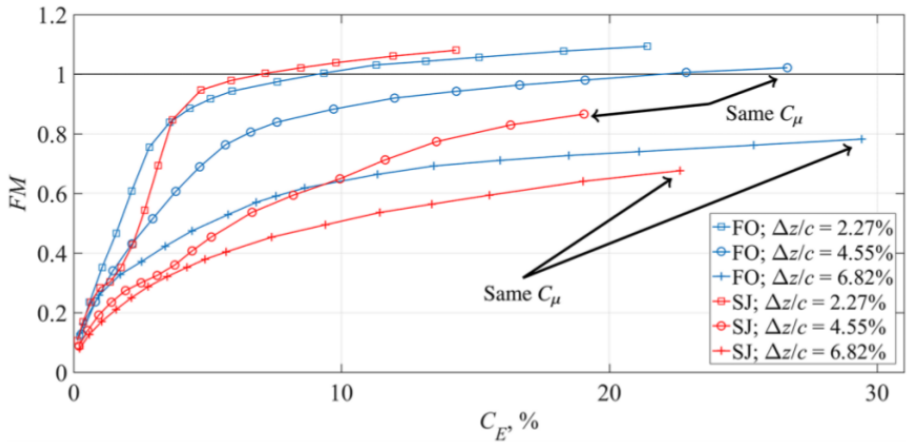

(b) Figure of merit

Figure 1.3: Comparison of steady jets and fluidic oscillators for flow separation control over the NASA wall-mounted hump(from Otto et al. [25])

Following earlier studies on periodic excitations, a few studies indicated that control of flow separation using sweeping jets is achieved not only by adding momentum directly to the boundary layer, but also by manipulating the vortical structure of the outer crossflow, thereby increasing turbulent mixing. Otto et al. [24, 25] experimentally demonstrated the superiority of sweeping jets, as compared to steady jets, to control the separation over the NASA wall-mounted hump (Fig. 1.3). To do so, they introduced two parameters to compare the two types of jets: the energy coefficient (C_E) and the actuation figure of merit (FM). The energy coefficient is defined as

$$C_E = \frac{p_{Actuator(g)}\dot{m}}{\frac{1}{2}\rho_\infty^2 V_\infty^3 A}\,, \tag{1.6}$$

where $p_{Actuator(g)}$ is the actuator gauge inlet pressure. The actuation figure of merit is a measure of the improvement from the baseline (unactuated) pressure distribution to the actuated pressure distribution, and it is given by

$$FM = \frac{\int_{x_1}^{x_2} |Cp_{actuated} - Cp_{baseline}|dx}{\int_{x_1}^{x_2} |Cp_{inviscid} - Cp_{baseline}|dx} \,. \tag{1.7}$$

The results of Otto et al. indicate that for a given momentum and energy coefficients, the fluidic oscillators yield a higher figure of merit than the steady jets, unless they are too close to one another (spacing $\Delta z/c = 2.2\%$ in Fig. 1.3). The superiority of fluidic oscillators was attributed to the presence of more coherent streamwise vortices formed due to the fluidic oscillators, a behavior that was also observed by other researchers [26, 27] during the interaction of sweeping jets with a crossflow over a flat plate.

1.2.3 CFD and turbulence modeling

The Navier-Stokes (NS) equations are a set of non-linear partial differential equations governing the behavior of fluids in a continuum. Due to their complexity, solutions on complex domains require intensive scientific computing giving rise to Computational Fluid Dynamics (CFD). More often than not, flows are turbulent, which significantly complicates the solution process. Three main approaches and their hybrids are employed, with varying degree of empiricism and computational cost: Direct Numerical Simulation (DNS), Large-Eddy Simulation (LES), and Reynolds-Averaged Navier-Stokes (RANS) turbulence models. Figure 1.4 summarizes the differences in the resolution of turbulent scales in DNS, RANS and LES.

In DNS, all space-time scales of the Navier-Stokes equations are resolved. These simulations become extremely expensive in the presence of turbulence and high Reynolds numbers, as the computational grids need to resolve the Kolmogorov microscale (η) [28], which is inversely proportional to $Re^{3/4}$. As a result, the number of points in a three-dimensional (3D) computational grid is proportional to $Re^{9/4}$ [29]. It follows that DNS is limited to academic applications at low Reynolds numbers, to under-

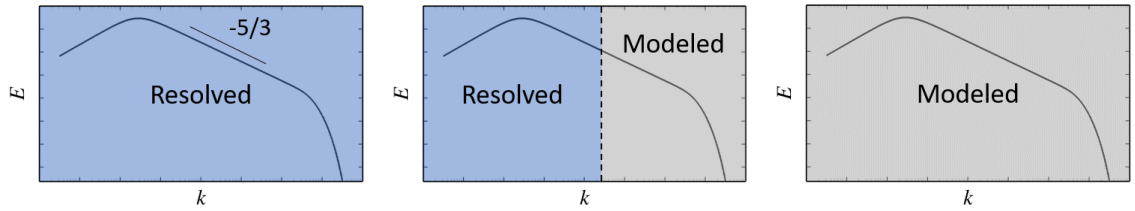

(a) DNS (b) LES (c) URANS

Figure 1.4: Illustration of resolved and modeled turbulent scales on a model energy spectrum

stand the fundamental nature of turbulence, while other models with a higher degree of empiricism are applied to realistic applications [30, 31].

Most commercial CFD solver use RANS and Unsteady RANS (URANS) approaches. Only the mean flow is resolved in the computational grid when these approaches are applied, while all turbulent scales are stochastically and empirically modeled. Turbulence models include simple algebraic models such as the Baldwin-Lomax [32], one-equation models like Spalart-Allmaras (SA) [33], two-equations models including $k-\omega$ Shear Stress Transport (SST) [34] and $k-\epsilon$ [35]. RANS approaches have been shown to be inadequate for massively separated and free shear flows [36–38]. More accurate methods are needed in these situations.

In LES, a spatial filter is applied to the NS equations, so that the large scales of motion are resolved with the computational grid, while the smaller scales (subgrid scales) are modeled [39]. Accurate LES for wall-bounded flows (Wall-Resolved LES, WRLES) requires to partially resolve the scales in the inertial subrange, which remains a restrictive requirement at high Reynolds numbers.

Hybrid RANS/LES (HRLES) closures offer a compromise between accuracy in separated flows, and computational cost. HRLES can be viewed as a Wall-Modeled LES (WMLES) [40, 41], where the turbulence is captured with URANS close to viscous walls and with LES away from the walls. The most widely used Hybrid RANS/LES closures are the Detached Eddy Simulation (DES) [42, 43] and its vari-

ants: Delayed DES (DDES) [44] and Improved DDES (IDDES) [45, 46]. DES closures lack the mechanisms to transfer momentum in the RANS to LES transition (RTLT) zone, which potentially leads to grid-induced separation, non-convergence of results upon successive grid refinements and "log-layer mismatch". The grid-related issues of the original DES were mitigated with the DDES formulation [44], where boundary layers are "shielded" from switching to LES, thereby increasing the extent of the RANS region. Several authors addressed the issue of log-layer mismatch in attached boundary layers by introducing an ad-hoc stochastic forcing or turbulent fluctuations at the interface between RANS and LES [47, 48]. The IDDES closure was designed to behave as WMLES when the inflow contains LES content and as DDES otherwise, and empirical adjustments to the model mitigated the log-layer mismatch issue [45].

Sánchez-Rocha [49] hybridized the $k-\omega$ SST model of Menter and the Localized Dynamic Kinetic-Energy Model (LDKM) of Kim and Menon [50] by applying the additive hybrid filter proposed by Germano [51]. He showed that the hybrid terms arising from the rigorous derivation of the hybridized equations are responsible for the proper transport of momentum in the RTLT zone. His HRLES simulations on an attached flat plate boundary layer did however require the implementation of realistic turbulent inflow boundary conditions. Hodara [52] later successfully deployed a transitional Hybrid RANS/LES (tHRLES) closure, combining the RANS-based Langtry-Menter $\gamma - Re_\theta$ transition model [53], and the fully turbulent HRLES closure of Sánchez-Rocha.

1.2.4 Numerical simulation of fluidic oscillators

Although the general principles of operation of fluidic oscillators are understood, the details of the resulting flow physics are not [8]. In particular, the nature of turbulence and the interaction of the sweeping jets with the separated flow remain the subject of active experimental and numerical research. High-fidelity numerical simulation can

provide a more detailed examination of the flow field that cannot be measured in experiments.

Two-dimensional computations

One of the first accurate CFD simulations of the internal flow in a fluidic oscillator was performed by Gokoglu et al. [54]. The geometry they employed had a double feedback loop, as well as a diverter at the nozzle. They performed two-dimensional (2D) simulations in Fluent 6 [55] with the $k-\omega$ SST-URANS turbulence model, and the resulting oscillation frequencies were in excellent agreement with experiments for frequencies as high as 7 kHz and peak Mach numbers as high as 2.6. Similarly, Krüger et al. [56] performed primarily 2D URANS simulations in ANSYS CFX [57] on a double feedback loop fluidic oscillator. The oscillation frequency in the simulations were within the 5% error band of the experiments. Krüger et al. also evaluated the sensitivity of the results to the grid, the outlet boundary condition and the turbulence model. Their 3D simulation resulted in a higher error in the oscillation frequencies (7.5%), which they attributed to their large time step and the presence of nonlinear effects such as separated flows. They concluded that the two-dimensional simulations were sufficient to obtain the correct oscillation frequencies.

Sitter [58] compared three different types of fluidic oscillators (single feedback, double feedback, and jet interaction) computationally and experimentally. The numerical studies were conducted with the modified Launder-Reece-Rodi Reynolds Stress model in ANSYS Fluent [55] on 2D grids. Frequencies up to 1 kHz were simulated, and though the slope of the linear increase of oscillation frequency with mass flow was correctly predicted by CFD, the frequencies were under-estimated with approximately 40% error. Sitter also noted a discrepancy between the experimental and simulated internal flow dynamics of the feedback-free fluidic oscillator, that is flow field inside the device cavity at a phase angle of π rad is not a mirror image

of that at 0 rad. This discrepancy persisted after time step refinements and longer simulation times.

Pandey and Kim [59] evaluated a double feedback loop fluidic oscillator with ANSYS CFX [57]. They applied the $k-\omega$ SST turbulence model to a 3D computational domain, making use of wall functions to reduce the computational cost. The resulting oscillation frequency (12.35 Hz on their finest mesh) was within 1.1% of the experiments.

Two-dimensional simulations [54, 56, 58, 59] generally limit their focus on the jet sweeping frequency and internal dynamics rather than the characteristics of the jets after they exit the fluidic oscillators.

Three-dimensional computations

Three-dimensional simulation have been employed in flow control applications and to better characterize the isolated jets.

Aram et al. [60] recently proposed a detailed computational analysis of the double feedback loop fluidic oscillator simulated by Krüger et al. [56]. They evaluated not only the oscillation frequencies, but also the jet width and time-averaged velocity profiles in the case of the sweeping jet in quiescent flow condition. They observed that 2D URANS simulations performed well at low supply mass flow rates for the prediction of the oscillation frequency, but were inadequate in predicting the characteristics of the ensuing sweeping jet. At higher supply mass flow rates, the oscillation frequency predicted by 2D URANS became less accurate, with up to 7.58% relative error compared to experiments. The numerical predictions of the oscillation frequency improved with 3D URANS and even more with 3D IDDES. The 3D IDDES approach predicted the oscillation frequencies within 1% relative error at high supply mass flow rates and proved to be necessary to capture the jet width and velocity profiles. The 2D URANS approach was not able to capture any of the key features of the

sweeping jet, over-predicting its velocity and penetration. The 3D URANS approach more accurately predicted both of these aspects, but the discrepancies remained significant compared to 3D IDDES. An important consideration in these studies is that the fluidic oscillator are large enough to permit Particle Image Velocimetry (PIV) measurements of the internal cavity, resulting in low oscillation frequency (approximately 5-20 Hz in this case), and essentially incompressible flow. The complexity of the computations increases as the scale of the actuators is decreased.

Schatzman et al. [61] evaluated the interaction between SaOB (Suction and Oscillatory Blowing) actuators and boundary layers. These actuators combine suction with a bi-stable fluidic oscillator. They performed a simulation of the internal flow and defined boundary conditions for future computations. They solved the incompressible Navier-Stokes equations with a DES closure for turbulence. During the simulation of the isolated actuator, they obtained a 10% and 30% deviation between computation and experiments for blowing and suction respectively. The differences were attributed to the complexity of the simulation and the assumption of incompressible flow though high subsonic flow conditions were encountered in the domain. The derived boundary conditions were obtained by a curve-fit of the variation of the actuator exit velocity in time and space, and there was no indication of the inclusion of turbulence in the formulation. Wilson et al. [62] reported the application of this modeling approach, though they provided little discussion on the effectiveness or accuracy of the approach.

Lakebrink et al. [63] performed three-dimensional simulations of a jet interaction fluidic oscillator and evaluated the effect of an array of such oscillators (21) on reducing the separation in an S-Duct diffuser. Little information was provided on the simulation parameters for a single oscillator. The results for the isolated fluidic oscillator indicated a 10% over-estimation of the oscillation frequency by the computational approach. The discrepancies were attributed to differences between the

simulated geometry and the bench-tested geometry. The authors' attempts to define a time-dependent boundary condition at the oscillators' throat or exit in the larger-scale simulation were not successful. The final solution consisted in only neglecting the supply region and resolving the actuators' plenum and throat. This approach provides little gain in computational cost compared to resolving the entire actuator internal flow.

Duda et al. [64] applied the Lattice-Boltzmann solver PowerFLOW [65] to a double feedback loop fluidic oscillator. Their turbulence modeling approach is a wall-modeled VLES (Very Large Eddy Simulation) on a 3D domain. The velocity contours outside the actuators showed significant differences between computations and experiments. The velocity decay was underestimated by the simulations. Based on the PSD (Power Spectral Density) of pressure at different points in the domain, the frequencies were generally over-predicted by the computations. Finally, pressure levels were initially overestimated in the simulations, and the authors had to increase the inlet stagnation pressure while maintaining the same mass flow in the simulations to match the experiments. Vatsa et al. [66, 67] used a similar numerical approach to simulate the internal flow of the fluidic actuators and the control of separation on a rudder integrating 32 actuators simultaneously (Figure 1.5). They compared the computational surface pressure distributions and integrated loads to wind-tunnel test data with approximately 10% error on the integrated loads. Since this approach relies on a time-accurate solution for the flow inside all actuators, it is relatively expensive.

Childs et al. [68] carried out the simulation of an isolated sweeping jet actuator and derived a boundary condition to evaluate the effect on a full Boeing 757 vertical tail containing 31 actuators. They applied SST-URANS and SST-DDES approaches in the CFD solver OVERFLOW [69]. They observed that the URANS approach resulted in a better solution for the internal flow than DDES. As a result, they opted

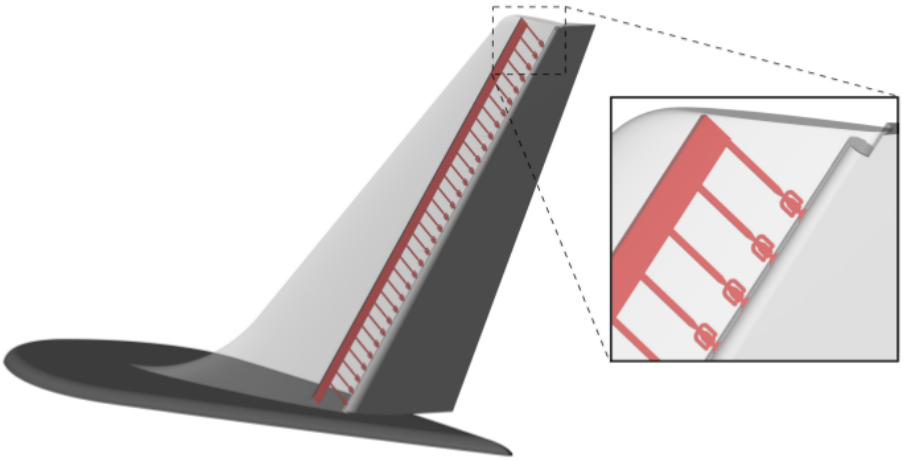

Figure 1.5: Actuator setup employed by Vatsa et al. [67]

to use URANS for the internal flow and DDES for the external flow. The resolution of frequencies in the simulation was limited by the short duration of the simulation. Although the shapes of the mean velocity distributions were in agreement with experiments, there were approximately $20-30\%$ difference in the values. The boundary conditions derived from the simulation of a single actuator consisted in specifying all time-dependent states at the actuator throats. Several corrections were applied to the raw data generated by the single oscillator simulation to ensure periodicity and permit interpolation of the variables onto the large-scale problem grids. The validation of the boundary condition was obtained with the sweeping jet in quiescent flow. The boundary condition resulted in agreement with experiments for the full vertical tail pressure coefficient distribution and integrated loads, though the actual values were not provided. The strength of the boundary condition described in this paper is the specification of all quantities, including turbulent variables. On the basis of the grid sizes, the authors estimated that the boundary condition reduced the computational cost by an order-of-magnitude. They reported that the simulation of the flow control application required approximately $715,000$ CPU hours, by taking advantage of the boundary condition.

Following their computations in a quiescent ambient [60] and the work of Childs et al. [68], Aram et al. [70] also developed a boundary condition model of their fluidic oscillators. The boundary condition was applied to evaluate the control of flow separation over the NASA wall-mounted hump. They investigated the effect of phase synchronization between two sweeping jets and showed that setting the phase shift at 0°, 60° or 180° resulted in a few percent variation in the pressure distributions. The pressure coefficients were overestimated by 20-30% in both the unactuated and actuated flows.

Shmilovich et al. [71] performed 3D simulations of double feedback loop fluidic oscillators from the characterization of the isolated oscillator in quiescent conditions to their application on the vertical tail of the Boeing 757 ecoDemonstrator airplane. In the latter case, the internal flow of each oscillator was resolved. They applied SST-URANS in the CFD solver OVERFLOW. The oscillation frequencies were on the order of 300 Hz and the computational predictions of the frequencies were within 5% of the experiments. Discrepancies were observed in the sweeping jet time-averaged velocity field and the pressure distributions at different sections of the vertical tail. These discrepancies were attributed to the turbulence model, uncertainties in the experimental setups and in the full-scale flight test [72]. In these studies, the side force could be increased by 14% at 30° rudder deflection over a critical range of sideslip angles corresponding to engine failure scenarios. The authors noted challenges associated with scaling the AFC from wind-tunnel tests to flight test, resulting in greater effectiveness in the wind tunnel. The main factors reported were a 16% difference in Mach number and rudder installation in the wind-tunnel. Computations proved very helpful in elucidating the effects of these variations.

Shmilovich and Vatsa [73] recently proposed a review of practical computational techniques that they have employed for flow control applications. The URANS (Unsteady Reynolds-Averaged Navier-Stokes) and Lattice-Boltzmann (with Very Large-

Eddy Simulation) approaches were reported to efficiently provide engineering accuracy at computational costs that were claimed to be practical. The reported computational cost (URANS) was approximately 30,000 CPU hours for actuators with an oscillation frequency of 225 Hz integrated into a Boeing 757 vertical tail. The computational cost is expected to increase with the oscillation frequency. Furthermore, as previously discussed, URANS has previously been shown to be insufficient for certain fluidic oscillators [60]. The accuracy of URANS in the simulation of fluidic oscillators seems to depend strongly on the type of devices, their oscillation frequencies and the relevant spatio-temporal scales involved.

1.2.5 Boundary conditions for large-scale simulations of fluidic oscillators arrays

The simultaneous simulation of flow control devices poses several challenges and therefore there exist very few widely accepted boundary conditions for active flow control.

For passive, porous surfaces, Frink et al. [74] presented a numerical boundary condition. While porosity is experimentally obtained by creating holes on the surface of interest, the boundary condition proposed by Frink et al. eliminates the need to construct a grid that is body-fitted to the hole configuration and the underlying plenum. In the model, a porous wall is characterized by its solidity s (closed surface divided by the total surface):

$$s = \frac{A_{solid}}{A_{total}} \, . \tag{1.8}$$

The plenum pressure is determined in the solution process, and the velocity normal to the wall and the pressure at the boundary are computed with isentropic relations. The approach was demonstrated on a 5.0-Caliber Tangent-Ogive Forebody and a General Aviation Whitcomb (GA(W)-1) wing. In both cases, the numerical simulations recovered the pressure coefficient distributions, and integrated lift and drag.

There are currently no such high-level boundary condition for active fluidic flow control in the published literature. The least expensive approaches employed for

fluidic oscillators consist in generating a boundary condition based on the simulation of a single device in a quiescent ambient. That boundary condition is then applied for each of the devices present in the large-scale configuration. As discussed in the previous section, this approach was applied by Childs et al. [68] and Aram et al. [70] on a double feedback loop fluidic oscillator. A similar boundary condition has not been derived for a jet interaction fluidic oscillator.

1.3 Thesis objectives

1.3.1 Conclusions from the literature review

The numerical simulation of fluidic oscillators has visibly drawn researchers' attention over the past decade. However, best practices to perform accurate simulations have yet to be clearly identified, resulting in different conclusions in the published literature. Many numerical simulations in the literature have been restricted to two-dimensional domains or URANS approaches. Recent studies [60] have demonstrated that while three-dimensional LES-based approaches are not always necessary to predict the oscillation frequencies, they are indispensable to capture the jet characteristics.

There exist very few accurate predictions of the sweeping jet time-averaged velocity distributions. The reasons for these discrepancies must be identified and addressed for CFD to become a reliable tool for such applications. Turbulence appears to be one key factor, as LES-based techniques have generally produced more accurate results. The resolution of the flow inside multiple fluidic oscillators to evaluate their effect on separation remains computationally expensive, making accurate approaches to model these oscillators necessary for design and analysis in engineering situations. Understanding the interaction between these actuators and other flows of interest remains an open problem. The computations of flow control applications [68, 70, 71] remain restricted to first-order statistics such as the time-averaged pressure and velocity. In-

vestigating the turbulent interactions can provide additional insight into the physics and further validation of the computational codes. Finally, numerical simulations of fluidic oscillators have primarily been devoted to double feedback loop variants, with little attention to feedback-free devices.

1.3.2 Overall thesis objectives

Following this literature review, the objectives of the proposed dissertation are:

1. To evaluate the internal physics of a feedback-free fluidic oscillator with high fidelity simulations. Unlike double feedback loop sweeping jet actuators, there are few studies of the flow inside feedback-free fluidic oscillators. Detailed analyses from CFD is especially lacking. The internal flow dynamics are investigated in details in this work and the physics are qualitatively compared to experimental observations reported in the literature.

2. To quantitatively characterize and correlate with experiments the relation between oscillation frequency, volume flow rate and pressure ratio.

3. To quantitatively characterize and correlate with experiments the physics of the sweeping jets in the external flow field, including turbulence.

4. To study the interactions between a sweeping jet and a flow of interest, and identify the physical mechanisms leading to flow reattachment. There is a fundamental lack of understanding of the flow control mechanisms and jet interactions, as many details of the flow cannot be assessed experimentally. In this work, the simulated first-order and second-order statistics are correlated with experiments, and the computations were leveraged to further understand the physics.

5. To develop and validate an outer mold line (aerodynamic surface) boundary condition for arrays of fluidic oscillators. Boundary condition models of flu-

idic oscillators are needed to reduce the computational costs and enable rapid assessment of flow control applications. A step-by-step approach is applied towards the identification of the relevant information that must be encoded in the models and evaluate the accuracy of different approaches.

1.3.3 Thesis outline

The remainder of this dissertation is articulated as follows:

- The CFD solver is introduced in Chapter II, with references to the initial implementation, and the new developments required to tackle the flow control applications considered. In particular, the initial single-block solver was extended with a multiblock approach in order to solve around more complex geometries. Test cases are presented to demonstrate the validity of the implemented methods.
- With the enhanced flow solver, a fluidic oscillator was simulated in a quiescent ambient to assess its characteristics (jet oscillation frequency, internal flow dynamics, external jet penetration and spreading). The results are presented in Chapter III and compared to experimental data. Several boundary condition models of the fluidic oscillator are presented and assessed.
- Chapter IV presents the design of a VR-12 airfoil-based wall-mounted model that exhibits flow separation without actuation, and the mitigation of that separation when actuation is applied via a spanwise array of fluidic oscillators. Computations are validated with experimental data, and the boundary condition models of the fluidic oscillator are leveraged to further explore the flow control design space.

CHAPTER 2

COMPUTATIONAL TOOLS

A state-of-the-art CFD solver, GTsim, initially developed by Hodara [52], is employed in this work. The code is finite-volume (cell-centered) and operates on structured grid topologies to achieve high efficiency and numerical accuracy. In this chapter, the numerical schemes implemented in GTsim will be described. The validation of the initial code was performed by Hodara [52]. Several extensions to the initial code have been added for flow control applications as part of the research in this thesis. Further validation of these extensions is included in section 2.5.

2.1 Governing equations

The unsteady compressible Navier-Stokes equations applied to a moving rigid body can be written in integral form as:

$$\frac{\partial}{\partial t}\int_{\Omega}\mathbf{U}dV + \oint_{\partial\Omega}\left(\mathbf{F_c}-\mathbf{F_v}\right)dS = 0\ , \tag{2.1}$$

where Ω represents the control volume and $\partial\Omega$ its enclosing surface. The Arbitrary Lagrangian-Eulerian (ALE) formulation is used for rigid-body rotations and translations [75], so that the state vector $\mathbf{U}$ and normal convective flux vector $\mathbf{F_c}$ are given by

$$\mathbf{U} = \begin{pmatrix} \rho \\ \rho u \\ \rho v \\ \rho w \\ \rho E \end{pmatrix} \qquad \text{and} \qquad \mathbf{F_c} = \begin{pmatrix} \rho\mathcal{V}_r \\ \rho u\mathcal{V}_r + n_x p \\ \rho v\mathcal{V}_r + n_y p \\ \rho w\mathcal{V}_r + n_z p \\ \rho H\mathcal{V}_r + \mathcal{V}_t p \end{pmatrix}\ . \tag{2.2}$$

$\mathbf{n} = (n_x, n_y, n_z)$ is the normal vector at the interface and $\mathcal{V}_r$ is the contravariant velocity relative to the grid motion $\mathbf{V}_t = (u_t, v_t, w_t)$:

$$\mathcal{V}_r = n_x u + n_y v + n_z w - n_x u_t + n_y v_t + n_z w_t = \mathcal{V} - \mathcal{V}_t \; . \tag{2.3}$$

The equation of state is that of a perfect gas, while the total energy is related to the total enthalpy:

$$\rho E = \frac{p}{\gamma - 1} + \frac{\rho}{2}\left(u^2 + v^2 + w^2\right) \qquad \text{and} \qquad \rho H = \rho E + p \, . \tag{2.4}$$

Some turbulence closures include additional equations for the turbulent kinetic energy, which must be included in Eq. (2.4). The viscous fluxes $\mathbf{F}_v$ are given by:

$$\mathbf{F}_v = \begin{pmatrix} 0 \\ n_x\tau_{xx} + n_y\tau_{xy} + n_z\tau_{xz} \\ n_x\tau_{xy} + n_y\tau_{yy} + n_z\tau_{yz} \\ n_x\tau_{xz} + n_y\tau_{yz} + n_z\tau_{zz} \\ n_x\Theta_x + n_y\Theta_y + n_z\Theta_z \end{pmatrix} \tag{2.5}$$

with

$$\begin{aligned} \Theta_x &= u\tau_{xx} + v\tau_{xy} + w\tau_{xz} - q_x \\ \Theta_y &= u\tau_{xy} + v\tau_{yy} + w\tau_{yz} - q_y \\ \Theta_z &= u\tau_{xz} + v\tau_{yz} + w\tau_{zz} - q_z \; . \end{aligned} \tag{2.6}$$

As the flow is Newtonian, the viscous stress and strain-rate tensors are linearly related:

$$\begin{aligned} \tau_{xx} &= \frac{2}{3}\frac{M_\infty}{Re}\left(\mu + \mu_T\right)\left(2\frac{\partial u}{\partial x} - \frac{\partial v}{\partial y} - \frac{\partial w}{\partial z}\right) \\ \tau_{yy} &= \frac{2}{3}\frac{M_\infty}{Re}\left(\mu + \mu_T\right)\left(2\frac{\partial v}{\partial y} - \frac{\partial u}{\partial x} - \frac{\partial w}{\partial z}\right) \\ \tau_{zz} &= \frac{2}{3}\frac{M_\infty}{Re}\left(\mu + \mu_T\right)\left(2\frac{\partial w}{\partial z} - \frac{\partial u}{\partial x} - \frac{\partial v}{\partial y}\right) \\ \tau_{xy} = \tau_{yx} &= \frac{M_\infty}{Re}\left(\mu + \mu_T\right)\left(\frac{\partial u}{\partial y} + \frac{\partial v}{\partial x}\right) \\ \tau_{yz} = \tau_{zy} &= \frac{M_\infty}{Re}\left(\mu + \mu_T\right)\left(\frac{\partial w}{\partial y} + \frac{\partial v}{\partial z}\right) \\ \tau_{xz} = \tau_{zx} &= \frac{M_\infty}{Re}\left(\mu + \mu_T\right)\left(\frac{\partial u}{\partial z} + \frac{\partial w}{\partial x}\right) \end{aligned} \tag{2.7}$$

while the heat flux vector is

$$
\begin{aligned}
q_x &= -\frac{M_\infty}{Re\,(\gamma-1)}\left(\frac{\mu}{Pr}+\frac{\mu_T}{Pr_t}\right)\frac{\partial T}{\partial x} \\
q_y &= -\frac{M_\infty}{Re\,(\gamma-1)}\left(\frac{\mu}{Pr}+\frac{\mu_T}{Pr_t}\right)\frac{\partial T}{\partial y} \\
q_z &= -\frac{M_\infty}{Re\,(\gamma-1)}\left(\frac{\mu}{Pr}+\frac{\mu_T}{Pr_t}\right)\frac{\partial T}{\partial z}\,.
\end{aligned}
\tag{2.8}
$$

These equations are written in non-dimensional form, which yields the freestream Mach number M_∞, Reynolds number Re and Prandtl number Pr. The dimensional variables (denoted by a tilde) are non-dimensionalized as follows:

$$
\begin{gathered}
\rho = \frac{\tilde{\rho}}{\tilde{\rho}_\infty} \qquad u = \frac{\tilde{u}}{\tilde{a}_\infty} \qquad v = \frac{\tilde{v}}{\tilde{a}_\infty} \qquad w = \frac{\tilde{w}}{\tilde{a}_\infty} \qquad p = \frac{\tilde{p}}{\tilde{\rho}_\infty \tilde{a}_\infty^2} \\
e = \frac{\tilde{e}}{\tilde{\rho}_\infty^2 \tilde{a}_\infty^2} \qquad a = \frac{\tilde{a}}{\tilde{a}_\infty} \qquad T = \frac{\tilde{T}}{\tilde{T}_\infty} = \frac{\gamma p}{\rho} = a^2 \qquad \mu = \frac{\tilde{\mu}}{\tilde{\mu}_\infty} \\
x = \frac{\tilde{x}}{\tilde{L}_R} \qquad y = \frac{\tilde{y}}{\tilde{L}_R} \qquad z = \frac{\tilde{z}}{\tilde{L}_R} \qquad t = \frac{\tilde{t}\tilde{a}_\infty}{\tilde{L}_R}\,,
\end{gathered}
\tag{2.9}
$$

where $\tilde{\rho}_\infty$, $\tilde{a}_\infty$, $\tilde{T}_\infty$ and $\tilde{\mu}_\infty$ are respectively the freestream density, speed of sound, static temperature and molecular viscosity. If $\tilde{L}$ is the physical characteristic length of the problem (in meters, feet, etc.), the corresponding length in the grid can be defined as L_{ref}. The Reynolds number in Eq. (2.7)-(2.8) is the Reynolds number based on $\tilde{L}_R = \tilde{L}/L_{ref}$, i.e. the Reynolds number per unit grid length. The Reynolds number, Mach number and Prandtl number are

$$
Re = \frac{\tilde{\rho}_\infty \tilde{V}_\infty \tilde{L}_R}{\tilde{\mu}_\infty} \qquad M_\infty = \frac{\tilde{V}_\infty}{\tilde{a}_\infty} \qquad Pr = \frac{C_p \tilde{\mu}_\infty}{\tilde{k}_\infty}\,,
\tag{2.10}
$$

respectively, with $\tilde{V}_\infty$ the velocity magnitude in the freestream. The Prandtl number can be assumed in this work to be constant ($Pr \simeq 0.72$ for air at moderate temperatures), while the molecular viscosity is obtained as a function of temperature using Sutherland's formula:

$$
\tilde{\mu} = \frac{C_1 \tilde{T}^{3/2}}{\tilde{T} + C_2}\,,
\tag{2.11}
$$

where the constants C_1 and C_2 are gas-dependent. For air at moderate temperatures, $C_1 = 1.458 \times 10^{-6}$ kg/(m.s.K$^{1/2}$) and $C_2 = 110.4$ K.

2.2 Numerical schemes

2.2.1 Spatial and temporal discretization

The original spatial and temporal discretization schemes in GTsim were not modified, except for terms affected by the addition of a preconditioner, as discussed in section 2.2.2. Here, a brief summary of the schemes is included for completion; the reader is referred to Hodara [52] for a detailed description.

Temporal discretization is achieved in physical time with second-order backward differencing. The implicit formulation permits larger time steps. However, it requires the computation of the flux Jacobian.

Three spatial discretization schemes were initially implemented in GTsim for the convective fluxes including second and fourth-order central-differences [76], as well as Roe's Flux Difference Splitting (FDS) [77] combined with van Leer's Monotone Upstream-Centered Schemes for Conservation Laws (MUSCL) reconstruction [78] at the interface. The central difference schemes are limited to low Mach number flows, while Roe's scheme is employed at compressible speeds, including supersonic flows.

In addition to the schemes initially implemented by Hodara, a fifth-order WENO (Weighted Essentially Non-Oscillatory) reconstruction was implemented to achieve high-order of accuracy in supersonic flows. There are multiple variants of this scheme; the WENO-JS and WENO-Z versions proposed respectively by Jiang and Shu [79] and Borges et al. [80, 81] were implemented in GTsim. The WENO-Z theoretically achieves less dissipation and higher resolution than the classical WENO-JS scheme. Roe's FDS is retained as the approximate Riemann solver.

In the WENO-JS and WENO-Z schemes, the face values for the left and right states are obtained by weighting third-order approximations obtained using three-point stencils. This procedure is given here for a dummy variable U in the i-direction:

$$
\begin{aligned}
U^L_{i+\frac{1}{2}} &= w_1^L\ U^{1,L}_{i+\frac{1}{2}} + w_2^L\ U^{2,L}_{i+\frac{1}{2}} + w_3^L\ U^{3,L}_{i+\frac{1}{2}}\ , \\
U^R_{i+\frac{1}{2}} &= w_1^R\ U^{1,R}_{i+\frac{1}{2}} + w_2^R\ U^{2,R}_{i+\frac{1}{2}} + w_3^R\ U^{3,R}_{i+\frac{1}{2}}\ .
\end{aligned}
\tag{2.12}
$$

The intermediary third-order approximations to the face values are given by

$$
\begin{aligned}
U^{1,L}_{i+\frac{1}{2}} &= \frac{1}{3}U_{i-2} - \frac{7}{6}U_{i-1} + \frac{11}{6}U_i\ , \quad & U^{1,R}_{i+\frac{1}{2}} &= -\frac{1}{6}U_{i-1} + \frac{5}{6}U_i + \frac{1}{3}U_{i+1}\ , \\
U^{2,L}_{i+\frac{1}{2}} &= -\frac{1}{6}U_{i-1} + \frac{5}{6}U_i + \frac{1}{3}U_{i+1}\ , \quad & U^{2,R}_{i+\frac{1}{2}} &= \frac{1}{3}U_i + \frac{5}{6}U_{i+1} - \frac{1}{6}U_{i+2}\ , \\
U^{3,L}_{i+\frac{1}{2}} &= \frac{1}{3}U_i + \frac{5}{6}U_{i+1} - \frac{1}{6}U_{i+2}\ , \quad & U^{3,R}_{i+\frac{1}{2}} &= \frac{11}{6}U_{i+1} - \frac{7}{6}U_{i+2} + \frac{1}{3}U_{i+3}\ .
\end{aligned}
\tag{2.13}
$$

The weights are computed as

$$
w_r^{L,R} = \frac{\alpha_r^{L,R}}{\sum_{l=1}^{3}\alpha_l^{L,R}}\ ,
\tag{2.14}
$$

with

$$
\begin{aligned}
\alpha_r^{L,R} &= \frac{\gamma_r^{L,R}}{\left(\beta_j^{L,R}+\epsilon\right)^p} && \text{, for WENO-JS} \\
\alpha_r^{L,R} &= \gamma_r^{L,R}\left(1+\left(\frac{\tau_5^{L,R}}{\beta_j^{L,R}+\epsilon}\right)^p\right) && \text{, for WENO-Z ,}
\end{aligned}
\tag{2.15}
$$

and $r = 1, 2, 3$ and $\gamma_r^{L,R}$ are the ideal weights $\gamma_1^L = \gamma_3^R = 0.1$, $\gamma_2^L = \gamma_2^R = 0.6$, $\gamma_3^L = \gamma_1^R = 0.3$. The parameter ϵ is used to avoid the division by zero in the denominator and $p = 2$ is chosen to increase the difference of scales of distinct weights at non-smooth parts of the solution. The left smoothness indicators β_r^L are given by

$$
\begin{aligned}
\beta_1^L &= \frac{13}{12}(U_{i-2} - 2U_{i-1} + U_i)^2 + \tfrac{1}{4}(U_{i-2} - 4U_{i-1} + 3U_i)^2\ , \\
\beta_2^L &= \frac{13}{12}(U_{i-1} - 2U_i + U_{i+1})^2 + \tfrac{1}{4}(U_{i-1} - U_{i+1})^2\ , \\
\beta_3^L &= \frac{13}{12}(U_i - 2U_{i+1} + U_{i+2})^2 + \tfrac{1}{4}(3U_i - 4U_{i+1} + U_{i+2})^2\ .
\end{aligned}
\tag{2.16}
$$

The right smoothness indicators β_r^R are obtained by shifting all indexes in β_r^L to the right by one, and $\tau_5^{L,R} = |\beta_1 - \beta_3|$ is a higher order smoothness indicator.

Unless otherwise specified, the WENO reconstruction is applied to the conserved variables. Preforming the reconstruction on the characteristic variables in known to be more robust, for an increased computational cost [82] due to the computation of eigenvectors and multiple projections from physical space to characteristic space. The characteristic-wise reconstruction was also implemented in GTsim and was found to be necessary in the presence of strong reflections and shocks, like the Double Mach Reflection problem (section 2.5.4).

The implementation of the fifth-order scheme requires a corresponding treatment of the boundary conditions. This is achieved by introducing a third layer of ghost cells to the computational domain. The scheme presented here can be shown to be fifth-order on a one-dimensional uniform grid. However, a dimension-by-dimension implementation in a finite-volume approach results in second-order accuracy for 3D non-linear fluxes. Quadratures must be used in multiple dimensions to preserve the fifth-order accuracy, which comes at a higher computational cost [83]. Finite-difference schemes do not have this limitation on the dimension-by-dimension method. Nonetheless, the dimension-by-dimension approach on the present scheme results in improvements compared to lower-order formulations, in particular when resolving turbulent structures on smoothly varying grids [81, 83, 84].

2.2.2 Dual time stepping and preconditioning

Numerical difficulties arise at low Mach number, due to the disparity in the eigenvalues of the system [85]. Approaches to address this problem can be classified as pressure-based or density-based [86]. Pressure-based methods originate from the incompressible form of the NS equations, while density-based methods originate from the compressible form. A pressured-based formulation employing the Chorin artificial compressibility method was implemented in GTsim and is presented in Appendix A. Pressure-based methods are inadequate in flowfields containing both low and high

Mach numbers simultaneously (all-speed flows [87]) such as a fluidic oscillator with a supersonic nozzle. Therefore, a robust low Mach preconditioning approach was also applied to the compressible NS equations. Gallagher [88] provides a review of low Mach preconditioning techniques and successfully added them to the MacCormack scheme. Preconditioning has also successfully been derived for the Roe [89] and central difference [90] schemes.

A low Mach number preconditioner serves three purposes: (1) rescaling the eigenvalues of the system; (2) changing the scaling of the numerical dissipation; (3) coupling pressure and velocity as it is done in pressure-based schemes. The first objective is accomplished by multiplying the time-dependent term of the NS equations by an appropriate preconditioning matrix. The second and third objectives are achieved by using a set of primitive variables. Because accuracy at high speeds remains important for flows that span both incompressible and compressible flow regimes, primitive variables are only implicitly included with transformation matrices, while the governing equation remain written in terms of the conservative variables.

A dual-time stepping approach is employed to mitigate the various linearization errors, including the linearization of the fluxes, and the loss of time accuracy due to preconditioning. Preconditioning is applied in pseudo time as:

$$\mathbf{\Gamma}_C \frac{\partial}{\partial \tau} \int_\Omega \mathbf{U} dV + \frac{\partial}{\partial t} \int_\Omega \mathbf{U} dV + \oint_{\partial\Omega} \left(\mathbf{F_c} - \mathbf{F_v}\right) dS = 0 \tag{2.17}$$

The Weiss-Smith [89] preconditioning matrix ($\mathbf{\Gamma}$) is one of the most recognized preconditioners for viscous flows. It is defined in its simplest form for the following set

of primitive variables $\mathbf{W} = (p\ u\ v\ w\ T)^T$ as

$$\mathbf{\Gamma} = \begin{pmatrix} \Theta & 0 & 0 & 0 & \rho_T \\ \Theta u & \rho & 0 & 0 & \rho_T u \\ \Theta v & 0 & \rho & 0 & \rho_T v \\ \Theta w & 0 & 0 & \rho & \rho_T w \\ \Theta H - 1 & \rho u & \rho v & \rho w & \rho_T H + \rho H_T \end{pmatrix} , \tag{2.18}$$

where Θ is a parameter that rescales the eigenvalues of the system

$$\Theta = \frac{1}{U_r^2} - \frac{\rho_T}{\rho h_T} , \tag{2.19}$$

with ρ_T and h_T denoting the derivatives of density and enthalpy with respect to temperature. For a perfect gas, $\rho_T = -\dfrac{\gamma p}{T^2}$ and $h_T = \dfrac{1}{\gamma - 1}$. U_r is a reference velocity is obtained from the relation

$$U_r = \min\left(\max\left(|\mathbf{V}|, \frac{L_{ref}}{\pi \Delta t}, \frac{\nu \Delta S}{\Omega}\frac{M_\infty}{Re}, \frac{|\Delta p|}{\rho |\mathbf{V}|}\right), a\right) . \tag{2.20}$$

The preconditioning matrix for the conservative state vector is related to the preconditioning matrix for the primitive variables by:

$$\mathbf{\Gamma}_C = \mathbf{\Gamma}\frac{\partial \mathbf{W}}{\partial \mathbf{U}} . \tag{2.21}$$

The preconditioning matrix ($\mathbf{\Gamma}_C$) is such that $\lim_{U_r \to a} \mathbf{\Gamma}_C = \bar{\mathbf{I}}$, where $\bar{\mathbf{I}}$ is the identity matrix, so that preconditioning is turned off when the flow approaches sonic conditions.

After discretization in time and space of Eq. (2.17), the system of equations has the form:

$$\begin{aligned} &\left[\frac{\Omega_{ijk}}{\Delta t}\left(\frac{\Delta t}{\Delta \tau}\mathbf{\Gamma}_C + \frac{3}{2}\bar{\mathbf{I}}\right) + \left(\frac{\partial \mathbf{R}}{\partial \mathbf{U}}\right)^m\right]\Delta \mathbf{U}^m \\ &= -\mathbf{R}^m - \left(\frac{\Omega_{ijk}}{\Delta t}\right)\frac{3\mathbf{U}^m - 4\mathbf{U}^n + \mathbf{U}^{n-1}}{2} , \end{aligned} \tag{2.22}$$

where

$$\Delta \mathbf{U}^m = \mathbf{U}^{m+1} - \mathbf{U}^m , \tag{2.23}$$

$$\mathbf{R} = \sum_{l=1}^{N_f} (\mathbf{F}_c - \mathbf{F}_v)_l \, \Delta S_l \ , \tag{2.24}$$

m and n indicate iterations in pseudo time and physical time respectively, with corresponding time steps $\Delta\tau$ and Δt. The linearization of the flux Jacobian is responsible for making the formulation implicit in pseudo time, thereby increasing the stability of the solver. The system of equations in Eq. (2.22) is solved in GTsim using the LU-SSOR scheme [91].

The characteristics-based boundary conditions and the convective flux Jacobian matrix are modified in the code to accommodate the preconditioned system. The viscous flux Jacobian is left unchanged [87]. The modification of the eigenvalues, eigenvectors and characteristic variables are presented in Appendix B. The implementation in GTsim has been limited to the central schemes.

2.3 Turbulence closure

The governing equations and numerical schemes have thus far focused on the NS equations. While these equations can be solved by Direct Numerical Simulation (DNS) for low Reynolds numbers flows, RANS and LES approaches remain the state of the art for practical applications. Both RANS and LES models require the solution of additional equations to affect the turbulence closures. In GTsim, the additional equations are loosely coupled to the NS equations. In loose coupling, the turbulence equations are solved separately from the NS equations, whereas all equations are solved simultaneously in tight coupling. For example, a two-equation turbulence closure will result in the solution of a system of seven equation when tightly coupled with the NS equations. The advantage of loose coupling is that the turbulence models can be interchanged, though tight coupling may result in faster convergence [92]. Pseudo time iterations are leveraged to ensure the convergence of all equations. The following approaches are employed in this effort:

- **Fully-Turbulent URANS:** $k - \omega$ SST of Menter, 2003 [34];
- **Fully-Turbulent URANS:** Spalart-Allmaras, 2012 [33];
- **Transitional URANS:** $\gamma - Re_\theta$ of Langtry and Menter, 2009 [53];
- **Fully-Turbulent HRLES:** Hybrid model of Sánchez-Rocha, 2009 [49];
- **Fully-Turbulent (I)DDES:** SST-based (Improved) Delayed Detached Eddy Simulation of Gritskevich et al. [46];

2.4 Block-structured approach

Flow control applications consist of an outer flow and the flow control mechanism that may need to be resolved simultaneously. The internal geometry of the actuator itself can be intricate enough that generating a single structured grid becomes challenging. Discretization of such complex geometries with structured grids requires a multiblock approach [93–95] or an overset capability [96]. Overset grids overlap one another and hole-cutting algorithms resolve the interface between the different grids. They are superior to block-structured grids for relative motion between the grids, but their implementation is more difficult, the interpolation between grids introduces additional errors, and the hole-cutting algorithm limits the parallel efficiency. As, there are no moving parts in fluidic oscillators, a multiblock approach was selected and implemented in GTsim.

Initial implementations of the multiblock approach in GTsim consisted in splitting each grid block among all available processors. Each processor was thus assigned a portion of all grid blocks, and solved the governing equation on each portion successively. This required two levels in the data structures: one global level storing all grid portions assigned and one level containing the grid being treated at a given instant in the procedure, thereby duplicating the memory. In addition to the memory operations required, this approach limited the parallel efficiency of the solver. The results

presented in this dissertation were obtained with a multiblock implementation that only assigns a portion of one grid to each processor. The code that partitions the grid became more complex, but there are no longer superfluous memory operations, and the parallel efficiency can be recovered. The drawback of this implementation is that the solver requires at least as many processors as there are grid blocks. That constitutes a lower limit that typically results in low parallel efficiency if the block sizes differ significantly. Choosing an adequate number of processors is generally not an issue on modern High Performance Computing (HPC) platforms. These considerations are just as important as the accuracy of the solver.

To offer additional flexibility, an interpolation procedure was implemented to support grids where both sides of a block interface do not have the same number of cells. Figures 2.1 and 2.2 illustrate these two types of interfaces, and the associated ghost cells. Only one ghost cell level is shown. GTsim uses two levels (second-order and fourth-order schemes), which was extended to three levels to accommodate the fifth-order WENO scheme.

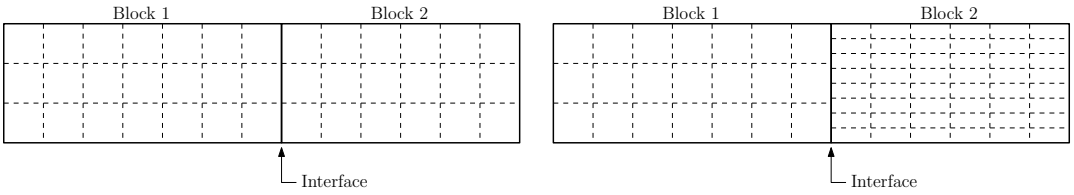

(a) One-to-one interface (b) Mismatching cell number at interface

Figure 2.1: Illustration of block interfaces

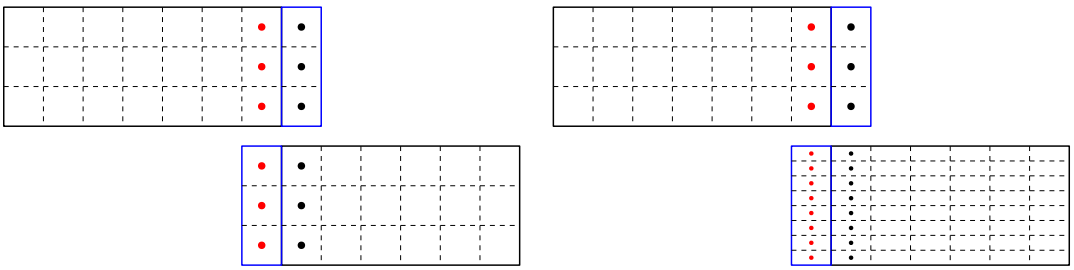

(a) One-to-one interface (b) Mismatching cell number at interface

Figure 2.2: Illustration of one layer of ghost cells. Ghost layer in blue.

Different types of interpolation techniques were tested such as a linear interpolation and a cubic spline for a 1D interface. When the interface is a plane (2D) aligned with one coordinate axis, such as encountered in a Cartesian grid, bilinear or bicubic interpolations could be employed. Unfortunately, these do not apply to general interfaces (not aligned with a coordinate axis) encountered on a curvilinear grid [97]. Instead, an inverse distance method is applied.

$$\phi = \frac{\sum_{i=1}^{N} \frac{\phi_i}{d_i}}{\sum_{i=1}^{N} \frac{1}{d_i}} \,, \tag{2.25}$$

where ϕ is the quantity interpolated, such as density or momentum, and d_i is the distance from the point of interest to its nearest neighbor i. The N nearest neighbors are determined in GTsim during the initialization phase to minimize the overhead of the interpolation.

Test cases demonstrating the correct implementation of the block-structured approach are provided in section 2.5: two cases pertaining to one-to-one interfaces, and one case evaluating the interpolation procedure at mismatching block interfaces.

2.5 Code verification and validation

The initial verification and validation of GTsim was carried out by Hodara [52]. The code was shown to be second-order accurate in time (order 1.89 more precisely), and capable of accurate predictions, including transitional flows. The superiority of hybrid RANS/LES over RANS was demonstrated on massively separated flows. Additional test cases are reported in the present dissertation to test applications that were not previously evaluated (high-speed flows), and newly implemented features (Incompressible solver and preconditioning, fifth-order WENO and multiblock).

2.5.1 Laminar flat plate

This test case serves as a basis to compare of the incompressible, compressible, and preconditioned formulations. Consider a laminar flat plate at Reynolds 20000 (based on the flat plate length L). Blasius' theoretical solution predicts the drag coefficient as

$$C_D \simeq \frac{1.328}{\sqrt{Re_L}} \,. \tag{2.26}$$

The rectangular grid consists of 161 points in the streamwise direction (including 130 points on the plate) and 65 points in the normal direction, 35 of which lie in the boundary layer. Low Mach numbers are tested to illustrate the effect of low Mach preconditioning, the efficiency of the incompressible solver, and to verify the correct implementation of these solvers. A second-order central difference scheme is employed, with a CFL number of 100 in all cases. Table 2.1 contains the values of the final drag coefficient for the three solvers at Mach 0.1, 0.01 and 0.001 and Fig. 2.3 is a comparison of the convergence histories.

Table 2.1: Drag coefficient for a laminar flat plate at Reynolds 20000

Mach	0.1	0.01	0.001
Theory		0.939×10^{-2}	
Compressible	0.982×10^{-2}	0.105×10^{-2}	0.149×10^{-2}
Preconditioning		0.956×10^{-2}	
Incompressible ($\overline{\beta} = 1$)		0.959×10^{-2}	
Incompressible ($\overline{\beta} = 10$)		0.971×10^{-2}	
Incompressible ($\overline{\beta} = 100$)		0.982×10^{-2}	

Convergence is severely degraded in the compressible solver as the Mach number decreases, resulting in significant variations in the drag coefficient (85% difference between Mach 0.1 and Mach 0.001). The solution is expected to be independent of Mach number as predicted by the preconditioning scheme, where the value obtained for the drag coefficient is within 1.8% of the theoretical value. The incompressible

solver exhibits little sensitivity to the artificial compressibility factor ($\overline{\beta}$): approximately 2% for the values considered. The value of the drag coefficient for $\overline{\beta} = 1$ is in close agreement with the value obtained with preconditioning (0.3% difference). For $\overline{\beta} \leq 10$, the incompressible solver converges the fastest to machine precision.

This test case demonstrates that methods adapted to low speed flows are necessary to obtain an accurate solution for a steady problem. An unsteady problem is evaluated next.

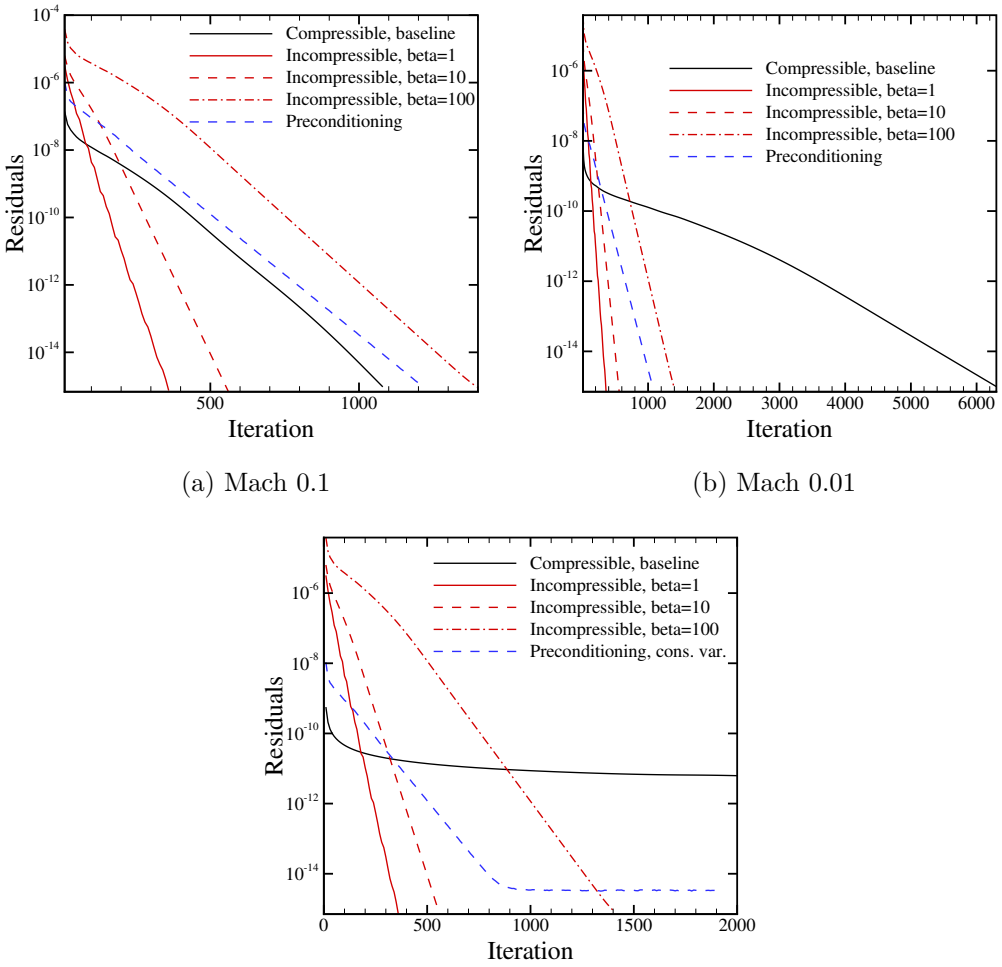

(a) Mach 0.1

(b) Mach 0.01

(c) Mach 0.001

Figure 2.3: Convergence history for a laminar flat plate at Reynolds 20000

2.5.2 Laminar vortex shedding behind a cylinder

Consider a flow past a circular cylinder at Reynolds 100. As illustrated in Fig. 2.4, a Von Kármán vortex street forms behind the cylinder. The objective of this test case is to evaluate compressible, incompressible and preconditioning schemes for an unsteady problem.

The grid is an O-grid containing 151 points in the circumferential direction, and 160 points in the wall-normal direction. The farfield extends 60 diameters away from the cylinder. The time step corresponds to $\Delta t = \dfrac{0.01D}{V_\infty}$, or approximately 600 iterations per vortex shedding cycle. A second-order central difference scheme is employed, with a CFL number of 100 in all cases and 10 sub-iterations.

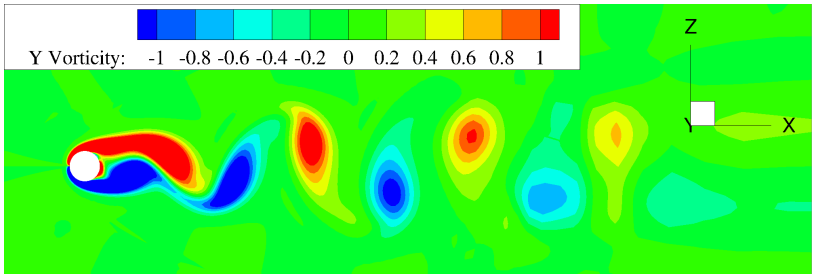

Figure 2.4: Von Kármán vortex street behind a cylinder at $Re_D = 100$ obtained from GTsim, incompressible solver

Table 2.2 summarizes the vortex shedding characteristics predicted, as well as values found in the literature. Similar to the laminar flat plate case, the compressible solver predicts the expected characteristics at Mach 0.1 and 0.01, and it fails at Mach 0.001. In fact, the mean lift coefficient increases in time and eventually diverges at Mach 0.001. Otherwise, the characteristics are predicted within 2% of other computations in the literature, including pressure-based solvers.

Figure 2.5 is a comparison of sub-iteration convergence of the solvers at different Mach numbers. The incompressible solver histories are simply repeated in the three plots, and a reduction of the sub-iteration residuals by three orders of magnitude is observed. The reduction in the sub-iteration residuals is comparable between the

Table 2.2: Comparison of vortex shedding characteristics for the flow past a cylinder at $Re_D = 100$

References	Mach	$\overline{C}_d$	C'_l	St
Roshko [98] (exp)	-	-	-	0.164
Kim et al. [99]	-	1.33	0.32	0.165
Choi et al. [100]	-	1.34	0.315	0.164
Karagiosis et al. [101]	0.05	1.317	0.320	0.168
Present, compressible	0.1	1.333	0.323	0.166
	0.01	1.316	0.322	0.160
	0.001	1.156	-	0.107
Present, preconditioning	0.1	1.333	0.323	0.166
	0.01	1.325	0.324	0.164
	0.001	1.326	0.327	0.163
Present, incompressible ($\overline{\beta} = 1$)	-	1.317	0.315	0.165

compressible and preconditioning schemes, and the level of convergence is dependent on the Mach number. The preconditioning scheme still predicts accurate vortex shedding characteristics at Mach 0.001, though the sub-iteration residual only decreases by approximately 1.5 orders of magnitude. Here, the subiteration residual convergence is not a sufficient indicator of accuracy.

Additional tests were conducted on the compressible solver, with lower time steps or more sub-iterations resulting in an improvement of the predictions. In particular, dividing the baseline time step by 10 yielded the following vortex shedding characteristics: $\overline{C}_d \simeq 1.255$, $C'_l \simeq 0.277$ $St \simeq 0.137$. This constitutes a significant improvement compared to the initial computations (16% error on the Strouhal number versus 34% error previously). This suggests that if the time step is small enough, an accurate solution can be obtained with the compressible solver, though the computation becomes very inefficient.

Finally, there is an upper limit to the physical time step permitted such that the solution does not diverge. This applies to all solvers, including the implicit preconditioning scheme. If the time is too large, the number of sub-iteration should be

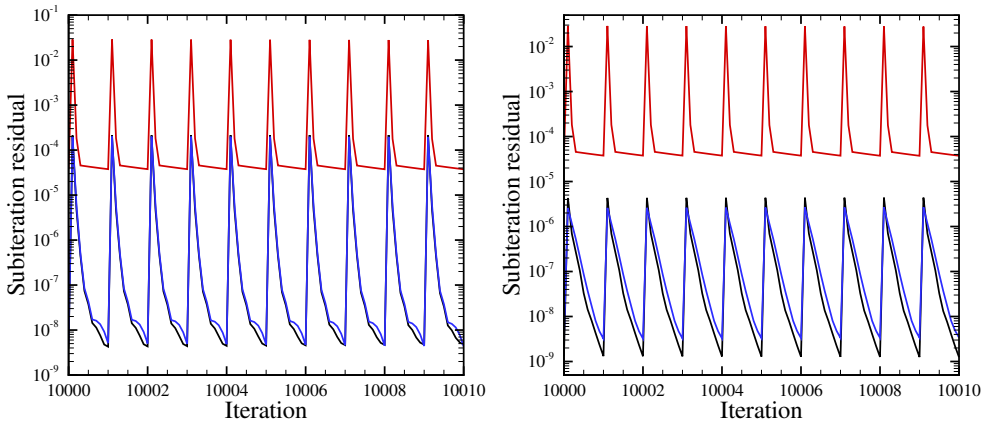

(a) Mach 0.1

(b) Mach 0.01

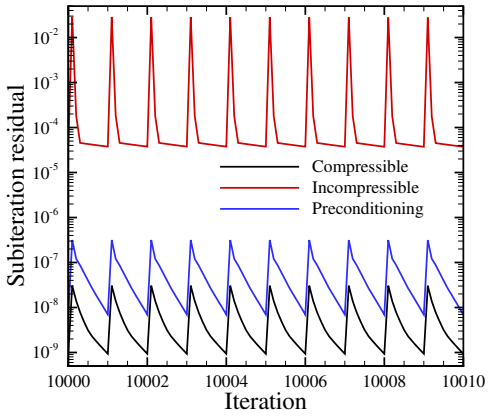

(c) Mach 0.001

Figure 2.5: Subiteration convergence history for the laminar vortex shedding behind a cylinder at $Re_D = 100$. Compressible (black), Incompressible (red), Preconditioning (blue)

increased to maintain the stability and accuracy. For the present case, everything else remaining the same, the preconditioning solver diverges at Mach 0.001 when the physical time step exceeds $\Delta t = \dfrac{0.2D}{V_\infty}$ (30 steps per vortex shedding cycle). The limit is typically much lower in turbulent flows.

This test case demonstrates the need for appropriate numerical schemes in time-accurate computations when very low speed flow regions are present. If an inaccurate solution is obtained with the compressible solver, precondition can provide significant improvements.

2.5.3 Two-dimensional supersonic flat plate

In order to validate GTsim's compressible solver for supersonic applications, the supersonic, turbulent flow past a flat plate is simulated using the $k-\omega$ SST turbulence model. This test case is part of the NASA Turbulence Modeling Resource (TMR) [102]. Of particular interest is the case of a freestream at Mach 2 with an adiabatic wall. The Reynolds number 15 million per unit length, while the length of the plate is 2 grid units. The mesh employed has 544 cells in the streamwise direction, and 384 cells in the wall-normal direction, with $y_1^+ < 0.2$ over the plate. The wall-unit distance from the wall to the first cell center in the wall-normal direction y_1^+ is given by Eq. 2.27, where u_τ is the friction velocity $\sqrt{\tau_w/\rho}$, and ν is the kinematic viscosity.

$$y_1^+ = \frac{y_1 u_\tau}{\nu} \tag{2.27}$$

Figure 2.6 is a schematic of the computational domain and boundary conditions. The left and top boundaries are farfields, allowing characteristics to leave the domain. The domain is extended upstream of the flat plate to avoid conflicts between the inflow and wall boundary conditions. A zero-th order extrapolation is applied at the downstream boundary, even within the boundary layer, for stability considerations.

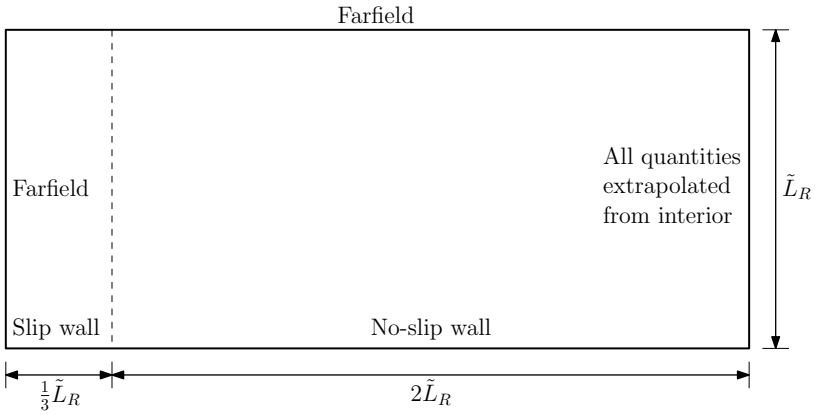

Figure 2.6: Computational domain and boundary conditions for the supersonic flat plate

The solution obtained is in excellent agreement with theory and other codes. The reference theory uses a combination of the Karman-Schoenherr (K-S) relation and the Van Driest II transformation. The skin friction and velocity profile from GTsim are compared to theory and the solution from CFL3D [102] in Figs. 2.7 and 2.8 respectively. GTsim's skin friction is within 2% of CFL3D's.

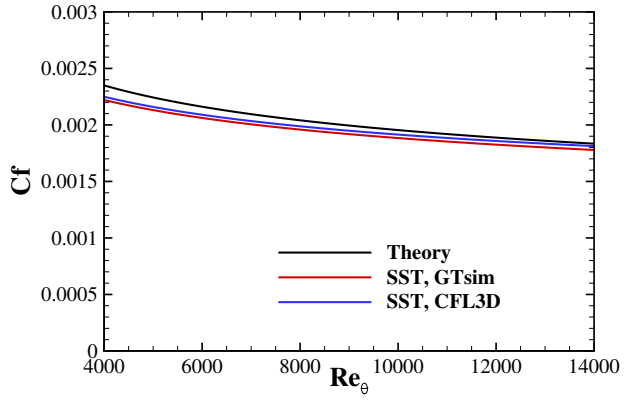

Figure 2.7: Coefficient of friction distribution along the supersonic flat plate at $M_\infty = 2$

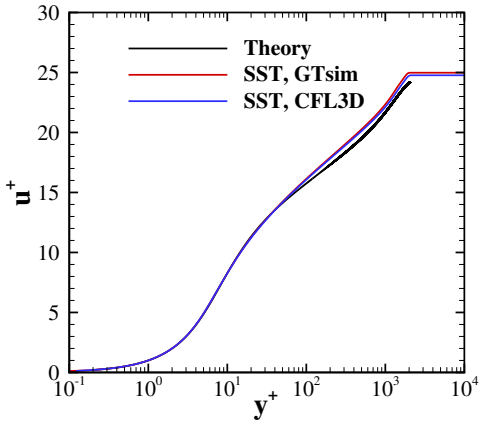

Figure 2.8: Velocity profile in wall units for the supersonic flat plate at $M_\infty = 2$ extracted at $Re_\theta = 10000$

2.5.4 Double Mach Reflection

The Double Mach Reflection problem was simulated to verify the implementation of the fifth-order WENO scheme. This problem, originally suggested by Woodward and Colella [103], has extensively been used in the literature as a benchmark for Euler codes. Figure 2.9 is the schematic of the setup for this problem, and the important flow features expected are labeled in Fig. 2.10.

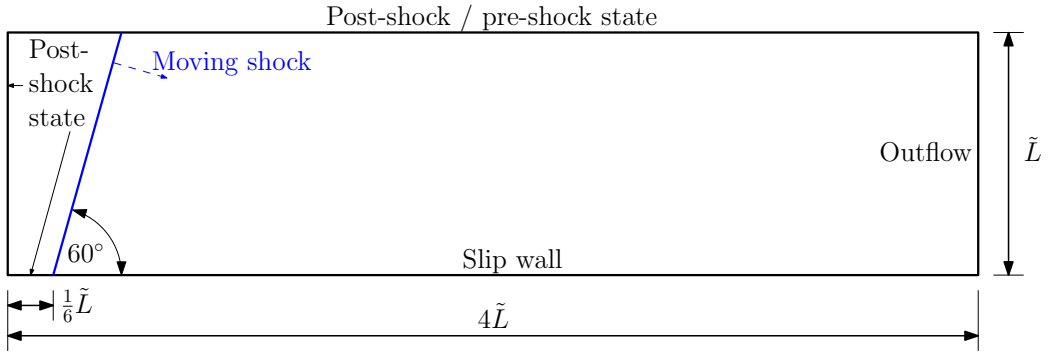

Figure 2.9: Computational domain and boundary conditions for the Double Mach Reflection test case, $\tilde{L} = 1$

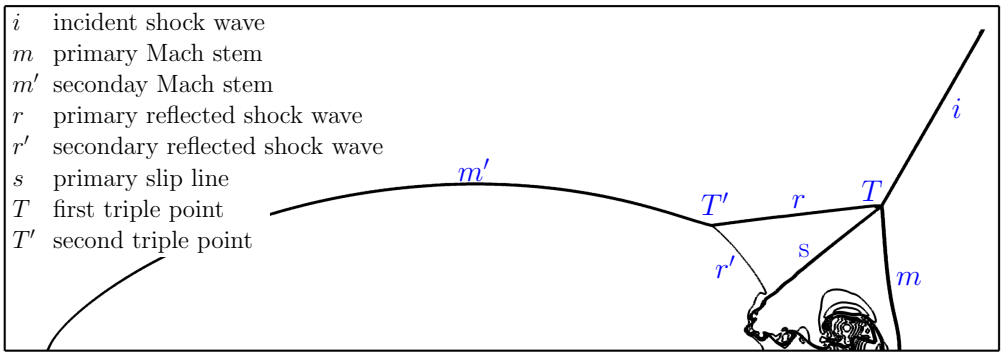

Figure 2.10: Double Mach Reflection key flow features nomenclature

The fifth-order WENO reconstruction is compared to the second-order MUSCL reconstruction. Harten's entropy correction [104] is applied to remedy the kinked Mach stem phenomenon otherwise observed with the Roe scheme [105]. In addition, if the solution contains two discontinuities which are too close to one another, the reconstruction procedure will not be able to find a smooth stencil, and spurious oscillations will appear possibly causing the scheme to diverge [106]. Therefore, only for the present test case, the MUSCL is applied instead of the WENO reconstruction when the reconstructed value leads to a negative density or temperature, similar to the work of Titarev and Toro [106]. This issue was encountered at the right most triple point of Fig. 2.10.

The initial conditions are given by

$$[\rho, u, w, p] = \begin{cases} [8, 8.25, \sin(60°), -8.25\cos(60°), 116.5] & x < \frac{1}{6} + \frac{z}{\sqrt{3}} \\ [1.4, 0, 0, 1] & x \geq \frac{1}{6} + \frac{z}{\sqrt{3}} \end{cases} \tag{2.28}$$

The top boundary has a Dirichlet condition given by

$$[\rho, u, w, p] = \begin{cases} [8, 8.25, \sin(60°), -8.25\cos(60°), 116.5] & x < \frac{1}{6} + \frac{1+20t}{\sqrt{3}} \\ [1.4, 0, 0, 1] & x \geq \frac{1}{6} + \frac{z}{\sqrt{3}} \end{cases} \tag{2.29}$$

The solution was carried out until $t = 0.2$ on three different uniform grids. The coarsest grid had 480 cells in the wall-parallel direction, and 120 cells in the wall-

normal direction (480×120). The medium and fine grids have dimensions 960×240 and 1920×480 respectively. The non-dimensional time step is taken as 10^{-4} on the coarse and medium grid, and 10^{-5} on the fine grid, with enough sub-iterations to guarantee at least three orders of magnitude reduction in the residuals.

Figures 2.11 and 2.12 are comparisons of the second-order and fifth-order schemes on the three grids evaluated. It is clear that the fifth-order scheme provides a better resolution of the structures below the primary slip line. The structures resolved on the middle grid with WENO-Z are comparable to those resolved on the fine grid with the MUSCL reconstruction.

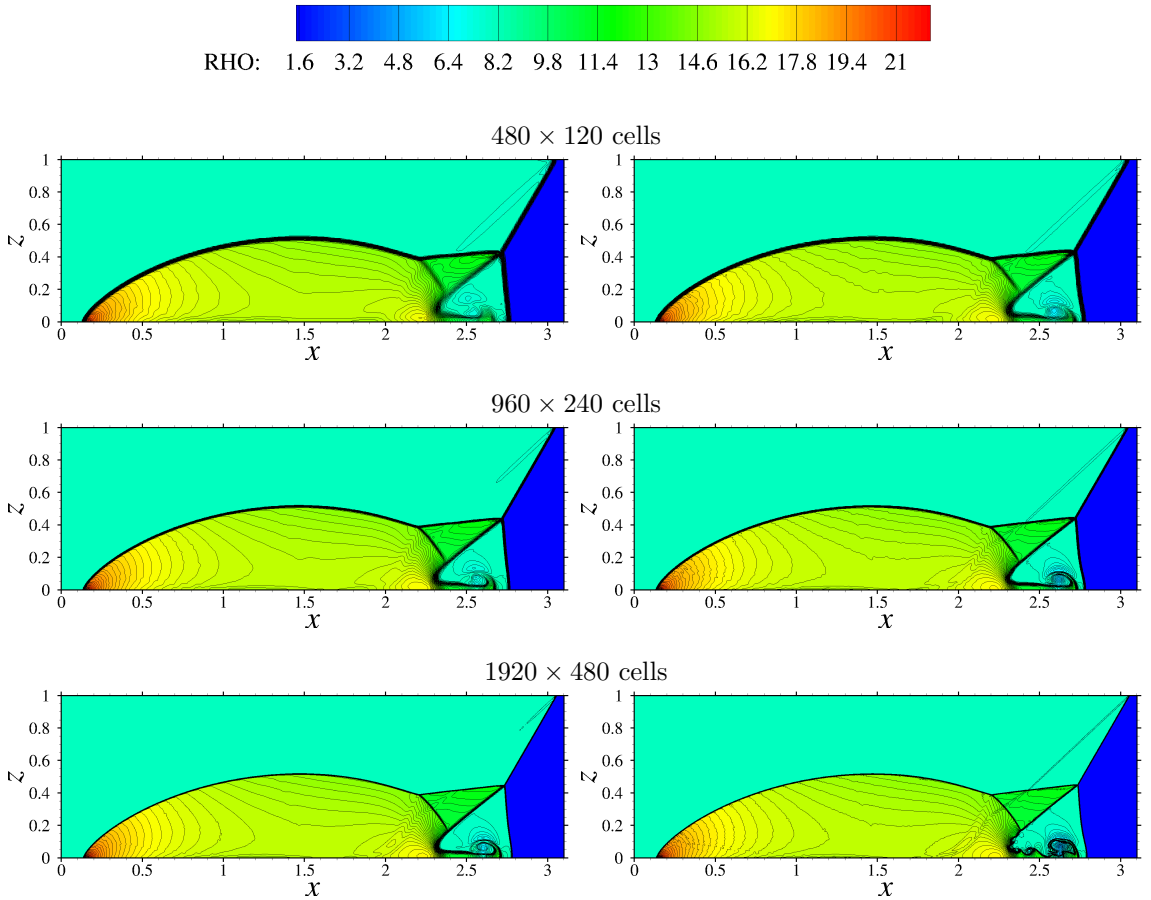

Figure 2.11: Overview of density contours overview for the Double Mach Reflection test case at $t = 0.2$. Left: MUSCL, Right: WENO

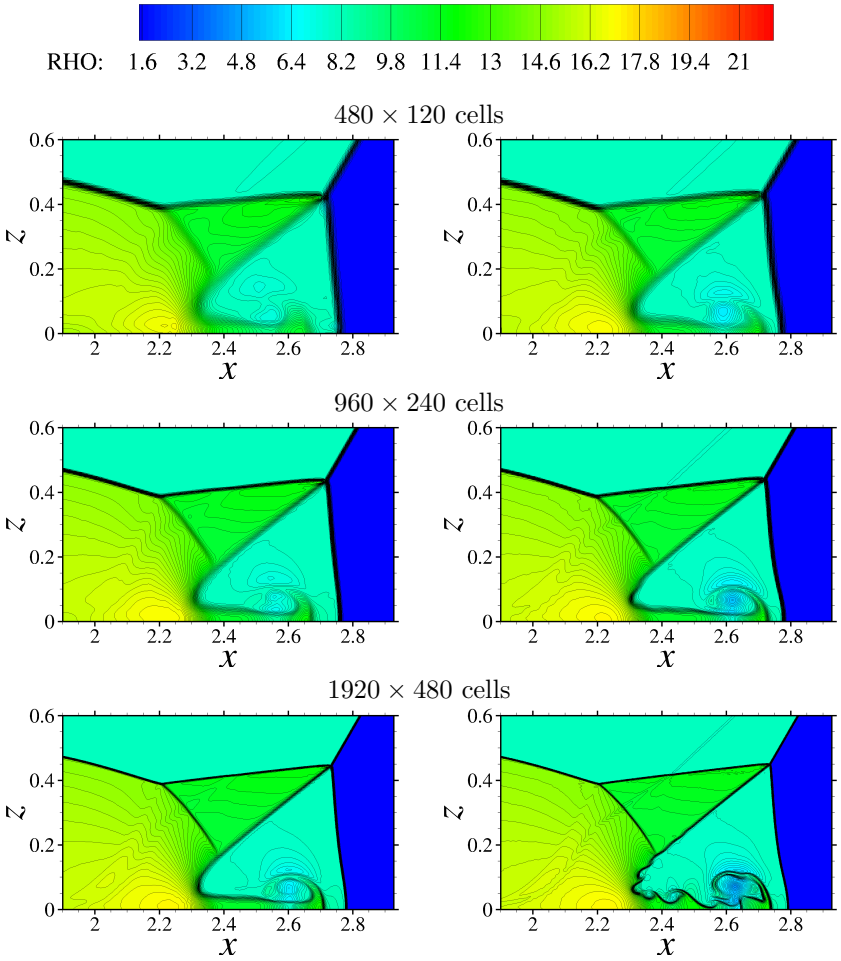

Figure 2.12: Close view of density contours below the Mach stem for the Double Mach Reflection test case at $t = 0.2$. Left: MUSCL, Right: WENO

2.5.5 Two-dimensional Backward-Facing Step

This test case is also part of the NASA Turbulence Modeling Resource (TMR) [102]. The grid is block-structured as illustrated in Fig. 2.13, with one-to-one interfaces. The second finest grid provided in the TMR was used. Validation results from other codes have also relied on the same mesh.

The Reynolds number based on the step height and the velocity at $x/H = -4$ is $36,000$. The freestream temperature is set to 298.33 Kelvin. The $k - \omega$ SST turbulence model is employed, and the simulation is carried out until convergence to a steady state.

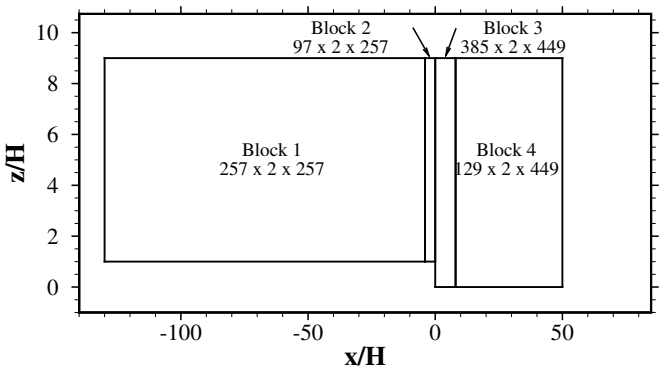

Figure 2.13: Illustration of the grid blocks for the BFS. The axes are not to scale.

The left boundary of the first block has a farfield condition, with a Mach number of 0.128 and a non-dimensional pressure of 1. The pressure at the outlet (right boundary of the fourth block) is set to recover the reference Mach number of 0.128 at $x/H = -4$. The upper and lower boundaries of all blocks are viscous walls, with the exception of $-130 \leq x/H < -110$, where symmetry boundary conditions are applied to avoid possible incompatibilities between freestream inflow and the wall boundary condition [102].

The data provided in the TMR for the CFL3D results with the SST turbulence model and the experimental data form Driver and Seegmiller [107] were used to validate the GTsim results. Figure 2.14 illustrates the recirculation region after the step. Figure 2.15 shows the pressure and skin friction coefficient distributions along the bottom wall respectively. Figure 2.16 shows the velocity profiles at different axial locations. The solution obtained is in excellent agreement with reported results from CFL3D and OVERFLOW [102, 108].

The computational results obtained with GTsim are in agreement the CFL3D results. For example, the maximum relative error on the coefficient of friction is 2%. Differences between both computations and experiments are expected for RANS simulations. The objective here was to verify that the multiblock approach as implemented in GTsim does not introduce more error than other comparable solvers.

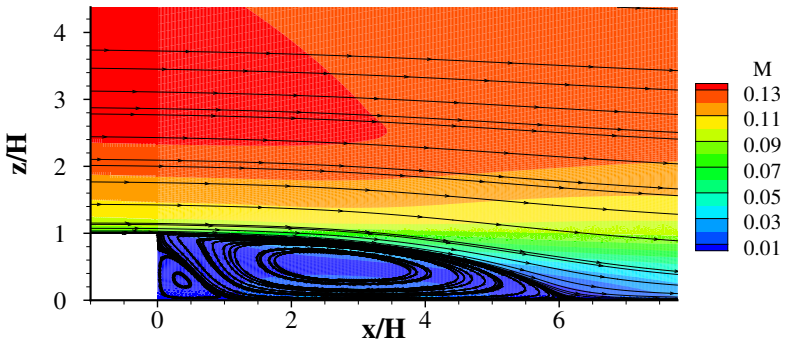

Figure 2.14: Mach number field and streamlines for the BFS, illustrating the recirculation bubbles

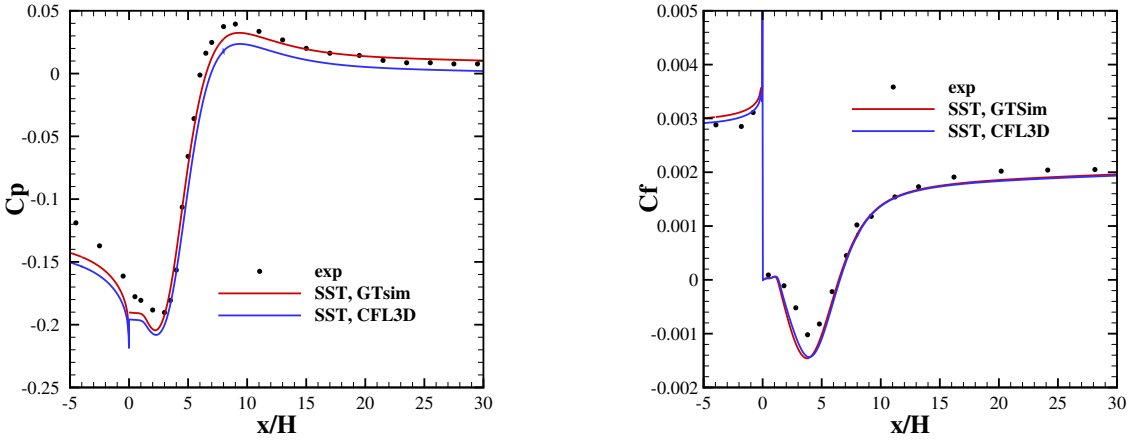

Figure 2.15: Pressure and skin friction coefficient distributions along the bottom wall of the BFS

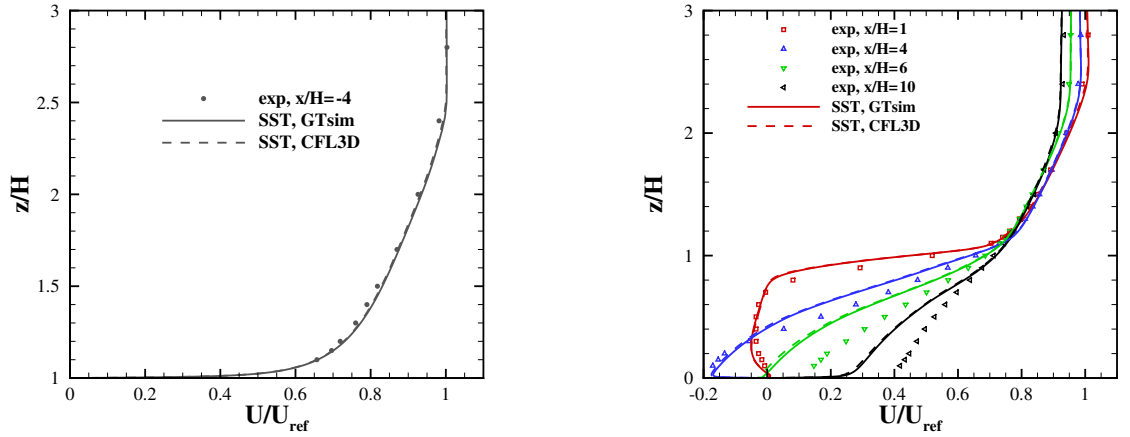

Figure 2.16: Velocity profiles at $x/h = 1$, $x/h = 4$, $x/h = 6$, and $x/h = 10$ for the BFS

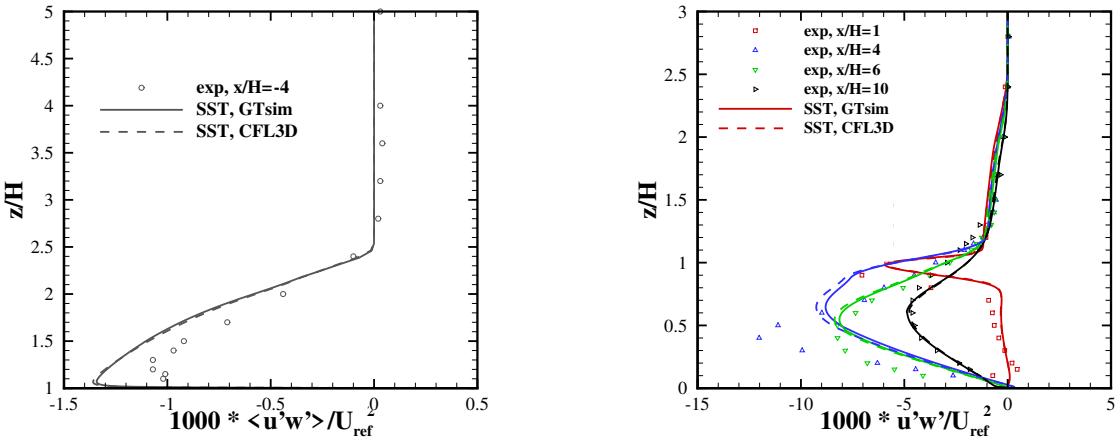

Figure 2.17: Turbulent shear stress profiles at $x/h = 1$, $x/h = 4$, $x/h = 6$, and $x/h = 10$ for the BFS

2.5.6 Two-dimensional Wall-Mounted Hump

This test case is also part of the NASA Turbulence Modeling Resource (TMR) [102]. The grid is block-structured (four blocks), as illustrated in Fig. 2.18 with one-to-one interfaces. Blocks 2 and 3 represent the plenum region used for flow control applications. The finest grid provided in the TMR was used to evaluate the baseline case and a case where steady suction is applied at the bottom of the plenum.

The Reynolds number for this problem is $936,000$. The dimensional freestream temperature is set to 298.33 Kelvin. The $k-\omega$ SST turbulence model is employed, and the simulation is carried out until convergence to a steady state.

The left boundary of the fourth block is a subsonic inflow with stagnation conditions based on the specified Mach number of 0.1 and a non-dimensional pressure of 1. A back pressure ratio $\dfrac{p}{p_{atm}} = 0.99962$ is set at the outlet. The bottom of the plenum has a slip wall condition in the baseline case, and the mass flow is specified in the case of steady suction. The top boundary is a slip wall, while the remaining boundaries of the domain are viscous walls.

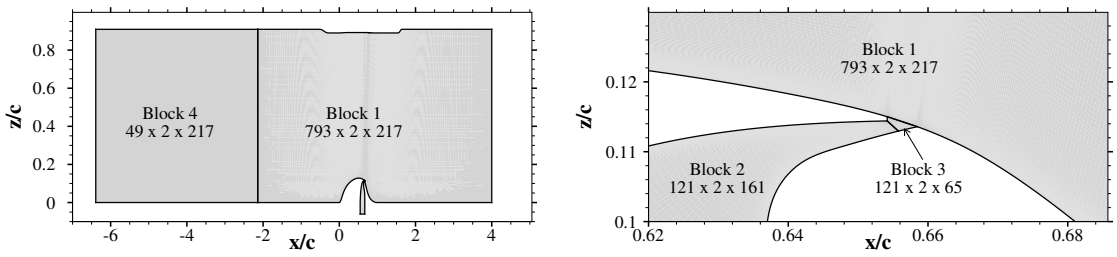

(a) Overview. The axes are not to scale.

(b) Close view to include blocks 2 and 3

Figure 2.18: Illustration of the grid blocks for the WMH

Baseline case

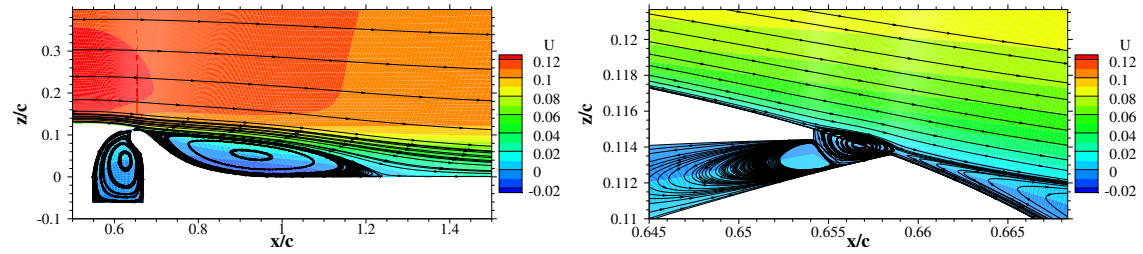

(a) Overview of the recirculation separation bubble and the plenum

(b) Close view of the interface between the plenum and the main flow

Figure 2.19: Non-dimensional streamwise velocity field and streamlines for the WMH (baseline)

First, consider the baseline case without flow control. The plenum is present, but does not affect the flow. Figure 2.19 is an overview of the solution field. A bubble forms at the interface between the bump and the plenum, essentially closing the plenum. The results obtained with GTsim are in excellent agreement with CFL3D results [102], as illustrated by the pressure and skin friction distributions in Fig. 2.20, the velocity profiles in Fig. 2.21 and the modeled turbulent shear stresses in Fig. 2.22. The numerical solutions are also compared to experiments. The computations over-predict the extent of the recirculation region, resulting in differences in the quantities compared. Nonetheless, the objective of verifying the multiblock implementation in

GTsim was achieved, as the relative error compared to CFL3D is less than 2% in all quantities of interest.

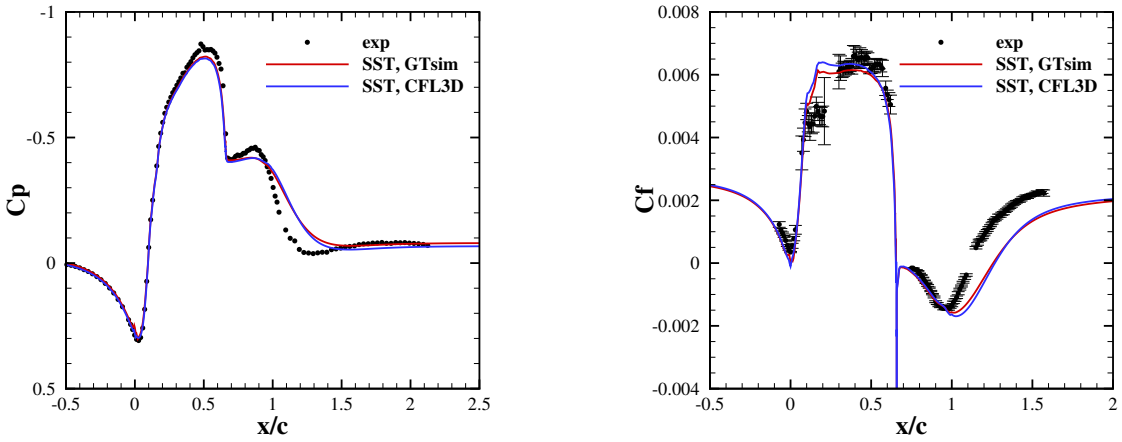

Figure 2.20: Pressure and skin friction coefficient distributions along the bottom wall of the WMH (baseline)

The under-predicted turbulent shear stresses are characteristic of RANS models in separated regions. Studies of this problem with LES in the literature have shown that significant improvements on the second-order statistics and the reattachment location are possible. That said, matching all quantities of interest to experiments (pressure coefficient, skin friction coefficient, velocity and turbulent shear stress profiles) precisely (e.g. within 5%) remains a challenge, even with LES [109–112].

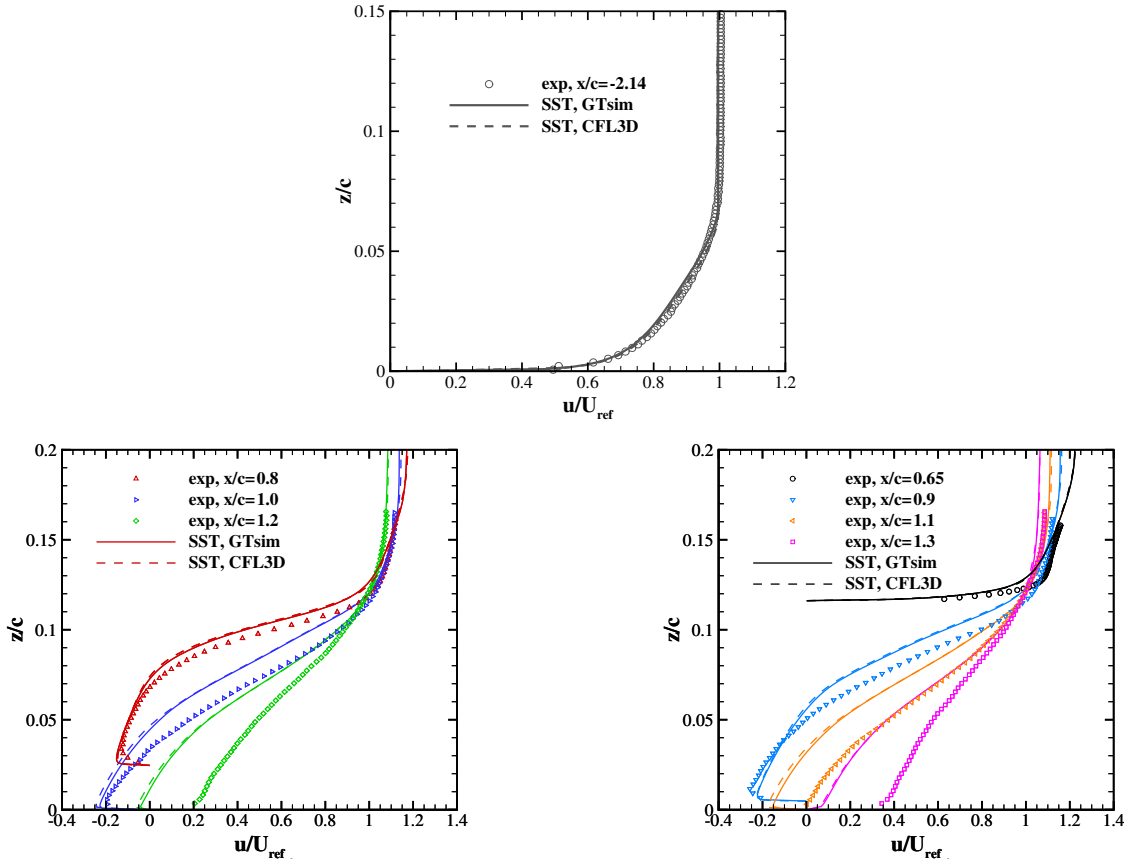

Figure 2.21: Velocity profiles for the WMH (baseline)

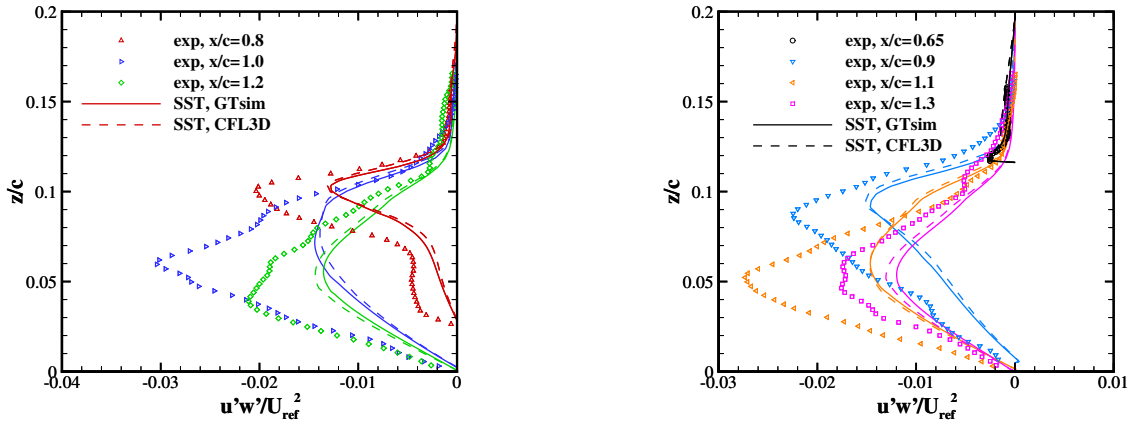

Figure 2.22: Turbulent shear stress profiles for the WMH (baseline)

Steady suction case

A steady suction case was simulated in GTsim. The mass flow at the bottom of the plenum is 0.01518 kg/s. As illustrated in Fig. 2.23, part of the main flow is now

diverted into the plenum to reduce the separation over the hump. Experimental data are only available for the pressure distribution, serving as a basis of comparison for the GTsim result (Fig. 2.24). The computation over-estimates the pressure coefficient right before the plenum, and under-estimates it in the recirculation region. Fig. 2.24 also presents a comparison of the skin friction distribution between the baseline and steady suction cases; the differences are consistent with a decrease of the extent of the recirculation region when steady suction is applied.

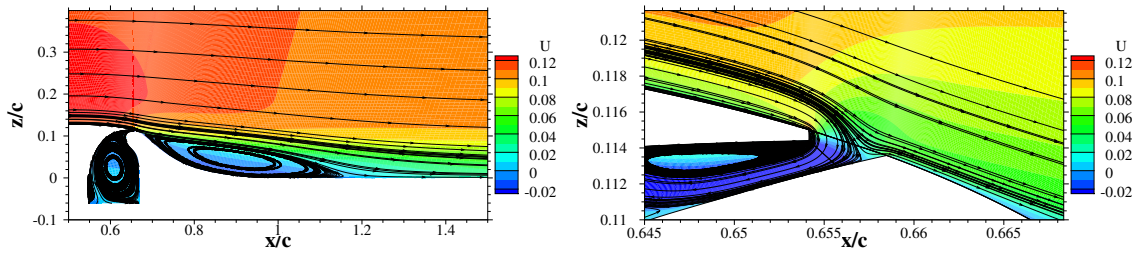

(a) Overview of the recirculation separation bubble and the plenum

(b) Close view of the interface between the plenum and the main flow

Figure 2.23: Non-dimensional streamwise velocity field and streamlines for the WMH (steady suction)

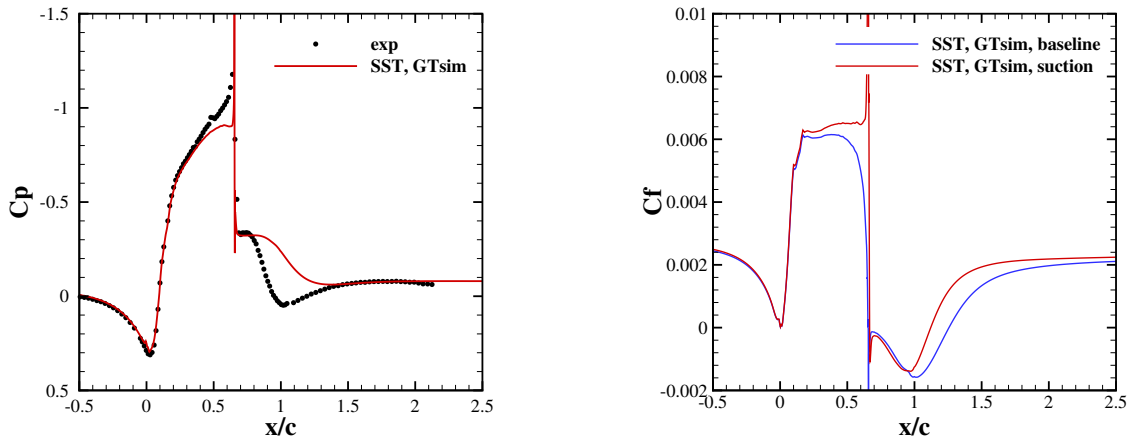

Figure 2.24: Pressure and skin friction coefficient distributions along the bottom wall of the WMH (steady suction)

The evaluation of the steady suction case provides a qualitative comparison with the baseline case. As with the baseline case, many considerations such as 3D, LES and turbulent inflows must be included to favorably compare with experimental data.

2.5.7 Square lid-driven cavity manufactured solution

Consider a two-dimensional laminar lid-driven square cavity over the domain $[0,1] \times [0,1]$. This test case serves as a validation for the interpolation procedure across multiblock zonal interfaces. The computational domain is illustrated by Fig. 2.25. The upper boundary is a viscous moving wall, while the other three sides of the domain are viscous stationary walls.

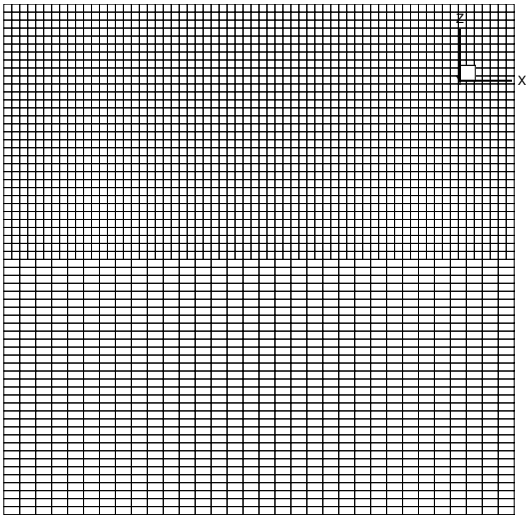

Figure 2.25: Two-block grid ($32 \times 32 + 64 \times 32$) for the square cavity manufactured solution

A manufactured solution can be designed for an incompressible flow, with the addition of a body force $\left(-\int_\Omega B dV\right)$ to the right hand side of the w-momentum equation. The problem then admits an exact solution [113] defined as

$$\begin{aligned} u(x,z) &= 8f(x)g'(z) \\ w(x,z) &= -8f'(x)g(z)\ , \end{aligned} \tag{2.30}$$

where

$$\begin{aligned} f(x) &= x^4 - 2x^3 + x^2 \\ g(z) &= z^4 - z^2\ . \end{aligned} \tag{2.31}$$

The moving wall has a Dirichlet boundary condition given by the exact solution $u(x,1)$, and the body force is given by

$$B(x,z,Re) = -\frac{8}{Re}\left[g''''F + 2f'g'' + f'''g\right] - 64\left[F_2G_1 - gg'F_1\right] \ , \tag{2.32}$$

where

$$\begin{aligned} F(x) &= \int f(x)dx \\ F_1(x) &= f(x)f''(x) - \left[f'(x)\right]^2 \\ F_2(x) &= 0.5\left[f(x)\right]^2 \\ G_1(z) &= g(z)g'''(z) - g'(z)g''(z) \ . \end{aligned} \tag{2.33}$$

The simulation is carried out with the incompressible solver with theoretically second-order central differences, $\overline{\beta} = 100$ and $Re = 1$. The compressible solver cannot be used in this case due to unphysical values of pressure that would result in negative temperatures. The solution obtained is illustrated in Fig. 2.26. The visualization software is configured to plot the exact cell-centered solution exported from GTsim. Figure 2.27 presents a comparison to the exact solution at the vertical and horizontal centerlines.

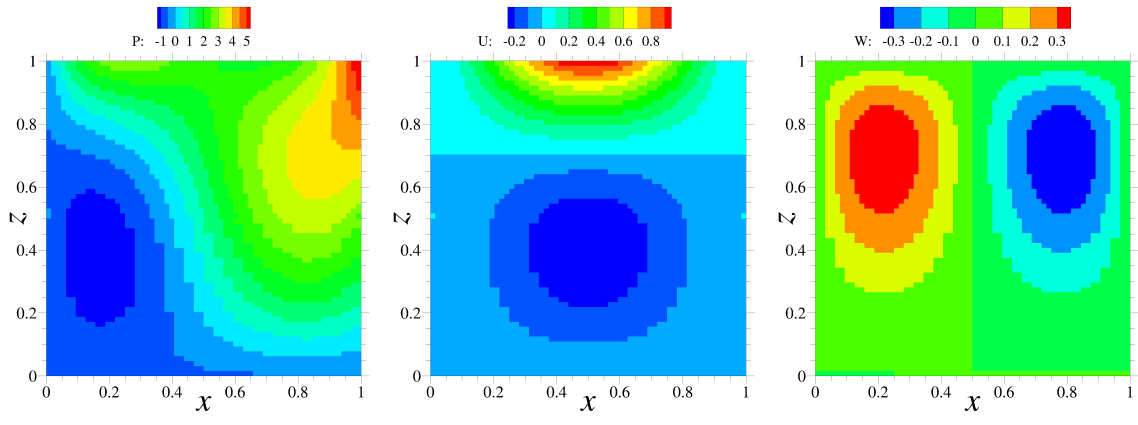

Figure 2.26: Cell-centered contours of pressure, horizontal and vertical velocities for the square cavity manufactured solution (two-block grid $32 \times 32 + 64 \times 32$)

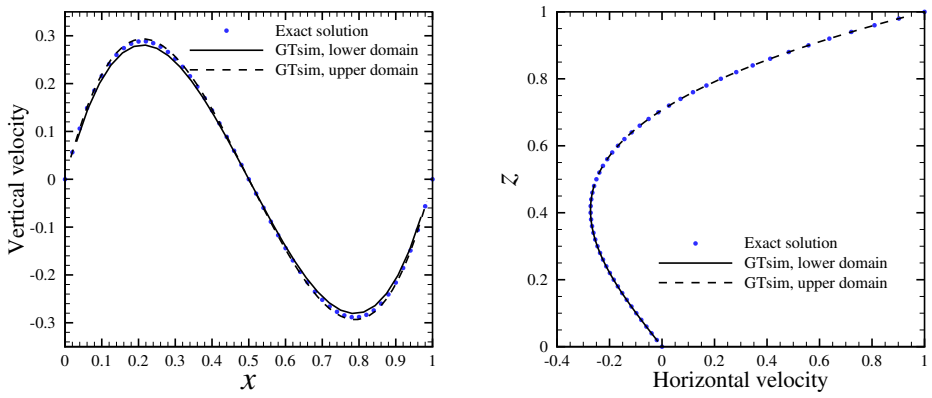

(a) Horizontal cut

(b) Vertical cut

Figure 2.27: Velocities for the square cavity manufactured solution (two-block grid $32 \times 32 + 64 \times 32$) at the vertical and horizontal centerlines

The numerical solution approximates the exact solution within discretization and interpolation errors. It is noteworthy that the pressure is correctly predicted with the artificial compressibility approach. The numerical errors were quantified on multiple grids (single-block and two-block) to assess the order of accuracy and evaluate the effect of the interpolation. Figure 2.28 illustrates the decrease of numerical error with grid refinement. The apparent order of accuracy varies between 1.61 and 1.94. Hodara [52] previously found that the formal spatial order of accuracy of GTsim is 1.32 rather than 2 on a flat plate, consistent with results obtained with FUN3D and CFL3D [102]. The reason for this behavior was identified as the leading edge singularity. The manufactured solution employed here has no such singularity and is a more appropriate case to recover the second-order accuracy. Here, the artificial compressibility remains a limiting factor on the finest grids. In fact, additional tests conducted with different values of $\overline{\beta}$ showed a dependence of the numerical accuracy on the chosen value.

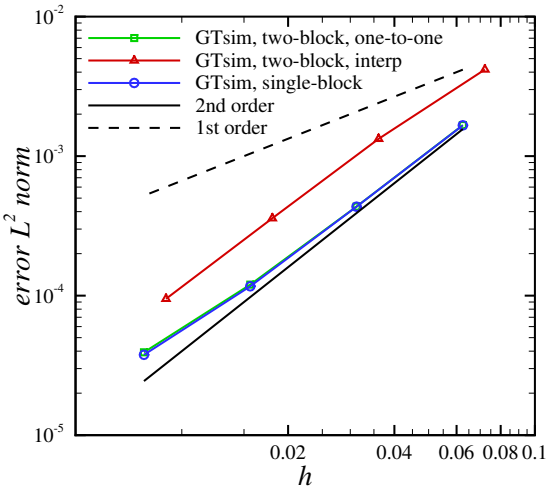

Figure 2.28: L^2 norm of the error for the square cavity manufactured solution, $h = \sqrt{\frac{1}{N_{cells}}}$

The block structured approach with one-to-one interfaces recovers the solution on a single block, whereas the interpolation shifts the curve to higher error values. Indeed the interpolation procedure introduces an error at the boundaries: points $(x,\ z) = (0,\ 0.5)$ and $(1,\ 0.5)$ when each block is attached to one processor. At these location, the solution is obtained on the finer grid by a convex average of the two closest points from the coarser grid (section 2.4).

In the present study, each grid block was assigned to one processor when the interpolation is employed. The more processors are used, the more boundaries are introduced. A linear interpolation formula extrapolates at the boundaries instead of the inverse distance weighting, which was verified to result in a similar increase in error while maintaining second-oder accuracy. To avoid the erroneous weighted averages or the extrapolation, the finer grid should be supplied with ghost cell values from the coarser grid. While the dependence of the interpolation accuracy on the number of processors can be mitigated using that approach for cell inside the computational domain, the approach cannot be applied at outer boundaries (walls in the present case), as no grid information is known.

In summary, the artificial compressibility method and the interpolation procedure implemented have been verified to yield close to second-order spatial accuracy. The interpolation introduces errors at domain boundaries, where there is not enough information to determine the fine-grid values accurately. Therefore, the remainder of the thesis employs one-to-one interfaces between grid blocks, with very few exceptions.

2.6 Technical findings

The numerical schemes implemented in GTsim were presented and evaluated on several test cases. The ability to predict high-speed flows including shock waves was verified, and the direction-by-direction fifth-order WENO scheme provided enhance resolution of flow structures. These features are needed to accurately capture the physics of the supersonic nozzle of fluidic oscillators in many situation. The multiblock capability, necessary to simulate flows around complex geometries on structured grids, compared favorably with another multiblock code (CFL3D).

In addition to the discussions in this chapter, both the incompressible solver and the multiblock approach in GTsim were successfully employed in other studies. Lefebvre et al. [114] employed the incompressible solver to investigate the interaction between an airfoil and a cylinder wake, while Grubb et al. [115] applied it to nonlinear transverse gust encounters.

Finally, the code improvements described herein were supplemented with the introduction of better software development practices: *git* was adopted for version control, and an automated suite of cases was implemented in *Python 3* for regression testing.

CHAPTER 3
CHARACTERIZATION OF A JET INTERACTION FLUIDIC OSCILLATOR IN A QUIESCENT AMBIENT

The first step in the simulation of fluidic oscillators for flow control is the characterization of their behavior. This is accomplished by considering an isolated sweeping jet issuing into a quiescent ambient without any external interaction. The purpose here is to quantify the computational requirements to accurately predict the characteristics of a fluidic oscillator, such as the oscillation frequency, jet penetration and spreading. Further, boundary condition models that would reduce the computational cost in arrays of oscillators are of interest. In particular the importance of turbulence in these boundary condition models is assessed.

3.1 Geometry and experimental data

A feedback-free fluidic oscillator from the isolated jet experimental investigations of Burrows et al. [116] was characterized numerically. Figure 3.1 defines the important regions of the fluidic oscillator, such as the dome (left of the internal cavity) and the upper/lower sides. Figure 3.2 summarizes the definition of device dimensions. In the present chapter, the inner orifice (or throat) is normal to the actuator's internal cavity centerline and has a width $\tilde{W} = 1$ mm (0.0394 in). The internal height of the actuator cavity normal to the plane of oscillations is $\tilde{H} = 1.5$ mm (0.059 in). The outer orifice (or exit) has a width $\tilde{A}/\tilde{H} = 1.68$ mm (0.0661 in), where $\tilde{A}$ is the area. The nozzle has a length $\tilde{l} = 0.74$ mm (0.029 in), and the distance from the cavity side to the throat is $\tilde{L} = 1.27$ mm (0.05 in). The dimensions of the exit plane orifice of the actuator can vary in experimental implementations depending on the curvature of the surface through which the actuation jet issues. The exit plane of the bench-top

model actuator in Burrows et al. [116] was normal to the centerline of the actuator's cavity.

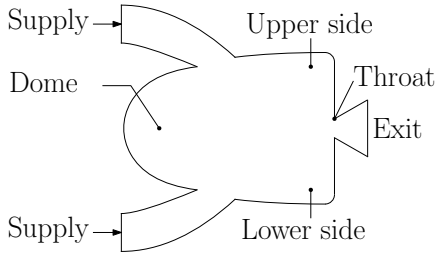

Figure 3.1: Key regions of a jet interaction fluidic oscillator

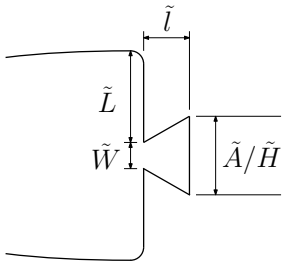

Figure 3.2: Definition of the key dimensions of the fluidic oscillator

The numerical solution is compared to experiments for the sweeping frequency and the sweeping jet velocity distribution obtained using hot wire anemometry at multiple streamwise locations (x-direction). The hot-wire has diameter 5 μm (0.197×10^{-3} in) and length 1.25 mm (0.0492 in). Figure 3.3 depicts the orientation of the hot wire and its relative size to the model. The wire was mounted on a traverse system that permits a vertical translation (z-direction in Fig. 3.3) at a given streamwise location. The velocities were time-averaged over a long time period (greater than 1000 cycles) in the experiments. Unfortunately, the raw experimental data (instantaneous) was no longer available a the time of the present computations. However, recent experimental data obtained by the same group for a different fluidic oscillator are described in Chapter 4. The latter instantaneous measurements were acquired at a sampling frequency of 46 kHz.

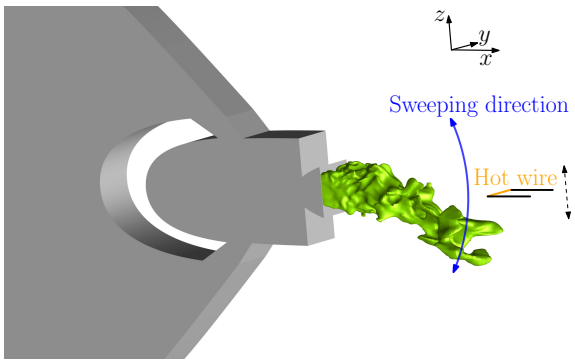

Figure 3.3: Hot wire placement over iso-surface of local Mach number ($M = 0.9$)

3.2 Computational setup

The computational mesh is block-structured, composed of six blocks. The reference temperature is 290.1 Kelvin, thereby setting the freestream speed of sound $\tilde{a}_\infty$. In the absence of exact information regarding the inflow conditions, the driving pressure was set to 2.45 atmospheres (following the work of Lakebrink et al. [63]) and the static temperature of the supply fluid was set to the reference temperature. These resulted in a volume flow rate of approximately 21.5 SLPM (standard liter per minute), where the experimental sweeping frequency is 12.6 kHz. A sensitivity analysis with respect to the inflow conditions was later conducted. The Reynolds number is 475, based on a reference length $\tilde{L}_R = 1$ mm (0.0394 in) and a velocity of 7.04 m/s (23.1 ft/s).

Simulations were performed with both the fully turbulent URANS (Menter SST [34]) and the HRLES [49] turbulence closures. Here, the HRLES model coefficients are kept constant, and the cross-coupling hybrid terms [49] are not included. One simulation was performed with the SST-DDES closure [46]. The second-order Roe scheme was selected for the majority of the computations with a MUSCL reconstruction, as supersonic conditions are reached within the computational domain. The fifth-order WENO reconstruction was also evaluated a posteriori to the initial computations.

Figure 3.4 illustrates the computational domain, where one grid unit corresponds to $\tilde{L}_R$, taken as the geometric throat width. The control volume for the quiescent field

extends 175 grid units in the streamwise direction (x-direction in Fig. 3.4) and 50 grid units in both lateral and spanwise directions. For comparison, the computational domain of Aram et al. [60] extended 341, 630 and 10 grid units in the streamwise, lateral and spanwise directions respectively. The left boundary is a subsonic inflow. Farfield boundary conditions are applied to the quiescent field, except its left boundary, with zero velocity, a pressure ratio of one and turbulence quantities extrapolated from the interior. Part of the left boundary of the quiescent field connects to the actuator, and the rest is either considered a farfield boundary or a viscous wall. The difference between these two boundary treatments is later discussed. The other boundaries of the computational domain are viscous adiabatic walls.

Multiple grids were evaluated to assess the level of refinement required to capture the quantities of interest. Table 3.1 summarizes these grid levels. The solutions on the finer grids were initialized from solutions on coarser grids to reduce the cost of simulating the initial transients. Grids *A* and *D* are considered coarse, as y_1^+ is not less than 1 everywhere. *Grid B* and *Grid E* have $y_1^+ < 1$ everywhere and are considered to be of medium resolution. The mixed *Grid C* was constructed by using the resolution of the coarse grids for the interior of the device, and a resolution even finer than the medium grids in the quiescent field. In this case, the interface between the actuator and the quiescent ambient is not one-to-one. Finally, a fine 3D grid was constructed by refining the quiescent field, while maintaining a one-to-one interface with the actuator.

It was immediately observed that the simulations must be time-accurate from the moment they are started. An initial simulation in pseudo-time to initialize the flow field was found to be inadequate as an attachment of the jet to the lower farfield boundary was observed after marching in pseudo-time, and subsequent time-accurate simulations were unsuccessful in starting the jet oscillations [117]. A large time step or insufficient number of sub-iterations also resulted in a non-oscillating jet. This

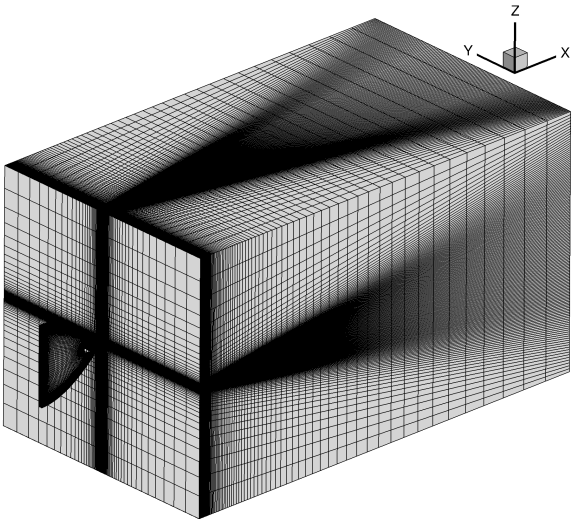

(a) Overview of 3D the grid

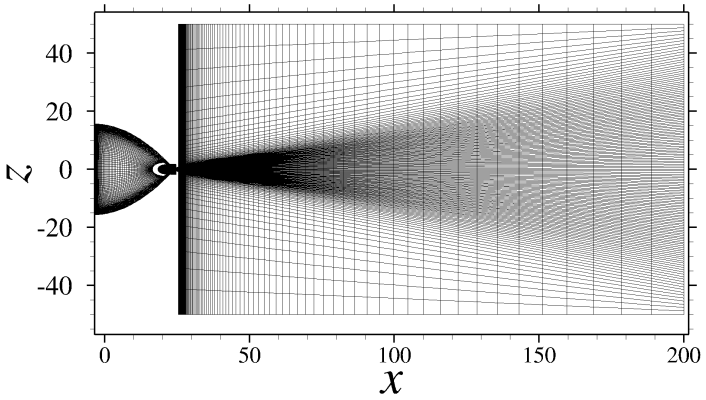

(b) Overview of the mid-plane

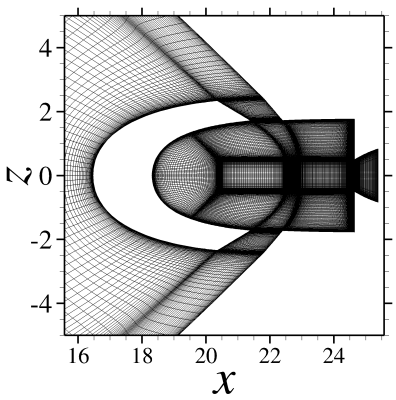

(c) Close view of the cavity

Figure 3.4: Coarse grid employed to characterize the fluidic oscillator in quiescent conditions

Table 3.1: Grids for the fluidic oscillator characterization. Detailed dimensions N_ξ, N_η and N_ξ pertain to the quiescent ambient.

Grid name	Grid level	2D/3D	N_ξ	N_η	N_ξ	N_{cells} (Exterior)	N_{cells} (Total)
Grid A	Coarse	2D	119	1	148	17,612	94,258
Grid B	Medium	2D	239	1	298	71,222	380,708
Grid C	Mixed	2D	479	1	598	286,442	1,530,208
Grid D	Coarse	3D	119	147	148	2,588,964	6,344,718
Grid E	Medium	3D	239	297	298	21,152,934	51,792,048
Grid F	Fine	3D	479	297	518	73,692,234	104,331,348

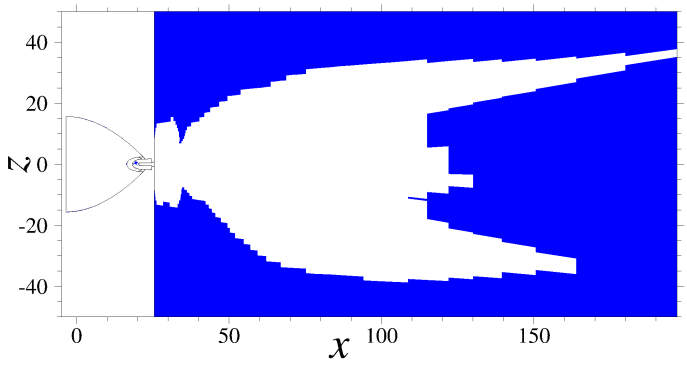

Figure 3.5: Instantaneous solution at the mid-plane of the medium 3D grid where regions of Mach > 0.01 have been blanked

appears to be a behavior specific to jet interaction fluidic oscillators, as Krüger et al. [56] reported starting from a steady-state solution for a double feedback loop fluidic oscillator.

The implementation of the preconditioning scheme introduced in section 2.2.2 was prompted by the solver's inability to obtain jet oscillation in the early stages of this work. Figure 3.5 is a map indicating that velocity scale inside the actuator and in the immediate vicinity of its exit exceeds Mach 0.01, which is expected to be large enough to obtain an accurate solution with the compressible solver based on earlier tests (sections 2.5.1 and 2.5.2).

Three time steps were evaluated on *Grid A* (coarse 2D grid), corresponding to 410, 820 and 3280 iterations per cycle, to determine the time steps needed to accurately capture the resulting frequency. Table 3.2 compares these time resolutions to other values found in the literature. Ten to fifteen sub-iterations are performed per time step to reduce the residuals by two to three orders of magnitude to local convergence.

3.3 Frequency characteristics

The sweeping frequency is estimated from the simulations by taking the Fourier transform of the velocity (stored at every iteration) at several points within the jet region.

Table 3.2: Time steps employed in simulations of fluidic oscillators

Reference	Oscillator type	Δt (μs)	f (kHz)	iter/cycle
Gokoglu et al. [54]	Double feedback	1 to 10	$\mathcal{O}(5)$	20 to 200
Krüger et al. [56]	Double feedback	10 to 100	$\mathcal{O}(0.02)$	500 to 5000
Childs et al. [68]	Double feedback	5	$\mathcal{O}(0.3)$	660
Duda et al. [64]	Double feedback	0.8 to 1.3	$\mathcal{O}(0.2)$	3850 to 6250
Lakebrink et al. [63]	Jet interaction	0.06	$\mathcal{O}(13)$	1230
Shmilovich et al. [71]	Double feedback	-	$\mathcal{O}(0.25)$	800 to 1750
Present	Jet interaction	0.025 to 0.2	$\mathcal{O}(13)$	420 to 3280

An accurate estimation of the sweeping frequency requires sufficient number of oscillation periods to be recorded. At least ten cycles were employed from the simulations, and many more from the experiments. In some cases, especially in 3D, the second harmonic of the oscillation frequency dominates the spectrum of the velocity magnitude. The vertical velocity can be used to unequivocally determine the natural frequency. Indeed, the velocity magnitude exhibits two peaks per period at the jet centerline, while the vertical velocity only exhibits one (Fig. 3.6). This is due to the sweeping jet passing through the centerline twice per cycle, and the frequency estimates from hot wire measurements must often be halved for this reason.

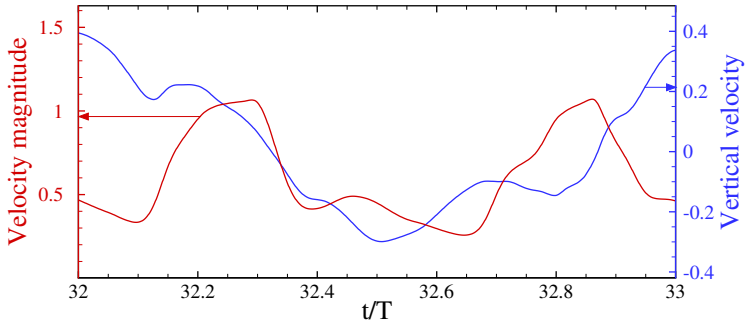

Figure 3.6: Non-dimensional vertical velocity (w) and velocity magnitude ($\sqrt{u^2+v^2+w^2}$) over one period of oscillation, coarse grid, 3D URANS

Figures 3.7a and b are comparisons of the power spectral densities for the different time steps and levels of turbulence closure fidelity. The frequencies obtained in the

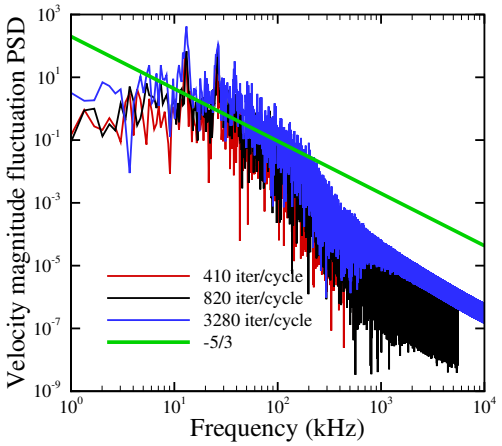

(a) Multiple time steps, 2D SST-URANS

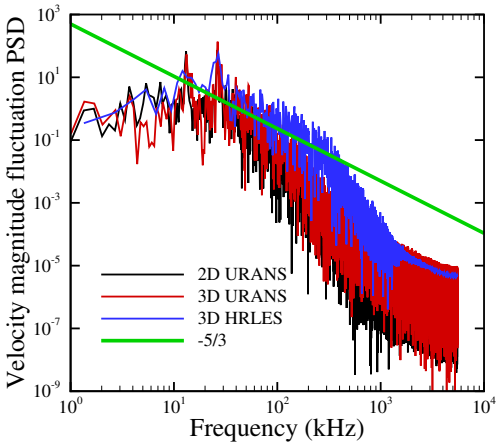

(b) Multiple levels of fidelity from 2D SST-URANS to 3D HRLES, 820 iterations per cycle

Figure 3.7: Power spectral density for multiple time steps and levels of fidelity, coarse grids

simulations are within 5% of the experimental value for the volume flow rate examined (12.6 kHz), even with 2D SST-URANS and/or interpolation across blocks in 2D (Table 3.3). Accuracy in the prediction of the frequencies is improved with grid refinement in 3D. The frequency content from 30 kHz to 400 kHz more accurately predicts the negative 5/3 slope with HRLES, confirming the resolution of turbulent scales in the inertial subrange. The different time steps evaluated on the coarse 2D grid with URANS resulted in similar frequency contents up to 300 kHz, indicating that the solution is time step independent in 2D. In order to achieve adequate convergence in the sub-iterations in 3D, the time step corresponding to 820 iterations per cycle was selected for all other simulations in the present chapter.

The resolution of turbulent scales, suggested by the spectra, is also reflected in the Q-criterion iso-surfaces presented in Fig. 3.8. The flow structures are better resolved with finer grids and higher-order reconstructions. As expected, the URANS closure resolves the least the turbulent structures (Fig. 3.8a and b). URANS models most of the turbulence with large values of eddy viscosity that dissipate small-scale

Table 3.3: Fluidic oscillator natural frequency for different grids and turbulent closures, 820 iterations per cycle

Grid name	2D/3D	Turbulence model	f (kHz)	Error (%)
Grid A	2D	$k-\omega$ SST	13.1	4.0
Grid B	2D	$k-\omega$ SST	12.0	4.8
Grid C	2D	$k-\omega$ SST	13.1	4.0
Grid D	3D	$k-\omega$ SST	13.1	4.0
Grid D	3D	HRLES	13.1	4.0
Grid E	3D	SST-DDES	12.7	0.8
Grid E	3D	HRLES	12.6	0.0

structures. In contrast, HRLES resolves more turbulent scales, and the density of the resolved scales increases with grid refinement (Fig. 3.8c versus e), and higher-order reconstruction (Fig. 3.8c versus d).

3.4 Sweeping jet velocity characteristics

The flow fields from the simulations were also time-averaged to compare the different numerical approaches. Time-averaging is only performed after a periodic steady state has been reached. Periodic steady state is characterized by an oscillation of the flow variables about a constant value at the natural frequency. An example of convergence to a periodic steady stated is presented in Fig. 3.9 for the density, which experiences the slowest convergence. In this case, time-averaging is performed for $t/T > 30$. The density evolution exhibits an initial oscillation around $\rho \simeq 0.95$, before transitioning to an oscillation about $\rho \simeq 1.2$. The first oscillation around $\rho \simeq 0.95$ is misleading and the transition to the higher densities takes a long time, especially on refined grids. The approach employed to minimize the computational cost on the refined grids consisted of interpolating a solution that had already converged to periodic steady state onto the finer grid to initialize the flow field, thereby bypassing the initial transients.

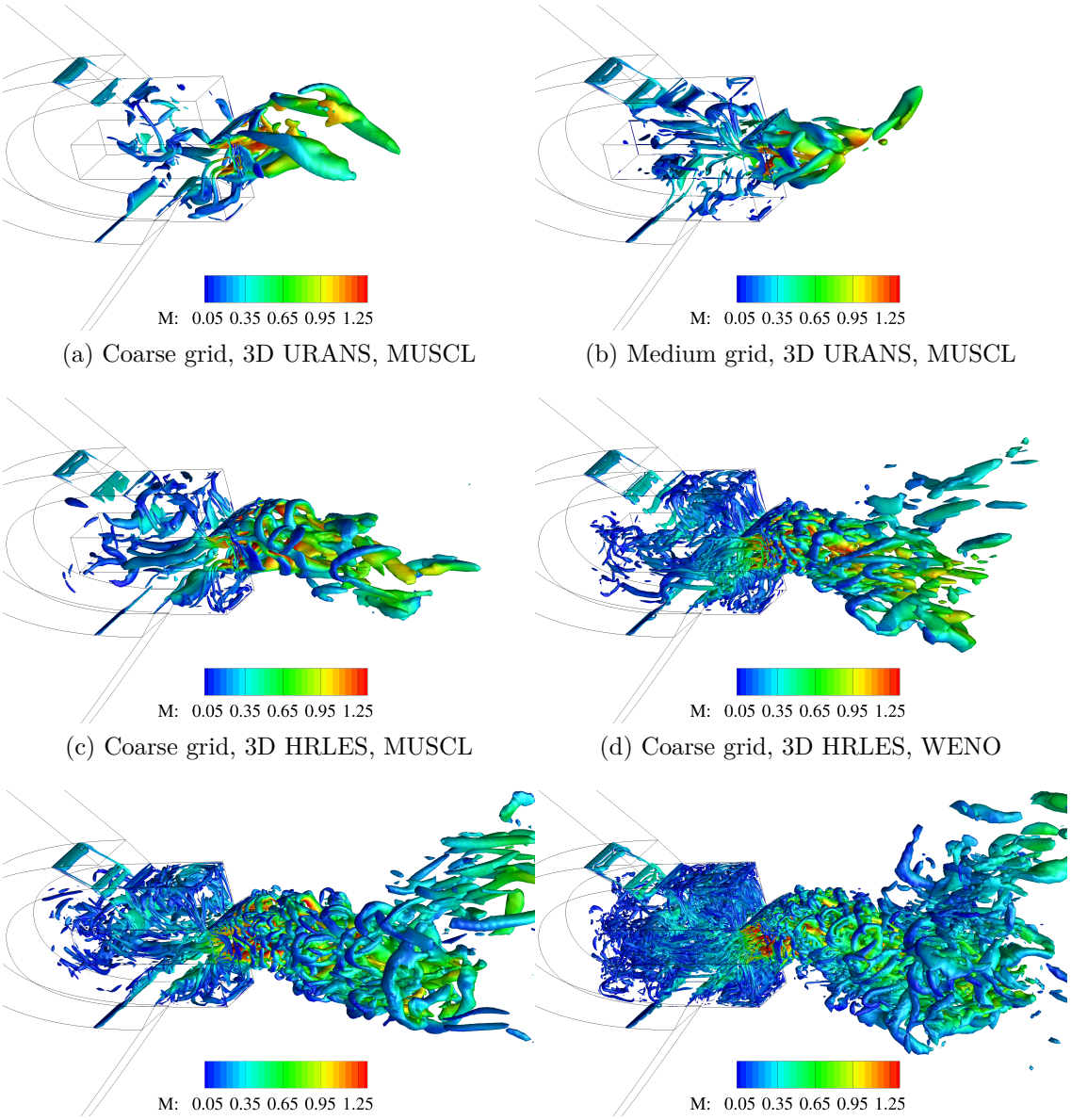

(a) Coarse grid, 3D URANS, MUSCL

(b) Medium grid, 3D URANS, MUSCL

(c) Coarse grid, 3D HRLES, MUSCL

(d) Coarse grid, 3D HRLES, WENO

(e) Medium grid, 3D HRLES, MUSCL

(f) Medium grid, 3D HRLES, WENO

Figure 3.8: Iso-surfaces of second invariant of the velocity gradient tensor ($Q = 1$) colored with values of local Mach number.

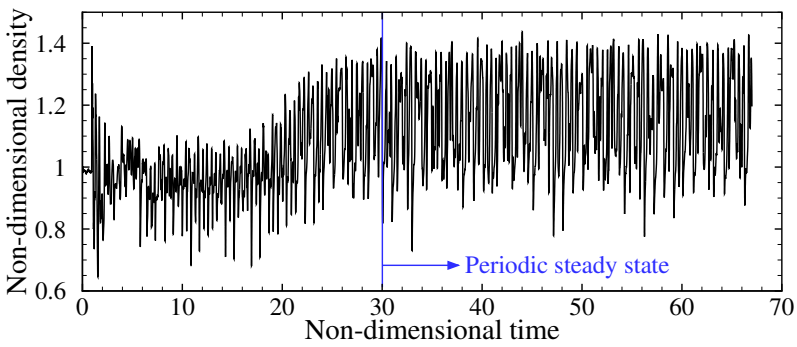

Figure 3.9: Convergence of density to a periodic steady state at the jet centerline, coarse 2D grid, 820 iterations per cycle

There are fundamental differences between 2D and 3D simulations noticeable in the mean local Mach numbers of the sweeping jet (Fig. 3.10 and Fig. 3.11). The 3D solution exhibits two dominant directions in the time-averaged jet, where the 2D solution does not. This concurs with the recent findings of Aram et al. [60]. Changing the boundary condition at the plane adjacent to the actuator exit from a viscous wall to a farfield resulted in small variations in the velocities (Fig. 3.10d). This zero velocity farfield boundary condition was found to be less stable compared to the viscous wall boundary condition. Figures 3.12 and 3.13 illustrate the HRLES blending function and time-averaged turbulent kinetic energy (TKE or k). A large part of the internal cavity is resolved with LES, as well as the nozzle and quiescent ambient. The TKE contours show that turbulence develops inside the nozzle and exhibits two dominant directions in the quiescent ambient.

The length of the hot wire is 1.25 mm, which is almost as large as the depth of the fluidic oscillator, as illustrated in Fig. 3.3. As a result, a spanwise average was taken from the CFD data over the hot wire length. The averaged value was then corrected as described by Polsky and Ghee [118] to account for the spanwise flow in the hot wire probe experiments. With this correction, the average velocity is given by:

$$V_{mean} = \sqrt{u^2 + w^2} \left(\cos \left[\tan^{-1} \left(\frac{v}{\sqrt{u^2 + w^2}} \right) \right] \right) \ . \tag{3.1}$$

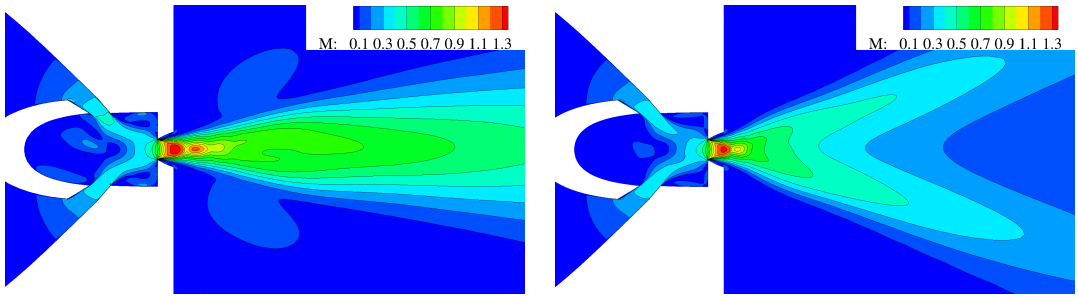

(a) 2D SST-URANS (b) 3D SST-URANS

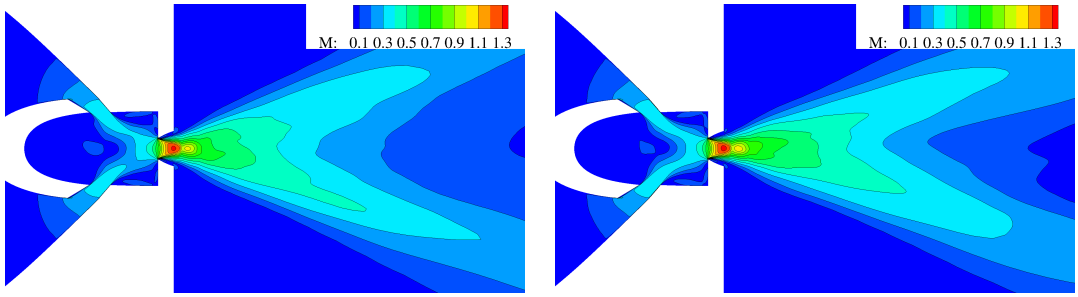

(c) 3D HRLES (d) 3D HRLES with the boundary condition changed from a viscous wall to a farfield next to the actuator exit

Figure 3.10: Time-averaged Mach number contours, coarse grids (MUSCL reconstruction)

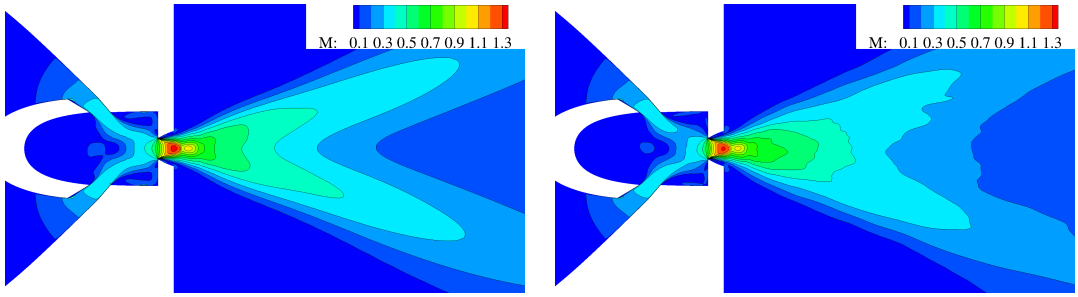

(a) 3D SST-URANS (b) 3D HRLES

Figure 3.11: Time-averaged Mach number contours, medium grids (MUSCL reconstruction)

This correction was on the order of 1% for the present velocity profiles. These profiles are compared to experiments in Fig. 3.14, where all velocity profiles are non-dimensionalized by the peak velocity magnitude five throat widths downstream of the exit (V_0). This peak velocity magnitude is overestimated by 10% in the computations. Factors affecting this value are later discussed. For the moment, consider

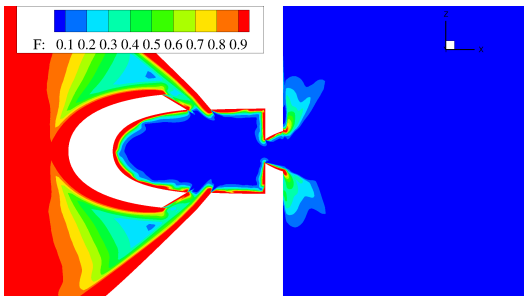

Figure 3.12: Instantaneous HRLES blending function, 0 (LES) $\leq F \leq$ 1 (RANS) at the mid-plane of *Grid D*

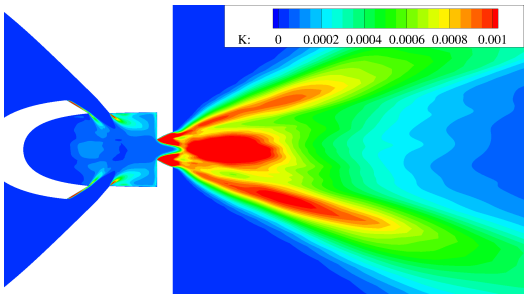

Figure 3.13: Time-averaged hybrid turbulent kinetic energy (non-dimensionalized by $M_\infty^2 = 0.0206^2$) at the mid-plane of *Grid D*

the non-dimensional profiles. The main features of the sweeping jet are captured in the simulation: dual peak in the velocity profiles, spreading of the jet, decrease in the peak velocities with distance from the actuator exit. However, up to 35% relative error in the peak jet velocities is obtained on the coarse grid, seen at $z/w \simeq \pm 4$ in Fig. 3.14a and b.

The error is reduced to 30% on the medium grid (Fig. 3.14 d) with the HRLES closure, but discrepancies still persist. Grid refinement does not improve the URANS solution (Fig. 3.14c). With the HRLES solution on the medium grid, the correlation between computation and experiment is best close to the jet exit in the streamwise direction, and close to the centerline in the transverse direction (10% error approximately). The correlations worsens as the distance from the jet orifice increases. One possible reason for this is that the grid becomes coarser than required away from the jet orifice. Computations with WENO and HRLES performed on the fine 3D grid did

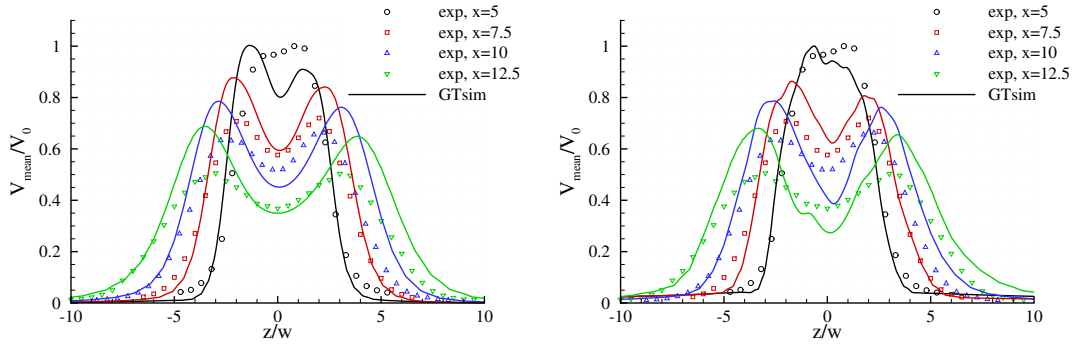

(a) Coarse grid, 3D URANS

(b) Coarse grid, 3D HRLES

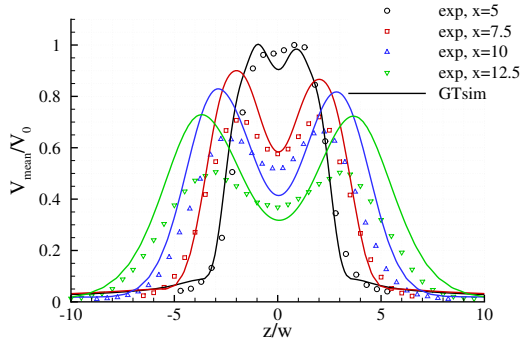

(c) Medium grid, 3D URANS

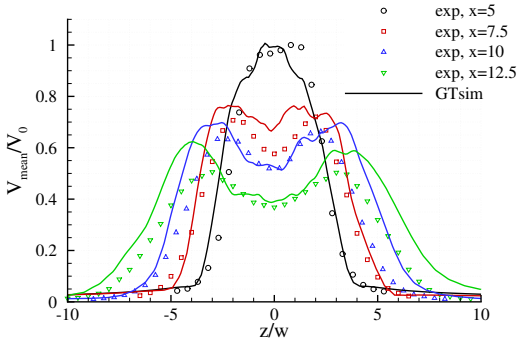

(d) Medium grid, 3D HRLES

Figure 3.14: Jet velocity distributions with MUSCL reconstruction. x indicates the distance between the measurement plane and the device exit as multiples of the throat width.

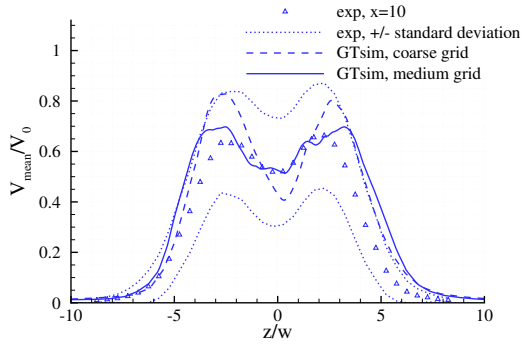

(a) Comparison between the coarse and medium grids, 3D HRLES

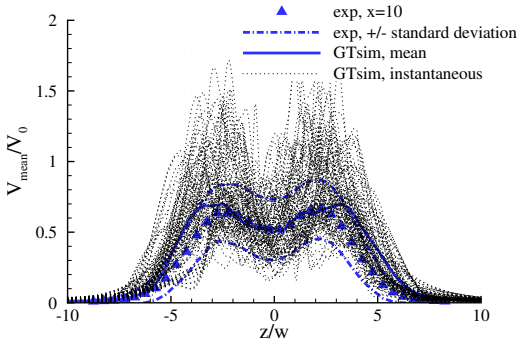

(b) Reduced set of instantaneous profiles obtained with the medium grid, 3D HRLES

Figure 3.15: Jet velocity distributions 10 throat widths downstream of the exit with experimental standard deviation

not further improved the correlations with experimental data, indicating that there are other considerations than the grid involved.

Further analysis of the instantaneous data was undertaken to fully characterize the CFD and experimental results, as performing the 3D simulations for a long enough time to collect smooth second-order statistics would be expensive. In Fig. 3.15a, the velocity profiles ten throat widths downstream of the actuator exit are plotted with the standard deviation from the experimental data. The time-averaged computational data is within one standard deviation of the experimental everywhere. Computations with both HRLES and SST-DDES turbulence closure resulted in similar velocity distributions on the medium grid. The instantaneous computational profiles (not spanwise-averaged or corrected for hot wire spanwise flow) are included in Fig. 3.15b to illustrate the unsteadiness of the distributions.

3.5 Internal flow dynamics

In a series of publications, Tomac and Gregory [119–121] presented PIV measurements for the interior of a jet interaction fluidic oscillator. They identified key physics leading to the self-sustaining oscillation of the jet exiting the device: jet bifurcation, deflection and vortical balance.

Experimental PIV measurements are not feasible at the scale and frequency of the fluidic oscillators considered in this thesis; the actuators are generally scaled to larger sizes and/or lower frequencies to permit time-resolved PIV measurements. Tomac and Gregory [121] employed an aqueous solution as a working fluid to achieve frequencies lower than 100 Hz. Computations can therefore provide some insight into the internal physics of the devices at the same scale as the experiment with frequencies higher than 10 kHz. The resolved flow field in the present simulations of the fluidic oscillators are consistent with the findings of Tomac and Gregory.

To illustrate the simulated device behavior over an oscillation period, Mach number contours and vorticity contours are presented in Fig. 3.16 and 3.17 respectively. These contours are taken at the mid-plane of the fluidic oscillator. Dense inlet stream-

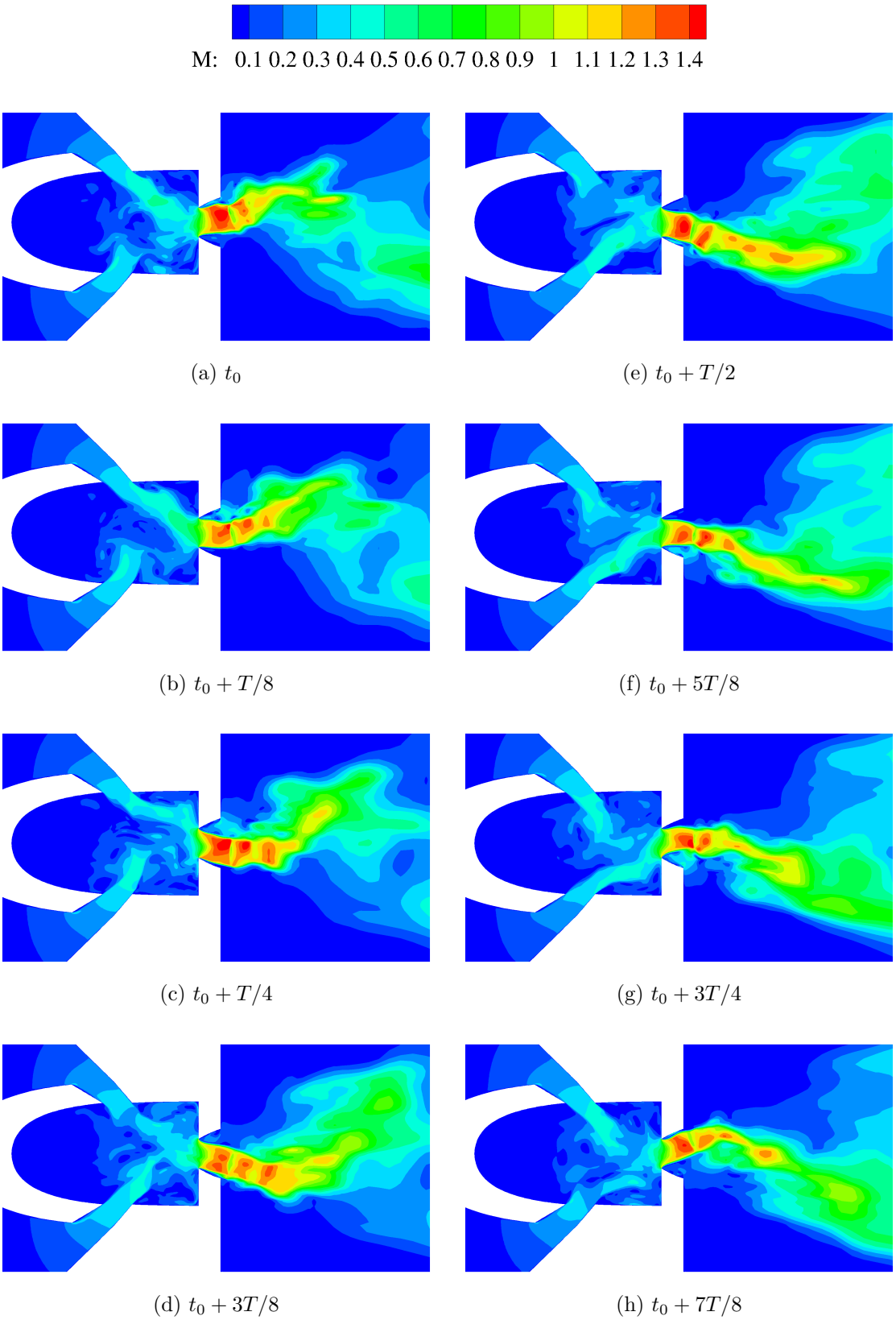

(a) t_0 (e) $t_0 + T/2$

(b) $t_0 + T/8$ (f) $t_0 + 5T/8$

(c) $t_0 + T/4$ (g) $t_0 + 3T/4$

(d) $t_0 + 3T/8$ (h) $t_0 + 7T/8$

Figure 3.16: Instantaneous local Mach number contours at the mid-plane based on 3D HRLES simulations (coarse grid)

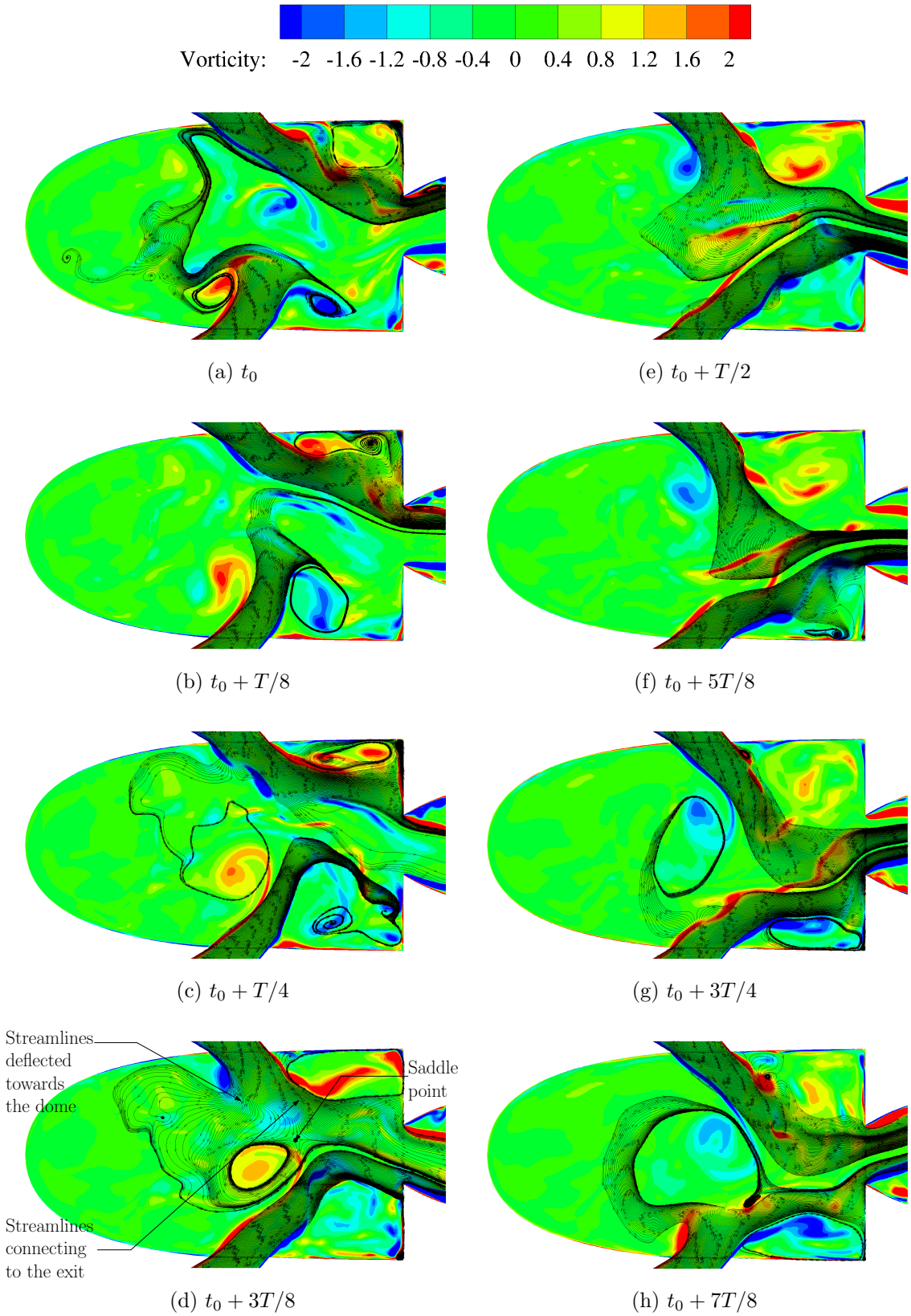

Figure 3.17: Dense inlet streamlines superimposed on vorticity contours at the mid-plane based on 3D HRLES simulations (coarse grid)

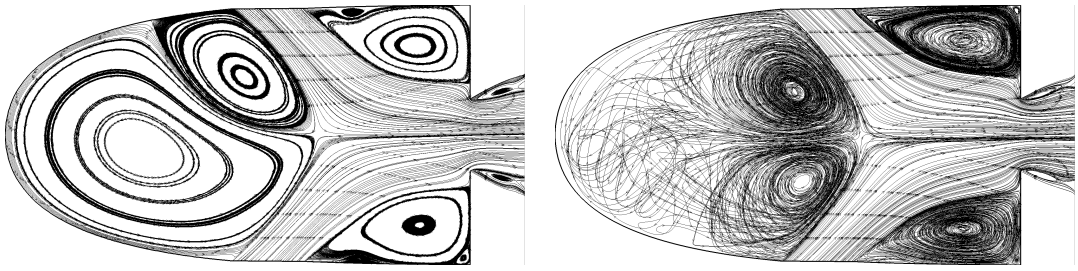

(a) 2D URANS (b) 3D URANS

Figure 3.18: Streamlines of the time-averaged flow field at the mid plane, illustrating the asymmetry in the 2D flow field

lines [121] are superimposed to the vorticity contours to demonstrate the presence of jet bifurcations: part of the supply jets are deflected towards the dome while the other part flows towards the exit. This is clearly seen in Fig. 3.17d for example, in addition to a saddle point separating the streams leading to the exit or the dome. The ability to capture these physics in the computations, consistent with the experimental findings of other researchers, is key to using CFD for future studies of fluidic oscillators.

Figure 3.16 indicates the presence of shock waves at the device exit. Shock waves in the Mach number contours can be identified by regions of sudden decrease in Mach number. In Fig. 3.16, the shock waves are the regions in green (Mach < 1) separating regions in red (Mach > 1.3). This is expected at a pressure ratio of 2.45. These shock waves are smeared by the time-averaging of the Mach number contours in Fig. 3.10.

The instantaneous flow fields from the 3D simulations exhibit a top to bottom symmetry. In other words, the flow field at a phase angle of π rad is approximately a mirror image of that at 0 rad, as seen in Fig. 3.16c and Fig. 3.16g for example. This symmetry was not observed in the dome region from the 2D simulations, indicating that a 3D domain is necessary to correctly resolve the internal flow as well. The instantaneous asymmetry of 2D URANS is reflected in the streamlines of the time-averaged flow fields presented in Fig. 3.18a. In contrast, the time-averaged flow

field from the 3D simulations does exhibit symmetry (3.18b). A similar observation was made by Sitter [58], though they did not perform 3D simulations to identify the reason for this behavior. This effect appears to be restricted to jet interaction fluidic oscillators, as described by Sitter.

The internal flow is characterized by the formation of large recirculation regions created by the interaction of the two supply jets. These recirculation regions are known as dome and side vortices (Fig. 3.1). As proposed by Tomac and Gregory [121], three regions inside the actuator internal cavity are defined, as illustrated in Fig. 3.19a. Region I encompasses the dome vortices, while regions II and III encompass the bottom and top side vortices respectively. The unnamed volume between regions II and III was ignored in this analysis, as it does not contribute any significant vorticity. Consider the vorticity out of the mid-plane (ω_y in this chapter). The instantaneous average vorticity within each region is computed by integrating over each region separately. The instantaneous values of the spatially-averaged vorticity values are then phase-averaged to highlight the important behavior. The phase-averaging approach is similar to the zero-crossing method described by Ostermann et al. [122], where the frequency is first determined through an FFT (Fast-Fourier Transform) of the transverse velocity at a point in the jet region. The instantaneous values are then placed into 8°-wide bins to be averaged. This window size was found to smooth out the cycle-to-cycle variations while retaining the dominant sinusoidal shape. Figure 3.19b illustrates the vorticity balance resulting from the 3D HRLES simulations on the medium grid, and Fig. 3.20 illustrates the phase-averaging process. It is clear that there are significant cycle-to-cycle variations, as high as 30% of the phase-averaged values. Figure 3.21 illustrates the convergence of the phase-average as the number of cycles utilized increases. The maximum relative change in the phase-averaged decreases from 18% between 1 and 2 cycles to 2.5% between 9 and 10 cycles (Fig. 3.21b).

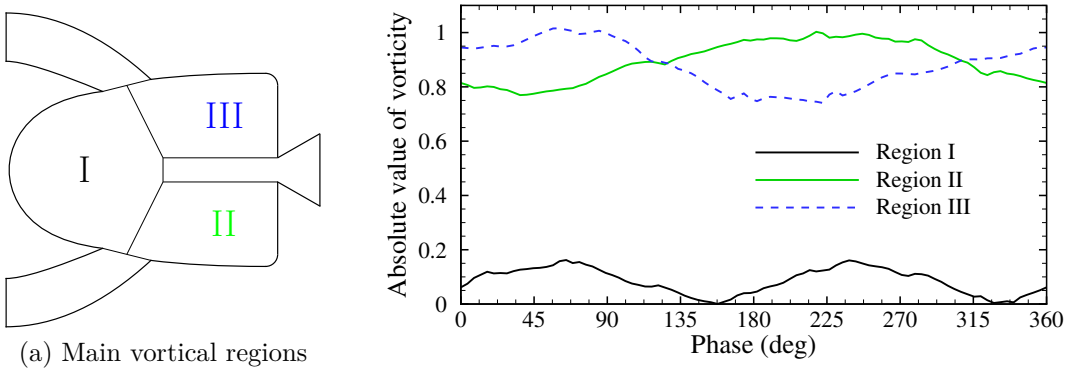

(a) Main vortical regions

(b) Absolute value of the phase-averaged vorticity

Figure 3.19: Vortical balance based on 3D HRLES simulations (medium grid): dome vortices (I), bottom side vortex (II), top side vortex (III)

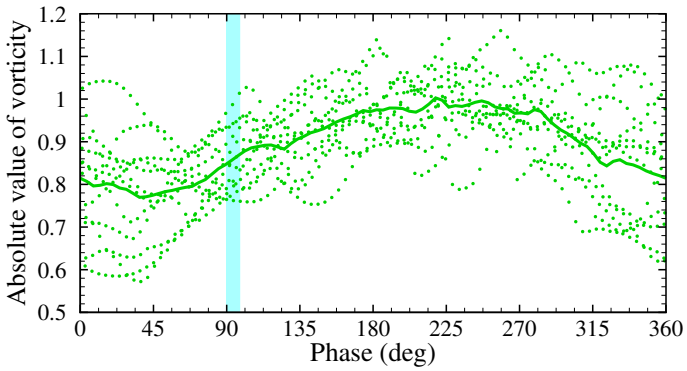

Figure 3.20: Illustration of the phase-averaging technique for region II: instantaneous values (symbols), phase-average (solid line), averaging window $90° < \phi < 98°$ (cyan box)

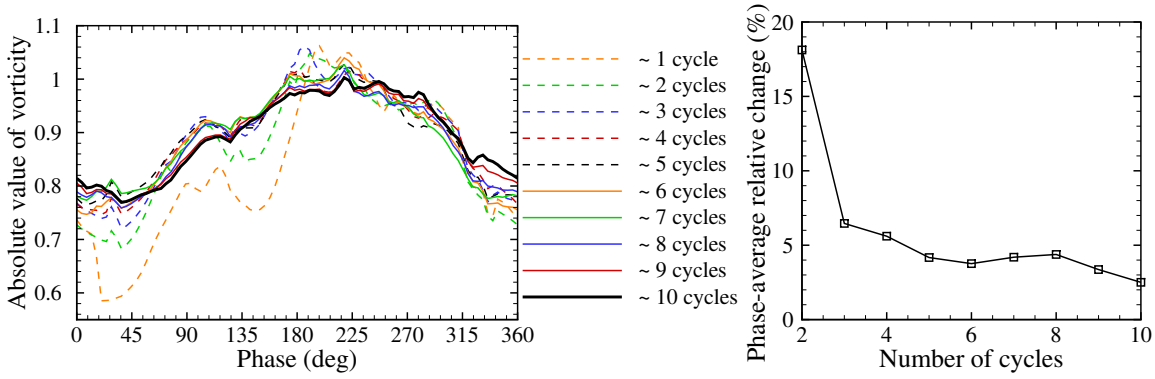

(a) Phase-averaged vorticity

(b) Maximum relative change

Figure 3.21: Convergence of the phase-averaged vorticity in region II for increasing numbers of cycles

Absolute values of vorticity are plotted in Fig. 3.19b, so that it can be readily seen that the average vorticity of the top and bottom side vortices oscillate between the same values. This reaffirms the top to bottom symmetry previously discussed. The average vorticity in region II is always negative and the average vorticity in region II is always positive. Interestingly, the absolute value of average vorticity in regions II and III become equal at phase angles of $\sim 120^{\circ}$ and $\sim 300^{\circ}$, while the zeros of the absolute value of average vorticity in region I are shifted by $\sim 40^{\circ}$ (Fig. 3.19). The summation of the average vorticity in the three regions of interest is not a constant, but rather, oscillates about zero. The oscillation of the vorticity levels in regions I, II and III is accompanied with oscillations in pressure (not shown here). As the side vorticity increases and the supply jet is bifurcated into the dome, the viscous losses induce a decrease in pressure that eventually starts to pull the jet back towards the side vortex. When the top supply jet is bifurcated into the dome, the bottom supply jet connects to the throat and conversely. This self-sustained oscillation in vorticity and pressure dictates the oscillation of the jet ensuing from the actuator.

3.6 Discussion on sensitivities

The simulation results obtained are not in perfect agreement with the experiments. The peak velocity observed at five throat widths downstream of the actuator exit is overestimated by 10%, and, even accounting for this, the non-dimensionalized peaks at other locations remain overestimated by 10% close to the jet orifice and up to 30% further away. Similar results were observed by Lakebrink et al. [63], though they provided fewer details of their computational setup, and attributed the differences to the fact that their device nominal dimensions were different from the device tested in the experiments. In the present work, the device evaluated numerically has the same nominal dimensions as the device with which it is correlated.

The usual numerical errors are discretization errors, iterative convergence error, and physical approximation errors. Discretization errors were minimized by employing different grids and time steps, and part of the modeling errors were addressed by utilizing different turbulence closures. A few other parameters that can impact the results are discussed in the remainder of this section.

Experimental sensitivities

The experimental velocity profiles are expected to be sensitive to manufacturing, as reported by Jhaveri et al. [123]. Figure 3.22 indicates that the velocity distributions at the exit plane varies with different manufacturing processes for the same CAD (Computer Aided Design) model. In this figure, the velocity distributions were non-dimensionalized by the average velocity. Though the actual values in the vertical axis were not provided, it is clear that the non-dimensional peak velocity varies by as much as 40%.

One of the factors identified by Jhaveri et al. is the relative capabilities of the manufacturing processes to produce sharp edges. The present computations are compared to hot wire measurements for a bench top model manufactured by stereolithography with a tolerance of 0.1 mm approximately, which corresponds to 10% of the throat width. This provides an idea of the experimental uncertainties. A computational assessment of these manufacturing sensitivities is not as simple as modifying the dimensions at the throat or the exit, as the spatial variations in the physical device are unknown.

Effect of inlet conditions

The baseline computations were performed with a pressure ratio of 2.45 and an inlet temperature ratio of 1. The resulting flow rate was employed to compare the oscillation frequency with the experiments, as the pressure and temperatures were not

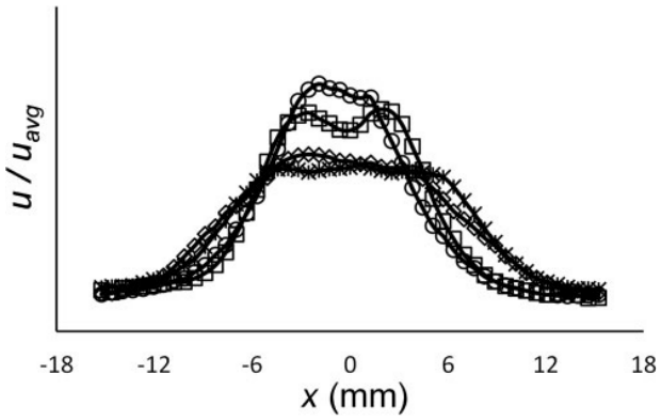

Figure 3.22: Spanwise variation of normalized jet speed along the exit plane for various manufacturing processes: selective laser sintering ($\star$), stereolithography ($\diamond$), machined aluminum ($\circ$), machined aluminum matching geometry of injection molding ($\square$). From Jhaveri et al. [123]

measured in this specific sets of experiments. Figure 3.23 illustrates the variation of the oscillation frequency with the inlet conditions obtained through 2D URANS computations. The frequency increases non-linearly with pressure ratio for a fixed temperature ratio, while it increases almost linearly with the temperature ratio at a high pressure ratio. The variation with pressure ratio is a well known behavior of fluidic oscillators [124, 125]. Of course, an incompressible flow experiences negligible variations in temperature and density by definition. What is rarely discussed is the importance of measuring the inlet temperature when the flow is compressible. For a given pressure ratio, increasing the temperature ratio increases the energy provided to the actuator and increases the volume flow rate and frequency. A measurement of the flow rate alone is therefore incomplete, as several combinations of pressure ratio and temperature ratio can result in the same flow rate. Measuring both the temperature and pressure simultaneously at the inlet of the actuator is the best way to fully determine the thermodynamic state.

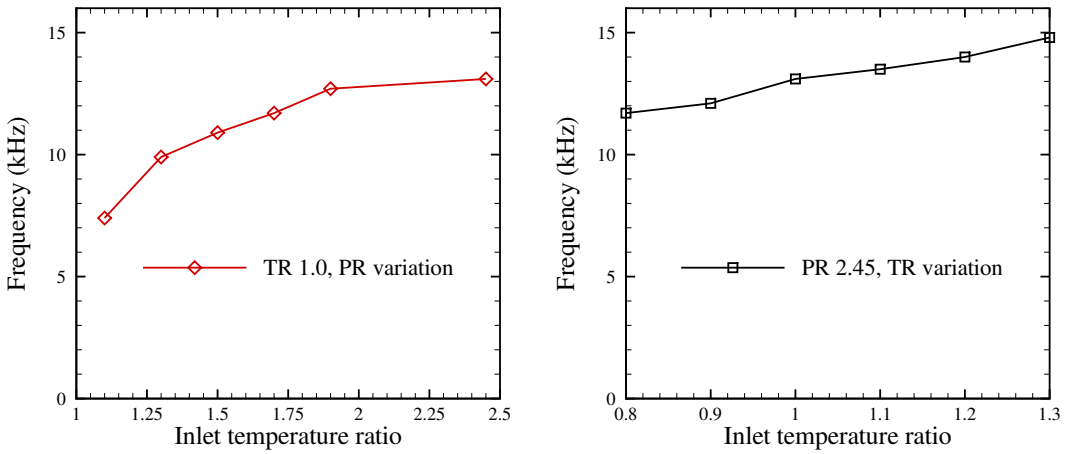

(a) Frequency versus inlet pressure ratio (b) Frequency versus inlet temperature ratio

Figure 3.23: Variation of fluidic oscillator frequency with pressure ratio and temperature ratio

3.7 Boundary condition models of the fluidic oscillator

Several boundary condition models were derived and implemented to predict the behavior of the fluidic oscillator engineering simulations. Ideally, the desired location to apply such a model is the outer mold line of the geometry of interest, obviating the need to resolve any part of the actuator or installation recesses. This has yet to be accomplished in the literature. For the fluidic oscillators considered in the present work, the inner and outer mold lines are defined as the throat and exit, respectively (Fig. 3.24), and these terms are used interchangeably in the remainder of this chapter.

The modeling approach consists of specifying flow variables at the throat or exit of the actuator based on the simulation of the fluidic oscillator in quiescent conditions. The full device simulation employed to inform the models is later referred to as a precursor simulation. The term is borrowed from the literature on inlet conditions of LES [126]. The flow variables are recorded at the throat and exit of the device at every iteration of the precursor simulation. The quantities of interest are the density ρ, momenta (ρu, ρv, ρw), stagnation energy E, modeled TKE, and specific dissipation

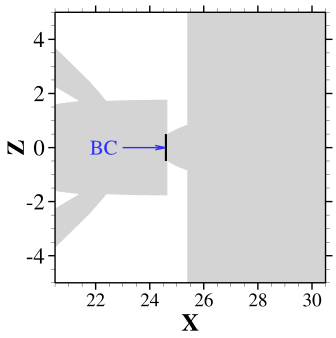

(a) Inner mold line (throat) boundary condition

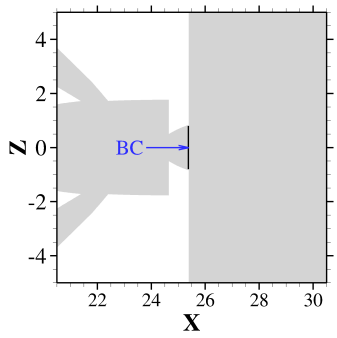

(b) Outer mold line (exit) boundary condition

Figure 3.24: Definition of the inner and outer mold lines

rate (ω). Identical grids and time steps were employed for the precursor simulation and the simulations evaluating the boundary conditions models.

Four variants to the boundary condition models were assessed, summarized in Table 3.4.

- In the first model, BC1 (Exact), the data recorded during the precursor simulation were directly applied to a second simulation (Dirichlet boundary condition) with linear interpolation during sub-iterations. With this formulation, the solution is restarted from the same initial condition as the precursor simulation and averaged over the same time period.
- In the second boundary condition variant, BC2 (Phase-averaged), the data recorded were first phase-averaged. Here, an averaging window of 4° is em-

Table 3.4: Summary of boundary condition models

Model name	Variables specified
BC1 (Exact)	ρ, ρu, ρv, ρw, ρE, ρk, $\rho\omega$
BC2 (Phase-averaged)	ρ, ρu, ρv, ρw, ρE, ρk, $\rho\omega$
BC3 (Exact, without modeled turbulence)	ρ, ρu, ρv, ρw, ρE
BC4 (Functional fit)	ρ, ρu, ρv, ρw, ρE, ρk, $\rho\omega$

ployed in order to generate 100 sets of data for phases between 0 and 2π rad. The definition of the phase in this analysis is independent from that employed to describe the internal flow physics. The sweeping frequency is given as an input for simulations relying on this formulation. The simulations were restarted from an arbitrary initial condition, and the boundary condition model was applied until converged to a periodic steady state. The boundary condition model BC2 has the advantage that is more general: its application does not require matching the precursor simulation time-step and initial condition. Hence, it allows the introduction of random phases in arrays of fluidic oscillators. Furthermore, BC2 requires less memory to store the quantities at a number of phases, compared to a number of iterations.

- The boundary condition model BC3 (Exact, without modeled turbulence) consists in omitting the turbulent variables from BC1. In that case, the turbulent variables are extrapolated to the boundary from the interior of the simulation domain (Neumann boundary condition). Only considering mass flow and momentum in the boundary conditions is a typical practice in flow control applications such as synthetic jets [127].

- Finally, functions are fitted to the time-averaged and phase-averaged flow variables from the precursor simulation to construct BC4. This approach was inspired by the work of Schatzman et al. [61] for a SaOB (Suction and Oscillatory Blowing) actuator, though they did not provide details of the performance of the boundary conditions that they derived. Defining BC4 consists in finding the functional fits $f_n(y,z) = f1_n(y) f2_n(z)$ and $g_n(z)$ satisfying:

$$\overline{\psi}_n(y,z) = f_n(y,z)\,, \tag{3.2}$$

and

$$\psi_n(y,z,\phi) = \overline{\psi}_n(y,z) + g_n(z)\sin\left(\phi + \phi_{0_n}\right)\,, \tag{3.3}$$

Table 3.5: Grids employed to evaluate the boundary condition models

Grid level	BC location	2D/3D	Turbulence model	N_{cells}
Coarse	Throat	2D	$k-\omega$ SST	$22,442$
Coarse	Exit	2D	$k-\omega$ SST	$17,612$
Medium	Throat	3D	HRLES	$23,079,474$
Medium	Exit	3D	HRLES	$21,152,934$

where $\overline{\psi}_n$ are the time-averaged flow variables, and $\psi_n(y,z,\phi)$ are the phase-averaged quantities. The phase offset ϕ_{0_n} is introduced to accommodate arbitrary definitions of the phase from the instantaneous simulation results. The functional form of $\psi_n(y,z,\phi)$ implies $\frac{1}{2\pi}\int_0^{2\pi}\psi_n(y,z,\phi)d\phi = \overline{\psi}_n(y,z),\ \forall\ g_n(z)$. The fit for the phase-averaged quantities is found independently from this equation for the mean quantities using the exact mean solution and phase-average values. The functions $f_n(y,z)$, $g_n(z)$, and the phase offset ϕ_{0_n} are found by least-square optimization. The identified functions used here are presented in Appendix C for application at the throat. The simple form of these equations make them very attractive to model a feedback-free fluidic oscillator. Because they are based on the phase, the sweeping frequency can easily be modified. A frequency change should be associated with a flow rate change, which is not included in the present model. Recent efforts are evaluating the effect of pressure ratio and flow rate on the boundary condition formulation [128].

Table 3.5 summarizes the grid and turbulence closures employed to assess the performance of these boundary condition models in quiescent conditions. These evaluations were first performed in 2D before being extended to 3D.

3.7.1 Two-dimensional evaluations

The boundary conditions were first evaluated in two dimensions to maintain reduced computational cost. The 2D simulations also have the advantage that they do not contain high frequency content, making comparisons of time histories possible.

Because the flow is choked, a boundary condition at the throat is guaranteed to be stable. Figure 3.25 is a comparison of the exact phase-averaged and functional fit boundary conditions, all prescribed at the actuator throat to the full actuator simulation. The exact formulation resulted in time histories and time-averaged Mach numbers identical to the full actuator simulation. The phase-averaged and functional fit formulations also recovered the average peak values, but missed the cycle-to-cycle variations which are approximately 20% of the phase-averaged values. This is not surprising since the cycle-to-cycle variations are removed by taking the phase-average. Cycle-to-cycle variations are generally due to turbulent structures, indicating the importance of turbulence. The Mach number contour lines in Fig. 3.25 indicates that the models are more accurate near the jet orifice. The contour lines start diverging spatially with increasing distance from the actuator exit. Interestingly, the functional fit model enforces a symmetry in the time-averaged Mach number contours that is not present even in the fully resolved simulation (see section 3.5). If a phase-averaged or an even less restrictive time-average of the quantities of interest is sought (in a flow control application), the phase-averaged formulation remains a potential candidate for modeling the sweeping jets. Further discussion is delayed until the three-dimensional results are presented.

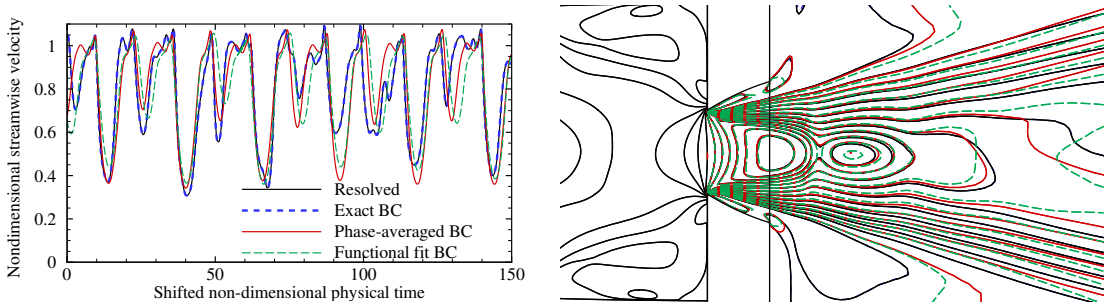

(a) Time histories at a point in the jet region (b) Time-averaged local Mach number contours

Figure 3.25: 2D evaluation of the boundary condition models applied at the device throat

The exact boundary conditions with and without the modeled turbulence (BC1 and BC3) were then applied at the device exit. The device exit constitutes a more desirable location, as it completely removes the need to mesh any part of the fluidic oscillator. Similar to its application at the throat, the exact formulation recovers the full actuator solution when applied at the outer mold line (Fig. 3.26). Cycle-to-cycle variations are present in both models, but the amplitudes are underestimated by an average 20% compared to the full cavity simulation when the modeled turbulence is not included. This indicates again the importance of the turbulent boundary conditions. Interestingly, neglecting the modeled turbulence at the device throat (not shown here) does not result in significant differences in the time-averaged behavior. Recall that Fig. 3.13 illustrates the time-averaged TKE. The important TKE production occurs in the shear layers downstream of the actuator geometric throat. Therefore, though the TKE is non-zero at the throat, its omission along with that of the specific dissipation rate has little influence on the solution. This is clearly not the case for boundary condition models at the device exit. In the results presented here, the performance of BC3 (Neumann boundary condition of the modeled turbulence) is aided by the initial condition, which is obtained after the periodic steady state is reached in the precursor simulation. Therefore, when the turbulent variables are

extrapolated to the boundary, the error introduced is lower than it would be if the solution were initialized from any other arbitrary condition.

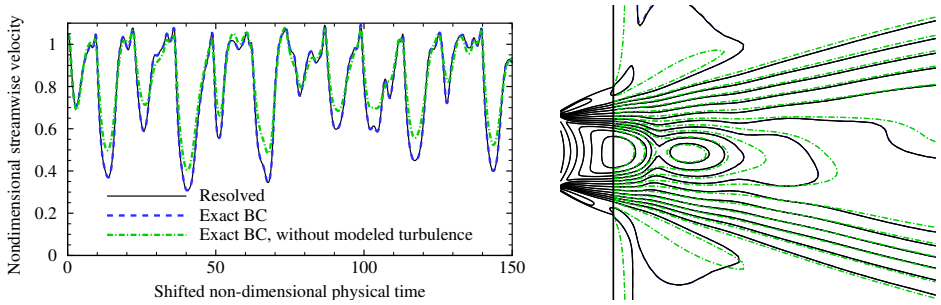

(a) Time histories at a point in the jet region

(b) Time-averaged local Mach number contours

Figure 3.26: 2D evaluation of the boundary condition models applied at the device exit

These two-dimensional evaluations show that the application of a boundary condition at the device throat or exit are sufficient to recover the oscillation frequency in quiescent flow. The exact formulation recovers the full actuator simulation identically in space and time, while phase-averaging neglects cycle-to-cycle variations, and omitting turbulent variables induces differences in peak values. The functional fit to the phase-average is also promising, given that it provides a complete abstraction from the precursor simulation.

3.7.2 Three-dimensional evaluations

As discussed previously, 2D predictions lack the dual peak in velocity distributions (Fig. 3.10), making any quantitative comparisons irrelevant. The performance of the boundary conditions developed is now discussed for a 3D grid. The medium 3D grid was employed with the HRLES turbulence closure. The conclusions drawn from the 2D evaluations remain valid for conditions for the exact formulation (with and without modeled the turbulent variables), based on simulations performed with

approximately 6 cycles of oscillations. These are not included here, as the number of cycles was too small to obtain a smooth time-average and compare with experiments.

More attention is dedicated to the phase-averaged and functional fit formulations here, as they do not suffer from the limitations of the other two models regarding the time steps that can be utilized and the memory requirements that are necessary. Indeed, when boundary conditions are directly applied in the time domain (BC1 and BC3), the initial condition must match the first step recorded in the model formulation, and all iterations of the precursor simulation must be stored. Phase-averaging reduces the amount of data stored and can be employed with any initial condition. Figures 3.27 and 3.29 illustrate the Mach number contours obtained at the throat and exit respectively to inform the boundary condition models. Figure 3.28 is the resulting formulation with the functional fit at the inner mold line.

Figure 3.30 illustrates the time-averaged Mach number contours and velocity profiles, as obtained by evaluating the phase-averaged and functional fit models. The full cavity result is repeated here for comparison. The phase-averaged model performs better when applied at the throat compared to the device exit. In this latter case, though the dual peak is present in the velocity profile, the peak value discrepancies observed earlier are exacerbated. This behavior is attributed to the removal of important high frequency content by phase-averaging, as the exact boundary condition performed satisfactorily at the actuator exit. Since the turbulence develops inside the nozzle (between the inner and outer mold lines), the boundary condition is not as affected by the removal of the high-frequency content at the throat. The relative error between the phase-averaged formulation and the full-cavity is on the order of 10%. Whether or not that is acceptable in a flow control application is evaluated in Chapter 4.

Given the inadequacy of the phase-averaged formulation at the actuator exit in 3D, and the expectation that the functional fit can only perform like phase-averaging

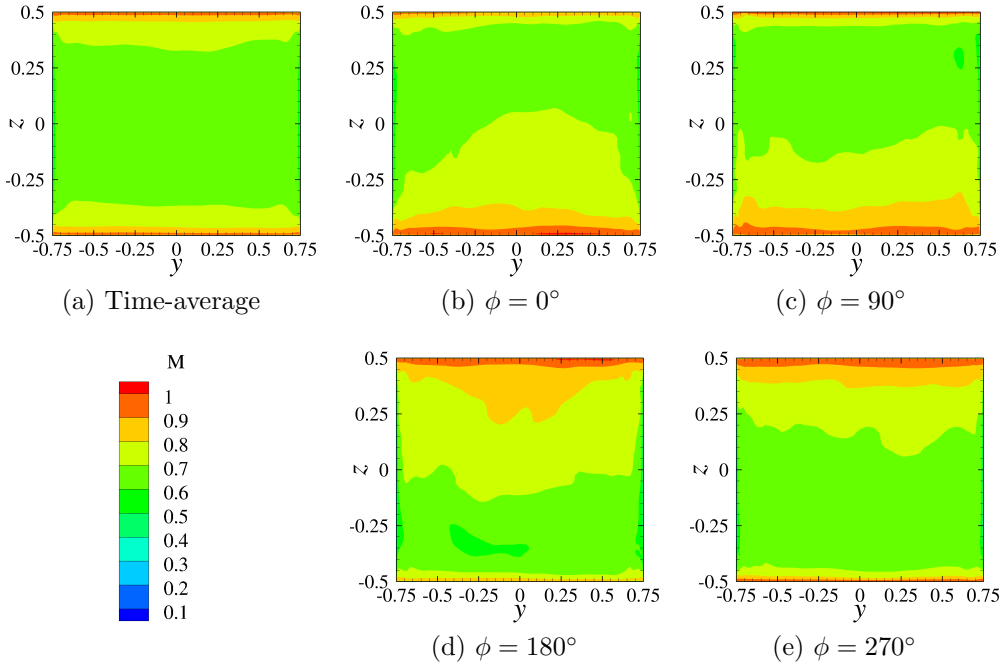

(a) Time-average (b) $\phi = 0°$ (c) $\phi = 90°$

(d) $\phi = 180°$ (e) $\phi = 270°$

Figure 3.27: Phase-averaged Mach numbers at the throat for the boundary condition evaluations in 3D. Axes are not to scale.

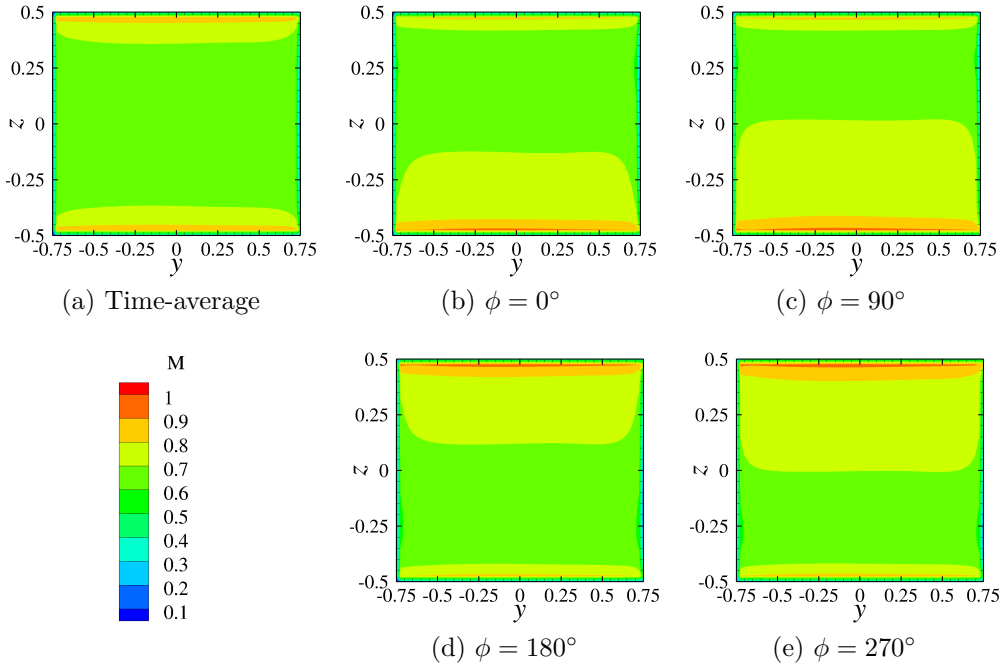

(a) Time-average (b) $\phi = 0°$ (c) $\phi = 90°$

(d) $\phi = 180°$ (e) $\phi = 270°$

Figure 3.28: Phase-averaged Mach numbers at the throat obtained by functional fit. Axes are not to scale.

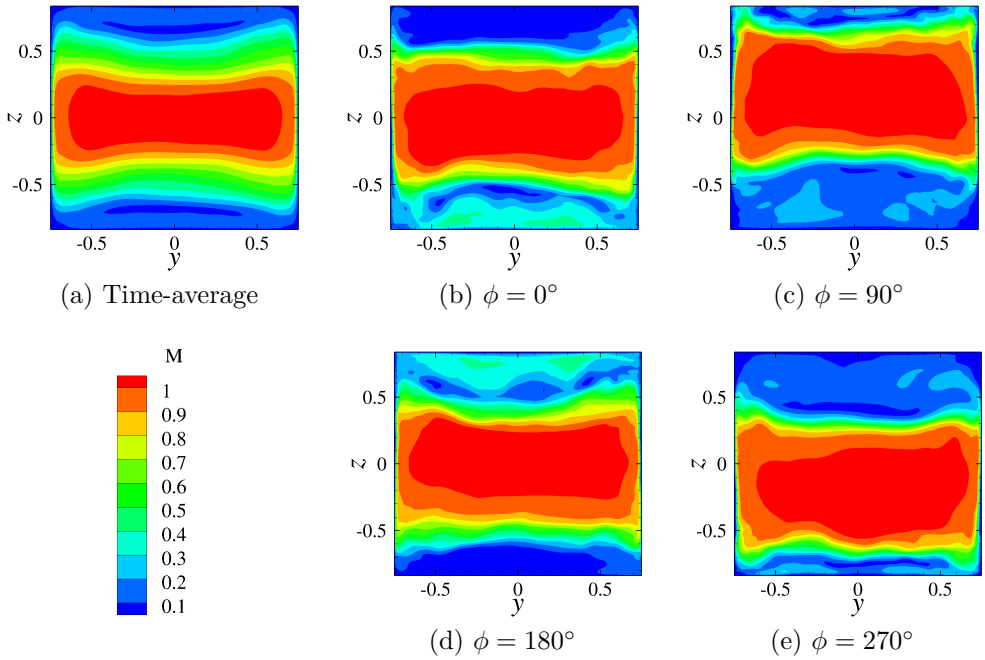

(a) Time-average (b) $\phi = 0°$ (c) $\phi = 90°$

(d) $\phi = 180°$ (e) $\phi = 270°$

Figure 3.29: Phase-averaged Mach numbers at the exit for the boundary condition evaluations in 3D. Axes are not to scale.

at best, the functional fit was only evaluated at the throat. The accuracy is clearly superior to that of the phase-average applied at the actuator exit. The agreement obtained with the experimental data for the two first velocity profiles ($x = 5$ and $x = 7.5$) is comparable to fully resolving the actuator cavity. However, the specification of the functional fit at the throat results in a higher jet spreading than the precursor simulations. This model formulation shows a lot of promise nonetheless and is a candidate for further extensions.

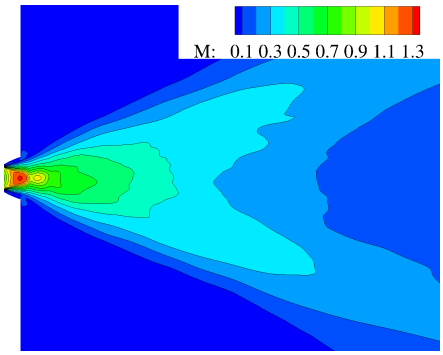

(a) Mach number contours, Full cavity

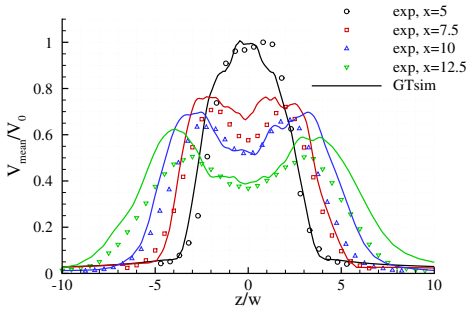

(b) Jet velocity distributions, Full cavity

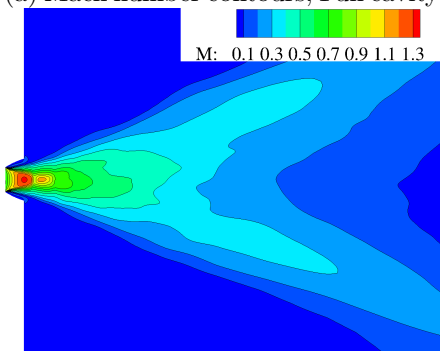

(c) Mach number contours, Phase-averged BC, throat

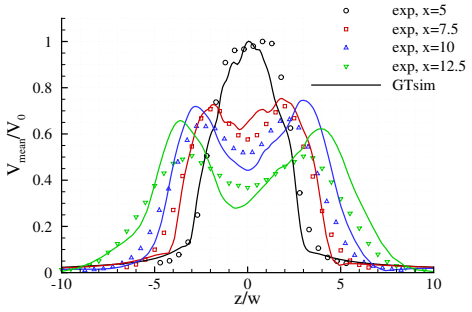

(d) Jet velocity distributions, Phase-averged BC, throat

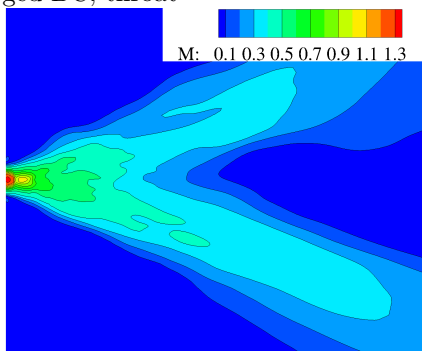

(e) Mach number contours, Phase-averged BC, exit

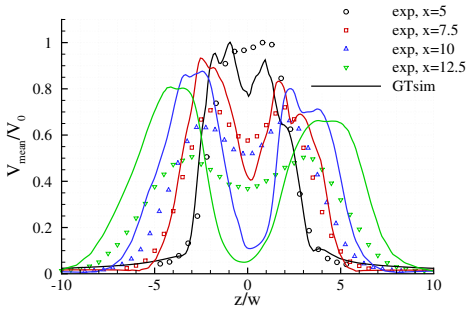

(f) Jet velocity distributions, Phase-averged BC, exit

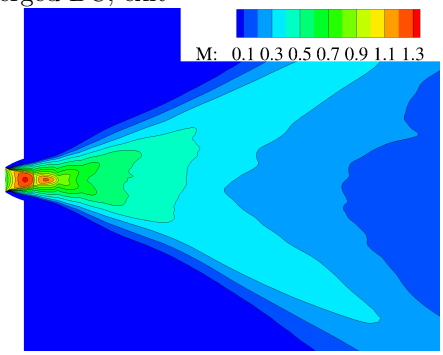

(g) Mach number contours, Functional fit BC, throat

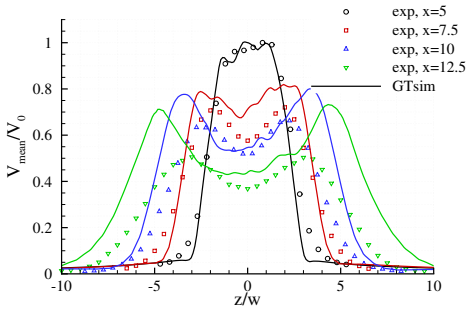

(h) Jet velocity distributions, Functional fit BC, throat

Figure 3.30: Time-averaged Mach number contours (left) and jet velocity distributions (right) from 3D HRLES boundary condition model evaluations

3.7.3 Turbulent fluctuations and phase-averaging

To further characterize the turbulence at the outer mold line of the fluidic oscillator, the resolved turbulence was quantified. To do so, the velocity was decomposed as:

$$u_i = \overline{u_i} + u_i' + u_i'' = \widetilde{u_i} + u_i'' \,, \tag{3.4}$$

where $\overline{u_i}$ and $\widetilde{u_i}$ represent the time-averaged and phase-averaged quantities, respectively, u_i' is the fluctuating part included in the phase-average and u_i'' is the fluctuating part that is lost by phase-averaging. The phase-averaged fluctuating TKE is therefore $\frac{1}{2}\widetilde{u_i'' u_i''}$. The total TKE is approximated as the sum of this fluctuating TKE and the modeled TKE.

Figure 3.31 indicates that most of the turbulence at the outer mold line is resolved rather than modeled with HRLES on the medium grid. With the exception of a few locations near the spanwise walls where up to 90% of the turbulence is modeled, the ratio of the modeled TKE to the total TKE rarely exceeds 20%. This confirms how important these turbulent fluctuations are, and it is not surprising that their omission leads to significant losses in accuracy.

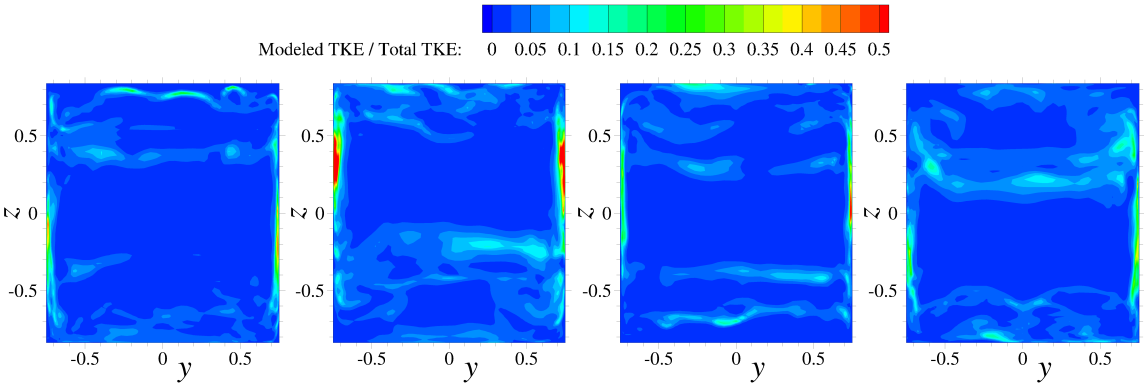

(a) $\phi \simeq 0°$ (b) $\phi \simeq 90°$ (c) $\phi \simeq 180°$ (d) $\phi \simeq 270°$

Figure 3.31: Exit phase-averaged ratio of modeled TKE to total TKE contours, medium grid, 3D HRLES

Initial attempts to employ a synthetic turbulence generator [129–131] to re-introduce the turbulent fluctuations resulted in unstable simulations, indicating the need to

modify the formulation of the synthetic turbulence generators to include the oscillatory nature of the sweeping jets. One aspect to address is to allow the generated eddies to convect at the local speed rather than at the bulk velocity speed of the plane where they are generated. Ideally, this should be accomplished with minimum computational overhead, so as to not defeat the purpose of employing a boundary condition model.

The evaluation of URANS for the boundary condition models has not been discussed for 3D simulation. URANS was also found to suffer from inaccurate solutions when a phase-averaged boundary condition is applied at the outer mold line, though a higher ratio of TKE is modeled. Synthetic turbulence generation is not an option in URANS, as any added fluctuation will be damped out by the high eddy viscosity. Simply adding the TKE removed by phase-averaging to the modeled TKE was insufficient and adding fluctuations in HRLES remains the most promising direction of future research.

3.7.4 Computational cost

The computational cost of the boundary condition models was evaluated on the two-dimensional grids with the boundary condition applied at the throat. Table 3.6 summarizes the CPU time and memory used relative to the cost of resolving the entire fluidic oscillator, based on 1000 iterations of simulation. The ratio of the grid sizes between the two-dimensional coarse grids is 0.24. The memory requirements have a similar ratio for the case tested, though the memory requirement of the exact formulations (BC1 and BC3) is expected to increase with the number of iteration considered. The CPU time also scales linearly with the grid size.

The ratio of grid sizes in 3D is approximated 0.5 in the present work. Half the grid size (CPU time and memory) can thus be saved by not resolving the actuator cavity, up to its throat. Further savings can be obtained by increasing the time step, as the

Table 3.6: Computational cost of the boundary condition models applied at the throat in 2D

Approach	CPU time	Memory required
Fully resolved cavity	1.0	1.0
BC1 (Exact)	0.29	0.23
BC2 (Phase-averaged)	0.29	0.21
BC3 (Exact, without modeled turbulence)	0.23	0.23
BC4 (Functional fit)	0.26	0.21

time step chosen is driven by the internal mechanisms that generate the sweeping jets.

The simulations on the medium three-dimensional grids performed herein require on the order of $40,000$ CPU hours each. Therefore, initial characterization of the frequency in 2D is a valuable tool. Coarse three-dimensional grids can be used to rapidly initialize the flow, before more detailed analyses are conducted on refined grids.

3.8 Technical findings

A feedback-free fluidic oscillator was characterized numerically and the results were compared to experimental data. The solution was later used as a basis to derive several boundary condition models to avoid resolving the flow inside the actuator.

Inclusion of the time-accurate solution throughout the simulations is paramount to obtaining jets that oscillate for these actuators, and the experimental oscillation frequency was predicted computationally within 5%. Three-dimensional simulations are required to capture the correct flow physics, such as the symmetry of the internal flow dynamics and the dual peak in the sweeping jet velocity profiles. The recovery of internal symmetry in the time-average with 3D simulations answers a question that was raised by another researcher in the literature.

The time-averaged velocity profiles are predicted within 10% of experiments near the jet exit with 3D HRLES, but the correlation deteriorates further downstream. Sources of uncertainty were discussed. The internal flow dynamics could only be assessed computationally for the scale of the devices used for companion experiments. The observed dynamics (jet interaction and bifurcation,) are consistent with reports by other researcher for different feedback-free fluidic oscillators [119–121].

Boundary condition models applied at the actuator throat are an effective means to reduce the computational cost. Exact models based on specifying recorded temporal flow quantities recover the spatio-temporal behavior of the precursor simulation. These so called exact models are limited in their application, as they require more memory and pose challenges regarding the initial conditions and time steps that can later be employed. Phase-averaging provides an additional level of abstraction (arbitrary phase, initial conditions and time steps), and remains accurate (10% error) at the inner mold line.

An accurate outer mold line model, exact formulation aside, has yet to be identified. The failure of phase-averaging at the outer mold line was directly linked to the removal of important turbulence content. These findings advance the state of the art through a step-by-step approach identifying the important features that must be included in models of fluidic oscillators. Furthermore, earlier modeling studies have focused on double feedback fluidic oscillators [68, 70]. A flow control application of the models derived here is evaluated next.

CHAPTER 4
CONTROL OF FLOW SEPARATION OVER A WALL-MOUNTED MODEL USING FLUIDIC OSCILLATORS

A flow control application with fluidic oscillators is now presented. A test model was designed through computations and tested in a wind tunnel. The objective is to study in detail the physics of the interaction between the jets and an otherwise separating shear layer. The emphasis is placed on correlation of the present computations with experimental data for the base (unactuated) and actuated flows, including second-order statistics, and on the ability to leverage the fluidic oscillator boundary condition models to further explore the flow control design space.

4.1 Wind tunnel insert design

A surface model for wind tunnel experiments was designed using CFD, with the goal to provide a model that results in a flow separation comparable to what would be experienced by a rotor blade at high angle of attack or a helicopter fuselage. The nominally spanwise uniform model serves as a basis for the evaluation of flow control with sweeping jets. The design Mach number was 0.245, and the model chord was set to 2.45 inches based on the dimensions of the wind tunnel test section and the PIV viewing window.

Three hill shapes were designed considering the VR-12 airfoil at an angle of attack. Two-dimensional SST-URANS computations were performed to provide an initial assessment of the separation zone. The solution was first obtained for the VR-12 airfoil in free air over a range of angles of attack. The streamlines were then collected to define the shape of the hill upstream of the airfoil, as illustrated in Fig. 4.1. Several points were removed from the streamlines approaching the airfoil for a smooth tran-

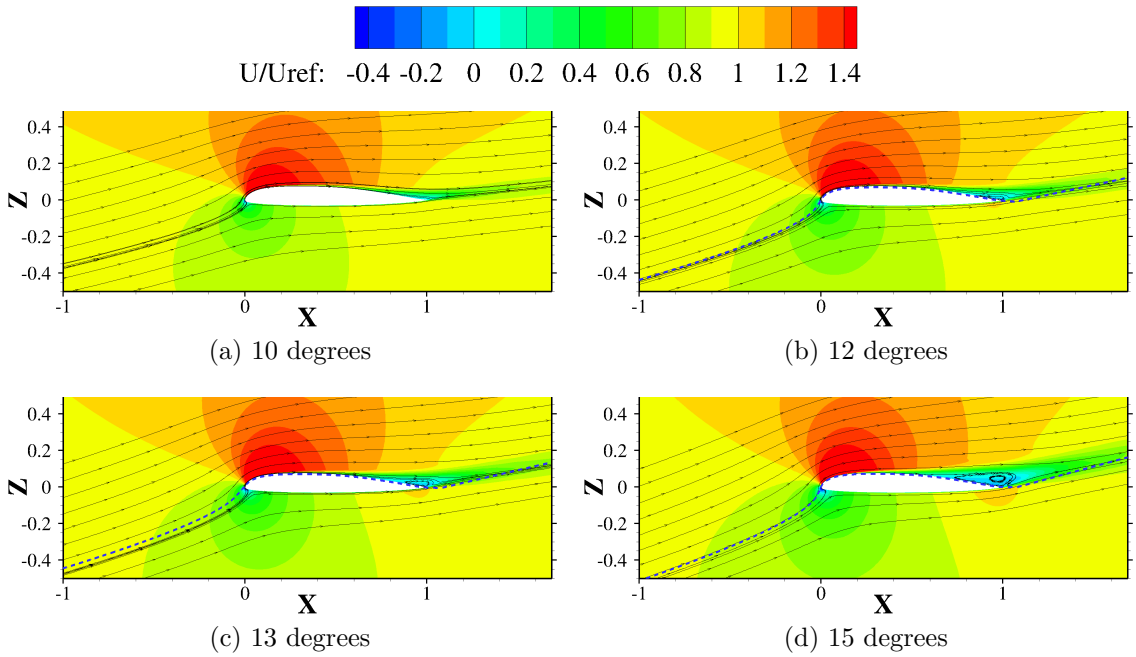

(a) 10 degrees (b) 12 degrees

(c) 13 degrees (d) 15 degrees

Figure 4.1: VR-12 airfoil in free air, based on 2D simulations with $k-\omega$ SST

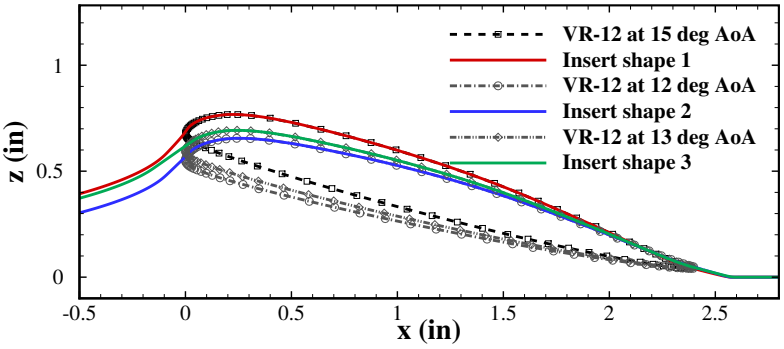

Figure 4.2: Hill designs considered

sition between the streamline and the airfoil geometries, and a multiquadric Radial Basis Function (RBF) [97] interpolation was applied. The resulting geometries are presented in Fig. 4.2 for three hill shapes based on 12°, 13° and 15° angles of attack.

A 2D grid with 1171 points in the streamwise direction and 300 points in the wall normal direction was generated for each of the proposed shapes. The domain extends upstream and downstream of the hump by seven chord lengths. The lower wall is considered viscous, except for the first 2.45 chord lengths after the inlet, where

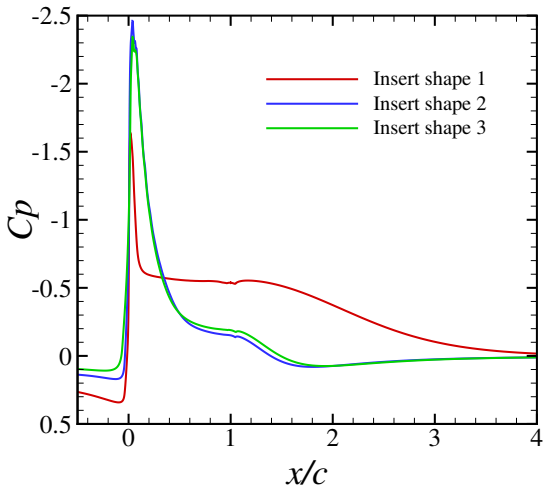

Figure 4.3: Pressure coefficient distribution over the proposed hill shapes.

a slip wall boundary condition was applied to avoid a conflict between the inflow and wall boundary conditions. The upper boundary was modeled as a slip wall. The left boundary was a subsonic inflow, while a back pressure ratio of one was specified at the right boundary. Figure 4.3 compares of the pressure distributions over the three insert shapes. The 2D SST-URANS simulations predict flow separation at 7%, 46%, and 40% chord for insert shapes 1, 2 and 3, respectively. Shape 3 was eventually selected to be manufactured and evaluated in the wind tunnel.

A grid refinement study was carried out on the selected model a posteriori to the comparison of the three shapes with 2D SST-URANS. Table 4.1 summarizes the grids considered, all with $y^+ < 1$. Figure 4.4 compares the pressure distributions obtained with the different grids. The error analysis on the mean drag coefficient and the separation location indicate convergence as the grid is refined. The grids employed in the remainder of this chapter to evaluate the flow past the wall-mounted geometry have a resolution comparable to the fine grid in and downstream of the separation region, and a resolution comparable to the medium grid upstream.

Table 4.1: 2D Grid independence study for the characterization of the base flow over the wind tunnel insert

Grid level	$N_\xi \times N_\eta \times N_\zeta$	N_{cells}	Mean C_D	x_{sep}/c	x_{sep} relative error (%)
Coarse	$342 \times 2 \times 75$	$25,234$	0.155	0.105	72.7
Medium	$644 \times 2 \times 150$	$95,807$	0.080	0.355	7.8
Fine	$1171 \times 2 \times 300$	$349,830$	0.077	0.394	2.3
Very Fine	$1626 \times 2 \times 450$	$729,625$	0.077	0.385	-

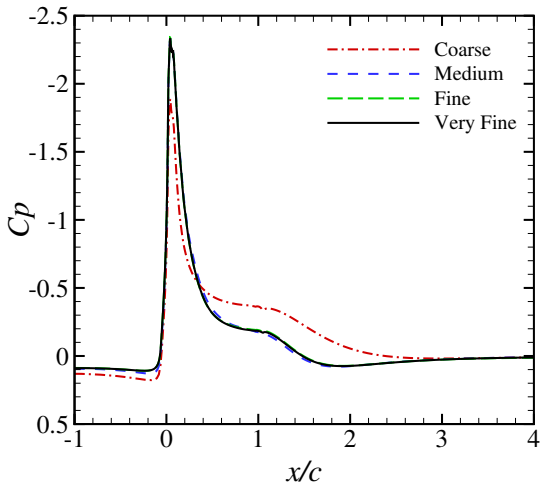

Figure 4.4: Grid refinement study for the wind tunnel insert

4.2 Tested model and experimental data

A schematic of the wind tunnel test section is depicted in Fig. 4.5. The test section length, width, and height are $\tilde{L} = 660.4$ mm (26 in) and $\tilde{W} = \tilde{H} = 127$ mm (5 in), respectively. With a nominal Mach number of 0.25, and a model chord $\tilde{c} = 62.23$ (2.45 in), the Reynolds number based on the chord length is approximately $345,000$.

To fix the location of flow separation, a trip wire of diameter 0.43 mm (0.0169 in) was glued to the physical model at $x/c \simeq -0.0355$ [132] and was represented in the simulations as illustrated in Fig. 4.6. The latter figure also indicates a region of the wall-mounted model that covers the jet exit, coined the overhang, which plays

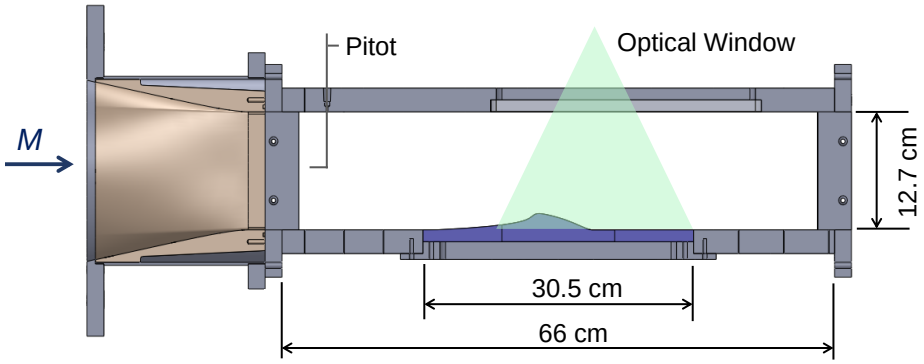

Figure 4.5: Wall-mounted model in the wind-tunnel test section

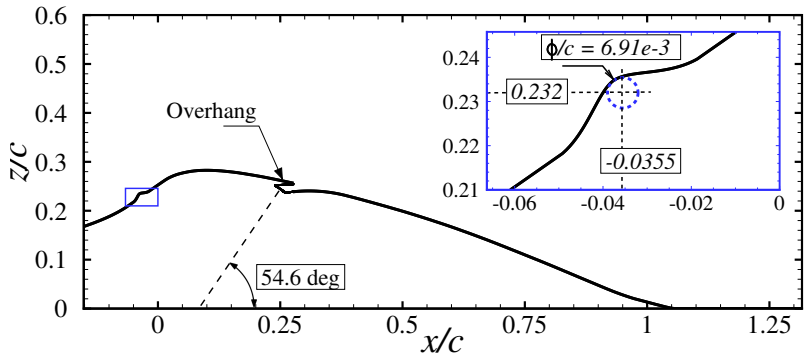

Figure 4.6: Modified surface shape to mimic the presence of a trip wire

an important role in this configuration. The locations $x/c = 0$ and $x/c = 1$ are later referred to as the leading and trailing edges, respectively, adapting the terminology from the underlying airfoil. The model integrates an array of seventeen spanwise oscillating fluidic oscillators oriented approximately 54.6° with respect to the horizontal axis due to spatial constraints. Indeed, there needs to be enough space for the plenum supplying compressed air to the jets, which could not be achieved if the fluidic oscillators were oriented at a lower angle. The effect of jet orientation were later computationally evaluated, and the results are presented in sections 4.6.9 and 4.6.10. The jets are spaced by 7 mm (0.276 in) or approximately 0.1125 $\tilde{c}$.

The inner orifice (or throat) of the fluidic oscillators implemented in the wall-mounted model is $\tilde{W} = 0.5$ mm (0.0197 in) wide. The internal height of the actuator cavity normal to the plane of oscillations is $\tilde{H} = 1$ mm (0.0394 in). The outer orifice

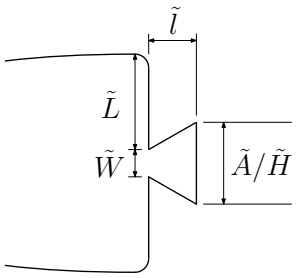

Figure 4.7: Definition of the key dimensions of the fluidic oscillator

(or exit) has a width $\tilde{A}/\tilde{H} = 1.24$ mm (0.0488 in), where $\tilde{A}$ is its area. The nozzle has length $\tilde{l} = 1$ mm and the distance from the cavity side to the throat is $\tilde{L} = 1.58$ mm (0.0622 in). Figure 4.7 is a schematic defining the these quantities.

Experiments were conducted to study the flow over the wall-mounted model within a wind tunnel, as well as to characterize the oscillation frequency of the fluidic oscillators in quiescent conditions. Initial measurements of the centerline pressure and mid-plane PIV data were reported by Peterson et al. [132]. Details of the measurement techniques were presented by Peterson et al. [132] and Koukpaizan et al. [133]. Additional measurements were recently obtained with stereo PIV at multiple planes downstream of the actuation location to characterize the spanwise behavior of the flow.

4.3 Base flow characterization over the wall-mounted model

The base flow over the wall-mounted model, including trip wire and the region immediately after the actuator exit, was evaluated computationally with the URANS approach (Menter SST [34]).

Computations of the wall-mounted model were performed on the grid depicted in Fig. 4.8. The complete three-dimensional grid contains 42.8 million cells, including 7 million cells for the actuators, 1.6 million cells for the domain between the actuators' exits and the surface of the model, and 34.2 million cells for the wind tunnel section. The size of the latter domain is driven by the relatively large number of cells (194) in

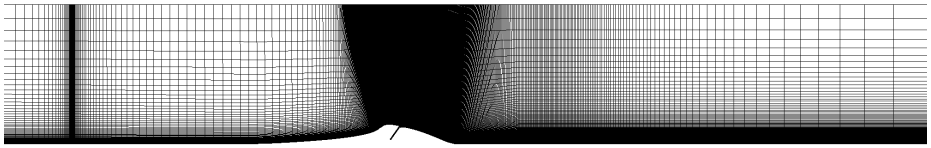

(a) Overview

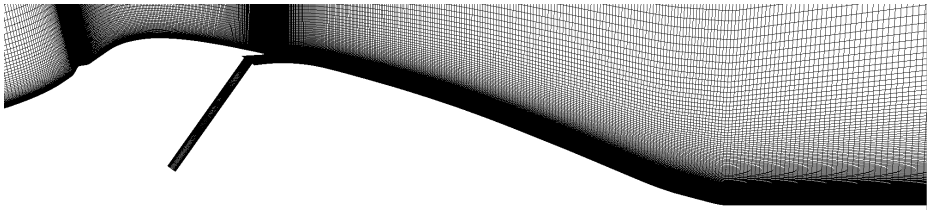

(b) Close view of the curved surface

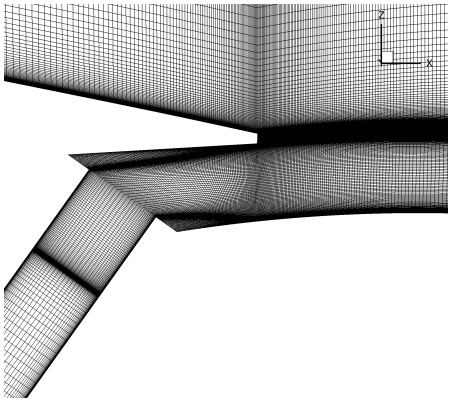

(c) Close view of the actuator exit

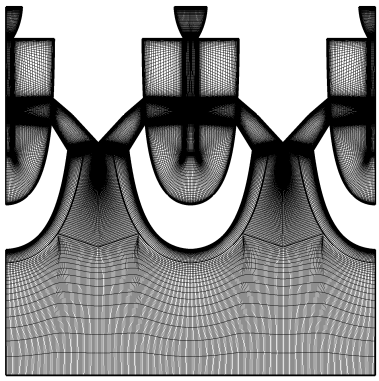

(d) Close view of the fluidic oscillators

Figure 4.8: Grid system including the curved surface and the fluidic oscillators

the spanwise direction, which was necessary to provide a one-to-one interface with the actuators. The resolution of the actuators is relatively coarse, in order to maintains the computational cost on the order of $50,000$ CPU hours. The actuator domains were disregarded during the base flow characterization and when boundary condition models were evaluated. Subsonic inflow conditions were applied at the left boundary of the wind tunnel, and a back pressure of 1.0 was specified at the right boundary. The upper boundary of the wind tunnel was modeled as a slip wall. The initial computations did not resolve the entire test section including the spanwise walls to reduce the computational cost. These viscous walls are expected to modify the

blockage in the tunnel and the resulting velocity and pressure recovery. The effects of blockage are discussed for the actuated flow in section 4.6.4.

The resulting pressure distribution is compared to experiments in Fig. 4.9, where the reference pressure is taken as the pressure far downstream of the model. Additionally, velocity profiles at multiple locations are presented in Fig. 4.10. There is approximately a 10% error on the velocity profiles. The error persists across the entire boundary layer, including its edge. The lower values of the velocity and the pressure coefficient offset upstream of the leading edge ($x/c < 0$ in Fig. 4.9) indicate that the acceleration over the model is underestimated in the computations. As a result, separation occurs earlier and reattachment later in the computations compared to the experiments, as seen with the streamlines of Fig. 4.11. Experimentally, separation occurs at $x/c \simeq 0.43$, while reattachment occurs at $x/c \simeq 1.65$. The baseline computations predict flow separation at $x/c \simeq 0.17$, and reattachment at $x/c \simeq 2$. Several effects influencing the correlations are discussed later.

Figures 4.12 and 4.13 provide comparisons between computation and experiments of the time-averaged vorticity and TKE respectively. Here, the simulation TKE is entirely modeled with URANS. The base flow separates early over the curved surface, and the separated flow exhibits regions of large vorticity and TKE. In Fig. 4.13, the in-plane TKE is defined as $\overline{u'^2 + w'^2}/2$, as the spanwise component of the velocity cannot be experimentally measured with a simple PIV. This in-plane TKE is approximated from the modeled TKE as $\frac{2}{3}k_{model}$, according to the isotropic assumption inherent with URANS. The total TKE ($\overline{u'^2 + v'^2 + w'^2}/2$ from experiments approximated from computations as k_{model}) is presented in Fig. 4.14 based on recent stereo PIV measurements, where all components of the velocity vector were measured.

The shear layer (region of high TKE concentration in Fig. 4.13 and 4.14) moves further away from the model surface in the computation compared to the experiments, consistent with an overestimation of the extent of the separation bubble. The

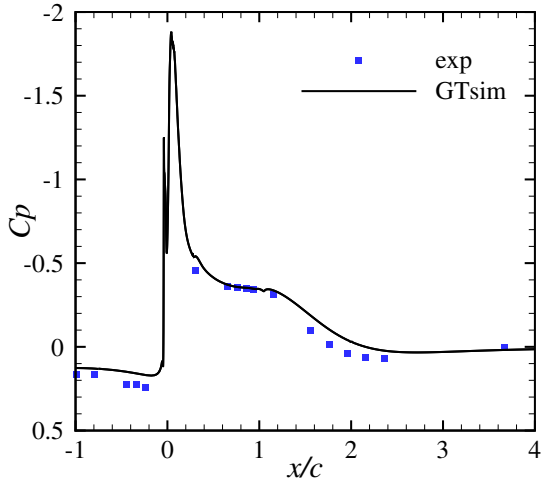

Figure 4.9: Base flow pressure coefficient distribution over the curved surface

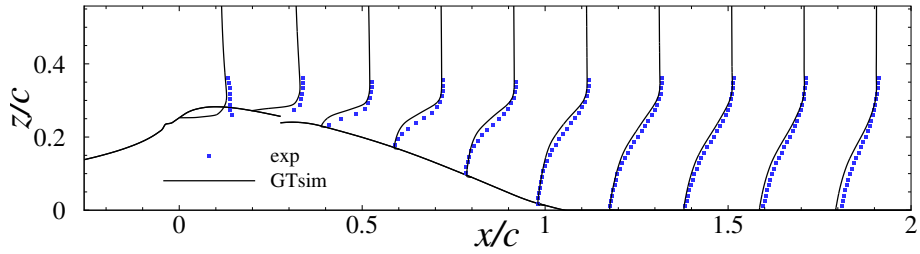

Figure 4.10: Base flow time-averaged streamwise velocity profiles ($x_0 + \frac{0.1u}{U_0}$) at different streamwise locations ($x/c = 0, 0.2, 0.4, 0.6, 0.8, 1.0, 1.2, 1.4, 1.6, 1.8$)

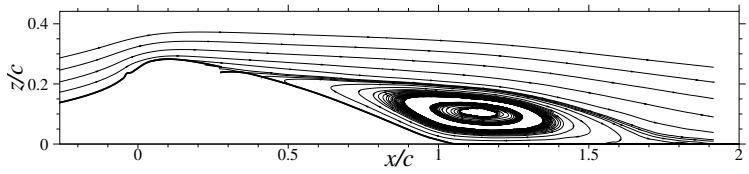

(a) Experiments

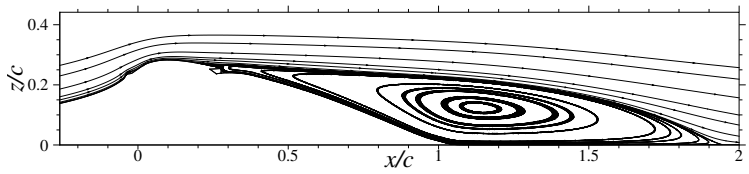

(b) Computations

Figure 4.11: Base flow streamlines

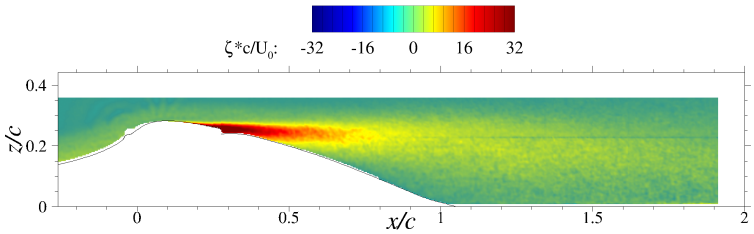

(a) Experiments

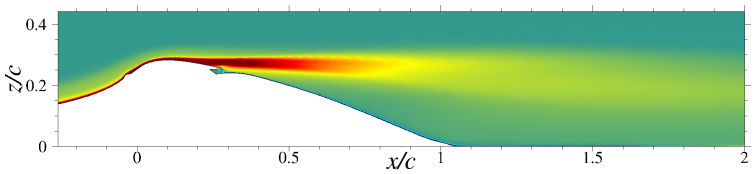

(b) Computations

Figure 4.12: Base flow mean spanwise vorticity contours

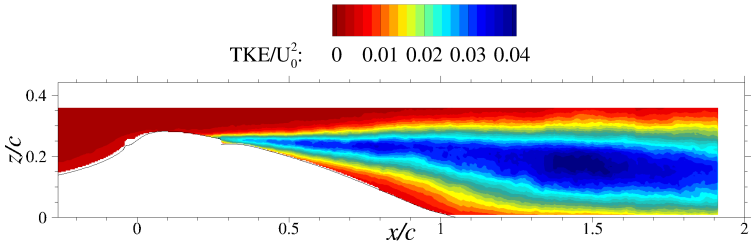

(a) Experiments

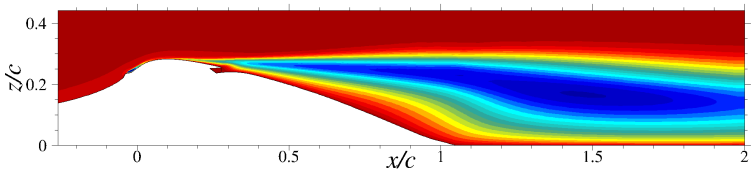

(b) Computations

Figure 4.13: Base flow mean in-plane TKE ($\overline{u'^2 + w'^2}/2$) contours

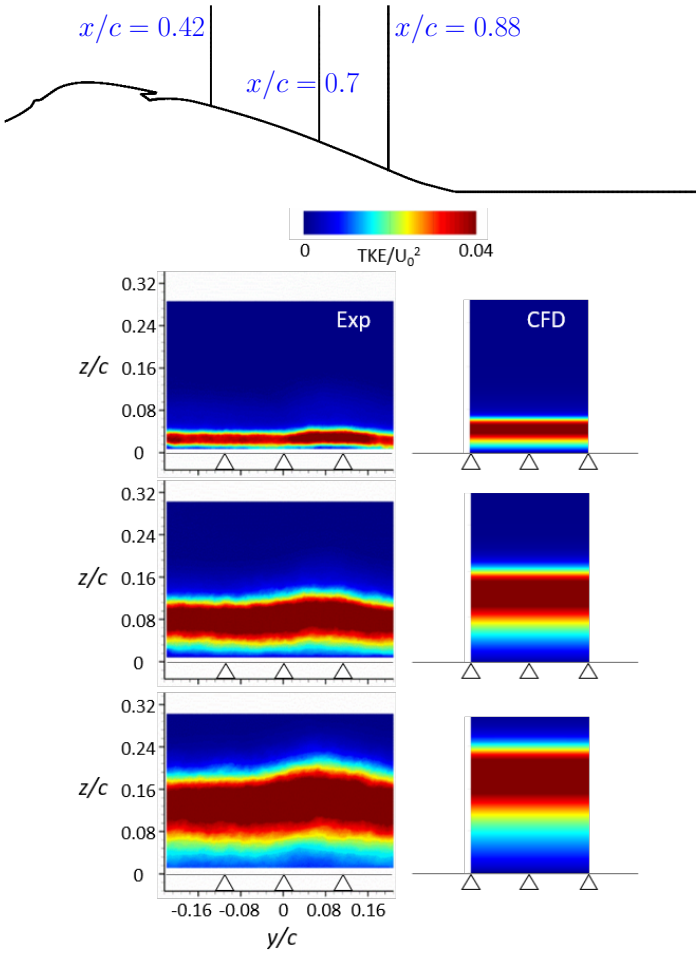

Figure 4.14: Base flow comparison of TKE ($\overline{u'^2 + v'^2 + w'^2}/2$) between computation and experiments at three spanwise planes downstream of the jets: $x/c = 0.42$ (top), $x/c = 0.7$ (middle), $x/c = 0.88$ (bottom)

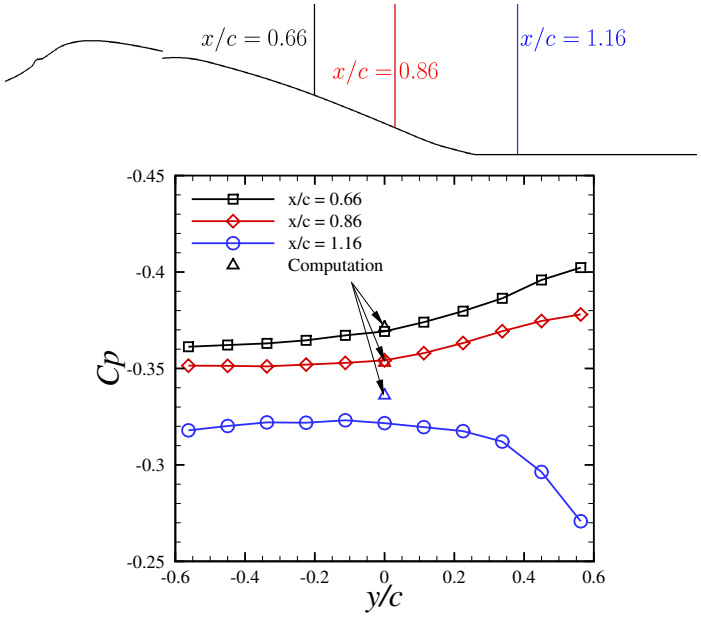

Figure 4.15: Base flow experimental spanwise variation of the pressure coefficient

shear layer offset is approximately 0.04 chords (2.5 mm) at $x/c = 0.88$ (Fig. 4.14). Furthermore, the experiments exhibit a spanwise variation of the TKE stemming from the experimental setup rather that fundamental physical phenomena. Figure 4.15 illustrates the variation of the experimental pressure coefficient with spanwise location, with up to 15% change in the values.

The temporal variation of the base flow pressure coefficient was assessed numerically by extracting multiple instantaneous flow fields at the mid-plane of the computational domain. Figure 4.16 shows that the temporal fluctuations are on the same order of magnitude as the spanwise variation of the wind-tunnel measurements along the span and the difference between these measurements and the computational time-averaged data.

Variations on the baseline setup were simulated on two-dimensional grids to better understand the flow sensitivities. Of particular interest are the effects of the trip wire, the overhang, and the characteristics of the incoming boundary layer. Since the trip wire is glued to the surface, small imperfections associated with it's implementations are not known and cannot be reproduced computationally. Table 4.2 summarizes the

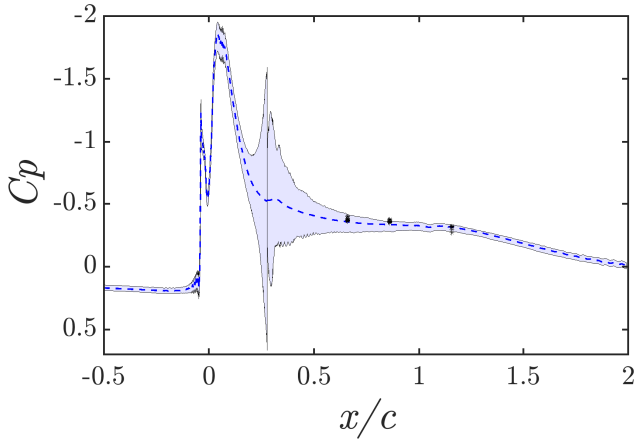

Figure 4.16: Base flow computational pressure coefficient fluctuation. Shaded area: region between minimum and maximum values; Dashed line: time average; Symbols: all experimental values along span.

Table 4.2: Base flow setup variations

Case	Turbulence closure	Trip wire	Overhang/Smooth	Top wall
Baseline	$k-\omega$ SST	0.43 mm	Overhang	Inviscid
1	SA	0.43 mm	Overhang	Inviscid
2	$\gamma - Re_\theta$	0.3 mm	Smooth	Viscous
3	$k-\omega$ SST	0.3 mm	Smooth	Viscous
4	$k-\omega$ SST	None	Overhang	Inviscid

computational variations evaluated and Fig. 4.17 illustrates the associated results. Figure 4.17a is a comparison of the pressure distributions, which exhibit up to 50% variations. The iso-surfaces of $u = 0$ are presented in Fig. 4.17b to permit a visualization of the separation and reattachment locations. The separation location moves upstream as a trip wire is introduced and as its size increases. When the $k-\omega$ SST model is substituted for the Spalart-Allmaras model [33] in the baseline geometrical setup, the separation point moves downstream (after the overhang), though the reattachment still occurs at $x/c = 2$. Computationally, ignoring the presence of the trip wire with the $k-\omega$ SST turbulence closure results in better predictions of the separation and reattachment locations (within 1% of the experimental location).

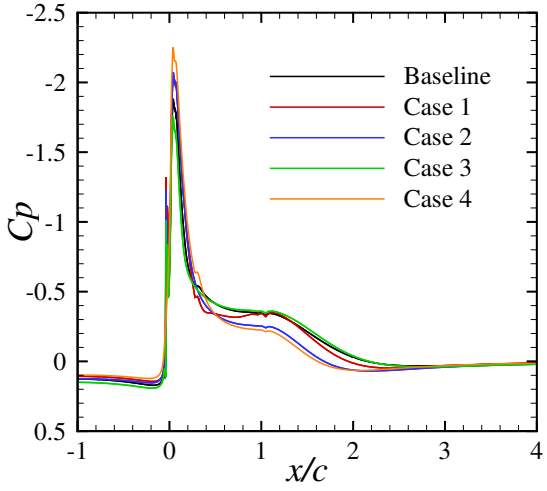

(a) Pressure coefficient distribution

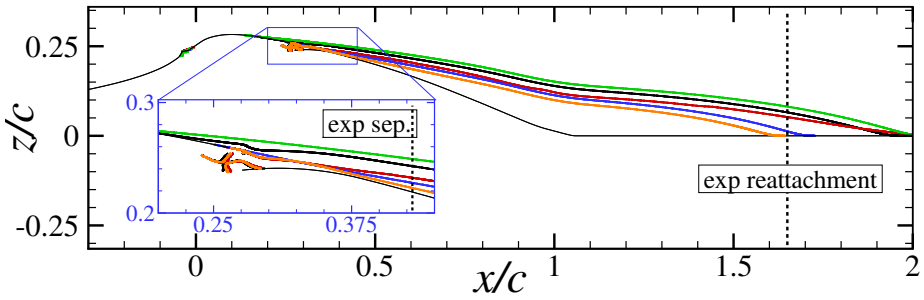

(b) Iso-surface of $u = 0$, indicating the reverse flow boundary

Figure 4.17: Effect of variations in the computational setup on the base flow over the curved surface

The transition model also makes a difference at a moderate trip wire diameter (0.3 mm instead of 0.43 mm in the baseline computations). When the overhang is not resolved, the transitional model predicts flow separation at $x/c \simeq 0.4$ and reattachment at $x/c \simeq 1.7$ (respectively 7% and 3% from the experimental locations). It is clear that the computations are sensitive to the turbulence closure, the trip wire implementation and the overhang.

At low levels of actuation ($0 < C_\mu < 0.36\%$) the reattachment location moves 20% chords downstream according to the mid-plane PIV data (Fig. 4.18). Only for actuation momentum coefficients higher than 0.36% does the flow control mechanism start reducing the size of the separation bubble. Peterson et al. [132] attributed this behavior to the jets pushing the outer shear layer away from the wall at low levels of actuation without entrainment. This indicates a bi-stable nature of the base flow. Similar to the small geometrical and modeling variations computationally evaluated, an infinitesimally small momentum addition in the experiments changes the separation and reattachment characteristics.

The origins of the spanwise variation in the experimental data should be further assessed, as well as a complete characterization of the incoming and outgoing boundary layers. While there is room for improvement in the computational methodologies, use of advanced turbulence closures (LDKM, WRLES) might not provide further insights unless the wind tunnel variations are well understood.

4.4 Fluidic oscillator in a quiescent ambient

An approach similar to that detailed in the Chapter 3 was adopted for the actuator design implemented in the wall-mounted model to characterize the oscillation frequency and develop adequate boundary conditions for the flow control application. Time-step refinement studies were not repeated here. The physical time step was selected to obtain approximately 1000 iterations per oscillation cycle. Multiple supply

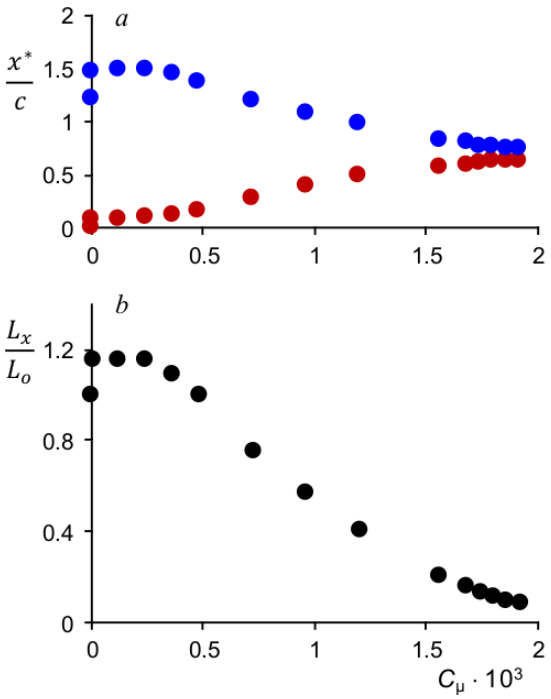

Figure 4.18: Migration of the separation (•) and reattachment (•) point, and the separation axial extent (•) with jet momentum coefficient C_μ. x^* is the streamwise location with respect to the base flow separation point, L_x is the length of the separation bubble, and L_0 is the length of the separation bubble in the base flow. (From Peterson et al. [132])

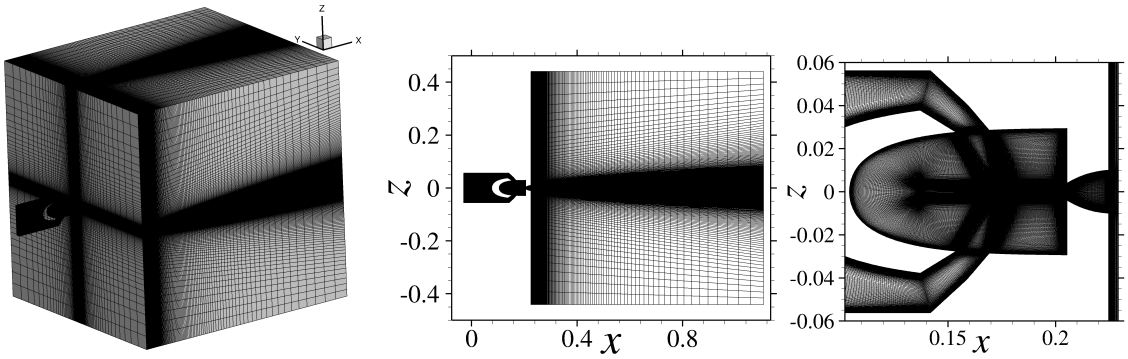

(a) Overview of 3D the grid (b) Overview of the mid-plane (c) Close view of the cavity

Figure 4.19: Grid employed to characterize the isolated fluidic oscillator in quiescent conditions

pressures were considered in both the computations and experiments. In addition, a simulation was performed with two oscillators in quiescent conditions to assess their interactions in the absence of a crossflow.

4.4.1 Single sweeping jet in quiescent conditions

A single isolated sweeping jet was first evaluated in quiescent conditions at two pressure ratios: 1.3 and 2.0. The baseline computational grid employed to characterize the actuators integrated into the wall-mounted model is presented in Fig. 4.19. It corresponds to a medium grid resolution, as defined in Chapter 3, and contains 33.9 million cells.

Figures 4.20, 4.21 and 4.22 illustrate the flow field obtained from these simulations for a pressure ratio of 2.0, indicating that the physics resolved are consistent with findings from Chapter 3. Specifically, a half cycle of oscillation is depicted in Fig. 4.20 with Mach number contours. Concomitant with the sweeping motion of the jet into the quiescent field, the deflection of the supply jets by the upper and lower side vortices can be observed by the swath of lighter green Mach contours inside the fluidic oscillator. The iso-surfaces of Q-criterion (Fig. 4.21) confirm that a significant amount of the turbulent scales are resolved rather than modeled due to the relatively

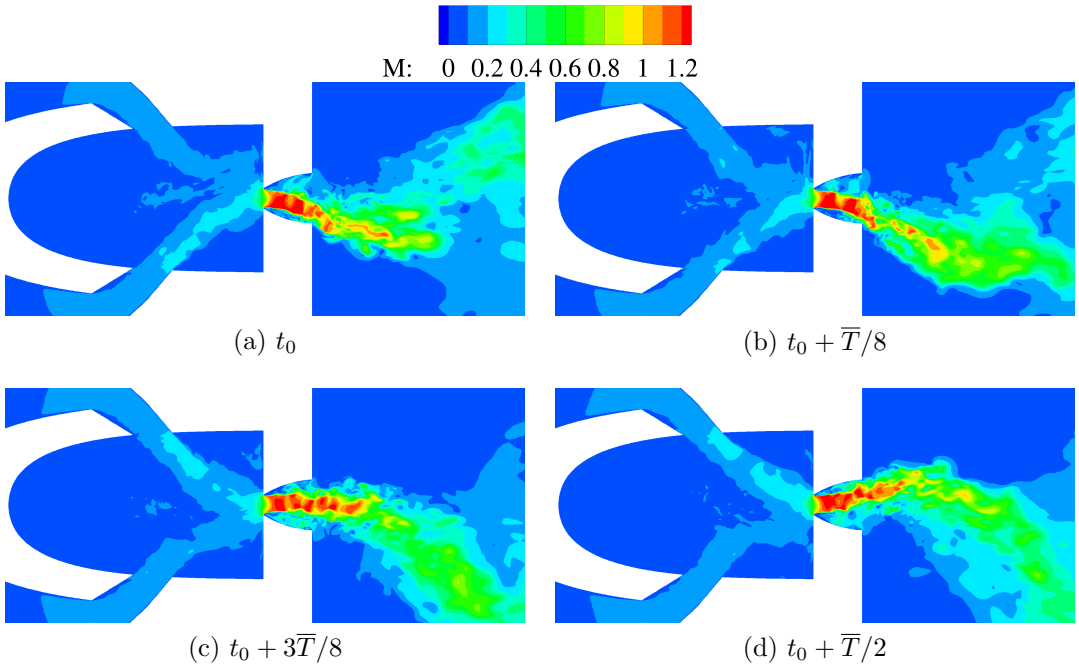

(a) t_0 (b) $t_0 + \overline{T}/8$

(c) $t_0 + 3\overline{T}/8$ (d) $t_0 + \overline{T}/2$

Figure 4.20: Instantaneous local Mach number contours at the mid-plane over a half-period of oscillation, 2.0 pressure ratio

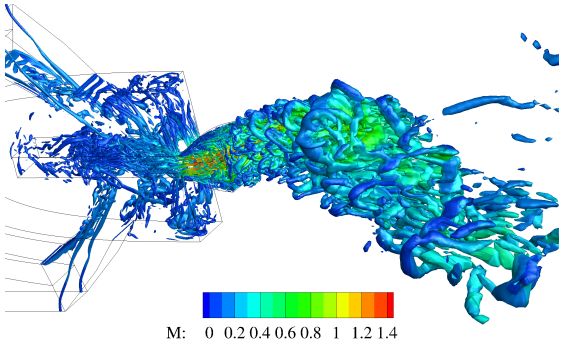

Figure 4.21: Iso-surfaces of the second invariant of the velocity gradient tensor ($Q = 2000$) colored with values of local Mach number for a single isolated fluidic oscillator in quiescent conditions, 2.0 pressure ratio

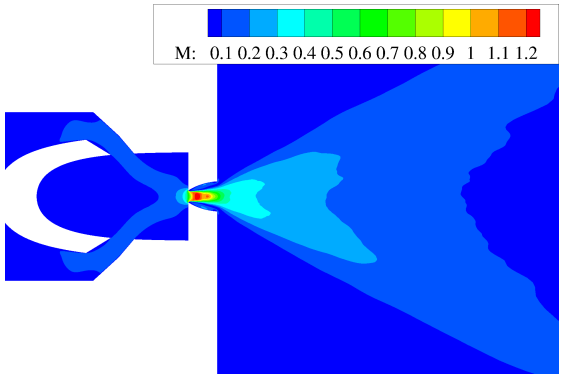

Figure 4.22: Time-averaged (10 cycles) Mach number contours for a single isolated fluidic oscillator in quiescent conditions, 2.0 pressure ratio

fine grid resolution, the WENO reconstruction and the HRLES turbulence closure. Finally, the time-averaged flow (Fig. 4.22) exhibits a dual peak in the Mach number contours as the jet exits into the quiescent ambient, characteristic of sweeping jets.

Figure 4.23 is a comparison between the simulated frequencies and the hot wire measurements. The experimental pressure ratios reported by Koukpaizan et al. [133] were overestimated, such that the correlation with computations was poor (up to 20% error at a pressure ratio of 1.3). While investigating the discrepancies, the pressure transducers were replaced, which resulted in lower pressure measurements. As a result, the error at a 1.3 pressure is now 2.5%. A 17% difference is still present between the medium grid computation and the experiments at a pressure ratio of 2.0. The evaluation of a coarser grid (4.3 million cells) revealed that the experimental frequency is predicted within 2.5% when the flow is evolved for a longer duration and with better sub-iteration convergence. That said, frequency variations at a high pressure ratio are not necessarily nonphysical. von Gosen et al. [124] reported up to 20% band of fluctuations of the oscillation frequency at high pressure ratios (Fig. 4.24) from their time-resolved measurements of the internal flow field and pressure inside a double feedback fluidic oscillator.

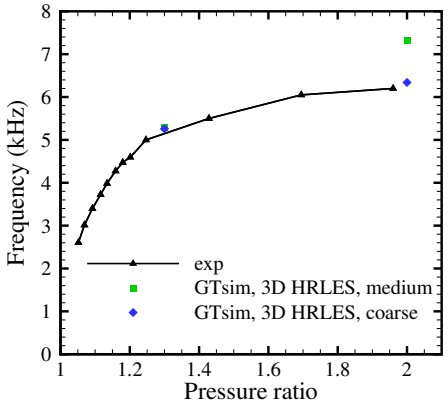

Figure 4.23: Sweeping jet frequency response at different pressure ratios

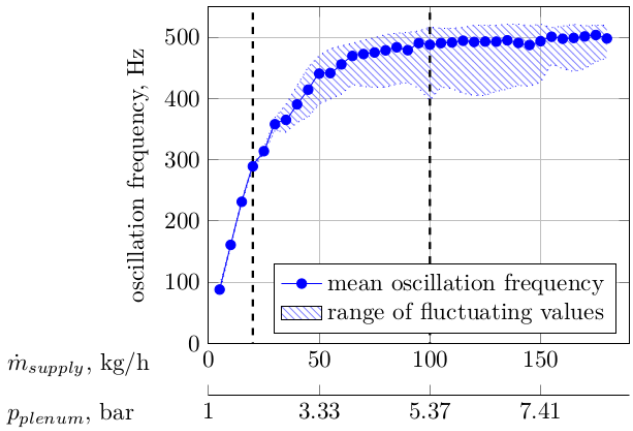

Figure 4.24: Average oscillation frequency as a function of the supply rate for a double feedback fluidic oscillator (from von Gosen et al. [124])

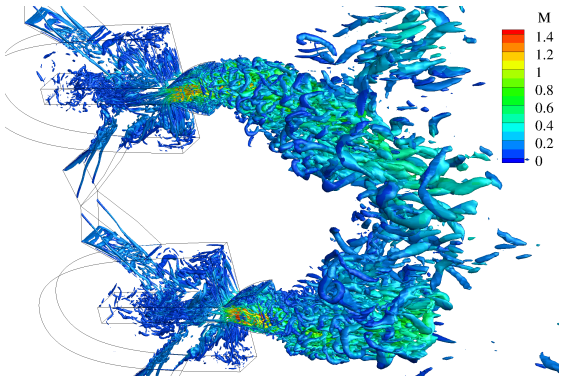

Figure 4.25: Iso-surfaces of the second invariant of the velocity gradient tensor ($Q = 2000$) colored with values of local Mach number for two isolated fluidic oscillator in quiescent conditions, 2.0 pressure ratio

4.4.2 Pair of sweeping jets in a quiescent ambient

A pair of sweeping jets was examined numerically in quiescent conditions to gain some insight into their interaction for the given spacing. A similar study was conducted experimentally by Hirsch and Gharib [134] using Schlieren visualization of a pair of sweeping jets. Their results indicated that the jets do not interact with one another, in the sense that their oscillation frequency does not vary significantly (less than 1%) in the presence of neighboring actuators. This behavior was observed to be independent of their separation distance. This does not mean that the ensuing sweeping jets do not interact with one another. These findings were assessed computationally for the fluidic oscillator design implemented in the wall-mounted model. In the present work, the separation distance is fixed and the interactions are considered both from internal and external perspectives. The baseline computational grid (medium resolution) contains 72.4 million cells, where the actuators' grid domains are identical to the ones used for the single actuator simulation. Only the 2.0 pressure ratio was evaluated for the pair of actuators.

Figures 4.25 and 4.26 illustrate the flow field obtained from these computations. Similar to the single isolated oscillator, the time-averaged flow field exhibits a dual peak in the Mach numbers for each actuator in the present configuration.

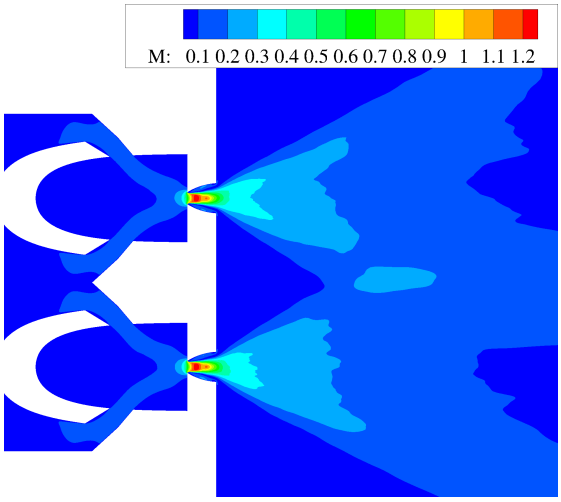

Figure 4.26: Time-averaged (9 cycles) Mach number contours for two isolated fluidic oscillators in quiescent conditions, 2.0 pressure ratio

The oscillation frequency of each jet was found to be unaffected by the presence of the other jet. This is consistent with the experiments, as the oscillation frequency did not vary from testing an array of actuators to testing a single actuator (by blocking the exit of the other actuators in the array). This finding also supports the conclusions of Hirsch and Gharib [134].

While the frequency is unaffected, the jets interact in the quiescent ambient. The time-averaged solution obtained with the pair of sweeping jets is compared to the isolated jet solution in Fig. 4.27 for the Mach number contours. The contour lines are superimposed inside the actuators up to their exit, indicating the interactions only result in differences outside of the oscillators. This further suggests that, deriving a boundary condition based on a single actuator and extending it to an array is a valid approach. A new contour line (Mach level 0.2) appears approximately 11 throat widths downstream of the actuator exit, indicating a merging of the two sweeping jets, due to their spreading, at that location. This can also be observed in the instantaneous iso-surfaces of Q-criterion (Fig. 4.25), which shows the intersection of the jets emanating from the pair of fluidic oscillators.

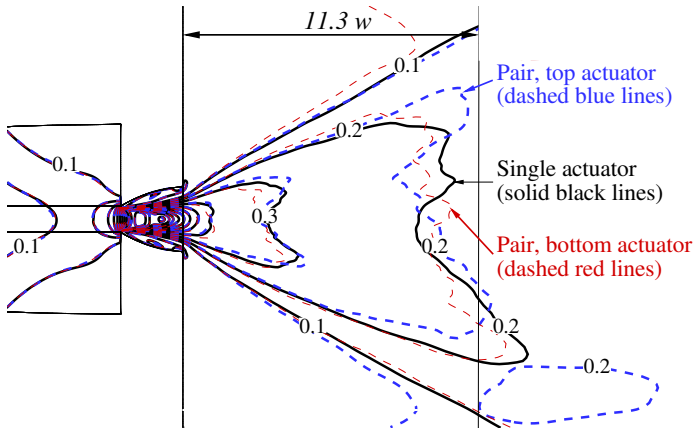

Figure 4.27: Comparison of the time-averaged Mach number contour lines between one and two fluidic oscillators in quiescent conditions, 2.0 pressure ratio.

A coarser grid containing 8.9 million cells was employed to perform longer simulations and assess the effect of the boundary condition between the actuators. The baseline computations on the medium grid were performed with slip wall boundary conditions at the bottom boundary of the lower actuator plenum and the top boundary of the upper actuator plenum. This approach was also evaluated on the coarser grid. A variation on the coarse grid consisted in replacing the slip walls by periodic boundary conditions coupling the two actuators.

Figure 4.28 is a comparison of frequency spectra obtained with the two sweeping jets and with the two boundary condition treatments. The periodic boundary condition effectively synchronizes the jets, as they operate in phase, and their oscillation frequencies differ by less than 0.5%. When slip walls are applied at the opposite faces of the plenum, the upper jet oscillates at a frequency 4% higher than the lower jet. This small variation in frequencies is enough for the phase between the jets to vary throughout the simulation. This was partially observed during the baseline computations (slip wall boundary condition on the medium grid), but the duration was too short and contained too much high-frequency to draw definitive conclusions. The number of oscillation cycles recorded on the coarse grids was more than double the

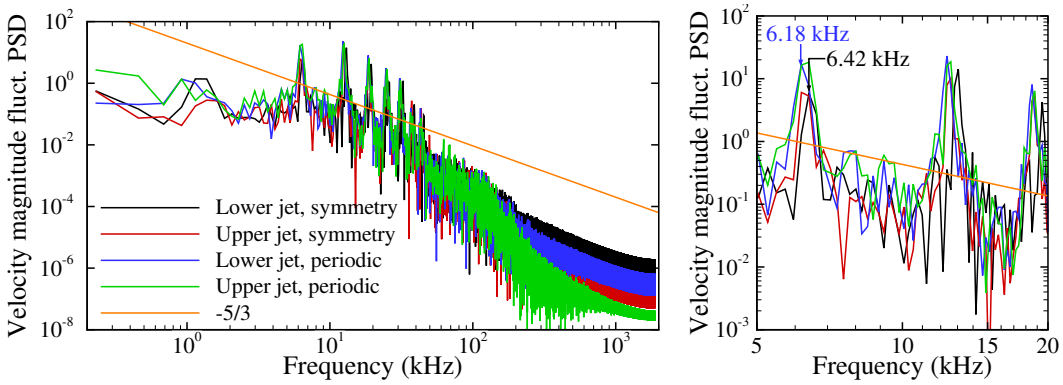

(a) Overview (b) Close view, $5 < f < 20$ kHz

Figure 4.28: Power spectral densities of velocity magnitude fluctuations for two fluidic oscillators in a quiescent ambient: effect of symmetry and periodic boundary conditions

number recorded on the medium grid (20 cycles). In experiments, there is no reason to expect a synchronization of the sweeping jets.

4.4.3 Boundary condition model of the fluidic oscillators

A boundary condition model was developed based on the behavior of the single isolated oscillator in quiescent conditions. Following the conclusions of Chapter 3, the approach retained consists in a phase-averaged representation of the flow variables and includes the modeled turbulence: the density ρ, momenta (ρu, ρv, ρw), stagnation energy E, TKE and specific dissipation rate ω. The variables were recorded at the throat (inner mold line) and exit (outer mold line) of the device at every iteration of the precursor simulation. Phase-averaging was applied by placing the instantaneous flow variable in 1°-wide bins, in order to generate data at 100 phases between 0 and 2π rad. The phase-averaged data were then interpolated onto the coarser grid of the actuator throat employed to simulate the control of flow separation. In deriving the boundary condition model, the momentum vector from the precursor simulation was rotated by 54.6° about the spanwise axis to match the actuator orientation in the

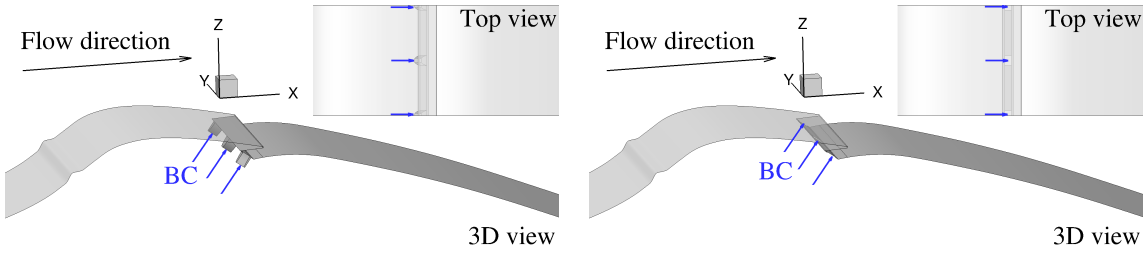

(a) Inner mold line (b) Outer mold line

Figure 4.29: Illustration of the application of the boundary condition model of the fluidic oscillators to control the separation over a wall-mounted geometry

flow control grid. Figure 4.29 illustrates the application of the boundary condition to control the flow over the wall-mounted model.

4.5 Control of flow separation over the wall-mounted model

The control of flow separation over the wind-tunnel model via an array of fluidic oscillators was next investigated. Numerical simulations were performed for the maximum actuation case experimentally evaluated corresponding to a jet momentum coefficient $C_\mu = 0.21\%$. According to the experimental calibration in quiescent conditions, this flow rate is achieved with a driving pressure ratio approximately equal to 2.0.

Two fluidic oscillators were numerically modeled for comparison with the associated wind tunnel test section. Periodic boundary conditions were applied to the spanwise boundaries to generate an infinite array of actuators. An overview of the computational grid is presented in Fig. 4.8; part of the grid (without the fluidic oscillators) was utilized to simulate the base flow (section 4.3). The computations of the controlled cases were carried out by two separate methods and compared: either by resolving the interior of the fluidic oscillators or via the new boundary condition model. The periodic boundary condition effectively synchronizes the actuators when the full cavity is resolved, and the phase is an input of the boundary condition model.

First, the boundary condition model is employed by considering the jets in phase. An investigation of the effect of the phase is discussed in section 4.6.2.

While resolving the full cavity, the computational physical time step was set to capture 500 iterations per cycle. Since there is less restriction on time step with the boundary condition model, this time step was increased to perform 1000 iterations per chord in the outer flow at the nominal Mach number, which corresponds to approximately 165 iterations per cycle. These time steps are only sufficient to obtain 2 orders of magnitude of local convergence with the sub-iterations. Therefore, increasing the time step significantly, by an order of magnitude for example, is not an option. The numerical solution was averaged over more than 30 cycles of sweeping jet oscillations. This lower limit is sufficient for convergence of the first-order statistics (pressure, time-averaged velocity), but not necessarily for the second-order statistics (TKE, Reynolds stress tensor). Both the URANS (Menter SST [34]) and the HRLES [49] approaches were evaluated.

4.5.1 Instantaneous flow

The presence of the overhang introduces very specific flow physics and attachment mechanisms that are different from the behavior of jets in crossflow. The instantaneous flow field resulting from the simulations are presented here with a discussion of the flow physics.

Flow structures

Figure 4.30 is an overview of the instantaneous Mach number contours in the spanwise mid-plane of the actuators and test section. It provides an overview of the entire flow field, including the actuator internal cavity. The sweeping jets impinge on the overhang, from which small scale spanwise vortices are shed into the outer flow. The impingement of the jets on the overhang results in a triple deck in the velocity field,

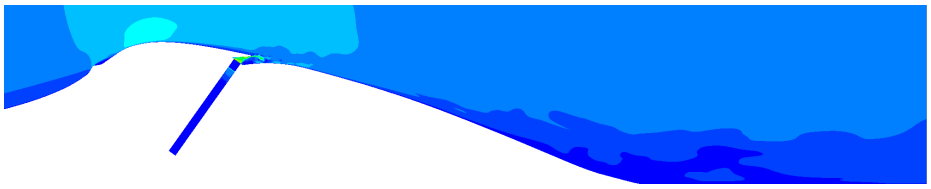

(a) Test section mid-plane slice overview

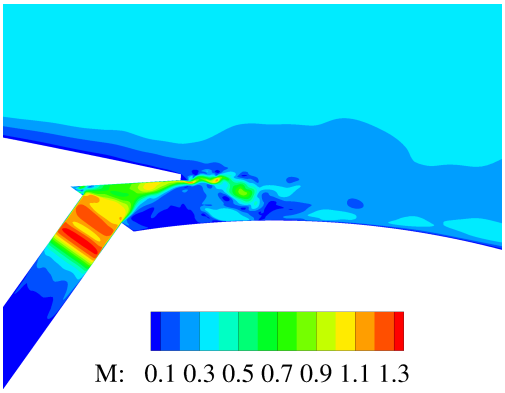

(b) Close view of the actuator exit

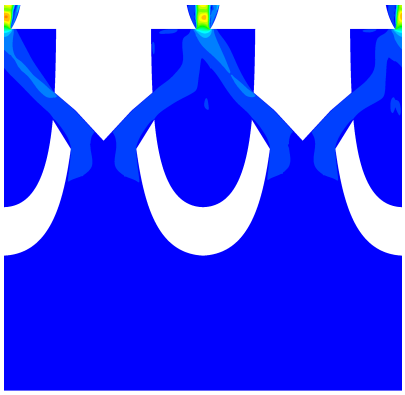

(c) Actuator interior

Figure 4.30: Instantaneous Mach number contours for the simulation of the curved surface and two fluidic oscillators, full cavity HRLES

notwithstanding the boundary layers, as depicted in Fig. 4.30b. The upper layer is the shear layer above the overhang, the second layer is the high-speed jet, and the third layer is a recirculation region below the jets. The flow structure results from the interaction between these layers. Figure 4.31 depicts the iso-surfaces of Q-criterion for the full cavity solution, where the locations of the actuators are identified by black triangles. Both the URANS and HRLES results are depicted for comparison. Large-scale structures are formed between the sweeping jets and result in streaks convecting downstream. This is observed more clearly in the URANS figure (Fig. 4.31a), as the smaller scales are not resolved. Indicative of attached flow in the regions directly impacted by the sweeping jets, HRLES (Fig. 4.31b) exhibits smaller and wall-bound flow structures.

The computations can provide further insight into the physics, such as the flow behavior close to the actuator exits where cameras have no access. In addition to the flow inside the actuators, which is relatively well understood, the computations

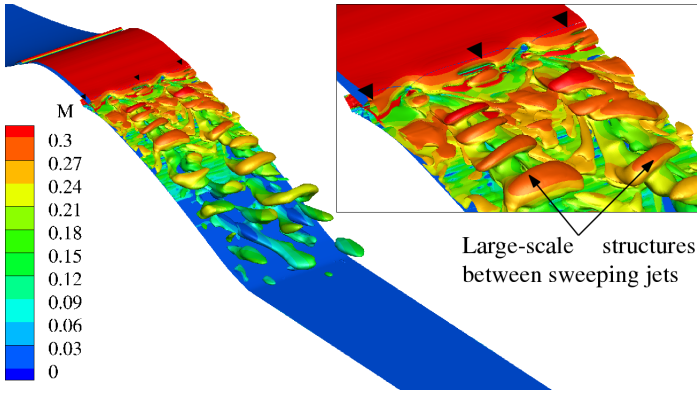

(a) Full cavity URANS

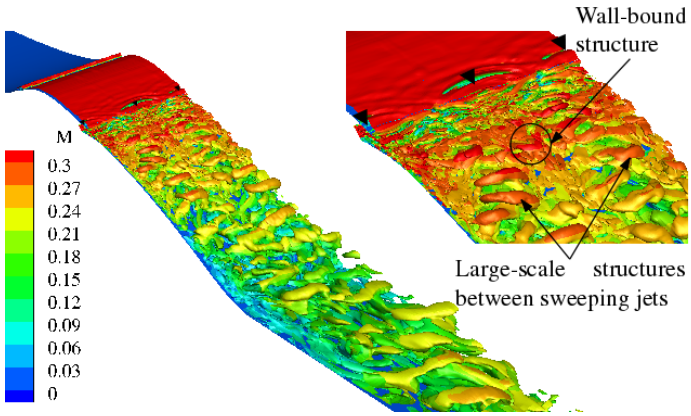

(b) Full cavity HRLES

Figure 4.31: Iso-surfaces of the second invariant of the velocity gradient tensor ($Q = 1$) colored with values of local Mach number for the controlled flow over the wind-tunnel model

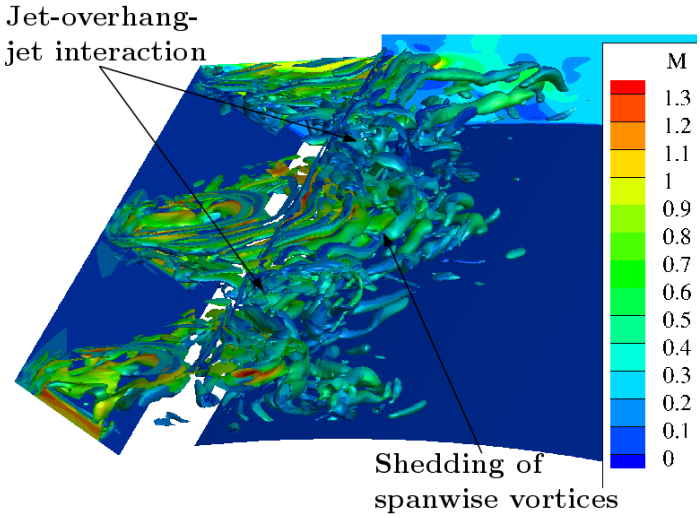

Figure 4.32: Iso-surfaces of the second invariant of the velocity gradient tensor ($Q = 10000$) colored with values of local Mach number for the controlled flow over the wind-tunnel model: close view of the overhang, full cavity HRLES

provide details of the interaction of the jets with the overhang. Figure 4.32 depicts Q-criterion iso-surfaces between the jet exit and the overhang. As the jets impinge on the overhang, they experience an additional spanwise spreading that leads to an intersection of the structures emanating from the jets. The radial shedding of spanwise vortices near the jet centerline is clearly visible in Fig. 4.32. Also visible is a complex interaction where the jets, that have been spread by the overhang, intersect. This interaction gives rise to the large-scale structures convecting between the jets (Fig. 4.31).

Figure 4.33 compares the top view of the structures depicted in Fig. 4.32 at three different times corresponding to a half-cycle of jet oscillation. From left to right, the central jet moves up in Fig. 4.33. The jet oscillation is small compared to its subsequent spanwise spreading at the overhang. By changing the iso-surface levels plotted and blanking the flow structures beneath the overhang, the generation of the large-scale structures at the intersection can be observed (Fig. 4.34). The spanwise vortices shed from the overhang break down into the wall-bound structures near the jet centerline and large-scale structures form between the jets. Recall that the unactuated flow has tendency to separate (section 4.3). Therefore, in regions where the jet velocity is not sufficient to maintain the flow attached, flow structures lift away from the wall. The spanwise oscillation of the jets cause a spanwise meandering of the large-scale structures between the jets, as depicted in Fig. 4.34.

Onset of the large-scale structures

The creation of the large-scale structures between the jets has been attributed to the interaction of the spanwise vortices shed at the overhang with the outer flow. A more detailed explanation of their origin is sought. This analysis relies on the URANS closure, as it does predict the large-scales, and the absence of the smaller flow structures provides a clearer result.

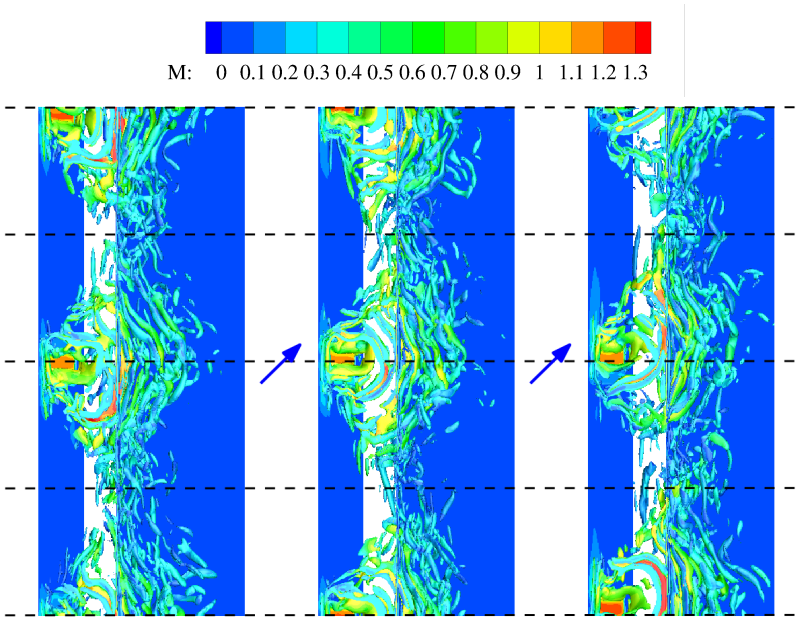

Figure 4.33: Iso-surfaces of the second invariant of the velocity gradient tensor ($Q = 10000$) colored with values of local Mach number, top view: spanwise motion of the jets, full cavity HRLES

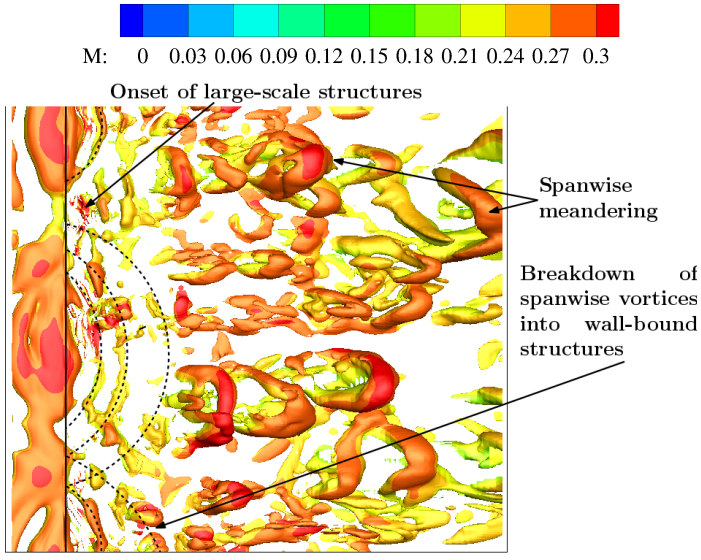

Figure 4.34: Iso-surfaces of Q criterion ($Q = 10$) colored by Mach number, $0.25 \leq x/c \leq 0.5$, full cavity HRLES. Flow structures below the overhang are blanked.

Figures 4.35 and 4.36 illustrate two components of the velocity and vorticity vectors immediately upstream and downstream of the overhang edge. The middle fluidic oscillator is centered at $y/c = 0$, and the center of the neighboring fluidic oscillator are at ± 0.112. To simplify the discussion, consider the interaction (halfway between two jets) at the right of the figures ($y/c \simeq 0.05$, $z/c \simeq 0.255$). Large opposite values of spanwise velocities are present to the left and right of this interaction location beneath the overhang, consistent with the spanwise spreading of the jets. The opposite signs indicate a collision of the two neighboring jet streams. Before the overhang edge ($x/c = 0.275$, left figures), the vertical velocity is negative above the overhang and positive near the jets. The vertical velocity is negative below the overhang between the jets, with a pocket of positive vertical velocity near the overhang upper surface. This small pocket of vertical velocity instantly grows past the overhang edge ($x/c = 0.28$, right figures) and splits the outer layer (up-welling). This is accompanied with counter-rotating streamwise vorticity. The structures then arise from the collision of the neighboring jets streams, in particular the strong spanwise velocities associated with the spreading of the jets at the overhang. The jet-overhang-jet interaction at the left of the figures ($y/c \simeq 0.06$) are approximately a mirror image of the interaction at the right ($y/c \simeq 0.05$).

The breakdown of spanwise vorticity into smaller wall-bound structures aligned with the jets can also be explained with the spanwise velocity field. Near the jet centers, the spanwise velocity also exhibits a change of sign. In contrast with the interaction region, the streams are moving away from each other rather than colliding. As a result, the coherence of the spanwise vortices cannot be maintained, the shedding occurs almost radially, and the structures break down.

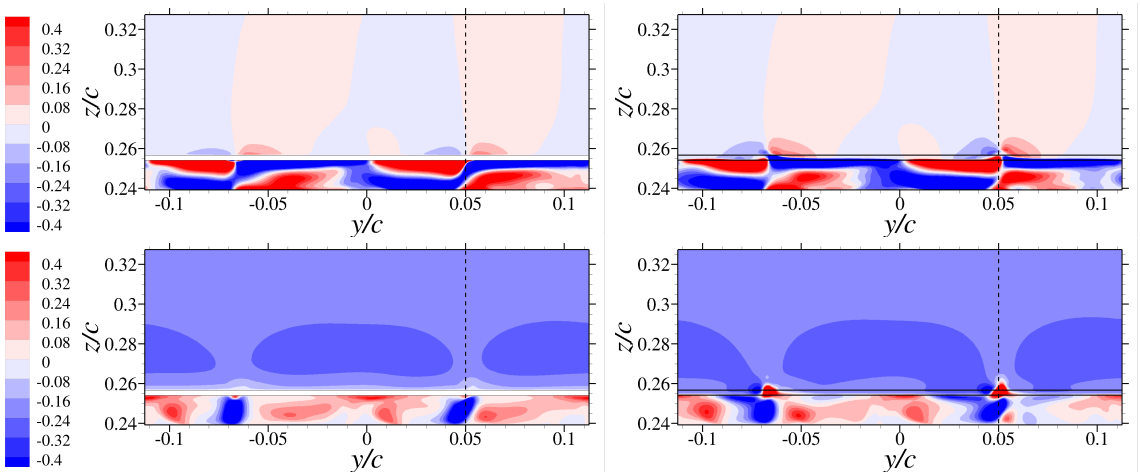

Figure 4.35: Instantaneous velocity contours at two streamwise planes. Upstream of the overhang edge ($x/c = 0.275$, left) and downstream of the overhang edge ($x/c = 0.28$, right). Spanwise velocity (v/U_0, top) and vertical velocity (w/U_0, bottom).

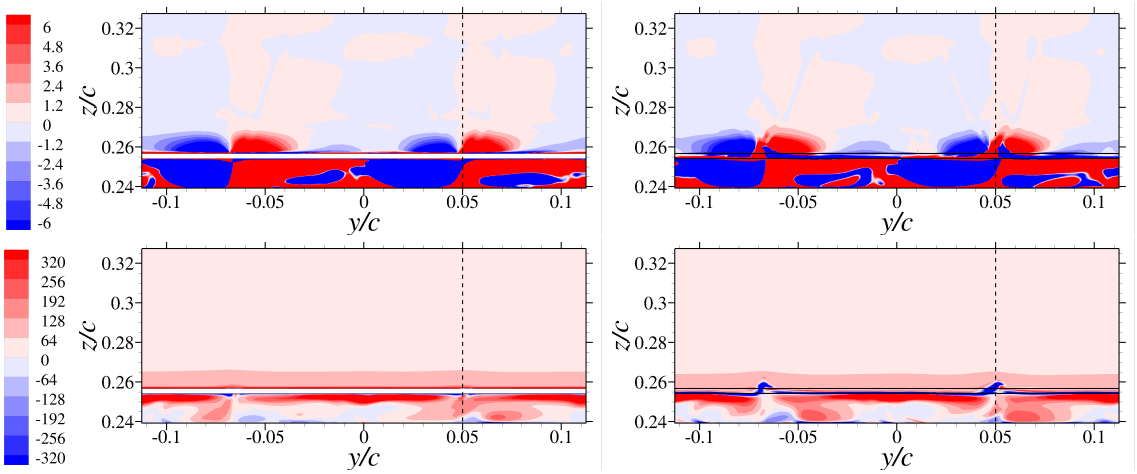

Figure 4.36: Instantaneous vorticity contours at two streamwise planes. Upstream of the overhang edge ($x/c = 0.275$, left) and downstream of the overhang edge ($x/c = 0.28$, right). Streamwise vorticity ($\zeta_x c/U_0$, top) and spanwise vorticity ($\zeta_y c/U_0$, bottom).

Mechanisms of flow separation delay

Further inspection of the vorticity in the flow field provide an insight into how the jets attach the flow. Figure 4.37 depicts the instantaneous spanwise vorticity contours obtained from the full cavity HRLES computations at the mid-plane (through jet centers) and between the jets. As previously discussed, the flow structures near the jet centerline remain wall-bound (Fig. 4.37a) downstream of the jets. In contrast, the structures between the jets move away from the wall (Fig. 4.37b). The additional information that the spanwise vorticity provides is the direction of rotation. The jets attach the flow by introducing spanwise vortices rotating in the direction opposite to the outer layer, thereby preventing its separation (Fig. 4.37c). The vortices rotate in the direction because the jets move at a much higher velocity than the outer layer. Halfway between the jets, these counter-clockwise rotating vortices are much weaker, so the clockwise vorticity in the separating shear layer is not as affected, and the flow does not remain attached.

Hybrid RANS/LES blending function

The last information that must be obtained from the instantaneous flow is the HRLES blending function (Fig. 4.38) to understand where the different closures are utilized. The incoming boundary layer is entirely resolved with RANS until the jets are encountered. In the absence of turbulent fluctuations in the boundary condition, the HRLES closure reverts to RANS as expected. The LES content is excited by the jets and their interaction with the overhang. The interaction between the jets and the outer flow results in a triple deck in the blending function (not including the region above the incoming boundary layer). Downstream of the jet location, the near-wall region and the outer shear layer are treated with RANS, while LES is active between these two layers. It is in this intermediary region that the flow structures depicted in

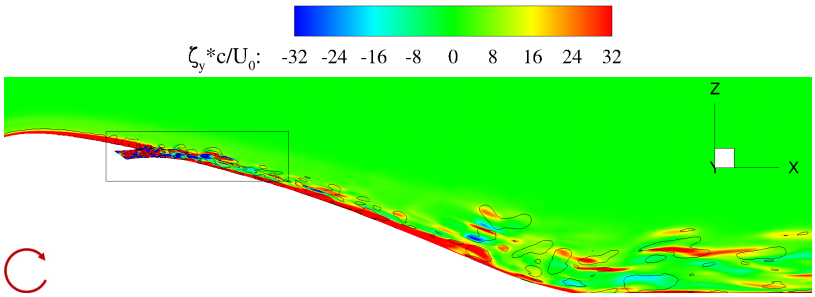

(a) Actuator center ($y/c = 0$), overview, $Q = 1$

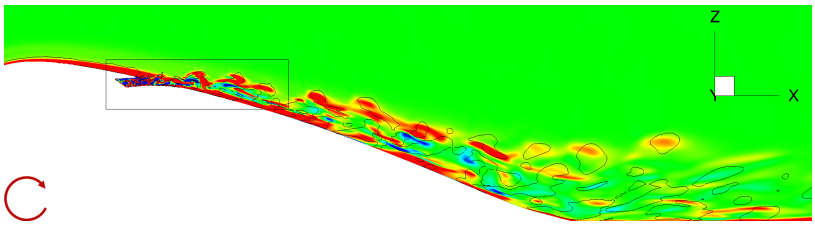

(b) Between actuators ($y/c = 0.055$), overview, $Q = 1$

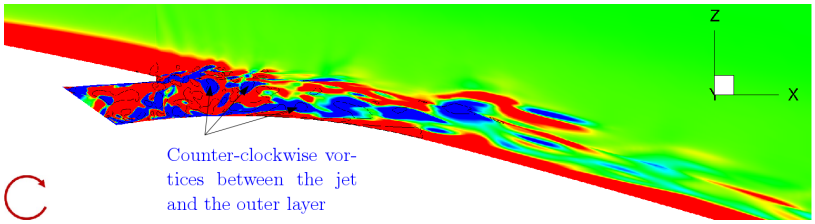

(c) Actuator center ($y/c = 0$), close view of the overhang, $Q = 100$

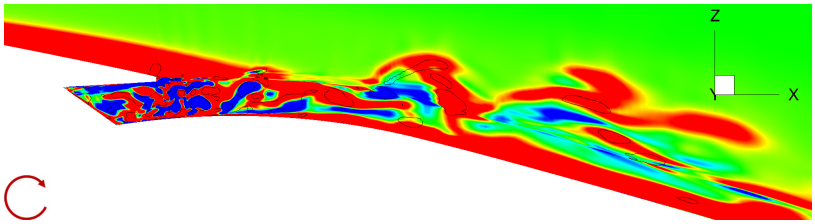

(d) Between actuators ($y/c = 0.055$), close view of the overhang, $Q = 100$

Figure 4.37: Instantaneous spanwise vorticity contours overlayed with iso-lines of the second invariant of the velocity gradient tensor (Q), full cavity HRLES

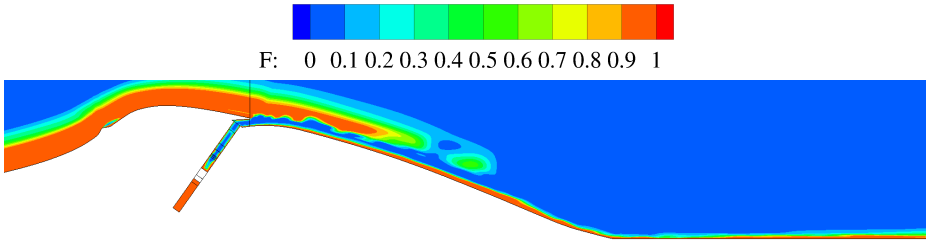

(a) Actuator center ($y/c \simeq 0$)

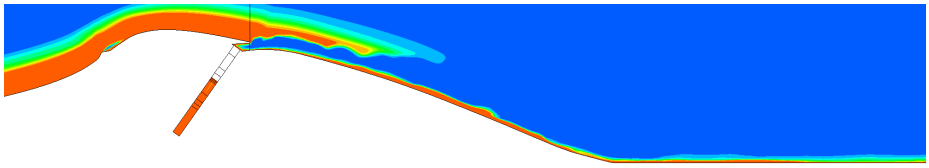

(b) Between actuators ($y/c \simeq 0.05625$)

Figure 4.38: Instantaneous HRLES blending function 0 (LES) $\leq F \leq 1$ (RANS) for the simulation of the curved surface and two fluidic oscillators, full cavity HRLES

Fig. 4.31 are resolved. The relevant structures are resolved with LES, and a variation on the blending function is presented in section 4.6.3.

Wall skin friction

The wall skin friction (Fig. 4.39) provides additional evidence that the flow is attached (positive skin friction) at the center plane. Furthermore, the skin friction distribution indicates the presence of separated flow regions between the jets (marginally negative skin friction), which spread in the spanwise direction further downstream. This observation is consistent with the large-scale structures, introduced earlier, that develop between the jets and meander in the spanwise direction (Fig. 4.31). Finally, the region immediately downstream of the jets also exhibits negative skin friction, consistent with the recirculation region between the jet and the lower wall, before the flow attaches to the wall.

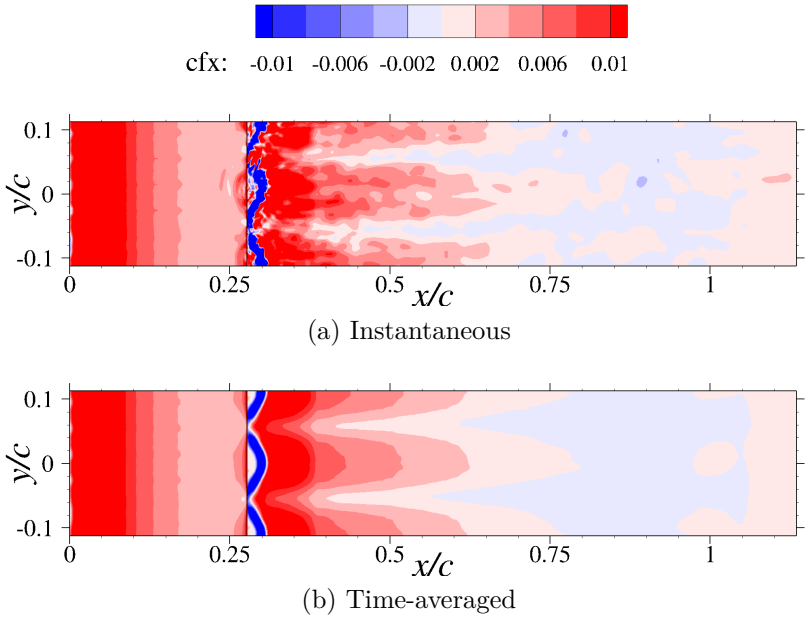

(a) Instantaneous

(b) Time-averaged

Figure 4.39: Wall skin friction contours, full cavity HRLES

4.5.2 Time-averaged flow

The computations are compared to time-averaged PIV in the test section center plane, stereo PIV measurements at three spanwise planes, and pressure measurement along the model centerline. Figure 4.40 is the pressure coefficient at the centerline of the model, and Fig. 4.41 contains the velocity profiles at multiple streamwise locations. The smoothness of the pressure distribution and velocity profiles confirm that the first-order statistics have converged. The pressure distributions and velocity profiles show that the simulations are able to correctly predict the suppression of separation.

According to the pressure coefficient distribution, the most accurate agreement with experimental data is obtained with the boundary condition model and the URANS closure. However, the latter computational approach predicts a small separation bubble at the trailing edge, which is not observed in the experiments and the other computational approaches ($x/c = 1.2$ in Fig. 4.41b). The maximum discrepancy between the simulation approaches and the experiments when comparing the pressure coefficients occurs at the trailing edge ($x/c \simeq 1$). Around this location,

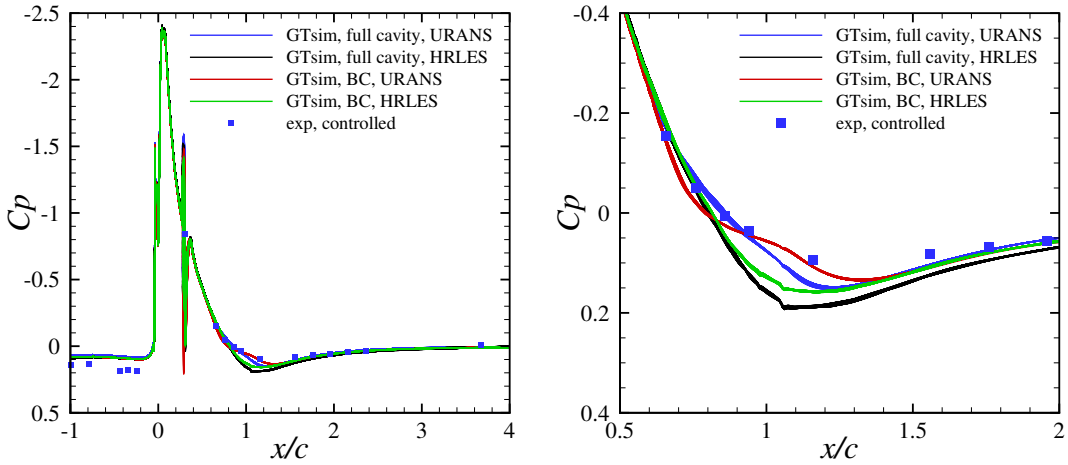

(a) Overview (b) Close view

Figure 4.40: Controlled flow time-averaged pressure coefficient distribution over the curved surface

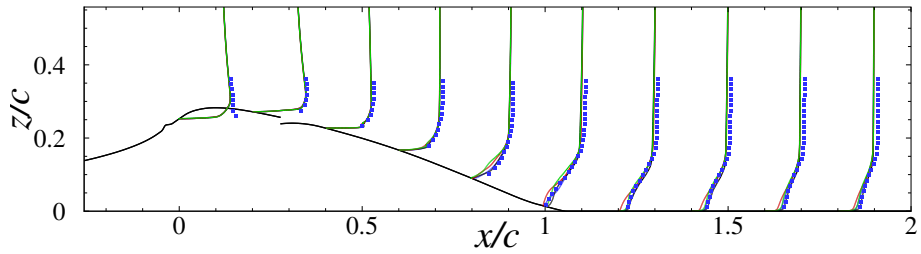

(a) Overview ($x/c = 0, 0.2, 0.4, 0.6, 0.8, 1.0, 1.2, 1.4, 1.6, 1.8$)

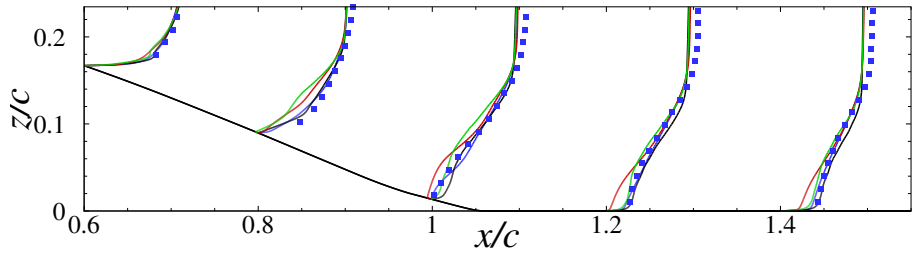

(b) Close view ($x/c = 0.6, 0.8, 1.0, 1.2, 1.4$)

Figure 4.41: Controlled flow time-averaged streamwise velocity profiles ($x_0 + \frac{0.1u}{U_0}$) at different streamwise locations. Legend as in Fig. 4.40.

the different simulation approaches have up to 100% relative error in pressure coefficient when compared to one another, whereas they are within 10% of one another in locations of non-zero pressure coefficient and away from the pressure spikes that occur near the overhang. Similar to the base flow, the error on the velocity profiles between computation and experiment is approximately 10% away from the wall. The maximum velocity at $x/c = 1.8$ is experimentally 10% higher than the estimated freestream velocity, which can be explained by the blockage introduced by the upper and side walls. The effect of increasing the freestream velocity in the computations to account for the blockage is discussed in section 4.6.4.

Figures 4.42 and 4.43 provide comparisons between computation and experiments for the time-averaged vorticity and TKE respectively at the mid-plane of the test section. For HRLES, the simulation TKE is a summation of its modeled and resolved components. Close views of the overhang for the vorticity and TKE are provided in Fig. 4.44. The range of the contour levels are extended in Fig. 4.44 to show more details of the behavior at the actuator exit. For instance, the TKE levels are extended from $0 \leq TKE/U_0^2 \leq 0.04$ to $0 \leq TKE/U_0^2 \leq 0.4$. Immediately after the actuator exit and as the flow is deflected by the overhang, concentrations of vorticity and TKE are apparent in the mid-plane. This results from interactions with the outer flow, and these interactions ultimately lead to a decrease in TKE downstream compared to the base flow, as the flow remains attached.

The TKE contours are very sensitive to the different simulation approaches. The full cavity HRLES method produces a thin trail of moderate non-dimensional TKE values (0.01-0.02 for $x/c > 0.5$) at the mid-plane, similar to the experimental data. Conversely, the full cavity URANS presents values as high as 0.03 in the same region. The trend is reversed immediately downstream of the overhang ($x/c \simeq 0.28$), as HRLES exhibits a larger area for high TKE concentration. Thus, a higher TKE concentration near the overhang, resulting from the vortical interactions, reduces the

TKE levels far downstream. The TKE concentrations near the overhang can only be assessed computationally.

Following the computations, additional experiments were conducted using stereo PIV to measure the spanwise effect of the jets on the wall-mounted model. Figure 4.45 is a comparison between computation and experiments of streamwise vorticity and TKE. The time-averaged streamwise vorticity exhibits a positive rotation (counter-clockwise) to the right of the central jet when looking upstream and a negative rotation on the left of the jet. The time-averaged streamwise vorticity exhibits a similar sense of rotation near the neighboring jets, which results in up-welling between the jets. This is consistent with the previous observation of large-scale structures in the instantaneous flow. Shadows of these structures appear as loops in the time-averaged stereo PIV TKE contours. As discussed for the base flow, the experimental actuated flow exhibits a spanwise variation. The loops reflecting the presence of the large scale structures are clearly visible for $x/c = 0.88$ at the right of the PIV window of Fig. 4.45, but not at the left. It is very likely that variations in the behavior of the individual jets adds to the pre-existing spanwise variation of the base flow, resulting in variations that will not be reproduced computationally. The computational solution with HRLES best matches the experimental data obtained at the left of the stereo PIV window. The lower values of TKE downstream of the jets at the right of the stereo PIV window indicate that the associated jets introduce higher TKE concentrations near their orifice. Indeed, as previously discussed, higher concentration of TKE near the overhang result in lower values downstream.

The behavior observed with the pressure coefficient and the velocity distributions can be explained by the spanwise variation in the experiments. As previously discussed, the full cavity HRLES performs better in predicting the velocity profiles at the center plane, while the boundary condition URANS performs better in predicting the pressure coefficient. Figure 4.47 illustrates the spanwise variation of the pressure

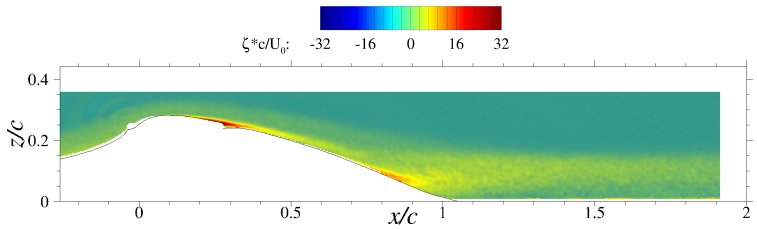

(a) Experiments

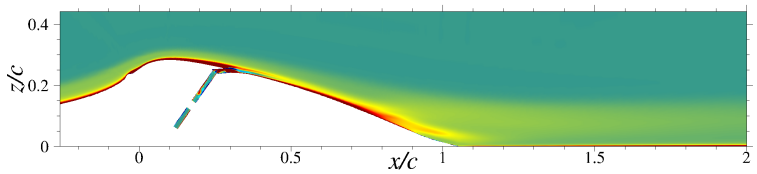

(b) Computations, full cavity URANS

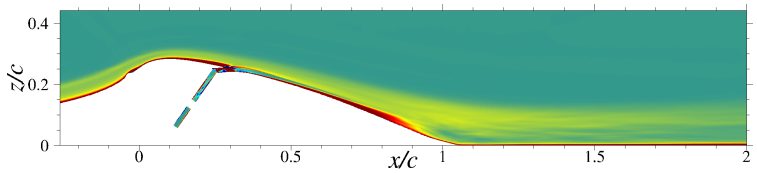

(c) Computations, full cavity HRLES

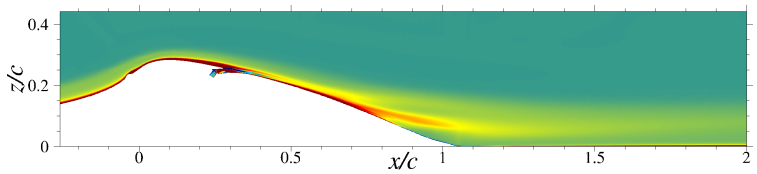

(d) Computations, BC URANS

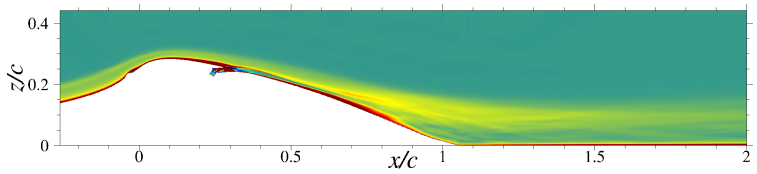

(e) Computations, BC HRLES

Figure 4.42: Controlled flow mean spanwise vorticity contours at the mid-plane

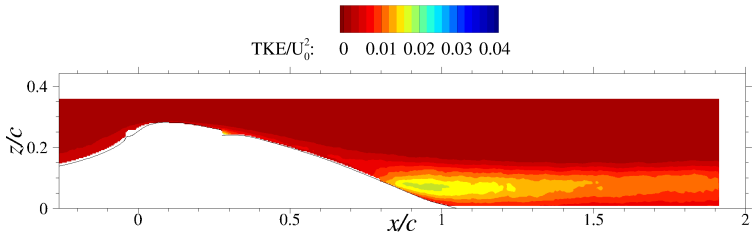

(a) Experiments

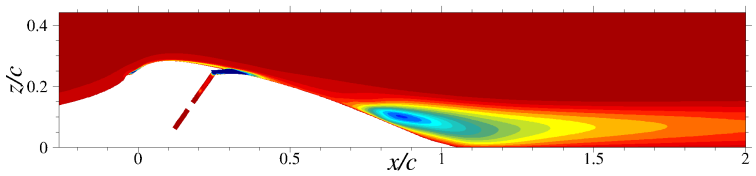

(b) Computations, full cavity URANS

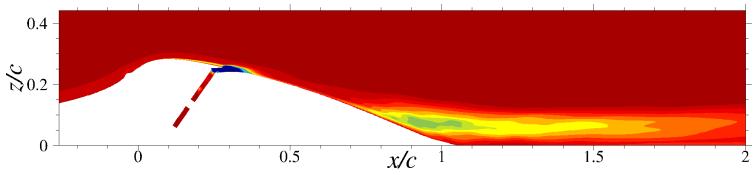

(c) Computations, full cavity HRLES

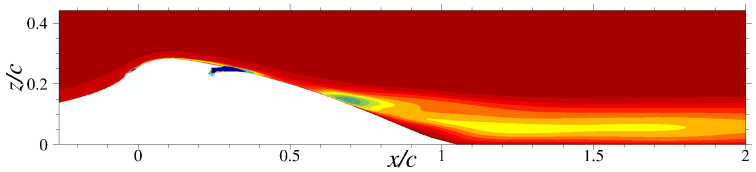

(d) Computations, BC URANS

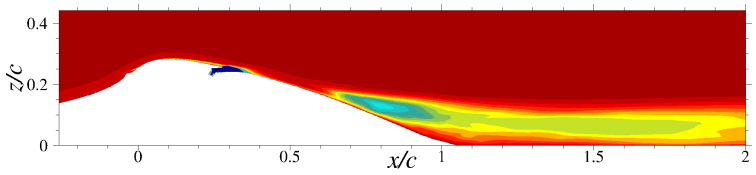

(e) Computations, BC HRLES

Figure 4.43: Controlled flow mean in-plane TKE ($\overline{u'^2 + w'^2}/2$) contours at the mid-plane

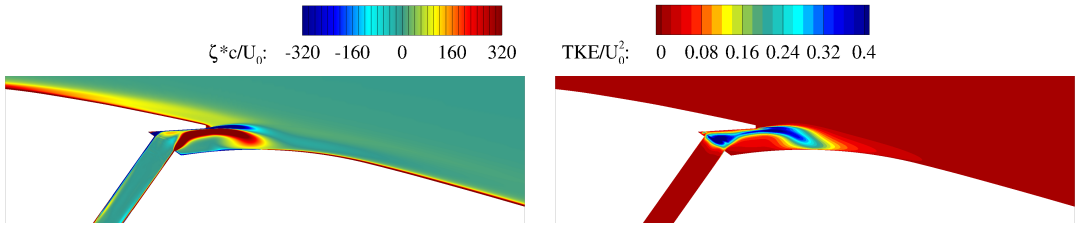

(a) Vorticity contours, full cavity URANS

(b) TKE contours, full cavity URANS

(c) Vorticity contours, full cavity HRLES

(d) TKE contours, full cavity HRLES

(e) Vorticity contours, BC URANS

(f) TKE contours, BC URANS

(g) Vorticity contours, BC HRLES

(h) TKE contours, BC HRLES

Figure 4.44: Controlled flow time-averaged spanwise vorticity and in-plane TKE ($\overline{u'^2 + w'^2}/2$) contours, close view of the overhang

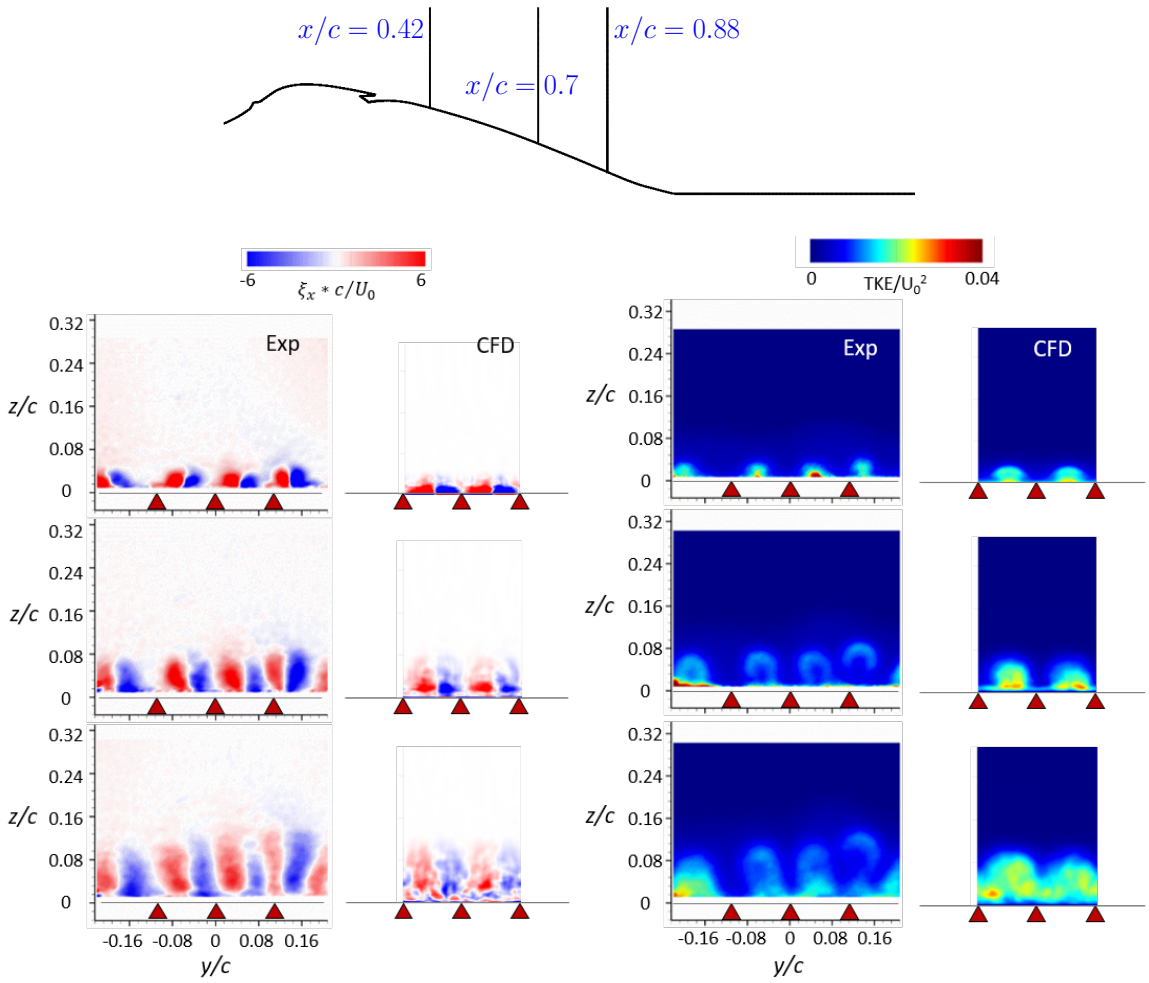

(a) Time-averaged streamwise vorticity contours (b) Time-averaged TKE contours

Figure 4.45: Actuated flow comparison between computation (full cavity HRLES) and experiments at three spanwise planes downstream of the jets: $x/c = 0.42$ (top), $x/c = 0.7$ (middle), $x/c = 0.88$ (bottom)

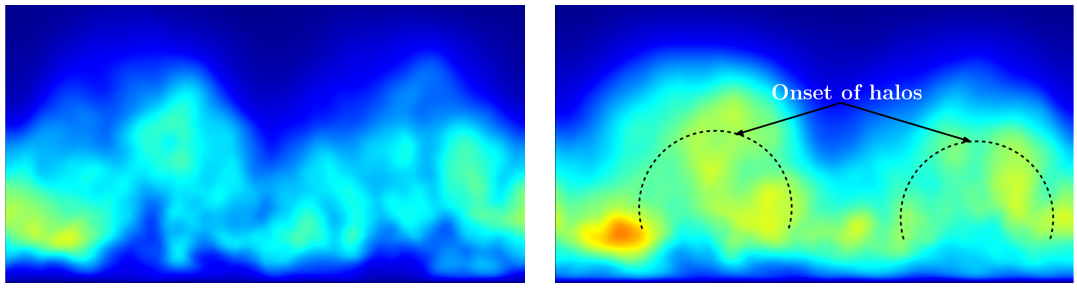

(a) Averaged over 57 cycles (b) Averaged over 136 cycles

Figure 4.46: Effect of time-averaging duration on TKE contours at $x/c = 0.88$, full cavity HRLES

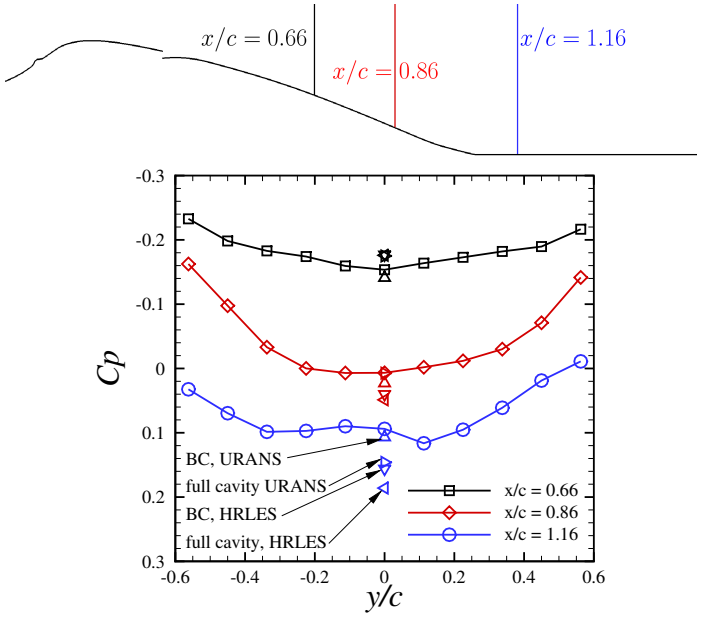

Figure 4.47: Actuated flow experimental spanwise variation of the pressure coefficient

coefficient at three different streamwise location and the computational results. It is clear that the flow is not nominally two-dimensional. While the magnitude of the variations due to the different computational approaches is comparable to the experimental spanwise variation (100% change at $x/c = 1.16$), directions of the variations are opposite. At $x/c = 1.16$, the pressure coefficient decreases away from the centerline experimentally, the boundary condition with URANS matches the experimental value at the centerline, and other computational approaches result in higher pressure coefficients. Since pressure waves propagate at the speed of sound, the pressure distribution at the center plane is easily influenced by the behavior at other spanwise locations. The instantaneous pressure distributions exhibit large fluctuations about the time-averaged value, as illustrated in Fig. 4.48. These pressure fluctuations were taken at the mid spanwise plane of the computational domain, in line with the center of the middle jet. The amplitude of the fluctuations are lower with URANS compared to HRLES due to the dissipative nature of URANS, and they are an order of magnitude larger than the difference in mean values.

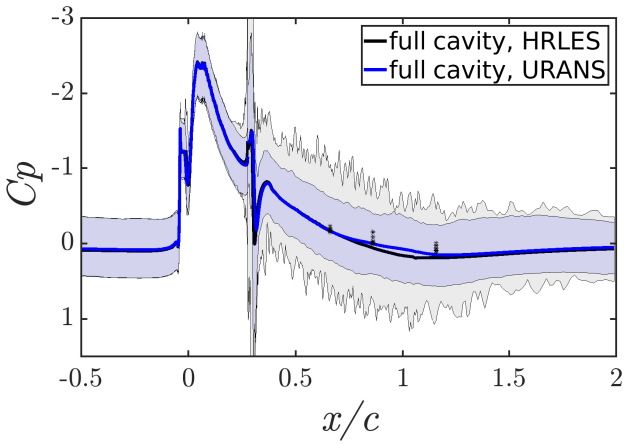

Figure 4.48: Controlled flow pressure coefficient fluctuation in full cavity simulations. Shaded area: region between minimum and maximum values; Solid and dashed lines: time average; Symbols: all experimental values along span.

An important factor influencing the TKE contours from a computational standpoint is the duration of the time-averaging process. Indeed, there are significant differences between averaging over 57 cycles of jet oscillation or 136 cycles (Fig. 4.46). The TKE takes a longer time to converge with the HRLES closure, as smaller scale structures (small spatial and time scale) are resolved. Figure 4.49 is a comparison of streamwise vorticity and TKE for URANS and HRLES at different planes. Shadows of the large-scale structures appear between the jets in the time-averaged TKE with URANS, though the levels (Fig. 4.49b) are higher than expected, and there is significant spanwise variation. The streamwise vorticity contours are also smoother with URANS than HRLES, as can be expected. The challenge in the present simulations stem from the difference in scales between the jets and the outer flow they interact with. A significantly longer time-average duration would be computationally prohibitive. Averaging over 136 cycles already requires more than $100,000$ CPU hours. It is shown later (section 4.6.9), that stronger flow structures are reflected in the time-average with HRLES for a similar averaging duration as the results discussed here. What is captured in the TKE contours is therefore a function of the dynamics of the flow structures.

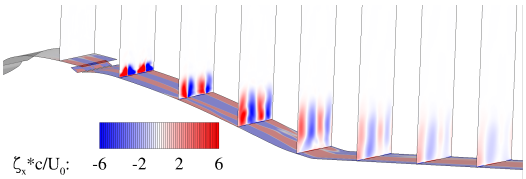

(a) Streamwise vorticity contours, full cavity URANS

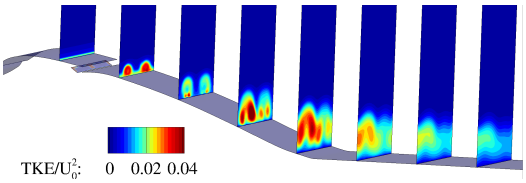

(b) TKE contours, full cavity URANS

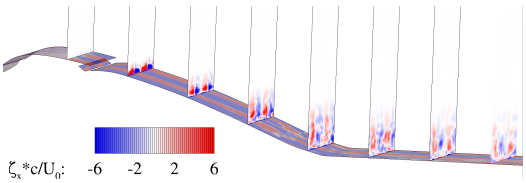

(c) Streamwise vorticity contours, full cavity HRLES

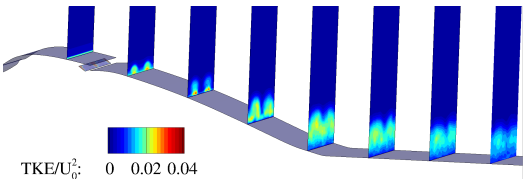

(d) TKE contours, full cavity HRLES

Figure 4.49: Controlled flow time-averaged streamwise vorticity and TKE ($\overline{(u'^2 + v'^2 + w'^2}/2$) contours

The character of the instantaneous streamwise vorticity contours (Fig. 4.50) is very different from the time-averaged flow, as many vortices of opposite directions interact in the flowfield. When more of these structures are resolved, a longer time-averaging duration must be be utilized to converge the second-order statistics. Furthermore, as discussed in section 4.5.1, the instantaneous flow provides many insights into the physics that can not be obtained by only inspecting the time-averaged flowfield.

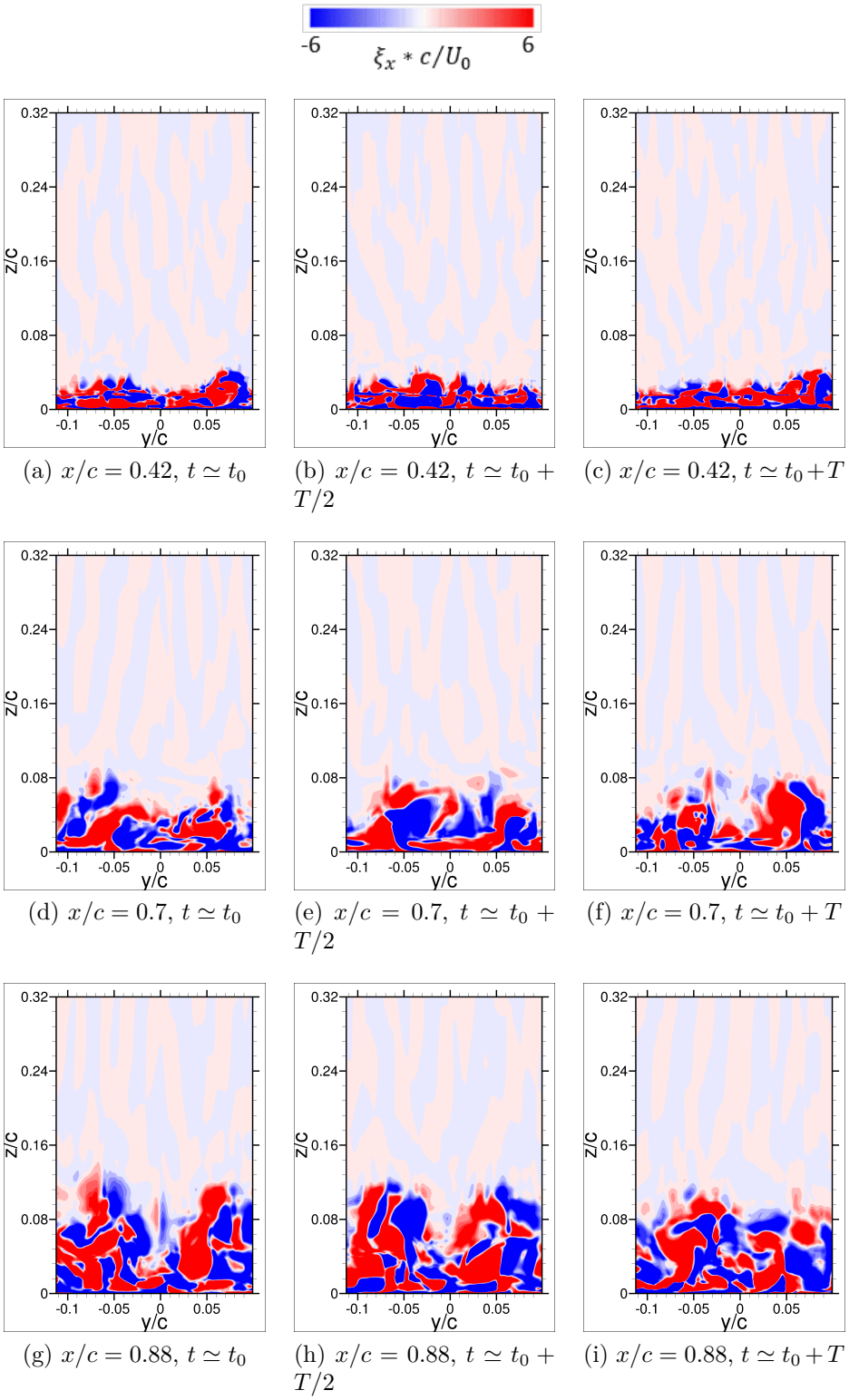

(a) $x/c = 0.42$, $t \simeq t_0$ (b) $x/c = 0.42$, $t \simeq t_0 + T/2$ (c) $x/c = 0.42$, $t \simeq t_0 + T$

(d) $x/c = 0.7$, $t \simeq t_0$ (e) $x/c = 0.7$, $t \simeq t_0 + T/2$ (f) $x/c = 0.7$, $t \simeq t_0 + T$

(g) $x/c = 0.88$, $t \simeq t_0$ (h) $x/c = 0.88$, $t \simeq t_0 + T/2$ (i) $x/c = 0.88$, $t \simeq t_0 + T$

Figure 4.50: Actuated flow instantaneous streamwise vorticity (full cavity HRLES) at three spanwise planes downstream of the jets: $x/c = 0.42$ (top), $x/c = 0.7$ (middle), $x/c = 0.88$ (bottom). See Fig. 4.45 for the illustration of the plane locations and jet locations.

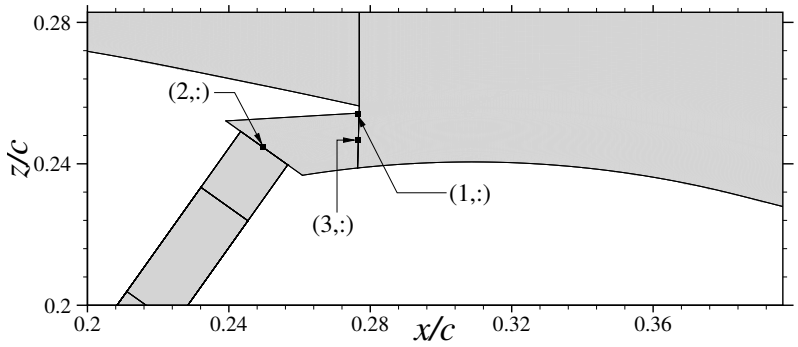

(a) $x - z$ plane

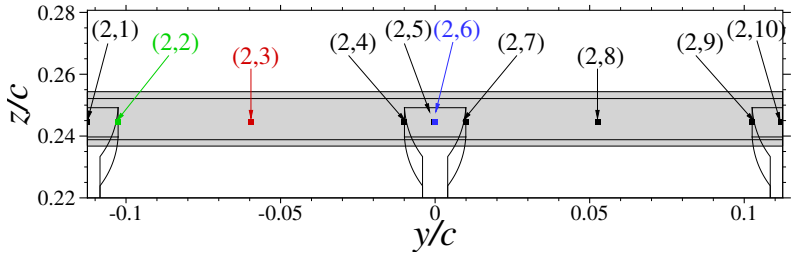

(b) $y - z$ plane

Figure 4.51: Illustration of the points where the instantaneous solution was collected

4.5.3 Temporal characteristics of the fluidic oscillators in the controlled flow

To complete the description of the actuated flow, time histories of the velocity at multiple points are presented, as well as their frequency spectra. Figure 4.51 illustrates the points near the overhang where data were collected at every iteration of the full cavity HRLES simulation over approximately 68 jet oscillation cycles (10.4 milliseconds). The points are identified with two coordinates, where the first coordinate is the streamwise location (right below the overhang, at the jet orifice and halfway between the overhang and the lower surface), and the second coordinate is the spanwise location.

Figures 4.52 and 4.53 depict the spanwise velocity and spectra of the velocity magnitude fluctuations. The spanwise velocities downstream of the jet centers clearly exhibit oscillation at 6.6 kHz, which is 4% higher than the value obtained in a quiescent ambient. This corresponds to a non-dimensional excitation frequency

$F^+ = \frac{\tilde{f}\tilde{c}}{\tilde{U}_\infty} \simeq 4.9$. The second harmonic is also clearly captured at several locations. The negative 5/3 slope is captured in the spectra between 3 kHz and 100 kHz near jet centers. The jets operate in phase, as there is not significant phase lag seen in Fig. 4.52 a, c and e. As discussed in section 4.4.2, this is enforced by the spanwise periodicity, and the boundary condition model is later leveraged to evaluate a 180° phase difference (section 4.6.2). The flow between the jets in the spanwise direction is characterized by extreme events, that do not exhibit a specific frequency. As a result, the spanwise velocity shows no specific periodicity (red curves in Fig. 4.52 b, d and f).

The computational spectra exhibit an additional high frequency peak at 125 kHz. According the spanwise velocity time histories, this high frequency peak corresponds to instantaneous spanwise oscillations of the jet in addition to the sweeping motion. Lakebrink et al. [63] also reported a frequency peak at 200 kHz in their computations of a fluidic oscillator. There is currently no experimental data to validate this peak. After inspection of several other points (including in the actuator cavity) collected at every 20 iteration, only the oscillator nozzle and overhang region are affected by this high-frequency peak. While the computational temporal resolution (3.6 MHz) is high enough to capture such a high peak, the observed behavior is similar to a spurious TKE pile-up near the LES cutoff frequency, as reported by multiple authors [135, 136]. Potential remedies include the application of a high-order filter to the numerical solution [137] and variations in the dissipation properties of the LES closure [136]. These are not explored here, as the high frequency peak is dissipated downstream of the overhang, and it is not expected to be a significant driver of the computational accuracy.

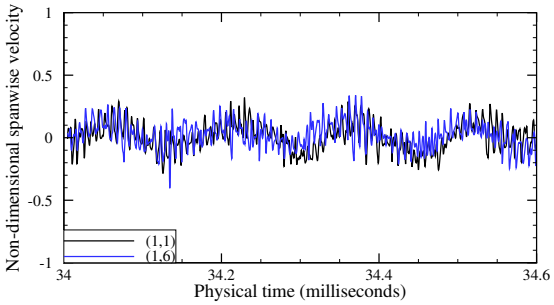

(a) Near the overhang, comparison between jet centers

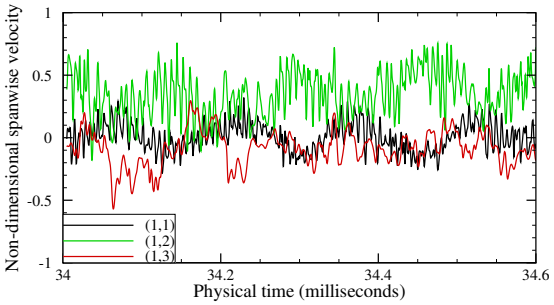

(b) Near the overhang, comparison between different spanwise locations

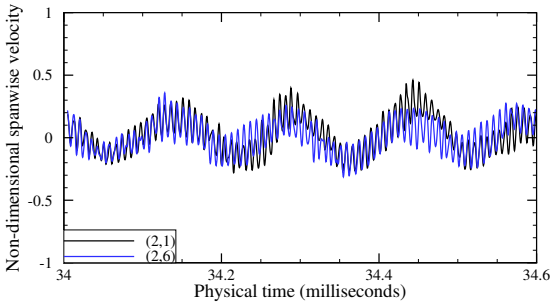

(c) Actuator exit, comparison between jet centers

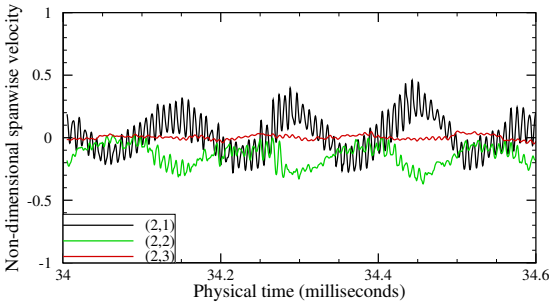

(d) Actuator exit, comparison between different spanwise locations

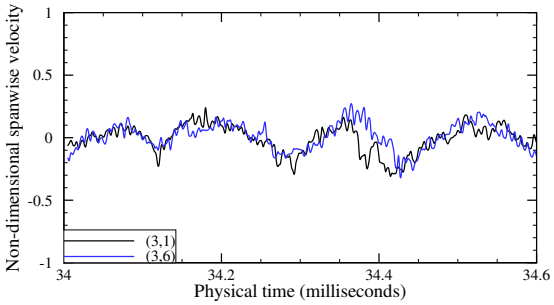

(e) Halfway between the lower surface and the overhang, comparison between jet centers

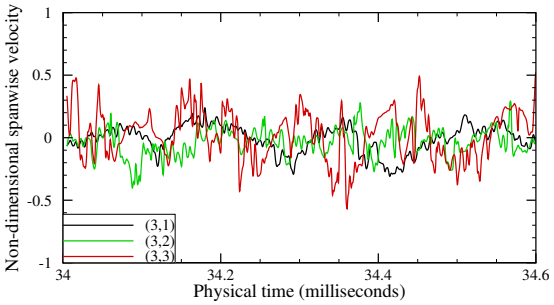

(f) Halfway between the lower surface and the overhang, comparison between different spanwise locations

Figure 4.52: Instantaneous spanwise velocity at different points in the controlled flow field: comparisons between the centers of two different jets (left), comparison between different spanwise locations (right)

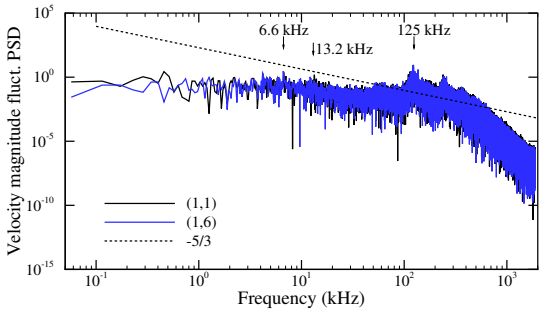

(a) Near the overhang, comparison between jet centers

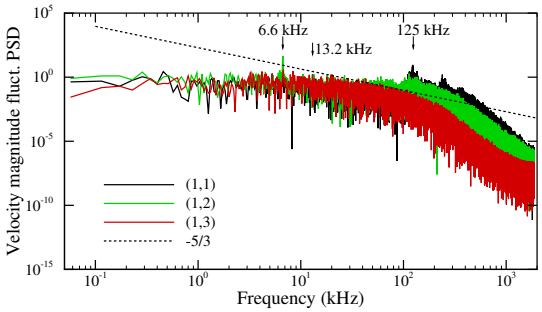

(b) Near the overhang, comparison between different spanwise locations

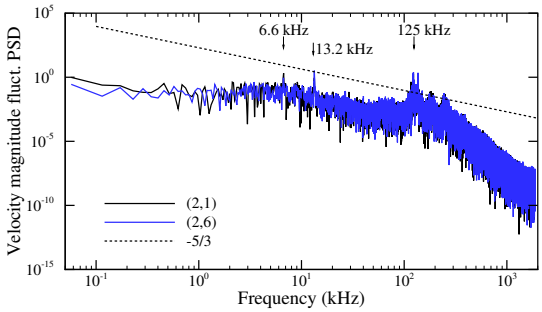

(c) Actuator exit, comparison between jet centers

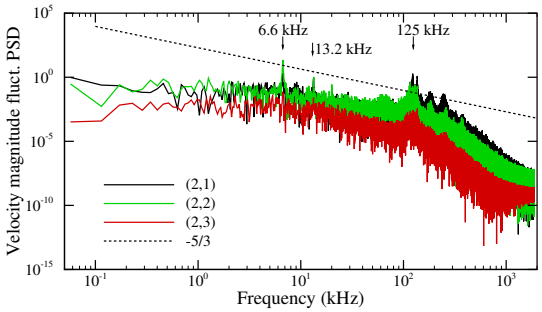

(d) Actuator exit, comparison between different spanwise locations

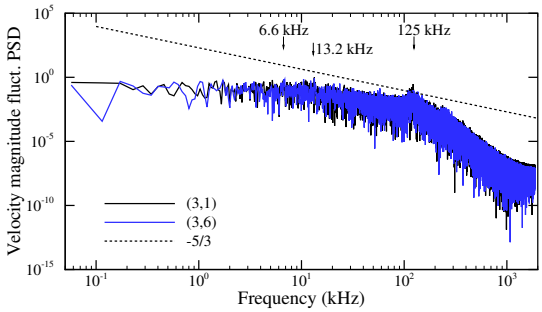

(e) Halfway between the lower surface and the overhang, comparison between jet centers

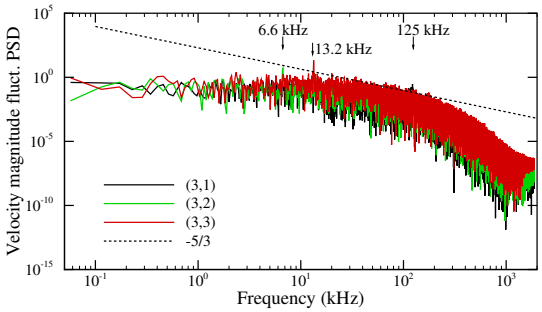

(f) Halfway between the lower surface and the overhang, comparison between different spanwise locations

Figure 4.53: Power spectral density of the velocity magnitude fluctuations at multiple points in the controlled flow field, based on 10.4 milliseconds of recorded data: comparisons between the centers of two different jets (left), comparison between different spanwise locations (right)

4.6 Variations on the computational methodology and jet configuration for the actuated flow

Multiple variations on the initial computations were performed to assess sensitivities to the computational methodologies and acquire a deeper understanding of the physics of the flow actuation.

4.6.1 Effect of grid refinement

The grid refinement study proposed in section 4.1 was limited to the base flow, 2D grids and the URANS turbulence closure. For the actuated flow, the sensitivity of the HRLES solution to the grid resolution was assessed by doubling the number of cells in the streamwise and wall-normal direction for the wind tunnel domains (outer flow). To maintain one-to-one interfaces with the actuators, the number of cells across the depth of the fluidic oscillators was also doubled. The resulting grid had 126.5 million cells, while the initial grid had 42.8 million cells. The actuator cavity was fully resolved in this analysis, and the HRLES turbulence closure was employed.

The resulting pressure coefficient distribution is presented in Fig. 4.54, along with the initial computation results. The differences between the pressure coefficient distributions are very small, with differences lower than 0.05 on Cp, indicating that the wall-normal grid resolution is adequate.

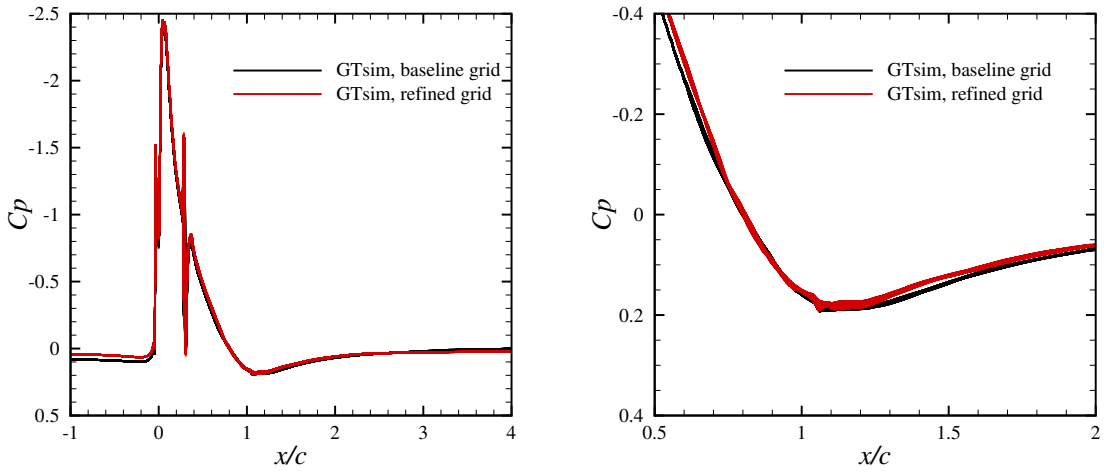

(a) Overview

(b) Close view

Figure 4.54: Controlled flow time-averaged pressure coefficient distribution over the curved surface: effect of wall-normal grid refinement, full cavity HRLES

4.6.2 Effect of the phase

The fluidic oscillators were synchronized in the initial computations, either with a spanwise periodic boundary condition or in the formulation of the sweeping jet model. Since there is no expectation of the jets being in phase in the experiments, the jets were modeled as out of phase with the jet boundary condition model and the HRLES turbulence closure.

Figure 4.55 compares the pressure coefficient distribution obtained when the jets are in phase or out of phase. The maximum difference in the pressure distributions is 0.026. Though this corresponds to a 16% relative local error, as the pressure coefficient is close to zero, it is a small difference compared to the entire range of pressure coefficient values (suction peak at -2.5). There are more important drivers of the flow control effectiveness than the phase. This conclusion is consistent with the observations of Aram et al. [70], where varying the phase (0°, 60°, 180°) in their computations only resulted in a few percent difference in pressure coefficient distributions over the NASA wall-mounted hump.

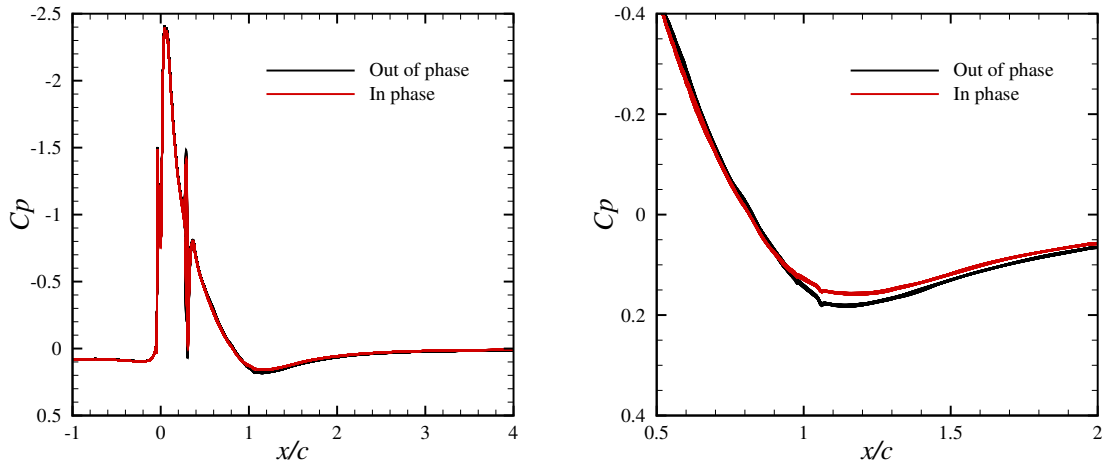

(a) Overview (b) Close view

Figure 4.55: Controlled flow time-averaged pressure coefficient distribution over the curved surface: effect of the phase between the jets, BC HRLES

4.6.3 Effect of the triple deck in the blending function

As previously discussed (section 4.5.1), the hybrid RANS/LES blending function exhibits a triple deck downstream of the actuators, which could potentially affect the accuracy of the solution in regions where the switch occurs. An evaluation was therefore performed by setting the blending function to 0 (LES) downstream of the overhang in a full cavity HRLES simulation, so that the outer shear layer is entirely resolved with LES. Figure 4.56 illustrates the blending function thereby obtained, confirming that URANS was not present downstream of the jets.

Figure 4.57 compares of the pressure coefficient distributions obtained with and without the triple deck in the blending function downstream of the overhang. The change in the blending function has very little effect on the pressure coefficient. Furthermore, the TKE contours (Fig. 4.58) still indicate significant spanwise mixing, rather than clear coherent structures, similar to the results obtained with the initial blending function. This analysis demonstrates that the triple deck in the blending function does not have adverse effects on the ability to resolve the flow structures.

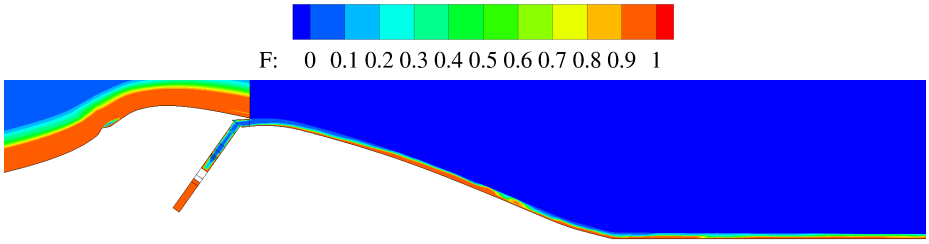

(a) Actuator center ($y/c \simeq 0$)

(b) Between actuators ($y/c \simeq 0.05625$)

Figure 4.56: Instantaneous HRLES blending function 0 (LES) $\leq F \leq 1$ (RANS) for the simulation of the curved surface and two fluidic oscillators, full cavity HRLES, modified blending function: $\mathcal{F} = 0$ above the lower boundary layer ($k \geq 108$ downstream of the overhang)

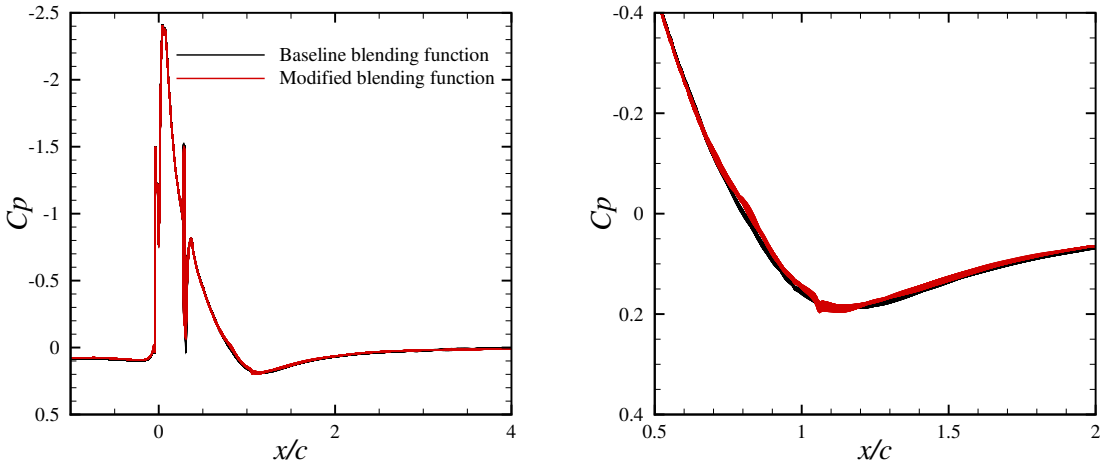

(a) Overview

(b) Close view

Figure 4.57: Controlled flow time-averaged pressure coefficient distribution over the curved surface: effect of the triple deck in the hybrid RANS/LES blending function

4.6.4 Effect of downstream velocity recovery

As discussed in section 4.5.2, the experimental velocity outside the boundary layers downstream of the model is 10% higher than the estimated freestream velocity. The

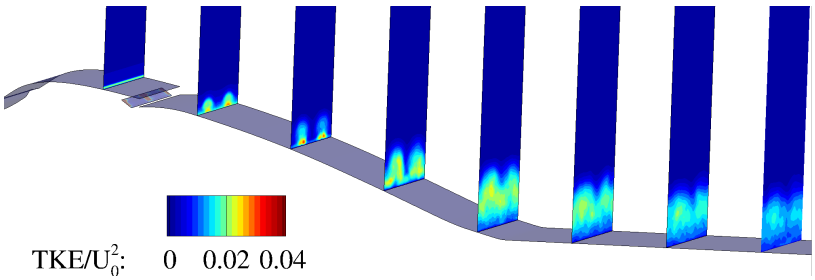

(a) Baseline blending function

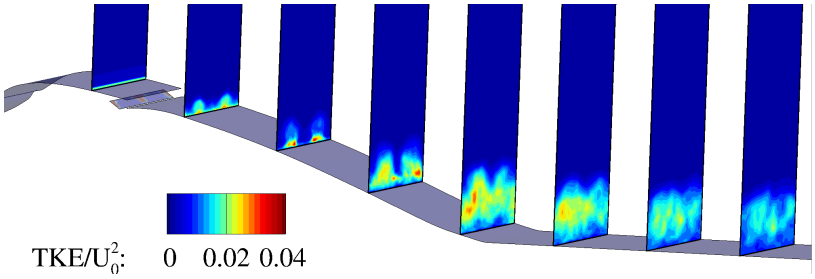

(b) $\mathcal{F} = 0$ above the lower boundary layer ($k \geq 108$ downstream of the overhang)

Figure 4.58: Controlled flow time-averaged TKE ($\overline{u'^2 + v'^2 + w'^2}/2$) contours: effect of the blending function

computational freestream velocity was increased by 10% to evaluate the effect on the solution. Of course, this approach introduces a constant offset of the freestream velocity, while a blockage from the wind tunnel walls would increase the velocity non-linearly. This analysis relies on the full cavity HRLES computational approach.

Figure 4.59 illustrates the velocity profiles obtained with the initial computations and the experimental data. With the modified freestream velocity, the computational velocity outside the boundary layer downstream of $x/c = 0.8$ matches the experimental value. This was the desired effect of increasing the freestream velocity. A side effect of this is that the velocity is also increased upstream of the model. A a result, the velocity at the edge of the boundary layer is now overestimated at $x/c = 0$. This is not unexpected, as blockage effects would introduce an increase in velocity that is not constant.

An interesting result obtained by increasing the freestream velocity is the appearance of loop features in the TKE contours ($x/c = 0.8$ in Fig. 4.60) with only 57 jet

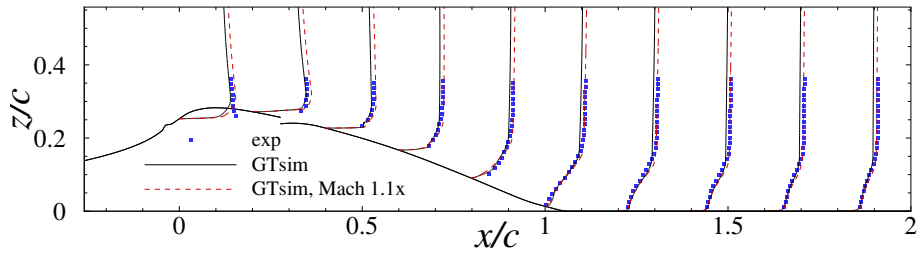

(a) Overview ($x/c = 0, 0.2, 0.4, 0.6, 0.8, 1.0, 1.2, 1.4, 1.6, 1.8$)

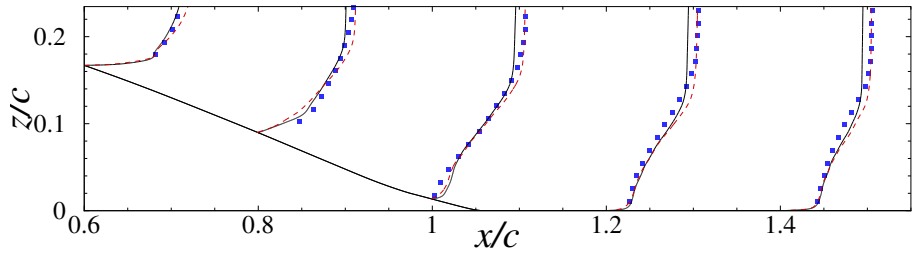

(b) Close view ($x/c = 0.6, 0.8, 1.0, 1.2, 1.4$)

Figure 4.59: Controlled flow time-averaged streamwise velocity profiles ($x_0 + \frac{0.1u}{U_0}$) at different streamwise locations: effect of downstream velocity recovery.

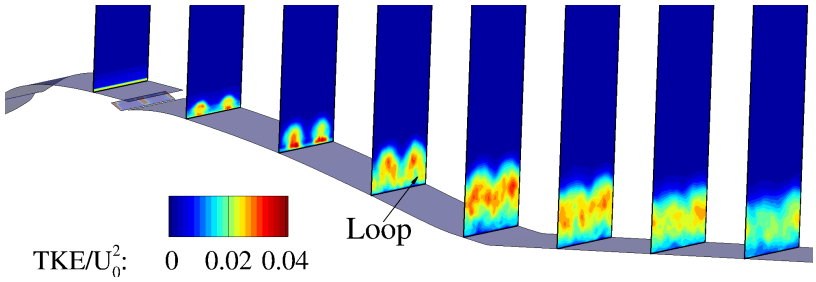

Figure 4.60: Controlled flow time-averaged streamwise TKE at different streamwise planes ($x/c = 0.2, 0.4, 0.6, 0.8, 1.0, 1.2, 1.4, 1.6$): effect of downstream velocity recovery.

oscillation cycles. This provides further evidence that part of the spanwise variations observed in the experimental stereo PIV are due to local changes in the jet intensities compared to the outer flow (Fig. 4.45).

4.6.5 Boundary condition applied at the actuator exit

In a quiescent ambient (Chapter 3), the phase-averaged boundary condition at the actuator exit lack details of the turbulent fluctuations. The boundary condition was therefore first specified at the throat to evaluate its accuracy for a flow control

application. The phase-averaged model of the fluidic oscillators was then evaluated at the exit of the device considered to be the outer mold line (Fig. 4.29). The turbulence is resolved with HRLES, and the boundary condition model includes the modeled turbulence.

Figure 4.61 is a comparison of pressure coefficient distributions between the previously discussed phase-averaged boundary condition at the actuator throat and a boundary condition applied at the actuator exit. The maximum difference in pressure coefficient is 0.05 at the airfoil trailing edge. As with the effect of the phase, this difference is considered small compared to the relevant physics.

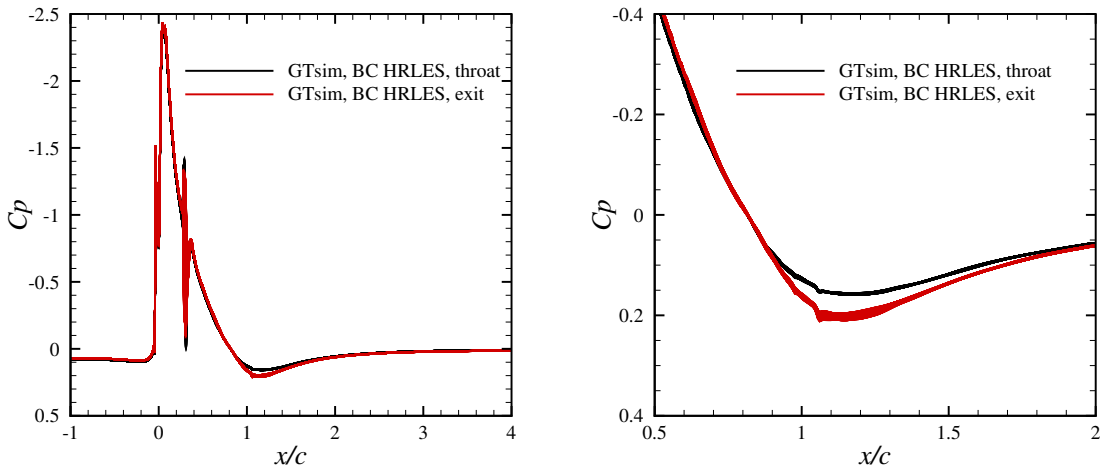

(a) Overview

(b) Close view

Figure 4.61: Controlled flow time-averaged pressure coefficient distribution over the curved surface: effect of moving the boundary condition from the throat to the exit, BC HRLES

4.6.6 Effect of modeled turbulence in the boundary condition formulation

The boundary condition model of the actuators was evaluated with URANS, where the turbulence is omitted from the formulation. Instead, a Neumann boundary condition is set in the turbulence equations (see BC3 in section 3.7).

Figure 4.62 is a comparison of the resulting pressure coefficient distribution with a formulation including the modeled turbulence and experimental data. The omission of the modeled turbulence in URANS introduces a 0.05 difference in the pressure distributions, which is similar to the differences observed by moving the boundary condition from the inner mold line to the outer mold line with the HRLES closure. Therefore, the same conclusions apply: the effect of the modeled turbulence is small compared to the relevant physics of separation control via an overhang.

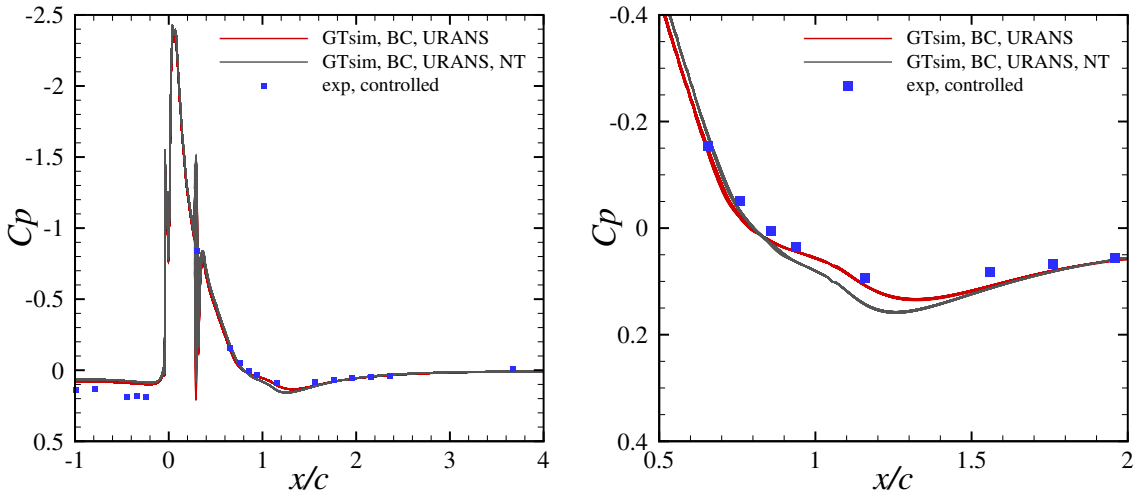

(a) Overview

(b) Close view

Figure 4.62: Controlled flow time-averaged pressure coefficient distribution over the curved surface: with modeled turbulence (red), without modeled turbulence (gray)

4.6.7 Effect of domain spanwise width

The sensitivity to the spanwise periodic boundary conditions is assessed by doubling the spanwise width of the computational domain, while maintaining the same spacing between jets, thereby doubling the number of actuators evaluated. In this evaluation, the full cavities of the four fluidic oscillators are resolved and the HRLES closure employed. As a result, the grid size doubled (from 42.8 to 85.6 million cells), with 33 computational blocks instead of 21.

Figure 4.63 is a comparison of the time-averaged pressure coefficient distributions between the 14 mm and 28 mm domains. The maximum difference between the pressure coefficients is only 0.02. The vorticity dynamics (Fig. 4.64) and vorticity and TKE (Fig. 4.65) comparisons also indicate that the solution is not significantly sensitive to the spanwise width.

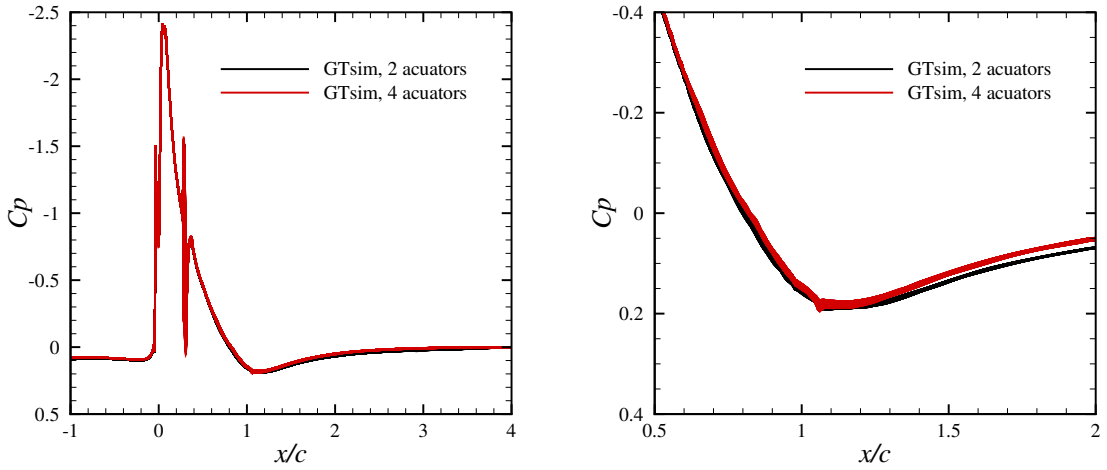

(a) Overview

(b) Close view

Figure 4.63: Controlled flow time-averaged pressure coefficient distribution over the curved surface: effect of domain spanwise width, full cavity HRLES

4.6.8 Effect of jet spacing

The effect of jet spacing on the flow control effectiveness is now considered. In this assessment, the spanwise width of the computational domain were maintained, while the number of jets was halved or doubled. In the former case, only one actuator remains, and it was fully resolved. After removing the other actuator from the initial grid, the computational grid consists of 13 blocks and 39.3 million cells. In the latter case, the boundary condition formulation of the actuators was leveraged, as the corresponding internal cavity modification is not trivial. Shortening the supply channels to fit additional jets can have an unpredictable effect on the characteristics

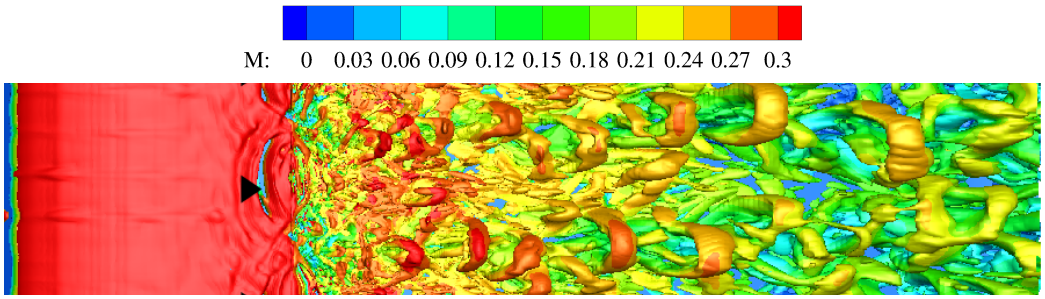

(a) Two actuators resolved (full cavity HRLES), spacing 7 mm

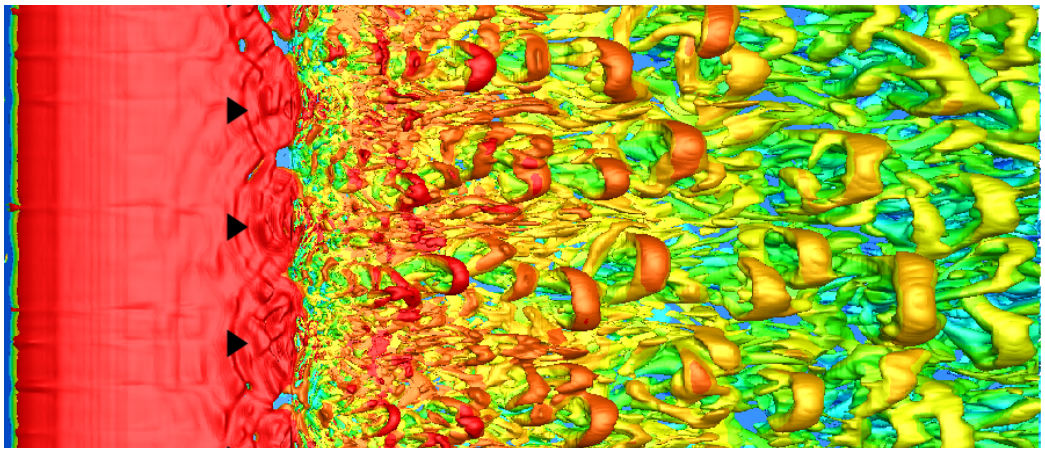

(b) Four actuators resolved (full cavity HRLES), spacing 7 mm

Figure 4.64: Iso-surfaces of the second invariant of the velocity gradient tensor ($Q = 1$) colored with values of local Mach number for the controlled flow over the wind-tunnel model, top view, $0 \leq x/c \leq 1$. The black triangles indicate the spanwise location of the actuators.

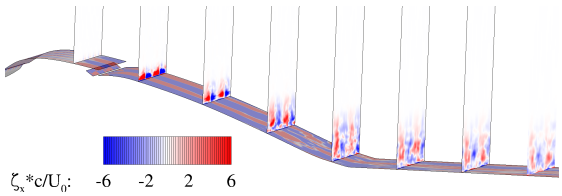

(a) Vorticity contours, 2 actuators

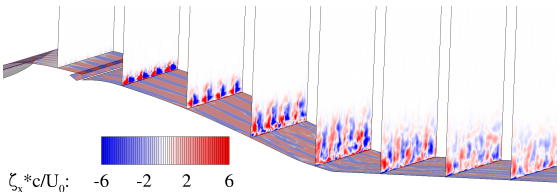

(b) Vorticity contours, 4 actuators

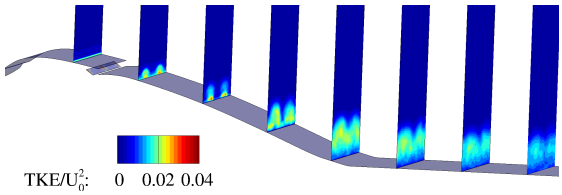

(c) TKE contours, 2 actuators

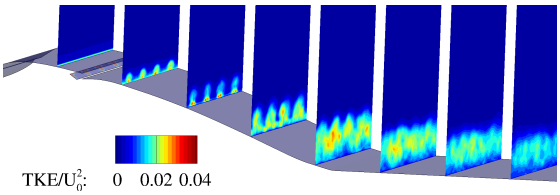

(d) TKE contours, 4 actuators

Figure 4.65: Controlled flow time-averaged streamwise vorticity and TKE at different streamwise planes ($x/c = 0.2, 0.4, 0.6, 0.8, 1.0, 1.2, 1.4, 1.6$): effect of domain spanwise width, full cavity HRLES

of each actuator. This test is nonetheless important, in order to fully understand the vorticity dynamics. The grid consists of 10 blocks and 70.9 million cells in the case where the distance between the jets was halved. The HRLES turbulence closure was employed to assess the effect of jet spacing. The momentum per jet remains unchanged.

Figure 4.66 is a comparison of the pressure distributions. The coefficient of pressure near $x/c = 1$ decreases with the spacing between the jets, indicating that the flow control is more effective. These variations in pressure coefficient (0.04 to 0.06) are relatively small, but the differences in the flow fields are not negligible.

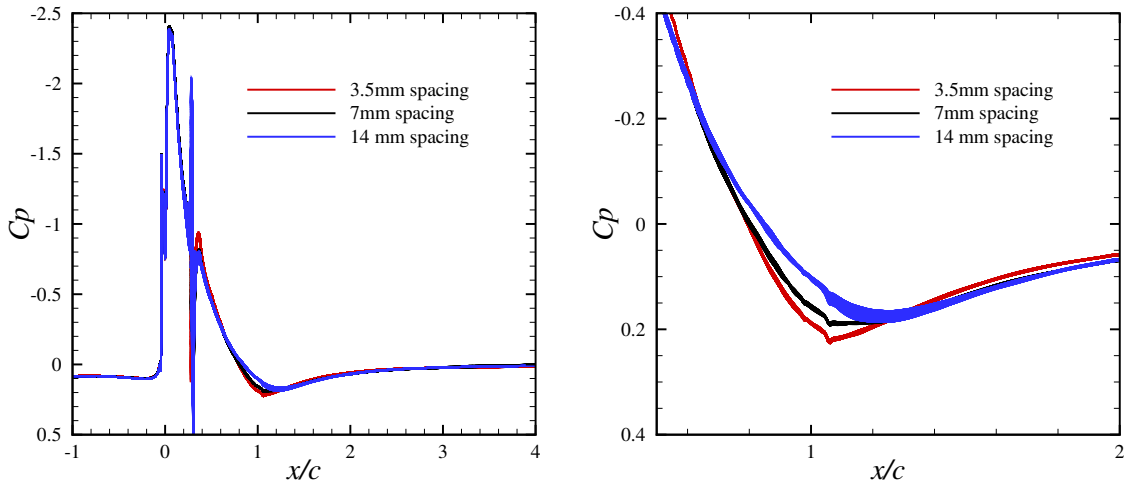

(a) Overview

(b) Close view

Figure 4.66: Controlled flow time-averaged pressure coefficient distribution over the curved surface: effect of jet spacing

Figures 4.67, 4.68 and 4.69 illustrate the flow structures for different actuator spacings. They depict the top, side and isometric views of the flow field, respectively. As the spacing between the jets decreases, the flow structures move closer to the wall. This is reflected in the time-averaged TKE (Fig. 4.70), where the layers of TKE concentration move closer to the wall. Furthermore, the TKE at downstream planes decreases with the jet spacing, consistent with an increased flow control effectiveness.

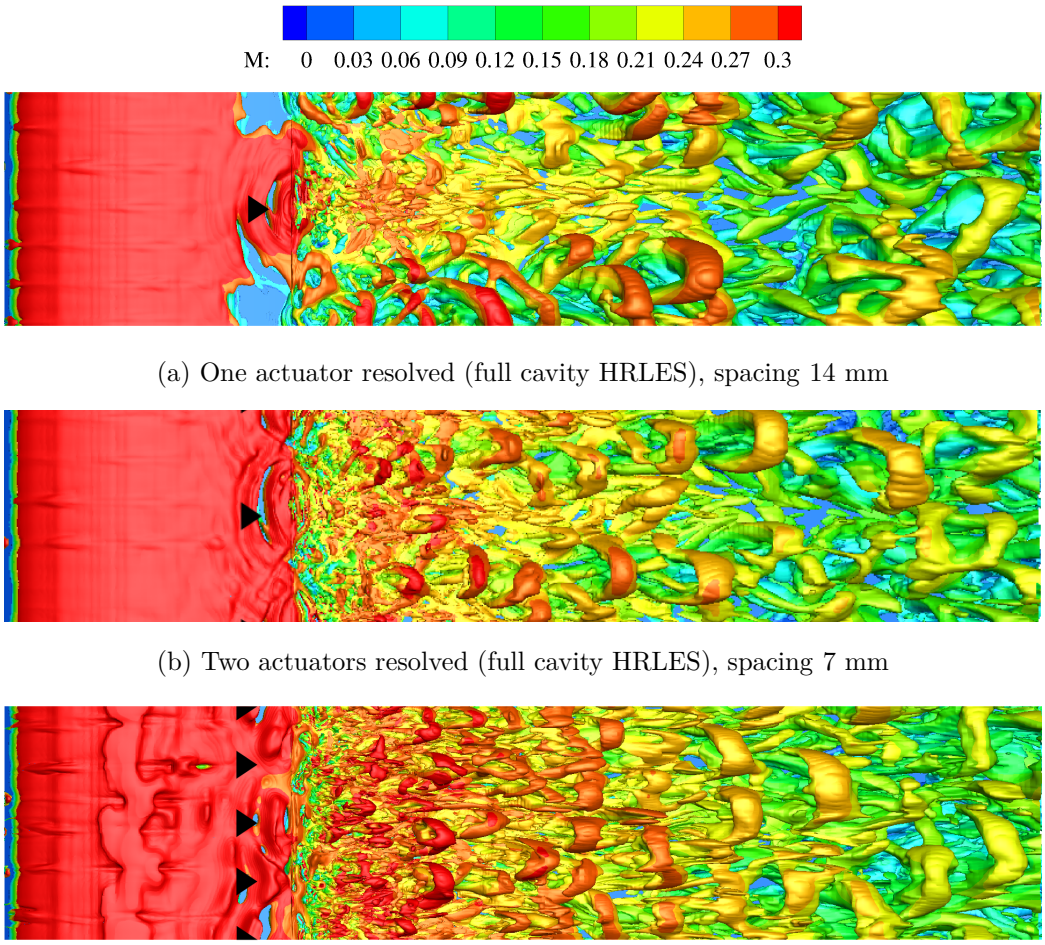

(a) One actuator resolved (full cavity HRLES), spacing 14 mm

(b) Two actuators resolved (full cavity HRLES), spacing 7 mm

(c) Four actuators resolved (BC HRLES), spacing 3.5 mm

Figure 4.67: Iso-surfaces of the second invariant of the velocity gradient tensor ($Q = 1$) colored with values of local Mach number for the controlled flow over the wind-tunnel model, top view, $0 \leq x/c \leq 1$: effect of jet spacing. The black triangles indicate the spanwise location of the actuators.

The spanwise character of the flow structures varies with the spacing. When the spacing is 14 mm or 28 mm, large-scale structures clearly develop between the jets, while the flow remains wall-bound in the line of action of the jets. A spacing of 28 mm is large enough that there is no direct interaction between neighboring jets, yet the upward motion of the jet is sufficient for large-scale structures to form. When the spacing is 3.5 mm, the flow is almost uniform spanwise. In that case, the jets actually merge before reaching the overhang (Fig. 4.69f), so a spanwise uniform jet

interacts with the overhang and the outer shear layer. This defines a lower limit on the spacing, as the jet oscillations become irrelevant when the spacing is that small, making the flow control less efficient. Quantitatively, the flow structures (Fig. 4.68) do not move as much towards the wall when the spacing is decreased from 7 mm to 3.5 mm compared to when the spacing is decreased from 14 mm to 7 mm (0.02 chords versus 0.04 chords at $x/c = 1$).

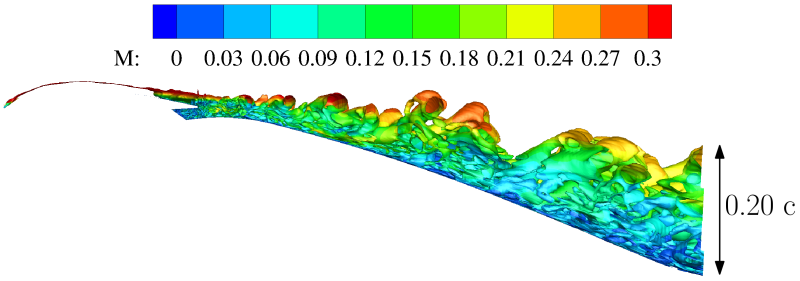

(a) One actuator resolved (full cavity HRLES), spacing 14 mm

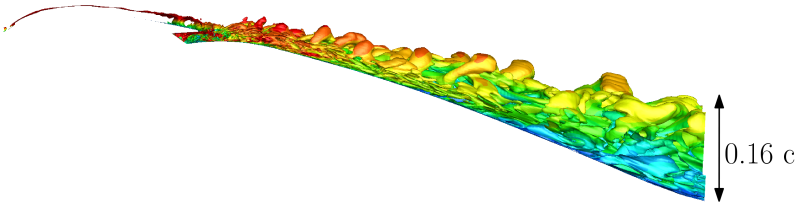

(b) Two actuators resolved (full cavity HRLES), spacing 7 mm

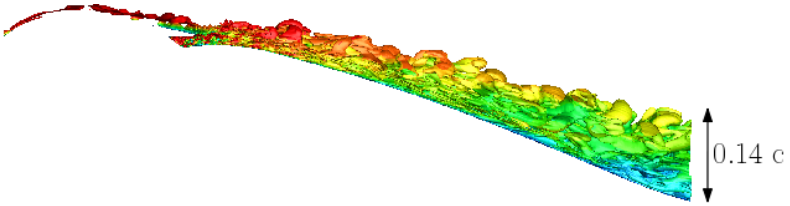

(c) Four actuators resolved (BC HRLES), spacing 3.5 mm

Figure 4.68: Iso-surfaces of the second invariant of the velocity gradient tensor ($Q = 1$) colored with values of local Mach number for the controlled flow over the wind-tunnel model, side view, $0 \leq x/c \leq 1$: effect of jet spacing.

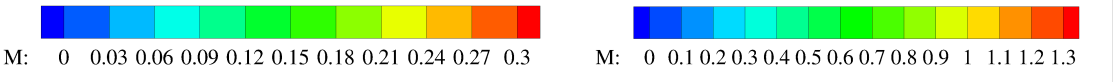

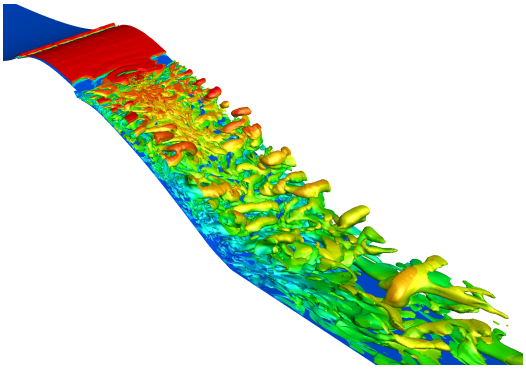

(a) One actuator resolved (full cavity HRLES), spacing 14 mm, $Q = 1$

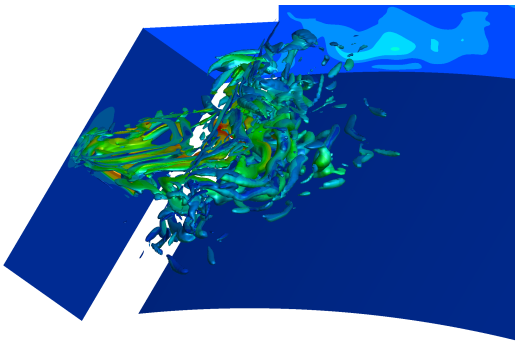

(b) One actuator resolved (full cavity HRLES), spacing 14 mm, $Q = 10000$

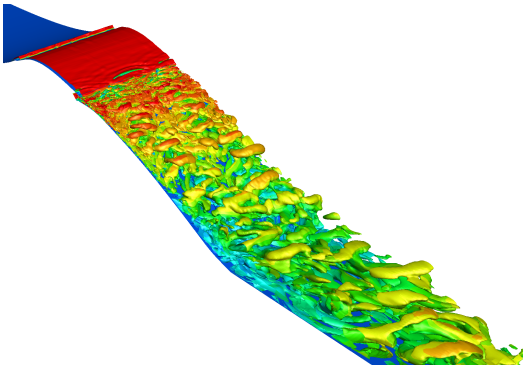

(c) Two actuators resolved (full cavity HRLES), spacing 7 mm, $Q = 1$

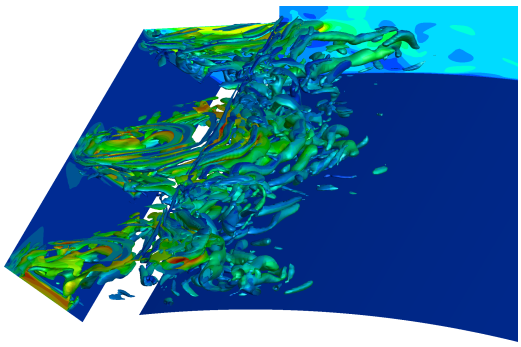

(d) Two actuators resolved (full cavity HRLES), spacing 7 mm, $Q = 10000$

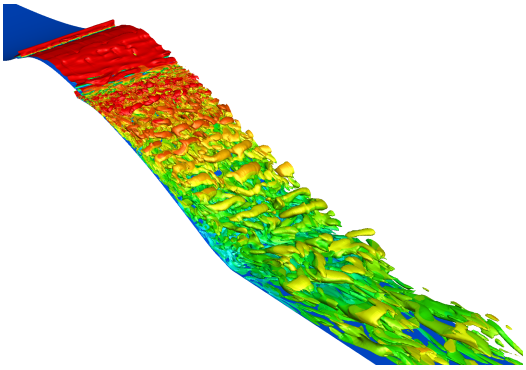

(e) Four actuators resolved (BC HRLES), spacing 3.5 mm, $Q = 1$

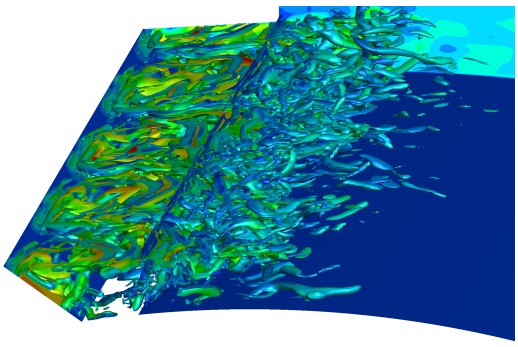

(f) Four actuators resolved (BC HRLES), spacing 3.5 mm, $Q = 10000$

Figure 4.69: Iso-surfaces of the second invariant of the velocity gradient tensor colored with values of local Mach number for the controlled flow over the wind-tunnel model, 3D views: effect of jet spacing.

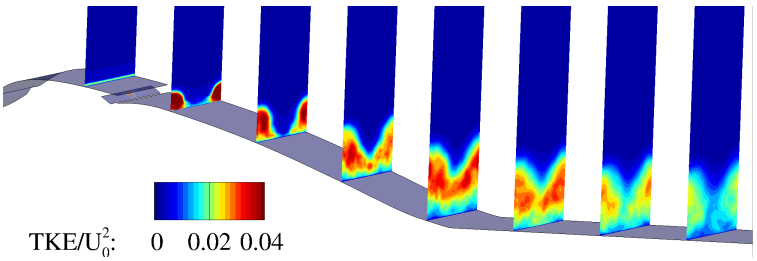

(a) One actuator resolved (full cavity HRLES), spacing 14 mm

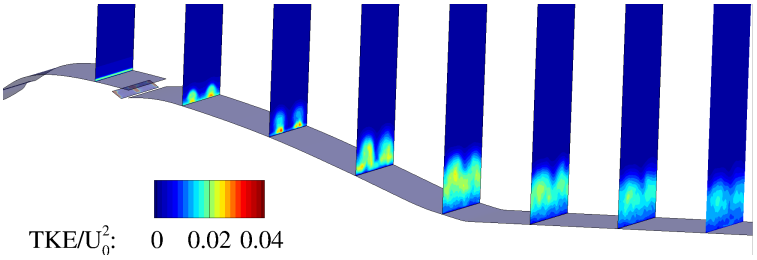

(b) Two actuators resolved (full cavity HRLES), spacing 7 mm

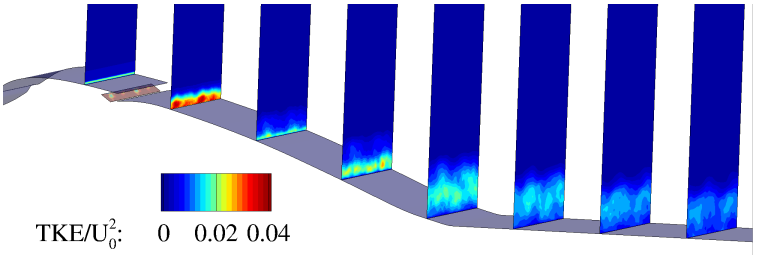

(c) Four actuators resolved (BC HRLES), spacing 3.5 mm

Figure 4.70: Actuated flow time-averaged TKE ($\overline{u'^2 + v'^2 + w'^2}/2$) contours at different streamwise planes ($x/c = 0.2, 0.4, 0.6, 0.8, 1.0, 1.2, 1.4, 1.6$): effect of jet spacing

4.6.9 Effect of the overhang

The effect of the overhang was evaluated by removing it from the computational domain, while keeping the baseline jet orientation of 54.6°. This provides some important insights to further understand the physics involved in sweeping jets. Figure 4.71 illustrates the modification of the computational domain that permitted this assessment of the effect of the overhang. The computations were performed with the HRLES turbulence closure, and a boundary condition model of the actuators was specified at the throat including the modeled turbulence.

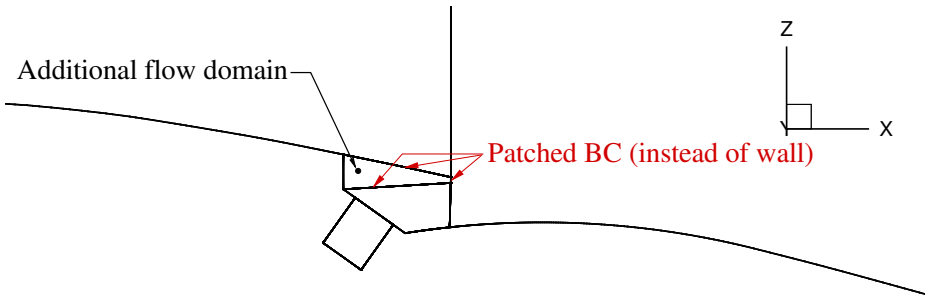

Figure 4.71: Illustration of the geometry modification to remove the overhang

Figure 4.72 is a comparison of the pressure coefficient distributions with and without the overhang. The maximum difference in the pressure coefficient is 0.15, and this occurs at the airfoil trailing edge. The removal of the overhang has a higher impact than the phase (section 4.6.2), modeled turbulence (section 4.6.5) and boundary condition model application location (section 4.6.6).

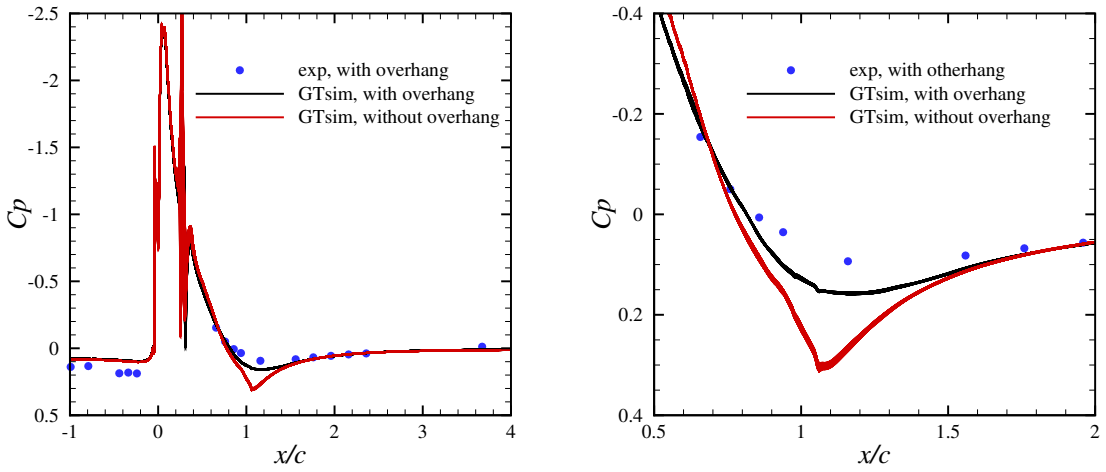

(a) Overview

(b) Close view

Figure 4.72: Actuated flow time-averaged pressure coefficient distribution over the curved surface: effect of removing the overhang

Figure 4.73 depicts of the instantaneous flow fields obtained with and without the overhang. Without the overhang, the jets (with an orientation of 54.6° with respect to the horizontal) behave like jets in crossflow [138]. Large scale structures are centered around the jets rather than between them, as observed with the overhang.

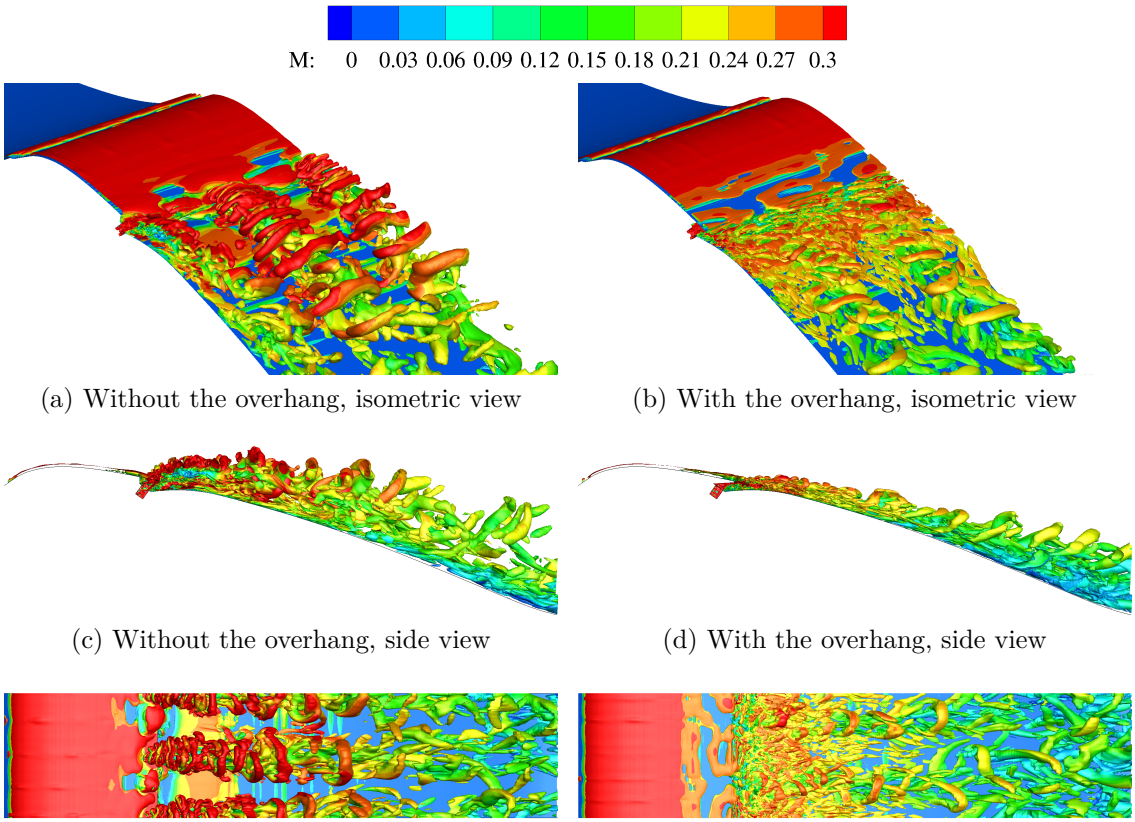

(a) Without the overhang, isometric view

(b) With the overhang, isometric view

(c) Without the overhang, side view

(d) With the overhang, side view

(e) Without the overhang, top view, $0 \leq x/c \leq 1$

(f) With the overhang, top view, $0 \leq x/c \leq 1$

Figure 4.73: Iso-surfaces of the second invariant of the velocity gradient tensor ($Q = 10$) colored with values of local Mach number for the controlled flow over the wind-tunnel model, BC HRLES

Furthermore, the flow remains attached between the jets. This is a completely different flow control mechanism than what has been studied up to this point. The jets do not interact with one another, as the overhang is no longer present to spread them early on in the spanwise direction. Further investigation of multiple instantaneous flow fields indicates that vortical structures between the jets, similar to the ones observed with the overhang, are still generated, but they rapidly merge into the large structures centered around the jets. Therefore, when the jets are free into the crossflow, they generate strong streamwise vortices that attach the flow between the jets (down-welling).

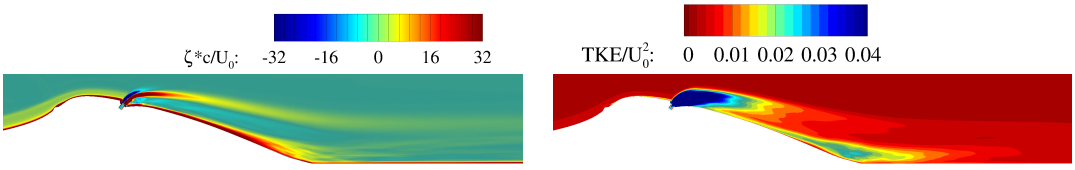

(a) Vorticity contours, without the overhang

(b) TKE contours, without the overhang

(c) Vorticity contours, with the overhang

(d) TKE contours, with the overhang

Figure 4.74: Actuated flow time-averaged spanwise vorticity and in-plane TKE ($\overline{u'^2 + w'^2}/2$) contours, overview, with and without the overhang, BC HRLES

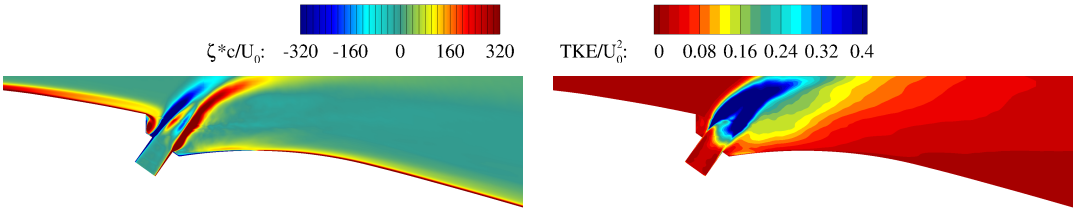

(a) Spanwise vorticity contours, without the overhang

(b) TKE contours, without the overhang

(c) Spanwise vorticity contours, with the overhang

(d) TKE contours, with the overhang

Figure 4.75: Actuated flow time-averaged spanwise vorticity and in-plane TKE ($\overline{u'^2 + w'^2}/2$) contours, close view of the jet, with and without the overhang, BC HRLES

Figures 4.74 and 4.75 compare the time-averaged spanwise vorticity and TKE at the mid-plane of the computational domain with and without the overhang. They provide further evidence of the convection of the jets away from the wall without the overhang.

The time-averaged streamwise vorticity (Fig. 4.76a) exhibits a sense of vorticity consistent with jets in crossflow and opposite to the sense observed in the presence of the overhang (Fig. 4.76b). Furthermore, the TKE (Fig. 4.76c) exhibits shadows of the streamwise vortices at $x/c = 0.8$, in contrast with the computational result in the

presence of the overhang (Fig. 4.76d). As previously discussed, shadows of large-scale structures between the jets are present in the experimental data (Fig. 4.45), which includes the overhang. The resolution of the structures centered around the jets with LES and the high strength of these vortices result in visible loop features in the TKE contours of present case ($x/c = 0.8$ in Fig. 4.76c), even though the duration of the time-average is not significantly longer that the initial computations in the presence of the overhang. Figure 4.77 shows the HRLES blending function at the jet centerline and between the jets. The flow field downstream of the jet is entirely captured with LES, because the jet excites the LES content, as it convects away from the wall. This is different from the behavior previously observed in the presence of the overhang (Fig. 4.38), where part of the shear layer above the jet was resolved with URANS. The flow between the jets is captured with URANS, as the flow remains attached.

In the present case, the jets make a high angle with respect to the outer flow, so that the vortical structured forming around the jets move away from the surface. Conversely, when the overhang was used to turn the flow into the streamwise direction, the flow remained attached in the line of action of the jets. Therefore, the overhang provides an effective means to turn the jets and attach the flow, when spacing constraints prevent the orientation of the jets directly tangential to the outer flow. The best of both worlds could be obtained with free jets oriented as close to the streamwise direction as possible without an overhang, as discussed in the next section.

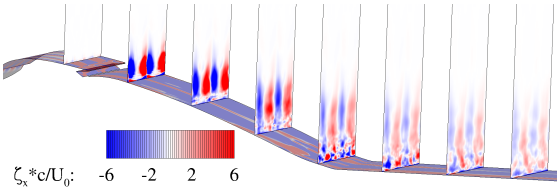

(a) Streamwise vorticity contours, without the overhang

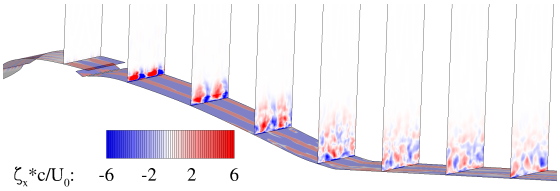

(b) Streamwise vorticity contours, with the overhang

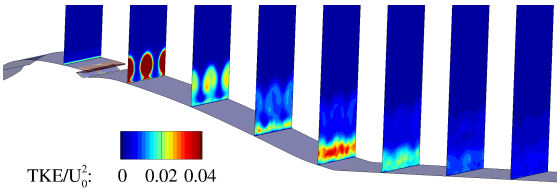

(c) TKE contours, without the overhang

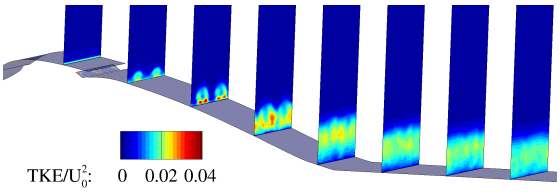

(d) TKE contours, with the overhang

Figure 4.76: Controlled flow time-averaged streamwise vorticity and TKE at different streamwise planes ($x/c = 0.2, 0.4, 0.6, 0.8, 1.0, 1.2, 1.4, 1.6$), with and without the overhang, BC HRLES

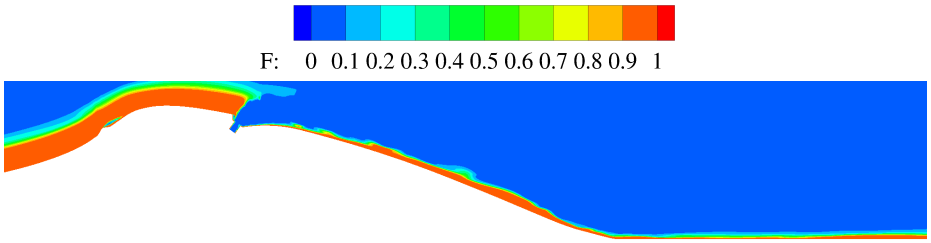

(a) Actuator center ($y/c \simeq 0$)

(b) Between actuators ($y/c \simeq 0.05625$)

Figure 4.77: Instantaneous HRLES blending function 0 (LES) $\leq F \leq$ 1 (RANS) for the simulation of the curved surface and two fluidic oscillators, without the overhang

4.6.10 Effect of jet orientation

In this variation, the orientation of the actuators was modified so that the jets do not impinge directly on the overhang. The flow control is more effective if the jets issue directly into the outer flow direction rather than using the overhang to turn the jets. Simulations were performed by rotating the actuators, as illustrated in Fig. 4.78. The computations are performed with a boundary condition model of the fluidic oscillators and the HRLES turbulence closure. The only modification to the boundary condition formulation was a rotation of the momentum vector. As such, the momentum coefficient remained the same.

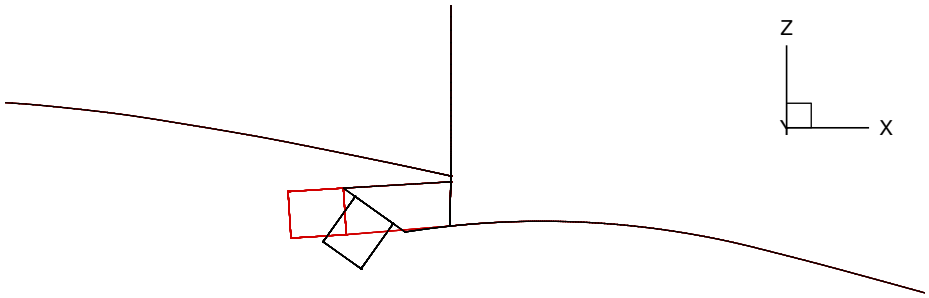

Figure 4.78: Comparison of the initial orientation and the modified orientation to bypass the overhang: initial (black), modified (red)

Figure 4.79 depicts the pressure coefficient distributions obtained with the two jet orientations and for an inviscid solution without flow control. In the inviscid limit, the pressure drag is minimized, and the controlled flow pressure distribution tends to the inviscid limit when the jets are oriented in the streamwise direction. To reiterate, the introduction of the overhang for the wind tunnel experiments is an effective way to turn the flow given the geometric constraints. However, as future designs are evaluated, especially in full-scale applications, it will be worth exploring the trade offs of the designs through computations and possibly high-fidelity optimization.

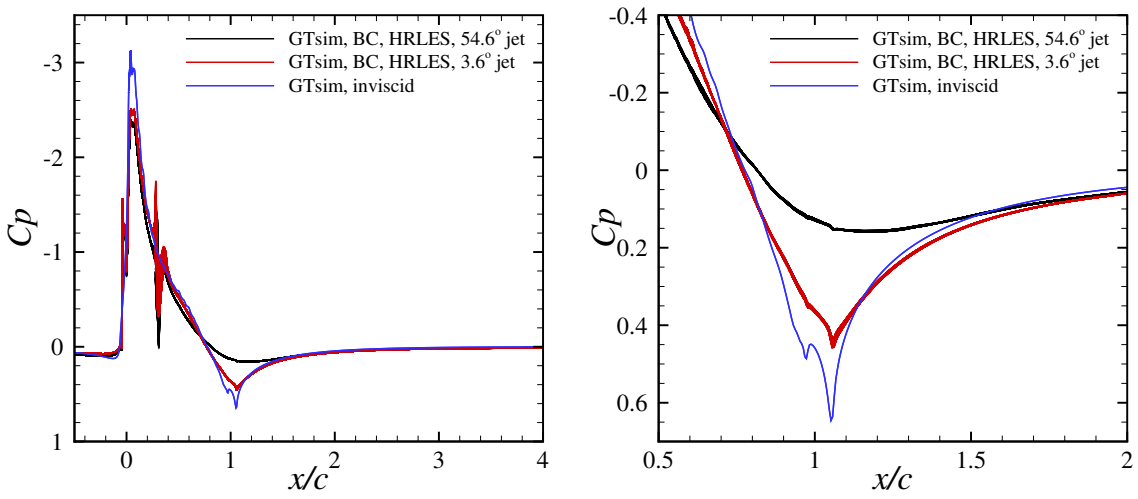

(a) Overview

(b) Close view

Figure 4.79: Controlled flow time-averaged pressure coefficient distribution over the curved surface: effect of changing the jet orientation

Figures 4.80 to 4.83 provide an overview of the flow field and how it compares to the initial computations. These figures depicts quantities that were previously introduced, such as time-averaged vorticity and TKE. The large-scale structures between the jets do not develop when the jets are oriented in the streamwise direction (Fig. 4.80a), and in contrast with the simple removal of the overhang, the jets remain wall-bound. As a result, all flow structures remain close to the wall (Fig. 4.80c). This results in low levels of TKE downstream, and the time-averaged spanwise vorticity no longer exhibits a long tail (Fig. 4.81a versus Fig. 4.81c).

The streamwise vorticity exhibits more complex patterns at $x/c = 0.4$ and $x/c = 0.6$ (Fig. 4.83a versus Fig. 4.83b), as the sign of the time-averaged vorticity alternates in the wall-normal direction. This behavior is similar to a wall jet [139] where small streamwise vortices convect beneath larger counter-rotating vortices. Similar to results obtained by removing the overhang, the 3.6° jets induce a negative streamwise vorticity at their right (looking upstream) and a positive vorticity at their left, indicating down-welling (Fig. 4.83a).

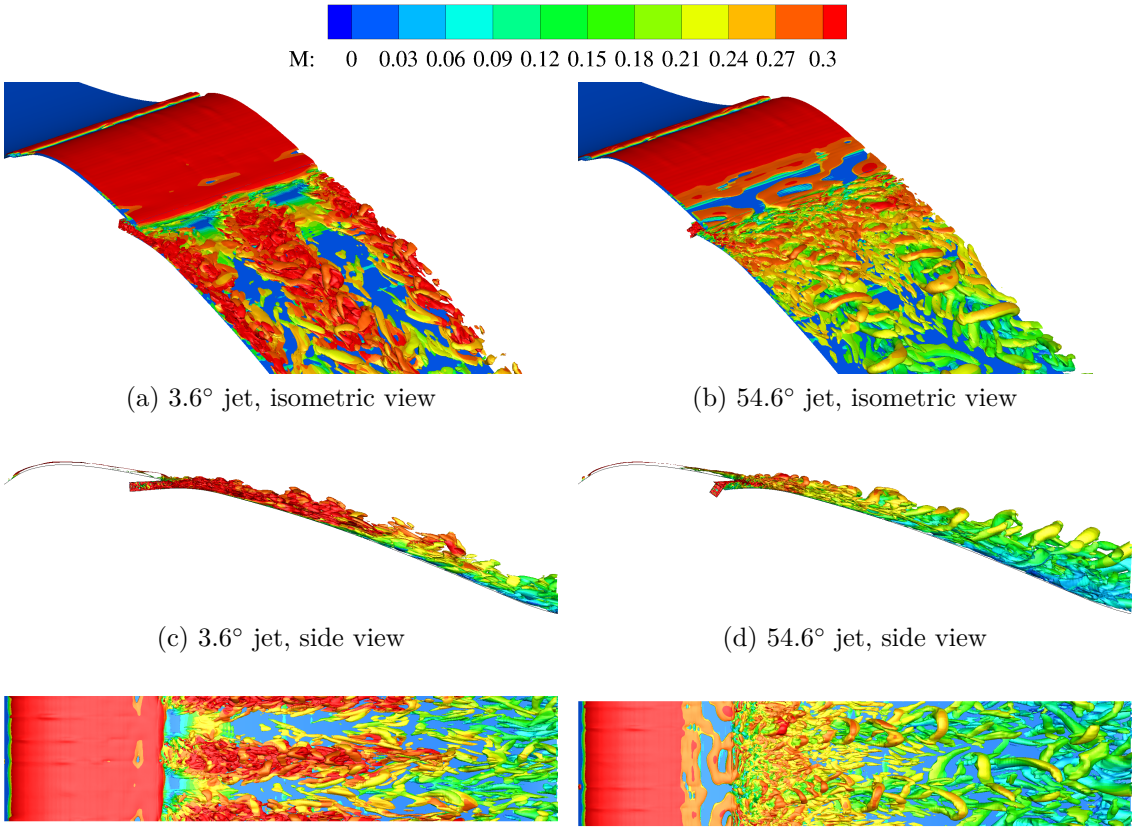

(a) 3.6° jet, isometric view

(b) 54.6° jet, isometric view

(c) 3.6° jet, side view

(d) 54.6° jet, side view

(e) 3.6° jet, top view, $0 \leq x/c \leq 1$

(f) 54.6° jet, top view, $0 \leq x/c \leq 1$

Figure 4.80: Iso-surfaces of the second invariant of the velocity gradient tensor ($Q = 10$) colored with values of local Mach number for the controlled flow over the wind-tunnel model, BC HRLES

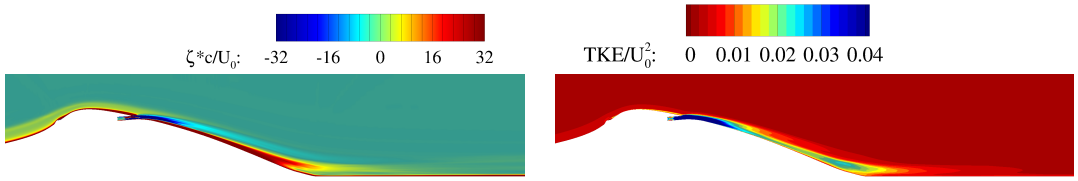

(a) Vorticity contours, 3.6° jet

(b) TKE contours, 3.6° jet

(c) Vorticity contours, 54.6° jet

(d) TKE contours, 54.6° jet

Figure 4.81: Actuated flow time-averaged spanwise vorticity and in-plane TKE ($\overline{u'^2 + w'^2}/2$) contours, overview, different jet orientations, BC HRLES

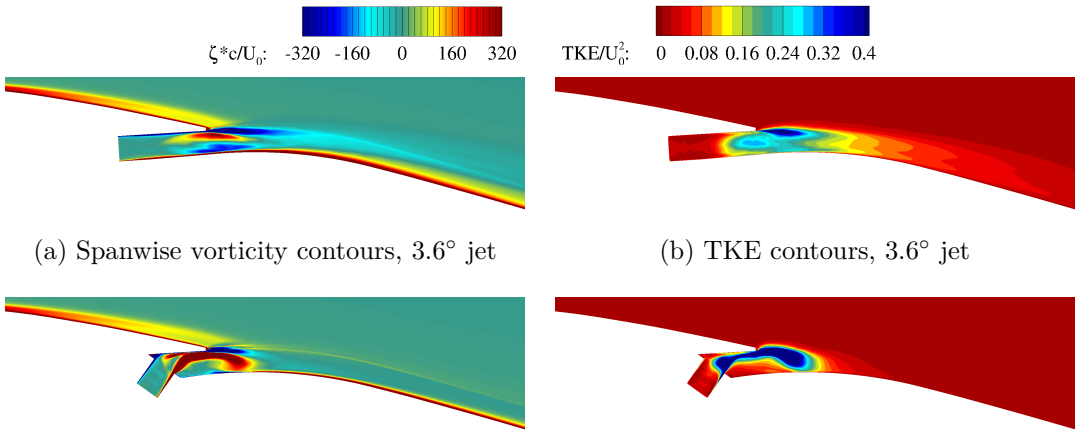

(a) Spanwise vorticity contours, 3.6° jet

(b) TKE contours, 3.6° jet

(c) Spanwise vorticity contours, 54.6° jet

(d) TKE contours, 54.6° jet

Figure 4.82: Actuated flow time-averaged spanwise vorticity and in-plane TKE ($\overline{(u'^2 + w'^2}/2$) contours, close view of the jet, different jet orientations, BC HRLES

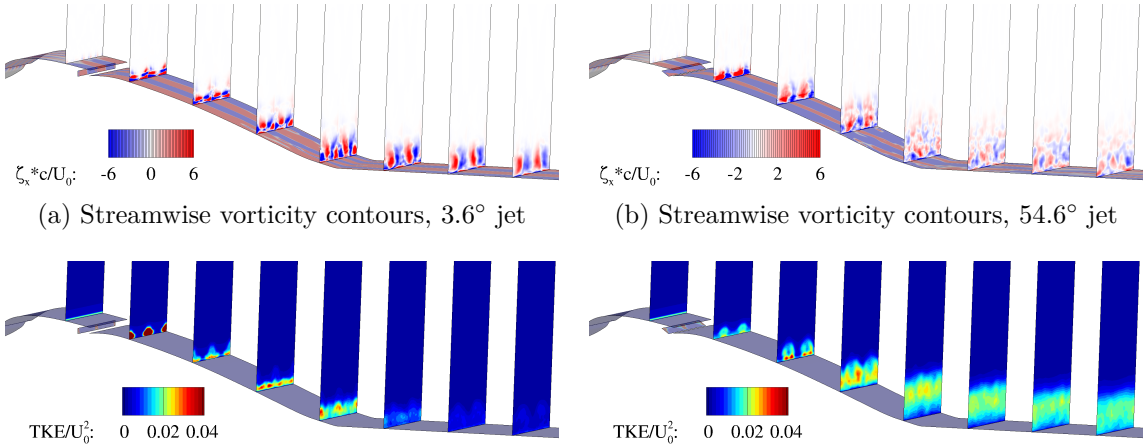

(a) Streamwise vorticity contours, 3.6° jet

(b) Streamwise vorticity contours, 54.6° jet

(c) TKE contours, 3.6° jet

(d) TKE contours, 54.6° jet

Figure 4.83: Controlled flow time-averaged streamwise vorticity and TKE at different streamwise planes ($x/c = 0.2, 0.4, 0.6, 0.8, 1.0, 1.2, 1.4, 1.6$), different jet orientations, BC HRLES

4.7 Technical findings

A flow control application of fluidic oscillator was evaluated computationally. The results were experimentally validated and provided further insights into the physics.

The base flow was characterized, and correlated with experimental data. The baseline computations over-predicted the amount of separation. The computations were found to be sensitive to the trip wire implementation, the overhang, and the turbulence closure. The spanwise variations in the experimental data and the migration of the reattachment location downstream at infinitesimally small actuation levels support the sensitivity of the setup, and the need to provide bounds in the experimental data.

The simulation of the isolated sweeping jet actuator in quiescent conditions resulted in a characterization of its oscillation frequency. The predicted frequencies are within 2.5% of the experiments at two different pressure ratios. Consistent with the experiments, the computed oscillation frequency of an isolated fluidic oscillator was found to be unaffected by the presence of a second actuator. This indicates that the external interaction of the neighboring sweeping jets does not affect the internal mechanisms generating them. This is an important finding in support of developing boundary condition models of the actuators based on the simulation of a single one.

Computations of the actuated flow provided important details of the physics near the jets exits, where experiments do not have access. In the configuration tested in the wind tunnel, the jets, oriented 54.6° with respect to the horizontal impinge on an overhang that turns the flow. The resulting shedding of counter-rotating spanwise vortices at the overhang cancels the vorticity of the outer layer, so that the flow attaches to the surface in line with the jet direction. The impingement of the jets on the overhang causes a spanwise spreading of the jets and an early interaction between

the neighboring jets. Large-scale structures form between the jets with streamwise vorticity of opposite signs to jets in crossflow.

The hybrid RANS/LES turbulence closure provided a better resolution of many flow structures. The pressure distributions over the wall-mounted model predicted with URANS were in better agreement with experimental data at the trailing edge compared to HRLES, though the time-averaged velocities exhibited the opposite trend. This was attributed to the strong spanwise variation in the experiments, which resulted in a pressure distribution that does not reflect a single jet behavior. The second-order statistics of the flow such as the turbulent kinetic energy were correlated with experiments, unlike other studies in the literature [68, 70, 71]. The experimental spanwise variations were clearly visible in the TKE contours and computational sensitivity analyses linked them to local variations in the local properties of the jets relative to the outer flow.

The boundary condition model of the actuators provided accurate predictions for this flow control application, including when it is applied at the outer mold line. The physics of flow separation control over the wall mounted model are dominated by the interaction with the overhang. Therefore, contrary sweeping jet issuing into a quiescent ambient, the omission of modeled and resolved turbulence does not result in significant differences in the flow control application.

Other variations on the flow control configuration leveraged the boundary condition model to further explore the design space (effect of spacing, jet orientation, phase, etc.). In particular, when the jets are oriented such that they issue directly into the streamwise direction without using the overhang to turn, the pressure coefficient distribution approaches the optimal inviscid limit.

Overall, this chapter provides a unique analysis of the physics driving the attachment of an otherwise separated flow over a wall-mounted model.

CHAPTER 5

CONCLUSIONS

5.1 Technical findings

The present work advances the state-of-the-art by investigating in detail the internal physics of a jet interaction fluidic oscillator, the characteristics of the sweeping jet generated, the interaction of such a flow control technique with a separating shear layer and the computational methods by which to predict them. Specific detailed technical findings are summarized at the end of each chapter. In addition, some overarching conclusions are presented here.

5.1.1 Simulation of jet interaction fluidic oscillators

The accurate simulation of jet interaction fluidic oscillators requires time-accuracy and three-dimensional grids to prevent spurious asymmetries in the internal flow and sweeping jet. Two-dimensional simulation are only useful to estimate the oscillation frequency. Frequencies were predicted within 5% of experimental data, for two different designs, at different pressure ratios and flow rates.

The detailed analysis of the internal flow physics from the computations revealed similar characteristics to the prior experiments by Tomac and Gregory [121] at a different actuator scale, such as jet bifurcation, deflection and vortical balance.

Interactions between sweeping jets outside fluidic oscillators do not have a significant impact on the oscillation frequencies, and they do not modify the internal dynamics. Therefore, boundary condition models of the actuators can be derived from a single isolated actuator and extended to multiple actuators in an array.

5.1.2 Fluidic oscillator boundary condition models

Boundary condition models are an effective way to reduce the computational cost, with regards to the grid size, the time-step, and the initial transients. They permit a rapid evaluation of different actuator implementations.

The most accurate boundary condition consists in applying the recorded data from a fully-resolved simulation exactly to subsequent evaluations. The turbulent variables computed by the turbulence closure (modeled turbulence) are included in this formulation, and it retains all flow structures (resolved turbulence). As a result, all spatio-temporal properties of the sweeping jets are recovered when this boundary condition is applied. However, it imposes a stringent requirement on the duration of the fully-resolved computation and data storage and the parameters (time step, initial condition) of subsequent analyses.

A phase-averaged boundary condition formulation, that includes the modeled turbulence but removes the resolved turbulence during the phase-averaging process, was proposed in this work. It can be applied with arbitrary initial conditions and phase shifts. A functional representation of the phase-averaged boundary condition was also introduced in this work. It relies on the periodic oscillation of the flow variables, and was shown to capture the important mechanism leading to the jet oscillations.

Boundary condition formulations that ignore the turbulence were shown to be inadequate at the exit of the actuator or outer mold line, unless other interactions in the flow field dominate the effect of the turbulence. Because turbulence production mostly occurs in the fluidic oscillator nozzle, a phase-averaged formulation is adequate a the throat (entrance of the nozzle). Such a model applied at the throat and including the modeled turbulence was found to introduce less than 10% error compared to fully-resolved simulations in a quiescent ambient.

5.1.3 Interaction of sweeping jets with a separating shear layer via an overhang

The jet interaction fluidic oscillators were shown to effectively mitigate flow separation on the wall-mounted model considered. The design evaluated in the wind tunnel included an overhang that covers the jet orifices, and its introduction was motivated by geometrical constraints. This overhang turns the jet flows into a direction parallel to the outer shear layer. Counter-rotating spanwise vortices at the interface between the jets and the outer shear layer keep the outer flow attached in line with the jets. However, large-scale structures form between the jets. The computations revealed that these large-scale structures are the result of the interaction between the jets and the overhang. This was further shown by removing the overhang in the computations or modifying the jet orientations. The computations were validated with experimental data. Relative errors were 10% on average. The spanwise pressures, stereo PIV and variations in the computational setup revealed a sensitivity of the results to local variations in the characteristics of the outer shear layer and the jets.

5.1.4 Interaction of sweeping jets with a separating shear layer in the absence of an overhang

The jets were found to be more effective when they are parallel to the outer flow. Not only is the shear layer kept attached in line with the jets, but down-welling-inducing streamwise vortices develop and attach the flow between the jets. In this configuration, the pressure distribution over the wall-mounted model approaches the pressure drag minimizing inviscid limit. This variation on the configuration tested in the wind tunnel was evaluated with the new phase-averaged boundary condition mode of the fluidic oscillators, thereby demonstrating its usefulness in exploring the design space.

5.2 Recommendation for future work

Several areas of improvements of the computations are proposed, along with suggestions for experimental studies to aid computational validation. Recommendations for future research on fluidic oscillators and flow control in a broader sense are also discussed.

5.2.1 Validation experimental data for computations

The approach taken in the present work to investigate the differences between computation and experiments consisted in performing multiple variations of the simulation and assessing the sensitivities to various parameters (trip wire, turbulence intensity, inlet temperature, etc.). Several recommendations for experimental studies can be addressed to provide improved validation for computational validation:

- Characterization of the incoming boundary layer, including at least the time-averaged velocity profile and the turbulence intensity in a region without pressure gradient.
- Reproducing the shape, size and location of the trip wire in the computations proved to be a challenge. Larger-scale testing that does not need a trip wire or that can be machined as part of the model and reproduced via CAD are preferable for computational validation tests.
- Experimental data for unsteady aerodynamics should include minimum and maximum values, in addition to the mean flow so that sensitivities can be assessed.

With a better understanding of experimental uncertainties, more advanced computational approaches can be explored. For example, the cross-coupling hybrid terms and the dynamic procedure for the coefficient in the HRLES closure. Exploring the influence of advanced Large Eddy Simulation (LES) on refined grids is a line of research

that can be undertaken so that further insights into the accuracy of the computational methods can be assessed. Whenever possible, the experimental and computational post-processing methods should be matched (sampling frequency, test duration, averaging techniques, spatial resolution, etc.), so that these do not introduce additional uncertainty.

5.2.2 Boundary condition models of fluidic oscillators

This study demonstrated the accuracy of boundary condition models at the fluidic oscillator throat, and the importance of the turbulence and interactions at the outer mold line. In situations where the outer mold line is regular (identical from one actuator to another), approaches to take into account the turbulence, such as synthetic turbulence generators could be explored.

Synthetic turbulence generators [129–131] have been developed for LES and hybrid RANS/LES and applied to various flows including boundary layers and jets. These boundary conditions can be adapted to represent the turbulent fluctuations removed by phase-averaging. In that case, the boundary condition would be extended to included the six components of the symmetric Reynolds-stress tensor. This is a possible extension for boundary condition formulation with HRLES and LES.

The inherent variation of the nozzle geometry when the actuators are implemented into a three-dimensional geometry (such as a helicopter fuselage) implies an actuator-dependent outer mold line. A general model of the fluidic oscillators at the outer mold line should take this aspect into account to result in accurate solution. The work in this thesis provides the baseline for these further analyses.

5.2.3 Further exploration of the flow control design space

In the present work, some preliminary studies were conducted to assess the effect of various parameters on the flow control effectiveness. For example, the effect of jet

orientation was assessed on the wall-mounted model. A systematic method to find the optimum actuation parameters would be coupling the flow solver with an optimizer. Techniques such as the adjoint method could be employed to evaluate the gradients in these high-fidelity optimizations. The design variables could be the reduced frequency F^+, the jet momentum coefficient C_μ, as well as the actuator placement and orientation. The adjoint methods can also be applied for error estimation by systematically propagating uncertainties in the computations.

Furthermore, there has been a general tendency in engineering to identify reduced-order models. Machine learning could be used as a tool on high-quality computational and experimental data to accelerate the optimization process, provided the identified models incorporate the necessary physics, so the models don't fall apart outside the training space.

5.2.4 Large scale simulations

More flow control applications should be investigated at large-scale in order to make fluidic active flow control implementation in flight vehicles a reality. Some work has been done in this area on the Boeing 757 ecoDemonstrator airplane [72]. Computational studies of boundary conditions and flow control effectiveness at different scales have also been undertaken for rotorcraft applications [128].

Appendices

APPENDIX A

INCOMPRESSIBLE FORMULATION

A pressure-based, constant density formulation was added to the flow solver for maximum efficiency when the Mach number is known to be low everywhere in the computational domain. A description of the approach is included here for completeness and posterity. The primitive variables $\mathbf{W} = (p\ u\ v\ w)^T$ are employed. Temperature is not included in the state vector, as the energy equation is uncoupled from the continuity and momentum equations.

In order to make use of the existing time-marching schemes in GTsim, the Chorin artificial compressibility method [140] was adopted. This method couples the continuity and momentum equations by introducing an artificial time-dependent pressure term in place of the time-dependent density term:

$$\frac{\partial \rho}{\partial \tau} = \frac{1}{\overline{\beta}} \frac{\partial p}{\partial \tau} \,, \tag{A.1}$$

where $\overline{\beta}$ is the artificial compressibility factor. The artificial compressibility is only applied in pseudo time, so that the exact incompressible equations are recovered after convergence of the sub-iterations.

The unsteady incompressible Navier-Stokes equations applied to a moving rigid body with the Chorin artificial compressibility can be written in integral form as:

$$\frac{\partial}{\partial \tau} \int_\Omega \mathbf{A}_\tau \mathbf{W} dV + \frac{\partial}{\partial t} \int_\Omega \mathbf{A_t} \mathbf{W} dV + \oint_{\partial\Omega} (\mathbf{F}_c - \mathbf{F}_v) dS = 0 \,. \tag{A.2}$$

The state vector $\mathbf{W}$ and flux vectors $\mathbf{F}_c$ and $\mathbf{F}_v$ are given by

$$\mathbf{W} = \begin{pmatrix} p \\ u \\ v \\ w \end{pmatrix}, \qquad \mathbf{F}_c = \begin{pmatrix} \overline{\beta}\mathcal{V}_r \\ u\mathcal{V}_r + n_x p \\ v\mathcal{V}_r + n_y p \\ w\mathcal{V}_r + n_z p \end{pmatrix}, \qquad \mathbf{F}_v = \begin{pmatrix} 0 \\ n_x\tau_{xx} + n_y\tau_{xy} + n_z\tau_{xz} \\ n_x\tau_{xy} + n_y\tau_{yy} + n_z\tau_{yz} \\ n_x\tau_{xz} + n_y\tau_{yz} + n_z\tau_{zz} \end{pmatrix} \tag{A.3}$$

The contravariant velocity defined in Chapter 2 still apply. The expressions for the viscous stresses are very similar as well, except that the Mach number does not appear in the non-dimensional form of the incompressible equations. The matrices $\mathbf{A_t}$ and $\mathbf{A}_\tau$ dictate the dependence of the state variables with respect to physical and real time. They are given by

$$\mathbf{A_t} = \begin{pmatrix} 0 & 0 & 0 & 0 \\ 0 & 1 & 0 & 0 \\ 0 & 0 & 1 & 0 \\ 0 & 0 & 0 & 1 \end{pmatrix}, \qquad \mathbf{A}_\tau = \begin{pmatrix} 1 & 0 & 0 & 0 \\ 0 & 1 & 0 & 0 \\ 0 & 0 & 1 & 0 \\ 0 & 0 & 0 & 1 \end{pmatrix}. \tag{A.4}$$

The following non-dimensionalization scheme [141] is applied:

$$\begin{gathered} u = \frac{\tilde{u}}{\tilde{U}_\infty} \qquad v = \frac{\tilde{v}}{\tilde{U}_\infty} \qquad w = \frac{\tilde{w}}{\tilde{U}_\infty} \qquad p = \frac{\tilde{p} - \tilde{p}_{norm}}{\tilde{\rho}_\infty \tilde{U}_\infty^2} \\ \tilde{p}_{norm} = \tilde{p}_\infty - \tilde{\rho}_\infty \tilde{U}_\infty^2 \qquad \rho = \frac{\tilde{\rho}}{\tilde{\rho}_\infty} = 1 \qquad \mu = \frac{\tilde{\mu}}{\tilde{\mu}_\infty} = 1 \\ x = \frac{\tilde{x}}{\tilde{L}_R} \qquad y = \frac{\tilde{y}}{\tilde{L}_R} \qquad z = \frac{\tilde{z}}{\tilde{L}_R} \qquad t = \frac{\tilde{t}\tilde{U}_\infty}{\tilde{L}_R}, \end{gathered} \tag{A.5}$$

With this non-dimensionalization, the pressure coefficient is defined as

$$Cp = 2(p-1). \tag{A.6}$$

Additional turbulence equations are modified accordingly.

The convective and viscous flux Jacobian matrices are respectively

$$\frac{\partial \mathbf{F}_c}{\partial \mathbf{W}} = \begin{pmatrix} 0 & \overline{\beta} n_x & \overline{\beta} n_y & \overline{\beta} n_z \\ n_x & \mathcal{V}_r + u n_x & u n_y & u n_z \\ n_y & v n_x & \mathcal{V}_r + v n_y & v n_z \\ n_z & w n_x & w n_y & \mathcal{V}_r + w n_z \end{pmatrix} \tag{A.7}$$

and

$$\frac{\partial \mathbf{F}_v}{\partial \mathbf{W}} = \frac{\mu \Delta S^2}{\Omega Re} \begin{pmatrix} 0 & 0 & 0 & 0 \\ 0 & 1+\frac{n_x^2}{3} & \frac{n_x n_y}{3} & \frac{n_x n_z}{3} \\ 0 & \frac{n_x n_y}{3} & 1+\frac{n_y^2}{3} & \frac{n_y n_z}{3} \\ 0 & \frac{n_x n_z}{3} & \frac{n_y n_z}{3} & 1+\frac{n_z^2}{3} \end{pmatrix} \tag{A.8}$$

According to the Steger and Warming flux Jacobian splitting, the convective flux jacobian can be diagonalized as follows:

$$\frac{\partial \mathbf{F}_c}{\partial \mathbf{W}} = \mathcal{L}\ \mathbf{\Lambda}\ \mathcal{L}^{-1} \tag{A.9}$$

The diagonal matrix can be written as

$$\mathbf{\Lambda} = \begin{pmatrix} \frac{1}{2}(\overline{\mathcal{V}}+c) & 0 & 0 & 0 \\ 0 & \frac{1}{2}(\overline{\mathcal{V}}-c) & 0 & 0 \\ 0 & 0 & \mathcal{V}_r & 0 \\ 0 & 0 & 0 & \mathcal{V}_r \end{pmatrix}, \tag{A.10}$$

where

$$\overline{\mathcal{V}} = \mathcal{V} + \mathcal{V}_r\ , \qquad c = \sqrt{\overline{\mathcal{V}}^2 + 4\overline{\beta}}\ , \qquad \alpha = \mathcal{V}\mathcal{V}_r + \overline{\beta} \tag{A.11}$$

There is no simple way to express the two eigenvectors associated with the eigenvalues $\mathcal{V}_r$, so that there is no singularity in the left matrix $\mathcal{L}^{-1}$. Therefore, three sets of eigenvectors are implemented, with singularities at $n_x = 0$, $n_y = 0$, and $n_z = 0$ respectively. All three formulations fail if the normal vector is identically null ($n_x = n_y = n_z = 0$). In that case, the flux Jacobian is also null.

The following right and left eigenvectors are valid, as long as $n_x \neq 0$.

$$\mathcal{L} = \begin{pmatrix} \overline{\beta}(\mathcal{V}_t + c) & \overline{\beta}(\mathcal{V}_t - c) & 0 & 0 \\ (u(\overline{\mathcal{V}} + c) + 2\overline{\beta}n_x) & (u(\overline{\mathcal{V}} - c) + 2\overline{\beta}n_x) & -n_z & -n_y \\ (v(\overline{\mathcal{V}} + c) + 2\overline{\beta}n_y) & (v(\overline{\mathcal{V}} - c) + 2\overline{\beta}n_y) & 0 & n_x \\ (w(\overline{\mathcal{V}} + c) + 2\overline{\beta}n_z) & (w(\overline{\mathcal{V}} - c) + 2\overline{\beta}n_z) & n_x & 0 \end{pmatrix} \tag{A.12}$$

$$\mathcal{L}^{-1} = \frac{1}{\alpha} \begin{pmatrix} \frac{\mathcal{V}(\overline{\mathcal{V}} - c) + 2\overline{\beta}}{4\overline{\beta}c} & \frac{-n_x(\mathcal{V}_t - c)}{4c} & \frac{-n_y(\mathcal{V}_t - c)}{4c} & \frac{-n_z(\mathcal{V}_t - c)}{4c} \\ \frac{-\mathcal{V}(\overline{\mathcal{V}} + c) - 2\overline{\beta}}{4\overline{\beta}c} & \frac{n_x(\mathcal{V}_t + c)}{4c} & \frac{n_y(\mathcal{V}_t + c)}{4c} & \frac{n_z(\mathcal{V}_t + c)}{4c} \\ \frac{\mathcal{V}n_z - w}{n_x} & -(w\mathcal{V}_r + n_z\overline{\beta}) & \frac{-n_y(w\mathcal{V}_r + n_z\overline{\beta})}{n_x} & \frac{(un_x + vn_y)\mathcal{V}_r + \overline{\beta}(n_x^2 + n_y^2)}{n_x} \\ \frac{\mathcal{V}n_y - v}{n_x} & -(v\mathcal{V}_r + n_y\overline{\beta}) & \frac{-n_y(v\mathcal{V}_r + n_y\overline{\beta}) + \alpha}{n_x} & \frac{-n_z(v\mathcal{V}_r + n_y\overline{\beta})}{n_x} \end{pmatrix}, \tag{A.13}$$

The following right and left eigenvectors are valid, as long as $n_y \neq 0$.

$$\mathcal{L} = \begin{pmatrix} \overline{\beta}(\mathcal{V}_t + c) & \overline{\beta}(\mathcal{V}_t - c) & 0 & 0 \\ (u(\overline{\mathcal{V}} + c) + 2\overline{\beta}n_x) & (u(\overline{\mathcal{V}} - c) + 2\overline{\beta}n_x) & 0 & -n_y \\ (v(\overline{\mathcal{V}} + c) + 2\overline{\beta}n_y) & (v(\overline{\mathcal{V}} - c) + 2\overline{\beta}n_y) & -n_z & n_x \\ (w(\overline{\mathcal{V}} + c) + 2\overline{\beta}n_z) & (w(\overline{\mathcal{V}} - c) + 2\overline{\beta}n_z) & n_y & 0 \end{pmatrix} \tag{A.14}$$

$$\mathcal{L}^{-1} = \frac{1}{\alpha} \begin{pmatrix} \frac{\mathcal{V}(\overline{\mathcal{V}} - c) + 2\overline{\beta}}{4\overline{\beta}c} & \frac{-n_x(\mathcal{V}_t - c)}{4c} & \frac{-n_y(\mathcal{V}_t - c)}{4c} & \frac{-n_z(\mathcal{V}_t - c)}{4c} \\ \frac{-\mathcal{V}(\overline{\mathcal{V}} + c) - 2\overline{\beta}}{4\overline{\beta}c} & \frac{n_x(\mathcal{V}_t + c)}{4c} & \frac{n_y(\mathcal{V}_t + c)}{4c} & \frac{n_z(\mathcal{V}_t + c)}{4c} \\ \frac{\mathcal{V}n_z - w}{n_y} & \frac{-n_x(w\mathcal{V}_r + n_z\overline{\beta})}{n_y} & -(w\mathcal{V}_r + n_z\overline{\beta}) & \frac{(un_x + vn_y)\mathcal{V}_r + \overline{\beta}(n_x^2 + n_y^2)}{n_y} \\ \frac{-\mathcal{V}n_x + u}{n_y} & \frac{n_x(u\mathcal{V}_r + n_x\overline{\beta}) - \alpha}{n_y} & u\mathcal{V}_r + n_x\overline{\beta} & \frac{n_z(u\mathcal{V}_r + n_x\overline{\beta})}{n_y} \end{pmatrix} \tag{A.15}$$

The following right and left eigenvectors are valid, as long as $n_z \neq 0$.

$$\mathcal{L} = \begin{pmatrix} \overline{\beta}(\mathcal{V}_t + c) & \overline{\beta}(\mathcal{V}_t - c) & 0 & 0 \\ (u(\overline{\mathcal{V}} + c) + 2\overline{\beta}n_x) & (u(\overline{\mathcal{V}} - c) + 2\overline{\beta}n_x) & 0 & -n_z \\ (v(\overline{\mathcal{V}} + c) + 2\overline{\beta}n_y) & (v(\overline{\mathcal{V}} - c) + 2\overline{\beta}n_y) & -n_z & 0 \\ (w(\overline{\mathcal{V}} + c) + 2\overline{\beta}n_z) & (w(\overline{\mathcal{V}} - c) + 2\overline{\beta}n_z) & n_y & n_x \end{pmatrix} \tag{A.16}$$

$$\mathcal{L}^{-1} = \frac{1}{\alpha} \begin{pmatrix} \dfrac{\mathcal{V}(\overline{\mathcal{V}} - c) + 2\overline{\beta}}{4\overline{\beta}c} & \dfrac{-n_x(\mathcal{V}_t - c)}{4c} & \dfrac{-n_y(\mathcal{V}_t - c)}{4c} \\ \dfrac{-\mathcal{V}(\overline{\mathcal{V}} + c) - 2\overline{\beta}}{4\overline{\beta}c} & \dfrac{n_x(\mathcal{V}_t + c)}{4c} & \dfrac{n_y(\mathcal{V}_t + c)}{4c} \\ \dfrac{-\mathcal{V}n_y + v}{n_z} & \dfrac{n_x(v\mathcal{V}_r + n_y\overline{\beta})}{n_z} & \dfrac{n_y(v\mathcal{V}_r + n_y\overline{\beta}) - \alpha}{n_z} \\ \dfrac{-\mathcal{V}n_x + u}{n_z} & \dfrac{n_x(u\mathcal{V}_r + n_x\overline{\beta}) - \alpha}{n_z} & \dfrac{n_y(u\mathcal{V}_r + n_x\overline{\beta})}{n_z} \end{pmatrix} \begin{pmatrix} \dfrac{-n_z(\mathcal{V}_t - c)}{4c} \\ \dfrac{n_z(\mathcal{V}_t + c)}{4c} \\ v\mathcal{V}_r + \overline{\beta}n_y \\ u\mathcal{V}_r + n_x\overline{\beta}) \end{pmatrix} \tag{A.17}$$

APPENDIX B

CONVECTIVE FLUX JACOBIAN FOR THE PRECONDITIONED SYSTEM

Splitting the convective flux Jacobian for the preconditioned system follow an approach similar to that presented by Hodara [52] for the original system. Consider the vector or conservative variables $\mathbf{U} = (\rho\ \rho u\ \rho v\ \rho w\ \rho E)^T$ and a vector of primitive variables $\mathbf{W} = (p\ u\ v\ w\ T)^T$. One can move from a representation to the other through the following conversion matrices (calorically perfect gas, $T = a^2 = \gamma p/\rho$):

$$\mathcal{M}^{-1} = \frac{\partial \mathbf{W}}{\partial \mathbf{U}} = \begin{pmatrix} \frac{\gamma-1}{2}\vec{u}^2 & -u(\gamma-1) & -v(\gamma-1) & -w(\gamma-1) & \gamma-1 \\ -u/\rho & 1/\rho & 0 & 0 & 0 \\ -v/\rho & 0 & 1/\rho & 0 & 0 \\ -w/\rho & 0 & 0 & 1/\rho & 0 \\ \frac{1}{2}(\gamma-1)\vec{u}^2 & -(\gamma-1)\frac{\gamma}{\rho}u & -(\gamma-1)\frac{\gamma}{\rho}v & -(\gamma-1)\frac{\gamma}{\rho}w & (\gamma-1)\frac{\gamma}{\rho} \end{pmatrix} \tag{B.1}$$

and

$$\mathcal{M} = \frac{\partial \mathbf{U}}{\partial \mathbf{W}} = \begin{pmatrix} \gamma/T & 0 & 0 & 0 & -\rho/T \\ \gamma u/T & \rho & 0 & 0 & -\rho u/T \\ \gamma v/T & 0 & \rho & 0 & -\rho v/T \\ \gamma w/T & 0 & 0 & \rho & -\rho w/T \\ \frac{1}{\gamma-1} + \frac{\gamma\vec{u}^2}{2T} & \rho u & \rho v & \rho w & -\frac{\rho\vec{u}^2}{2T} \end{pmatrix}. \tag{B.2}$$

For a correct treatment of preconditioning, the convective flux Jacobian in the conservative variables is written in terms of convective flux Jacobian in the primitive

variables as:

$$\frac{\partial \mathbf{F}_c}{\partial \mathbf{U}} = \mathbf{\Gamma} \left(\mathbf{\Gamma}^{-1} \frac{\partial \mathbf{F}_c}{\partial \mathbf{W}} \right) \frac{\partial \mathbf{W}}{\partial \mathbf{U}} \ , \tag{B.3}$$

where $\mathbf{\Gamma}$ is the Weiss-Smith preconditioning matrix. The matrix $\mathbf{\Gamma}^{-1} \dfrac{\partial \mathbf{F}_c}{\partial \mathbf{W}}$ can be diagonalized such that

$$\mathbf{\Gamma}^{-1} \frac{\partial \mathbf{F}_c}{\partial \mathbf{W}} = \mathcal{L} \Lambda \mathcal{L}^{-1} \ . \tag{B.4}$$

The eigenvalues are

$$\Lambda = \mathrm{diag} \left(3 \times \mathcal{V}_r, u' + c', u' - c' \right) \ , \tag{B.5}$$

where

$$u' = \mathcal{V}_r (1 - \alpha) \qquad c' = \sqrt{(\alpha \mathcal{V}_r)^2 + U_r^2} \qquad \alpha = \frac{1}{2}(1 - \beta U_r^2) \qquad \beta = \frac{1}{T} \tag{B.6}$$

The associated left eigenvectors are

$$\mathcal{L} = \frac{1}{\rho U_r^2} \begin{pmatrix} 0 & 0 & 0 & \rho U_r^2 & \rho U_r^2 \\ 0 & -n_z c' & n_y c' & n_x c' + n_x \alpha \mathcal{V}_r & -n_x c' + n_x \alpha \mathcal{V}_r \\ n_z c' & 0 & -n_x c' & n_y c' + n_y \alpha \mathcal{V}_r & -n_y c' + n_y \alpha \mathcal{V}_r \\ -n_y c' & n_x c' & 0 & n_z c' + n_z \alpha \mathcal{V}_r & -n_z c' + n_z \alpha \mathcal{V}_r \\ -n_x T & -n_y T & -n_z T & -\rho / a_1^\Gamma & -\rho / a_1^\Gamma \end{pmatrix} \ , \tag{B.7}$$

and the right eigenvectors are

$$\mathcal{L}^{-1} = \begin{pmatrix} -\rho n_x / (T a_1^\Gamma) & 0 & n_z \rho U_r^2 / c' & -n_y \rho U_r^2 / c' & -n_x \rho U_r^2 / T \\ -\rho n_x / (T a_1^\Gamma) & -n_z \rho U_r^2 / c' & 0 & n_x \rho U_r^2 / c' & -n_y \rho U_r^2 / T \\ -\rho n_x / (T a_1^\Gamma) & n_y \rho U_r^2 / c' & -n_x \rho U_r^2 / 2c' & 0 & -n_z \rho U_r^2 / T \\ \frac{1}{2}\left(1 - \alpha \mathcal{V}_r / c'\right) & n_x \rho U_r^2 / 2c' & n_y \rho U_r^2 / 2c' & n_z \rho U_r^2 / 2c' & 0 \\ \frac{1}{2}\left(1 + \alpha \mathcal{V}_r / c'\right) & -n_x \rho U_r^2 / 2c' & -n_y \rho U_r^2 / 2c' & -n_z \rho U_r^2 / 2c' & 0 \end{pmatrix} \ , \tag{B.8}$$

where

$$a_1^{\Gamma} = \rho \left(\frac{\Theta}{\gamma - 1} - \frac{1}{T} \right) \tag{B.9}$$

The split matrices are obtained by considering the positive eigenvalues for the positive Jacobian and negative eigenvalues for the negative Jacobian. The diagonal matrix Λ for the flux Jacobian is modified as

$$\mathbf{\Lambda}^{\pm} = \frac{1}{2} \left(\mathbf{\Lambda} \pm |\mathbf{\Lambda}| \right) . \tag{B.10}$$

The characteristic boundary conditions for the preconditioned system are derived from the characteristic variables $\mathbf{W}_c = \mathcal{L}^{-1}\mathbf{W}$.

APPENDIX C

FUNCTIONAL FIT COEFFICIENTS FOR FLUIDIC OSCILLATOR BOUNDARY CONDITIONS

The general functional fit for the flow variables in the fluidic oscillator boundary condition models are given by Eq. 3.2 and 3.3. These functions are detailed here, to be prescribed at the throat of the actuator. The throat is a rectangular domain $(y, z) \in [-0.75, 0.75] \times [-0.5, 0.5]$ in grid units. Testing this boundary condition model also requires the construction of a grid for the nozzle (expansion from the throat to the exit), and for the quiescent field. The actuator exit is a rectangular domain $(y, z) \in [-0.75, 0.75] \times [-0.84, 0.84]$ in grid units.

By trial-error on the 2D data, rational functions of fifth order polynomials were selected to fit $f_n(y, z)$ and third order polynomials were selected to fit $g_n(z)$. The advantage of the rational functions for $f_n(y, z)$ is that they do not exhibit Runge's phenomenon (spurious oscillations). Better accuracy is generally obtained with higher order polynomials, but the cost of evaluating these functions in the flow solver would increase, and the high-dimensionality makes the least-square problem harder to tackle.

The rational functions of fifth order polynomials can be written as

$$fi_n(\xi_i) = \frac{\sum_{k=1}^{6} n_k \xi_i^{k-1}}{\sum_{k=1}^{6} d_k \xi_i^{k-1}} \,, \tag{C.1}$$

where $\xi_i = y$ if $i = 1$, and $\xi_i = z$ if $i = 2$, and n_k, d_k are the coefficients determined by least-squares. The third order function $g_n(z)$ is written as

$$g_n(z) = \sum_{k=1}^{4} a_k z^{k-1} \,. \tag{C.2}$$

The coefficients n_k, d_k, a_k, and ϕ_{0_n} are given by Tables C.1 and C.2 for the 2D case. In that case, $f1_n(y) = 1$, and $\rho v = 0$. Realizability constraints for the turbulent variables are enforced in the flow solver, as the boundary condition itself does not

Table C.1: Coefficients of $f2_n(z)$ for the 2D case

n_k, d_k	ρ	ρu	ρw	ρE	ρk	$\rho\omega$
n_1	1.01e+0	8.83e−1	−2.04e−2	5.60e−1	9.56e−3	3.86e−4
n_2	−2.16e+0	−1.60e+0	−6.07e−1	1.17e+0	5.11e−3	6.30e−6
n_3	−5.93e+0	−6.00e+0	2.49e−1	−3.40e+0	−6.78e−2	−4.04e−3
n_4	1.29e+1	1.07e+1	3.86e+0	−7.16e+0	−3.20e−2	−1.59e−4
n_5	7.78e+0	9.89e+0	−6.67e−1	4.73e+0	1.18e−1	1.04e−2
n_6	−1.75e+1	−1.74e+1	−5.75e+0	1.02e+1	4.61e−2	6.02e−4
d_1	5.37e−1	6.97e−1	6.54e−1	1.59e−1	2.21e+0	6.55e−1
d_2	−1.14e+0	−1.26e+0	−1.66e−1	3.32e−1	2.19e+0	3.00e−2
d_3	−2.97e+0	−4.50e+0	−4.83e+0	−9.10e−1	−1.78e+1	−5.21e+0
d_4	6.46e+0	8.03e+0	1.17e+0	−1.93e+0	−1.76e+1	−2.35e−1
d_5	3.53e+0	6.95e+0	8.87e+0	1.14e+0	3.62e+1	1.04e+1
d_6	−8.06e+0	−1.21e+1	−2.01e+0	2.48e+0	3.58e+1	4.59e−1

Table C.2: Coefficients of $g_n(z)$ and phase shift (ϕ_{0_n}) for the 2D case

a_k	ρ	ρu	ρw	ρE	ρk	$\rho\omega$
a_1	3.79e−3	−5.09e−3	−4.83e−1	1.85e−3	8.67e−4	−7.41e−5
a_2	−3.63e−1	4.17e−1	−3.54e−2	−3.25e−1	−1.38e−2	1.61e−2
a_3	−5.39e−2	1.46e−2	1.11e+0	−7.20e−2	−3.29e−4	1.00e−3
a_4	5.94e−1	−2.74e+0	1.33e−1	1.50e−1	5.34e−2	−1.19e−1
ϕ_{0_n}	−5.75e−1	−1.09e+0	−1.18e+0	−9.69e−2	7.82e−1	1.57e+0

guarantee realizability. In particular, using the coefficients in Tables C.1 and C.2, the specific dissipation rate can become negative, which is not permissible. The equations given here are for non-dimensional flow variables, where density, velocity, temperature and lengths are non-dimensionalized with $\tilde{\rho}_\infty$, $\tilde{a}_\infty$, $\tilde{T}_\infty$ and $\tilde{L}_R$ respectively.

Similarly, the coefficients n_k, d_k, a_k, and ϕ_{0_n} are given by Tables C.3, C.4 and C.5 for the 3D case.

Table C.3: Coefficients of $f1_n(z)$ for the 3D case

n_k, d_k	ρ	ρu	ρv	ρw	ρE
n_1	5.74e−1	7.66e−1	7.17e−2	−1.89e+0	2.71e−1
n_2	−6.79e−1	−1.32e−1	3.53e+0	−4.73e+0	−8.68e−1
n_3	−9.09e−1	−2.66e+0	−3.02e+0	−2.30e+0	3.33e−1
n_4	2.32e+0	4.71e−1	−7.67e+0	5.43e−1	2.71e+0
n_5	−1.92e−1	2.31e+0	7.06e+0	−1.29e+0	−1.44e+0
n_6	−1.98e+0	−4.19e−1	−1.02e−1	−1.16e+0	−2.08e+0
d_1	2.66e−1	4.38e−1	3.57e+0	4.31e+0	7.36e−2
d_2	−3.17e−1	−7.75e−2	−9.99e−1	1.09e+1	−2.38e−1
d_3	−4.13e−1	−1.52e+0	−7.54e+0	6.40e+0	9.41e−2
d_4	1.08e+0	2.75e−1	−2.73e+0	7.08e−1	7.41e−1
d_5	−1.04e−1	1.31e+0	−8.39e−1	2.97e+0	−3.98e−1
d_6	−9.23e−1	−2.44e−1	1.22e+1	1.62e+0	−5.66e−1

Table C.4: Coefficients of $f2_n(z)$ for the 3D case

n_k, d_k	ρ	ρu	ρv	ρw	ρE
n_1	2.62e−1	1.18e+0	−5.51e−4	6.29e−4	2.52e−1
n_2	2.69e−2	5.16e−2	2.63e−3	7.21e−1	−9.44e−2
n_3	−1.80e+0	−5.00e+0	1.89e−2	−5.56e−2	−1.62e+0
n_4	−2.00e−1	−4.35e−1	−2.29e−3	−4.48e+0	5.70e−1
n_5	3.03e+0	1.21e+0	−6.51e−2	2.12e−1	2.48e+0
n_6	3.68e−1	9.16e−1	−2.93e−2	6.40e+0	−7.76e−1
d_1	2.98e−1	1.63e+0	1.90e−1	3.22e−1	2.62e−1
d_2	2.98e−2	5.01e−2	4.07e−1	−3.70e−2	−9.98e−2
d_3	−1.96e+0	−5.90e+0	−1.61e+0	−2.36e+0	−1.60e+0
d_4	−2.17e−1	−4.84e−1	−3.49e+0	2.58e−1	5.57e−1
d_5	3.09e+0	−1.81e+0	3.46e+0	4.31e+0	2.21e+0
d_6	3.92e−1	1.13e+0	7.54e+0	−4.40e−1	−6.44e−1

Table C.5: Coefficients of $g_n(z)$ and phase shift (ϕ_{0_n}) for the 2D case

a_k	ρ	ρu	ρv	ρw	ρE
a_1	−2.90e−3	2.46e−3	8.95e−4	4.36e−1	3.09e−3
a_2	2.98e−1	−2.70e−1	−6.85e−3	9.50e−2	−2.37e−1
a_3	3.02e−2	3.00e−2	−5.96e−4	−1.10e+0	−3.26e−2
a_4	−6.21e−1	2.15e+0	−1.41e−3	−2.73e−1	−8.47e−2
ϕ_{0_n}	1.21e+0	4.03e−1	−4.39e−5	3.37e−1	−1.38e+0

REFERENCES

[1] S. A. Gorton, I. Lòpez, and C. R. Theodore, "NASA Technology for Next Generation Vertical Lift Vehicles," *53rd AIAA Aerospace Sciences Meeting*, AIAA 2015-0949, Kissimmee, FL, Jan. 2015.

[2] S. Raghu, "Fluidic Oscillators for Flow Control," *Experiments in Fluids*, vol. 54, no. 2, p. 1455, Jan. 2013.

[3] S. S. Collis, R. D. Joslin, A. Seifert, and V. Theofilis, "Issues in Active Flow Control: Theory, Control, Simulation, and Experiment," *Progress in Aerospace Sciences*, vol. 40, no. 4, pp. 237 –289, 2004.

[4] M. Gad-el-Hak, "Flow Control," *Applied Mechanics Reviews*, vol. 42, pp. 261–292, 10 1989.

[5] M. Gad-el-Hak, A. Pollard, and J.-P. Bonnet, *Flow Control: Fundamentals and Practices*. Springer, 1998.

[6] M. Gad-el-Hak, "Flow Control: The Future," *Journal of Aircraft*, vol. 38, pp. 402–418, 3 2001.

[7] D. Greenblatt and I. J. Wygnanski, "The Control of Flow Separation by Periodic Excitation," *Progress in Aerospace Sciences*, vol. 36, no. 7, pp. 487 –545, 2000.

[8] L. N. Cattafesta and M. Sheplak, "Actuators for Active Flow Control," *Annual Review of Fluid Mechanics*, vol. 43, no. 1, pp. 247–272, 2011.

[9] L. D. Kral, "Active Flow Control Technology," *ASME FED, Technical Brief*, Jan. 2000.

[10] M. Amitay and A. Glezer, "Aerodynamic Flow Control Using Synthetic Jet Actuators," *Control of Fluid Flow*, P. Koumoutsakos and I. Mezic, Eds. Berlin, Heidelberg: Springer Berlin Heidelberg, 2006, ISBN: 978-3-540-36085-8.

[11] A. Seifert, T. Bachar, D. Koss, M. Shepshelovich, and I. Wygnanski, "Oscillatory Blowing, a Tool to Delay Boundary Layer Separation," *AIAA Journal*, vol. 31, no. 11, pp. 2052–2060, Nov. 1993.

[12] R. Seele, P. Tewes, R. Woszidlo, M. A. McVeigh, N. J. Lucas, and I. J. Wygnanski, "Discrete Sweeping Jets as Tools for Improving the Performance of the V-22," *Journal of Aircraft*, vol. 46, no. 6, pp. 2098–2106, 2009.

[13] J. Wilson, D. Schatzman, E. Arad, A. Seifert, and T. Shtendel, "Suction and Pulsed-Blowing Flow Control Applied to an Axisymmetric Body," *AIAA Journal*, vol. 51, no. 10, pp. 2432–2446, 2013.

[14] P. B. Martin, A. D. Overmeyer, P. E. Tanner, J. S. Wilson, and L. N. Jenkins, "Helicopter Fuselage Active Flow Control in the Presence of a Rotor," *Proceedings of the 70th American Helicopter Society Forum*, AHS 2014-002, Montréal, Canada, May 2014.

[15] L. P. Melton and M. Koklu, "Active Flow Control Using Sweeping Jet Actuators on a Semi-Span Wing Model," *54th AIAA Aerospace Sciences Meeting*, AIAA 2016-1817, San Diego, CA, Jan. 2016.

[16] Y. Yadlin, A. Shmilovich, and R. P. Narducci, "Application of Active Flow Control for Download Alleviation in Rotorcraft," *2017 AIAA Aviation Forum*, AIAA 2017-3045, Denver, CO, Jun. 2017.

[17] M. DeSalvo, E. Whalen, and A. Glezer, "High-Lift Enhancement using Fluidic Actuation," *48th AIAA Aerospace Sciences Meeting Including the New Horizons Forum and Aerospace Exposition*, AIAA 2010-863, Orlando, FL, Jan. 2010.

[18] G. Raman, S. Raghu, and T. Bencic, "Cavity Resonance Suppression Using Miniature Fluidic Oscillators," *5th AIAA/CEAS Aeroacoustics Conference and Exhibit*, AIAA 1999-1900, Bellevue, WA, 1999.

[19] J. Gregory and M. N. Tomac, "A Review of Fluidic Oscillator Development," *43rd AIAA Fluid Dynamics Conference*, AIAA 2013-2474, San Diego, CA, Jun. 2013.

[20] W. Warren, *Negative Feedback Oscillator*, US Patent 3158166, Nov. 1964.

[21] C. E Spyropoulos, "A Sonic Oscillator," *Proceedings of the Fluid Amplification Symposium*, vol. III, May 1964, pp. 27–52.

[22] G. Arwatz, I. Fono, and A. Seifert, "Suction and Oscillatory Blowing Actuator Modeling and Validation," *AIAA Journal*, vol. 46, no. 5, pp. 1107–1117, 2008.

[23] C. J. Campagnuolo and H. C. Lee, "Review of Some Fluid Oscillators," Harry Diamond Labs, Tech. Rep. AD0689445, 1969.

[24] C. Otto, P. Tewes, J. C. Little, and R. Woszidlo, "Comparison of Fluidic Oscillators and Steady Jets for Separation Control on a Wall-Mounted Hump," *2018 AIAA Aerospace Sciences Meeting*, AIAA 2018-1281, Kissimmee, FL, Jan. 2018.

[25] ——, "Comparison Between Fluidic Oscillators and Steady Jets for Separation Control," *AIAA Journal*, vol. 57, no. 12, pp. 5220–5229, 2019.

[26] S. Aram and A. DeJong, "Numerical Comparison Between Steady and Sweeping Jets for Active Flow Control Applications," *ASME Fluids Engineering Division Summer Meeting*, Montreal, QC, Jul. 2018.

[27] R. Woszidlo, F. Ostermann, and H.-J. Schmidt, "Fundamental Properties of Fluidic Oscillators for Flow Control Applications," *AIAA Journal*, vol. 57, no. 3, pp. 978–992, 2019.

[28] A. Kolmogorov, "The Local Structure of Turbulence in Incompressible Viscous Fluid for Very Large Reynolds' Numbers," *Akademiia Nauk SSSR Doklady*, vol. 30, pp. 301–305, 1941.

[29] D. R. Chapman, "Computational Aerodynamics Development and Outlook," *AIAA Journal*, vol. 17, no. 12, pp. 1293–1313, 1979.

[30] P. Moin and K. Mahesh, "Direct Numerical Simulation: A Tool in Turbulence Research," *Annual Review of Fluid Mechanics*, vol. 30, no. 1, pp. 539–578, 1998.

[31] P. K. Yeung, X. M. Zhaib, and K. R. Sreenivasan, "Extreme Events in Computational Turbulence," *Proceedings of the National Academy of Sciences of the USA*, vol. 112, no. 41, pp. 12 633–12 638, 2015.

[32] B. Baldwin and H. Lomax, "Thin-Layer Approximation and Algebraic Model for Separated Turbulent Flows," *16th AIAA Aerospace Sciences Meeting*, AIAA 1978-257, Huntsville, AL, Jan. 1978.

[33] S. R. Allmaras, F. T. Johnson, and P. R. Spalart, "Modifications and Clarifications for the Implementation of the Spalart-Allmaras Turbulence Model," *Seventh International Conference on Computational Fluid Dynamics*, ICCFD7-1902, Big Island, Hawaii, Jul. 2012, pp. 1–11.

[34] F. R. Menter, M. Kuntz, and R. Langtry, "Ten Years of Industrial Experience with the SST Turbulence Model," *Turbulence, Heat and Mass Transfer*, vol. 4, no. 1, pp. 625–632, 2003.

[35] B. E. Launder and D. Spalding, "The Numerical Computation of Turbulent Flows," *Computer Methods in Applied Mechanics and Engineering*, vol. 3, no. 2, pp. 269–289, 1974.

[36] M Strelets, "Detached Eddy Simulation of Massively Separated Flows," *39th AIAA Aerospace Sciences Meeting*, AIAA 2001-0879, Reno, NV, Jan. 2001.

[37] C. E. Lynch, "Advanced CFD Methods for Wind Turbine Analysis," PhD thesis, Georgia Institute of Technology, Atlanta, GA, May 2011.

[38] J. Hodara, A. Lind, A. Jones, and M. J. Smith, "Collaborative Investigation of the Aerodynamic behavior of Airfoils in Reverse Flow," *Proceedings of the 71st American Helicopter Society Forum*, AHS 2015-267, Virginia Beach, VA, May 2015.

[39] P. Sagaut, *Large Eddy Simulation for Incompressible Flows: an Introduction*. Springer Science & Business Media, 2006.

[40] U. Piomelli, "Wall-Layer Models for Large-Eddy Simulations," *Progress in Aerospace Sciences*, vol. 44, no. 6, pp. 437 –446, 2008.

[41] J. Larsson, S. Kawai, J. Bodart, and I. Bermejo-Moreno, "Large Eddy Simulation with Modeled Wall-Stress: Recent Progress and Future Directions," *Mechanical Engineering Reviews*, vol. 3, no. 1, pp. 15–00418–15–00418, 2016.

[42] P. Spalart, W. Jou, M Strelets, and S. Allmaras, "Comments on the Feasibility of LES for Wings, and on a Hybrid RANS/LES Approach," *Advances in DNS/LES*, vol. 1, pp. 4–8, 1997.

[43] P. R. Spalart, "Detached-Eddy Simulation," *Annual Review of Fluid Mechanics*, vol. 41, pp. 181–202, 2009.

[44] P. R. Spalart, S Deck, M. Shur, K. Squires, M. K. Strelets, and A Travin, "A New Version of Detached-Eddy Simulation, Resistant to Ambiguous Grid Densities," *Theoretical and Computational Fluid Dynamics*, vol. 20, no. 3, pp. 181–195, 2006.

[45] M. L. Shur, P. R. Spalart, M. K. Strelets, and A. K. Travin, "A Hybrid RANS-LES Approach with Delayed-DES and Wall-Modelled LES Capabilities," *International Journal of Heat and Fluid Flow*, vol. 29, no. 6, pp. 1638–1649, 2008.

[46] M. S. Gritskevich, A. V. Garbaruk, J. Schütze, and F. R. Menter, "Development of DDES and IDDES Formulations for the k-ω Shear Stress Transport

Model," *Flow, Turbulence and Combustion*, vol. 88, no. 3, pp. 431–449, Apr. 2012.

[47] U. Piomelli, E. Balaras, H. Pasinato, K. D. Squires, and P. R. Spalart, "The Inner-Outer Layer Interface in Large-Eddy Simulations with Wall-Layer Models," *International Journal of Heat and Fluid Flow*, vol. 24, no. 4, pp. 538 –550, 2003.

[48] L. Davidson and M. Billson, "Hybrid LES-RANS using Synthesized Turbulent Fluctuations for Forcing in the Interface Region," *International Journal of Heat and Fluid Flow*, vol. 27, no. 6, pp. 1028–1042, 2006.

[49] M. Sánchez-Rocha and S. Menon, "The Compressible Hybrid RANS/LES Formulation using an Additive Operator," *Journal of Computational Physics*, vol. 228, no. 6, pp. 2037–2062, 2009.

[50] W.-W. Kim and S. Menon, "An Unsteady Incompressible Navier-Stokes Solver for Large Eddy Simulation of Turbulent Flows," *International Journal for Numerical Methods in Fluids*, vol. 31, no. 6, pp. 983–1017, 1999.

[51] M. Germano, "Properties of the Hybrid RANS/LES Filter," *Theoretical and Computational Fluid Dynamics*, no. 17, pp. 225–231, 2004.

[52] J. Hodara, "Hybrid RANS-LES Closure for Separated Flows in the Transitional Regime," hdl.handle.net/1853/54995, PhD thesis, Georgia Institute of Technology, Atlanta, GA, May 2016.

[53] R. B. Langtry and F. R. Menter, "Correlation-Based Transition Modeling for Unstructured Parallelized Computational Fluid Dynamics Codes," *AIAA Journal*, vol. 47, no. 12, pp. 2894–2906, 2009.

[54] S. Gokoglu, M. Kuczmarski, D. Culley, and S. Raghu, "Numerical Studies of a Supersonic Fluidic Diverter Actuator for Flow Control," *5th AIAA Flow Control Conference*, AIAA 2010-4415, Chicago, IL, Jul. 2010.

[55] Fluent Inc., *FLUENT 6.3 User's Guide*, Lebanon, NH, Sep. 2006.

[56] O. Krüger, B. C. Bobusch, R. Woszidlo, and C. O. Paschereit, "Numerical Modeling and Validation of the Flow in a Fluidic Oscillator," *21st AIAA Computational Fluid Dynamics Conference*, AIAA 2013-3087, Jun. 2013.

[57] ANSYS Inc., *Ansys CFX-Solver Theory Guide*, Canonsburg, PA, Dec. 2006.

[58] M. Sitter, "Internal Flow of Fluidic Oscillators: A Numerical and Experimental investigation," Master's thesis, Delft University of Technology, 2015.

[59] R. J. Pandey and K.-Y. Kim, "Numerical Modeling of Internal Flow in a Fluidic Oscillator," *Journal of Mechanical Science and Technology*, vol. 31, no. 10, pp. 1–8, 2017.

[60] S. Aram, Y.-T. Lee, H. Shan, and A. Vargas, "Computational Fluid Dynamic Analysis of Fluidic Actuator for Active Flow Control Applications," *AIAA Journal*, vol. 56, no. 1, pp. 111–120, Jan. 2018.

[61] D Schatzman, J Wilson, L Marom, V Palei, A Seifert, and E Arad, "Suction and Oscillatory Blowing Interaction with Boundary Layers," *53rd AIAA Aerospace Sciences Meeting*, AIAA 2015-0808, Kissimmee, FL, Jan. 2015.

[62] J. Wilson, D. M. Schatzman, A. Seifert, E. Arad, L. Marom, N. Shay, and V. Palei, "Characterization of SaOB Actuators Interacting With Flat Plate Boundary Layers," *55th AIAA Aerospace Sciences Meeting*, AIAA 2017-1691, Grapevine, TX, Jan. 2017.

[63] M. T. Lakebrink, M. Mani, and C. Winkler, "Numerical Investigation of Fluidic Oscillator Flow Control in an S-Duct Diffuser," *55th AIAA Aerospace Sciences Meeting*, AIAA 2017-1455, Grapevine, TX, Jan. 2017.

[64] B Duda, M Wessels, E Fares, and V. Vatsa, "Unsteady Flow Simulation of a Sweeping Jet Actuator Using a Lattice-Boltzmann Method," *56th AIAA Aerospace Sciences Meeting*, AIAA 2016-1818, San Diego, CA, Jan. 2016.

[65] E. Fares, M. Wessels, Y. Li, P. Gopalakrishnan, R. Zhang, C. Sun, N. Gopalaswamy, P. Roberts, J. Hoch, and H. Chen, "Validation of a Lattice-Boltzmann Approach for Transonic and Supersonic Flow Simulations," *52nd AIAA Aerospace Sciences Meeting*, AIAA-2014-0952, National Harbor, MD, Jan. 2014.

[66] V. N. Vatsa, D. Casalino, J. C. Lin, and J. Appelbaum, "Numerical Simulation of a High-Lift Configuration with Embedded Fluidic Actuators," *32nd AIAA Applied Aerodynamics Conference*, AIAA 2014-2142, Atlanta, GA, Jun. 2014.

[67] V. N. Vatsa, B. Duda, E. Fares, and J. Lin, "Numerical Simulation of a High-Lift Configuration Embedded with High Momentum Fluidic Actuators," *8th AIAA Flow Control Conference*, AIAA 2016-3932, Washington, D.C., Jun. 2016.

[68] R. E. Childs, P. M. Stremel, J. A. Garcia, J. T. Heineck, L. K. Kushner, and B. L. Storms, "Simulation of Sweep-Jet Flow Control, Single Jet and Full Vertical Tail," *54th AIAA Aerospace Sciences Meeting*, AIAA 2016-0569, San Diego, CA, Jan. 2016.

[69] R. Tramel, R. Nichols, and P. Buning, "Addition of Improved Shock-Capturing Schemes to OVERFLOW 2.1," *19th AIAA Computational Fluid Dynamics Conference*, AIAA 2009-3988, San Antonio, TX, Jun. 2009.

[70] S. Aram and H. Shan, "Synchronization Effect of an Array of Sweeping Jets on a Separated Flow over a Wall-Mounted Hump," *2019 AIAA Aviation Forum*, AIAA 2019-3396, Dallas, TX, Jun. 2019.

[71] A. Shmilovich and Y. Yadlin, "Active Flow Control Computations: From a Single Actuator to a Complete Airplane," *AIAA Journal*, vol. 56, no. 12, pp. 4730–4740, 2018.

[72] E. A. Whalen, A. Shmilovich, M. Spoor, J. Tran, P. Vijgen, J. C. Lin, and M. Andino, "Flight Test of an Active Flow Control Enhanced Vertical Tail," *AIAA Journal*, vol. 56, no. 9, pp. 3393–3398, 2018.

[73] A. Shmilovich and V. N. Vatsa, "Practical Computational Methods for Airplanes with Flow-Control Systems," *AIAA Journal*, vol. 57, no. 1, pp. 35–52, 2019.

[74] N. T. Frink, D. L. Bonhaus, V. N. Vatsa, S. X. S. Bauer, and A. F. Tinetti, "Boundary Condition for Simulation of Flow Over Porous Surfaces," *Journal of Aircaft*, vol. 40, no. 4, pp. 692–698, 2003.

[75] S Darracq, S. Champagneux, and A. Corjon, "Computation of Unsteady Turbulent Airfoil Flows with an Aeroelastic AUSM+ Implicit Solver," *16th AIAA Applied Aerodynamic Conference*, AIAA 1998-2411, Albuquerque, NM, Jun. 1998.

[76] A. Jameson, W. Schmidt, and E. Turkel, "Numerical Solutions of the Euler Equations by Finite Volume Methods using Runge-Kutta Time-Stepping Schemes," *14th AIAA Fluid and Plasma Dynamics Conference*, AIAA 1981-1259, Palo Alto, CA, Jun. 1981.

[77] P. Roe, "Characteristic-Based Schemes for the Euler Equations," *Annual Review of Fluid Mechanics*, vol. 18, no. 1, pp. 337–365, 1986.

[78] B. van Leer, "Towards the Ultimate Conservative Difference Scheme. V. A Second-Order Sequel to Godunov's Method," *Journal of Computational Physics*, vol. 32, no. 1, pp. 101 –136, 1979.

[79] G.-S. Jiang and C.-W. Shu, "Efficient Implementation of Weighted ENO Schemes," *Journal of Computational Physics*, vol. 126, no. 1, pp. 202 –228, 1996.

[80] R. Borges, M. Carmona, B. Costa, and W. S. Don, "An Improved Weighted Essentially Non-Oscillatory Scheme for Hyperbolic Conservation Laws," *Journal of Computational Physics*, vol. 227, no. 6, pp. 3191 –3211, 2008.

[81] P. Buchmüller and C. Helzel, "Improved Accuracy of High-Order WENO Finite Volume Methods on Cartesian Grids," *Journal of Scientific Computing*, vol. 61, no. 2, pp. 343–368, Nov. 2014.

[82] C.-W. Shu, "Essentially Non-Oscillatory and Weighted Essentially Non-Oscillatory Schemes for Hyperbolic Conservation Laws," *Advanced Numerical Approximation of Nonlinear Hyperbolic Equations: Lectures given at the 2nd Session of the Centro Internazionale Matematico Estivo (C.I.M.E.) held in Cetraro, Italy, June 23–28, 1997*, A. Quarteroni, Ed. Berlin, Heidelberg: Springer Berlin Heidelberg, 1998, pp. 325–432.

[83] R. Zhang, M. Zhang, and C.-W. Shu, "On the Order of Accuracy and Numerical Performance of Two Classes of Finite Volume WENO Schemes," *Communications in Computational Physics*, vol. 9, no. 3, pp. 807–827, 2011.

[84] F. Ducros, F. Laporte, T. Soulères, V. Guinot, P. Moinat, and B. Caruelle, "High-Order Fluxes for Conservative Skew-Symmetric-like Schemes in Structured Meshes: Application to Compressible Flows," *Journal of Computational Physics*, vol. 161, no. 1, pp. 114 –139, 2000.

[85] E. Turkel, "Preconditioning Techniques in Computational Fluid Dynamics," *Annual Review of Fluid Mechanics*, vol. 31, no. 1, pp. 385–416, 1999.

[86] R. Pletcher, J. Tannehill, and D. Anderson, *Computational Fluid Mechanics and Heat Transfer*, 3rd. note in computational, physical processes in mechanics, and thermal sciences, 2013.

[87] J Blazek, *Computational Fluid Dynamics: Principles and Applications*, 3rd. Butterworth-Heinemann, 2015.

[88] T. P. Gallagher, "A Generalized MacCormack Scheme for Low Mach Number Chemically-Reacting Large-Eddy Simulations," PhD thesis, Georgia Institute of Technology, Atlanta, GA, Jun. 2017.

[89] J. M. Weiss and W. A. Smith, "Preconditioning Applied to Variable and Constant Density Flows," *AIAA Journal*, no. 11, pp. 2050–2057, 1995.

[90] E. Turkel, "Preconditioning Methods for Low-Speed Flows," *14th AIAA Applied Aerodynamics Conference*, AIAA 1996-2060, New Orleans, LA, Jun. 1996.

[91] S Yoon and A Jameson, "Lower-Upper Symmetric-Gauss-Seidel Method for the Euler and Navier-Stokes Equations," *AIAA Journal*, vol. 26, no. 9, pp. 1025–1026, 1988.

[92] F. Liu and X. Zheng, "A Strongly Coupled Time-3ing Method for Solving the Navier-Stokes and k-ω Turbulence Model Equations with Multigrid," *Journal of Computational Physics*, vol. 128, pp. 289–300, Oct. 1996.

[93] A. Rizzi, P. Eliasson, I. Lindblad, C. Hirsch, C. Lacor, and J. Haeuser, "The Engineering of Multiblock/Multigrid Software for Navier-Stokes Flows on Structured Meshes," *Computers and Fluids*, vol. 22, no. 2, pp. 341 –367, 1993.

[94] S. L. Krist, R. T. Biedron, and C. L. Rumsey, "CFL3D User's Manual (version 5.0)," *cfl3d.larc.nasa.gov - last accessed 12/16/2018*, 2013.

[95] J. Häuser, P. Eiseman, Y. Xia, and C. Zheming, "Parallel Multiblock Structured Grids," *Handbook of Grid Generation*, CRC Press, 1999, ch. 12.

[96] R. L. Meakin, "Composite Overset Structured Grids," *Handbook of Grid Generation*, CRC Press, 1999, ch. 11.

[97] W. H. Press, S. A. Teukolsky, W. T. Vetterling, and B. P. Flannery, *Numerical Recipes 3rd Edition: The Art of Scientific Computing*, 3rd ed. USA: Cambridge University Press, 2007, ISBN: 0521880688.

[98] A. Roshko, "On the Development of Turbulent Wakes from Vortex Streets," Tech. Rep. NACA technical report 1191, 1954.

[99] J. Kim, D. Kim, and H. Choi, "An Immersed-Boundary Finite-Volume Method for Simulations of Flow in Complex Geometries," *Journal of Computational Physics*, vol. 171, no. 1, pp. 132 –150, 2001.

[100] J.-I. Choi, R. C. Oberoi, J. R. Edwards, and J. A. Rosati, "An Immersed Boundary Method for Complex Incompressible Flows," *Journal of Computational Physics*, vol. 224, no. 2, pp. 757 –784, 2007.

[101] K. Karagiozis, R. Kamakoti, and C. Pantano, "A Low Numerical Dissipation Immersed Interface Method for the Compressible Navier-Stokes Equations," *Journal of Computational Physics*, vol. 229, no. 3, pp. 701 –727, 2010.

[102] C. Rumsey, "Turbulence Modeling Resource," *Turbulence Model Benchmarking Working Group, NASA Langley Research Center*, 2013, http://turbmodels.larc.nasa.gov/ - last accessed 12/07/2018.

[103] P. Woodward and P. Colella, "The Numerical Simulation of Two-Dimensional Fluid Flow With Strong Shocks," *Journal of Computational Physics*, vol. 54, no. 1, pp. 115 –173, 1984.

[104] A. Harten, "High Resolution Schemes for Hyperbolic Conservation Laws," *Journal of Computational Physics*, vol. 49, no. 3, pp. 357 –393, 1983.

[105] J. J. Quirk, "A Contribution to the Great Riemann Solver Debate," *International Journal for Numerical Methods in Fluids*, vol. 18, Mar. 1994.

[106] V. Titarev and E. Toro, "Finite-Volume WENO Schemes for Three-Dimensional Conservation Laws," *Journal of Computational Physics*, vol. 201, no. 1, pp. 238 –260, 2004.

[107] D. M. Driver and H. L. Seegmiller, "Features of Reattaching Turbulent Shear Layer in Divergent Channel Flow," *AIAA Journal*, vol. 23, no. 2, pp. 173–171, Feb. 1985.

[108] D. C. Jespersen, T. H. Pulliam, and M. L. Childs, "OVERFLOW Turbulence Modeling Resource Validation Results," NASA Ames Research Center, Tech. Rep. NAS-2016-01, 2016.

[109] A. Avdis, S. Lardeau, and M. Leschziner, "Large Eddy Simulation of Separated Flow over a Two-dimensional Hump with and without Control by Means of a Synthetic Slot-jet," *Flow, Turbulence and Combustion*, vol. 83, no. 3, pp. 343–370, 2009.

[110] E. K. Guseva, A. V. Garbaruk, and M. K. Strelets, "Assessment of Delayed DES and Improved Delayed DES Combined with a Shear-Layer-Adapted Subgrid Length-Scale in Separated Flows," *Flow, Turbulence and Combustion*, vol. 98, no. 2, pp. 481–502, 2017.

[111] A. Uzun and M. R. Malik, "Large-Eddy Simulation of Flow over a Wall-Mounted Hump with Separation and Reattachment," *AIAA Journal*, vol. 56, no. 2, 2018.

[112] A. Probst, D. Schwamborn, A. Garbaruk, E. Guseva, M. Shur, M. Strelets, and A. Travin, "Evaluation of Grey Area Mitigation Tools within Zonal and Non-Zonal RANS-LES Approaches in Flows with Pressure Induced separation," *International Journal of Heat and Fluid Flow*, vol. 68, pp. 237–247, 2017.

[113] T. M. Shih, C. H. Tan, and B. C. Hwang, "Effects of Grid Staggering on Numerical Schemes," *International Journal for Numerical Methods in Fluids*, vol. 9, no. 2, pp. 193–212, 1989.

[114] J. Lefebvre, A. R. Jones, L. Jarman, and M. J. Smith, "Experimental and Numerical Investigation of Airfoil Performance in Cylinder Wake," AIAA 2018-3232, Fluid Dynamics Conference, Atlanta, GA, Jun. 2018.

[115] A. L. Grubb, A. Moushegian, D. J. Heathcote, and M. J. Smith, "Physics and Computational Modeling of Nonlinear Transverse Gust Encounters," AIAA 2020-0080, AIAA Scitech 2020 Forum, Orlando, FL, Jan. 2020.

[116] T. J. Burrows, B. Vukasinovic, M. T. Lakebrink, M. Mani, and A. Glezer, "Control of Flow Distortion in Offset Diffusers using Trapped Vorticity," *International Journal of Heat and Fluid Flow*, vol. 75, pp. 122 –134, 2019.

[117] N. K. Koukpaizan, D. J. Heathcote, A. Glezer, and M. J. Smith, "Numerical Simulation of Fluidic Oscillators for Flow Control," *Proceedings of the 75th Annual VFS Forum and Technology Display*, VFS 2019-050, Philadelphia, PA, May 2019.

[118] S. A. Polsky and T. A. Ghee, "Application and Verification of Internal Boundary Conditions for Antenna Mast Wake Predictions," *Journal of Wind Engineering and Industrial Aerodynamics*, vol. 96, no. 6, pp. 817 –830, 2008, 5th International Colloquium on Bluff Body Aerodynamics and Applications.

[119] M. N. Tomac and J. W. Gregory, "Internal Jet Interactions in a Fluidic Oscillator at Low Flow rate," *Experiments in Fluids*, vol. 55, no. 1730, 2014.

[120] M. N. Tomac and J. W. Gregory, "Internal Flow Physics of a Fluidic Oscillator Spray in the Transition Regime," *Atomization and Sprays*, vol. 26, no. 7, pp. 673–686, 2016.

[121] ——, "Oscillation Characteristics of Mutually Impinging Dual Jets in a Mixing Chamber," *Physics of fluids*, vol. 30, no. 11, p. 117 102, 2018.

[122] F. Ostermann, R. Woszidlo, S. Gaertlein, C. Nayeri, and C. O. Paschereit, "Phase-Averaging Methods for a Naturally Oscillating Flow Field," *52nd Aerospace Sciences Meeting*, AIAA 2014-1142, National Harbor, MD, Jan. 2014.

[123] V Jhaveri, M DeSalvo, A Glezer, and J Colton, "Effects of Manufacturing Parameters on Performance of Fluidic Oscillators for Aerodynamic Flow Control," *Proceedings of the Institution of Mechanical Engineers, Part G: Journal of Aerospace Engineering*, 2018.

[124] F. von Gosen, F. Ostermann, R. Woszidlo, C. Nayeri, and C. O. Paschereit, "Experimental Investigation of Compressibility Effects in a Fluidic Oscillator," *53rd AIAA Aerospace Sciences Meeting*, AIAA 2015-0782, Kissimmee, FL.

[125] L. P. Melton, M. Koklu, M. Andino, and J. C. Lin, "Active Flow Control via Discrete Sweeping and Steady Jets on a Simple-Hinged Flap," *AIAA Journal*, vol. 56, no. 8, pp. 2961–2973, 2018.

[126] G. Tabor and M. Baba-Ahmadi, "Inlet Conditions for Large Eddy Simulation: A Review," *Computers & Fluids*, vol. 39, no. 4, pp. 553 –567, 2010.

[127] C. Rumsey, N. Schaeffler, I. Milanovic, and K. Zaman, "Time-Accurate Computations of Isolated Circular Synthetic Jets in Crossflow," *Computers & Fluids*, vol. 36, no. 6, pp. 1092 –1105, 2007.

[128] N. K. Koukpaizan, C. J. Peterson, A. Glezer, and M. J. Smith, "Towards Full-Scale Fuselage Drag Reduction Computations using Fluidic Oscillators," *Abstract accepted for the 76th Annual VFS Forum and Technology Display*, Virginia Beach, VA, Oct. 2020.

[129] N. Jarrin, R. Prosser, J. C. Uribe, S. Benhamadouche, and D. Laurence, "Reconstruction of Turbulent Fluctuations for Hybrid RANS/LES Simulations using a Synthetic-Eddy Method," *International Journal of Heat and Fluid Flow*, vol. 30, pp. 435–442, 3 2009.

[130] M. L. Shur, P. R. Spalart, M. K. Strelets, and A. K. Travin, "Synthetic Turbulence Generators for RANS-LES Interfaces in Zonal Simulations of Aerodynamic and Aeroacoustic Problems," *Flow Turbulence and Combustion*, vol. 93, pp. 63–92, 1.

[131] A. Skillen, A. Revell, and T. Craft, "Accuracy and Efficiency Improvements in Synthetic Eddy Methods," *International Journal of Heat and Fluid Flow*, vol. 62, pp. 386–394, 2016.

[132] C. Peterson, B. Vukasinovic, M. J. Smith, and A. Glezer, "Control of a Closed Separation Domain in Adverse Pressure Gradient Over a Curved Surface," *57th AIAA Aerospace Sciences Meeting*, AIAA 2019-1900, San Diego, CA, Jan. 2019.

[133] N. K. Koukpaizan, C. J. Peterson, A. Glezer, and M. J. Smith, "A Coupled Numerical/Experimental Study of Flow Separation Suppression over a Curved Surface using Fluidic Oscillators," *Proceedings of the 45th European Rotorcraft Forum*, ERF 2019-014, Warsaw, Poland, Sep. 2019.

[134] D. Hirsch and M. Gharib, "Schlieren Visualization and Analysis of Sweeping Jet Actuator Dynamics," *AIAA Journal*, vol. 56, no. 8, pp. 2947–2960, 2018.

[135] G. Constantinescu and S. K. Lele, "Large Eddy Simulation of a Near Sonic Turbulent Jet and Its Radiated Noise," *39th AIAA Aerospace Sciences Meeting & Exhibit*, AIAA 2001-0376, Reno, NV, Jan. 2001.

[136] P. Sagaut and V. Levasseur, "Sensitivity of Spectral Variational Multiscale Methods for Large-Eddy Simulation of Isotropic Turbulence," *Physics of Fluids*, vol. 17, no. 3, p. 035 113, 2005.

[137] T. Colonius and S. K. Lele, "Computational aeroacoustics: Progress on nonlinear problems of sound generation," *Progress in Aerospace Sciences*, vol. 40, no. 6, pp. 345–416, 2004.

[138] T. F. Fric and A. Roshko, "Vortical Structure in the Wake of a Transverse Jet," *Journal of Fluid Mechanics*, vol. 279, pp. 1–47, 1994.

[139] H. Matsuda, S.-i. Iida, and M. Hayakawa, "Coherent Structures in a Three-Dimensional Wall Jet," *Journal of Fluids Engineering*, vol. 112, no. 4, pp. 462–467, Dec. 1990.

[140] A. J. Chorin, "A Numerical Method for Solving Incompressible Viscous Flow Problems," *Journal of Computational Physics*, vol. 135, no. CP975716, pp. 1128–125, 1997 (reprint of the 1967 paper).

[141] R. T. Biedron, J. M. Derlaga, P. A. Gnoffo, D. P. Hammond, W. T. Jones, B. Kleb, E. M. Lee-rausch, E. J. Nielsen, M. A. Park, C. L. Rumsey, J. L. Thomas, and W. A. Wood, "FUN3D Manual: 13.3," NASA Langley Research Center, Tech. Rep. NASA/TM–2018–219808, 2018.

VITA

Nicholson Konrad Koukpaizan was born on June 2, 1994 in Cotonou, Benin. He grew up in Benin, attending primary and middle school at *La Providence* and *College Catholique Père Aupiais* respectively. He later moved to Mali where he completed high-school at *Lycée Français Liberté de Bamako*. Early on, he developed in interest for mathematics and physics, leading him to higher education in applied sciences.

After graduating high-school in 2010, he moved to Canada. He obtained his Bachelor degree in Aerospace Engineering from Polytechnique Montreal in May 2015. He then joined Georgia Tech in August 2015 to pursue his graduate studies, where he worked as a graduate research assistant under the guidance of Professor Marilyn Smith. He obtained his Masters degree from Georgia Tech in 2017 and was a recipient of a Vertical Flight Foundation scholarship in 2018. Outside of research, he enjoys playing the piano, singing and biking.